Design of Miniature Mobile Robots
for
Non-Destructive Evaluation

by
Markus Friedrich

A thesis presented in
fulfilment of the requirement
for the degree of Doctor of Philosophy.

Centre for Ultrasonic Engineering
Department of Electrical and Electronic Engineering
University of Strathclyde

2007

Copyright

Acknowledgement

Abstract

Small, high performance and low cost inspection vehicles, working together as teams of autonomous agents, are well suited to remote inspection tasks in areas that are only accessible through narrow passageways or are hazardous for humans. In particular, the evaluation of complex infrastructures that consist of numerous components with small structural dimensions motivate the application of robotic micro systems for inspection and on-site manipulation. This thesis describes the development of a synergetic multi-robot inspection system for Non-Destructive evaluation (NDE) of engineering structures, enabling magnetic (flux leakage and eddy current), ultrasonic and visual techniques in a complementary fashion. Particular emphasis is placed on the design of the miniature autonomous climbing vehicles, the Eddy Current and Magnetic Flux Leakage payload, the positioning and host system and the fusion of the different NDE data.

Table of Contents

List of Figures

List of Tables

Chapter 1

Introduction

1.1 Background

Renewable energy currently accounts for seven percent of the EU energy mix [288]. While it is ecologically crucial to achieve the targeted increase to 12% by 2010, taking into account that global energy demands will rise by 50% − 60% by 2030 [287], it is important to maintain and ensure safety of the infrastructure that supports existing energy supplies such as pipelines, railway networks, power transmissions systems, bridges as well as bulk cargo vessels, offshore platforms, storage tanks and the power generating plants themselves.

These assets need to be periodically inspected subject to the regulations of the respective controlling bodies in order to prevent unscheduled and costly outages, catastrophic failures which often lead to environmental disasters and loss of life. In particular the detection of corrosion, erosion, and fatigue cracks in welded regions is crucial. For example, statistics inidcate that 90% of ship failures are attributed to these defects, in many cases causing total loss of the vessel and often resulting in devastating environmental damage [175]. Furthermore, the network of buried and aboveground pipelines in the US consist of approximately 150,000 km of gathering lines, 450,000 km of transmission pipelines, and 1,400,000 km of distribution pipelines [2], and there are over 10 million kilometres of pipelines in Europe. Spills of hazardous fluids from these into the environment outnumber all other sources of contamination including the above mentioned tanker spills in oceans. Up to 4 million gallons of oil are leaked into the environment each year. Construction or replacement costs of a steel pipelines are of the order of £500K per km [49, 142, 181], and as the pipelines operate at as much 70% of their yield strength, companies spend over £3000K annually for detection and repair of leaks in urban and subur-

ban areas. Similarly, cleaning and inspecting a pair of tanks for floating production storage and offloading at offshore platforms costs £25–30K and involves 60–70 man days of work [190, 191]. Those manual inspections are not only time-consuming, but may also give false readings: PANI trials, carried out to assess the effectiveness of manual inspections [49], have shown that operators detect only 50 per cent of defects, which is due to the monotonous nature of the work and the fact that efficient concentration lasts for only 30–60 minutes. Furtherore, the inspection and repair of these engineering structures may involve the costly installation of scaffoldings or gondolas and is highly dangerous — Statistically two workers are killed per week on construction sites [181] and in the light of these facts, exploiting robotic technology is essential both for improving safety and accuracy and reducing cost.

Miniature mobile robots, that offer high mechanical and electrical robustness, flexibility, reliability and a high degree of autonomy with respect to energy, are well suited for such inspection of structures and are particularly effective in areas that are only accessible through narrow passageways or hazardous for humans due to biological, radioactive or chemical contamination. Moreover, the inspection task can be extended to a group of heterogeneous robots collaborating as a team to share information and resources. Though each robot is specialised and has only limited sensing, computation, and communication capabilities, the team is capable of performing more complex and demanding missions. Such distributed robotic systems may incorporate a large number of cooperating vehicles deploying sensors for purposes of defect detection and characterisation. Each robot can be built much smaller, lighter and less expensive. Furthermore, as individual robots are expendable, reliability can be obtained in numbers, facilitating system redundancy: if a single robot fails, only limited capabilities are lost, and the team can still continue the task with the remaining robots. In this way, the role of a human practitioner in such a Non-Destructive Evaluation (NDE) scenario is safer and more intellectually exciting.

1.2 Aims of this Thesis

- Design of a prototype inspection vehicle with particular focus on locomotion system, climbing technique, miniature overall size and robustness.

- Demonstrate complete autonomy of this mobile robot with regard to control, power management and communication

- Implementation and evaluation of a low cost 3D positioning system

2

- Expansion towards a heterogeneous team of inspection robots

- Development and evaluation of on board Eddy Current test equipment for autonomous operation

- Integration of required hardware for Visual Inspection and automated weld following

- Development and evaluation of a novel inspection technique based on Magnetic Flux Leakage inspection.

- Reliable interpretation of the collected NDE data.

- Integration of a set of air coupled ultrasonic transducers for Lamb Wave Inspection of thin plates

- Software development of a Graphical User Interface for overall system control

- Fusion and statistical interpretation of the collected NDE data

1.3 Contributions to the Field
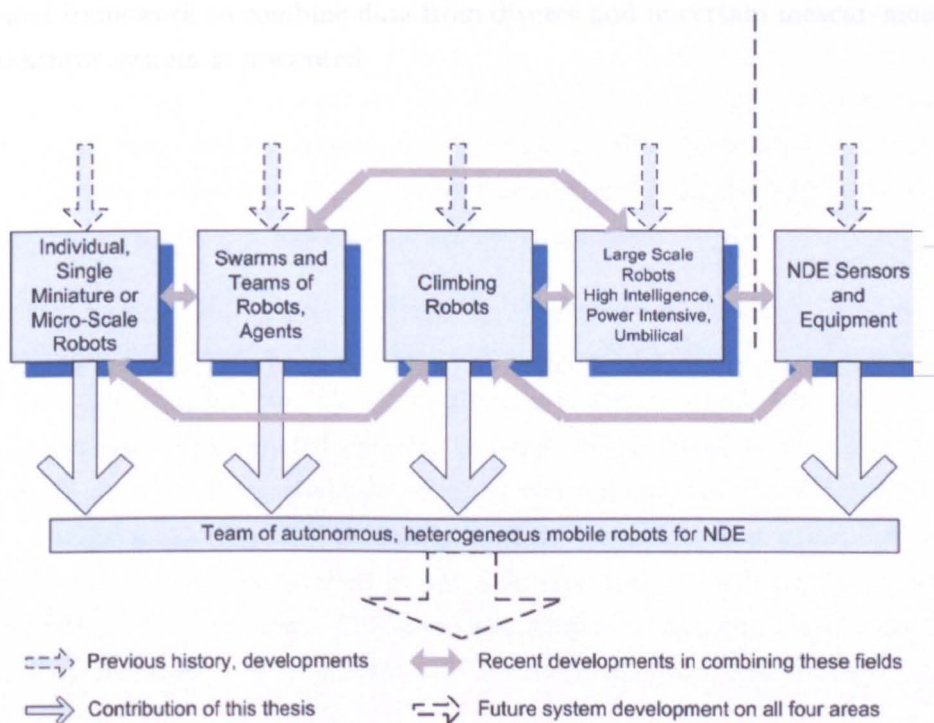
Figure 1.1: Contribution to the field of robotics and Non-Destructive Evalutaion.

3

Previous research in the field of robotics has been concentrated on the separate areas of individual miniature- and micro robots, swarms and teams of robots, climbing robots and sophisticated and complex large scale robots with high computing power and intelligence. In parallel, the development of NDE equipment has taken place, as visualised in Fig. 1.1. Recently work about efforts in fusing two or three of these fields has been reported, such as the development of teams of miniature robots or individual large scale robots for NDE tasks or miniature climbing robots. This thesis presents the successful development of a team of autonomous climbing robots of small size and capable of performing a variety of NDE tasks. Hence, for the first time all of the above mentioned areas are combined in a single inspection system. As part of this system, the first modular inspection vehicle has been built that offers complete autonomy, versatility and flexibility, while showing a size and weight reduction of factor 3 compared with designs that have previously been reported. Furthermore, a novel alternative for the Magnetic Flux Leakage Inspection technique has been developed which utilises the field of the magnetic wheels of the inspection robot thereby significantly reducing the overall vehicle size. This automatically collected data from multiple sources is combined by applying techniques for NDE data fusion to reduce uncertainty and create intelligible images of the test specimen. Thus, as an additional major contribution to the field of NDE, a formal framework to combine data from diverse and uncertain measurements in a multi-sensor system is presented.

1.4 Thesis Content

To identify the current state of the art of the numerous areas with relevance to the development of a team of miniature robotic sensor agents for NDE, *Chapter 2* contains a summary of an extensive literature review. The relevant robotic technology encompasses the fields of miniature and micro-robotic systems, groups and teams of robots, climbing robots, robots for NDE tasks and mobile robot positioning. In addition, a general review of NDE is carried out and a range of inspection techniques is presented.

Chapter 3 contains a detailed description of the final vehicle design, which is the result of a series of iteration steps. After an initial discussion about the optimal locomotion mechanism and climbing technique, the individual modular components are introduced and alternative design concepts investigated. The issue of mobile robot positioning is addressed in Section 3.3, where the absolute positioning system and the method of relative position measurement are presented. Furthermore, as the overall inspection system has to be regarded as a whole with all elements being linked to each other, this Chapter also covers both the programs running on the host and the programs running on board of the vehicles.

Chapter 4 focuses on the vehicle payload for Eddy Current Inspection. A description of the underlying theory is followed by a brief presentation of results which have been obtained by simulations. The design of the coils and the electronic drive circuitry are described in Section 4.4. Section 4.5 then presents the experimental results that have been obtained with this payload, including the required coordinate transformations and a probability of detection analysis.

Chapter 5 covers the vehicle payloads for Magnetic Flux Leakage, Ultrasonic and Visual inspection. Section 5.2 explains the underlying theory for Magnetic Flux Leakage Inspection followed by a presentation of results which have been obtained by simulations. Non-centred defects, the theoretical effect of lift-off and a high permeable back yoke are investigated using two dimensional simulations and complemented by a 3D Model of the magnetic field created by the wheels. A series of experimental results is presented in the following section with particular focus on identification of the optimum Hall array configuration. Sections 5.5 and 5.6 contain the theory and results of Ultrasonic and Visual Inspections, respectively.

In *Chapter 6* techniques for fusing the NDE data obtained in the preceding Chapters is employed, and images based on Bayesian Analysis and Dempster Shafer

Evidence Theory created. In this way, an intelligible statistical interpretation of the detected defects is obtained.

The performance of the overall inspection system is discussed in *Chapter 7*, with particular focus on the positioning system, the communication link and the micro controller. Additionally, the different NDE inspection techniques are compared and evaluated.

A conclusion of the thesis is given in *Chapter 8*, which also contains suggestions of where further work could start most reasonably.

1.5   Publications to Date arising from this Thesis

M. Friedrich, L. Gatzoulis, G. Hayward and W. Galbraith, "Small Inspection Vehicles for Non-Destructive Testing Applications," *Proc. of 8th International Conference on Climbing and Walking Robots*, 2006, pp. 927—934.

M. Friedrich, L. Gatzoulis, G. Hayward and W. Galbraith, "Small Inspection Vehicles for Non-Destructive Testing Applications," *Proc. of the 44th Annual British Conference on NDT*, Harrogate, 13-15 September 2005.

M. Friedrich, W. Galbraith and G. Hayward, "Buildings, Bats and Robots," *Royal Society Science Exhibition*, Glasgow, 12. – 14. September 2006.

M. Friedrich, G. Hayward and W. Galbraith, "Autonomous Mobile Robots for Ultrasonic NDE," *Proc. of 2006 IEEE International Ultrasonics Symposium*, Vancouver, 2006, pp. 902—905.

M. Friedrich, W. Galbraith and G. Hayward, "Miniature Robots Help Ensure Safety," *Set for Britain - Early Stage Researcher*, Poster Presentation and Reception at the House of Commons, Westminster, London, 2007.

M. Friedrich, W. Galbraith and G. Hayward, "A Heterogeneous Team of Robotic Sensors for Inspection of Structures", *IEEE Transactions on Robotics*, 2007, *under revision.*

M. Friedrich, W. Galbraith and G. Hayward, "Data Fusion in Automated Robotic Inspection Systems," *Proc. of the 44th Annual British Conference on NDT*, NDT Conference and Materials Testing Exhibition, 2007.
M. Friedrich, W. Galbraith and G. Hayward, "Data Fusion in Automated Robotic Inspection Systems," *Insight (BINDT Journal)*, 2007, under revision.

Chapter 2

Robotics and Non-destructive Evaluation

2.1 Miniature and Micro-Robotic Systems

As indicated in Fig. 1.1, there have been numerous reports in literature recently about the development of single miniature or micro- scale mobile robots. The motivation for size reduction is based on the fact that if the robot is scaled equally in all three dimensions, its weight will scale down with the third power of the scaling factor [10], which is a key issue when considering potential climbing capabilities of the vehicle. The term 'microrobot' is commonly separated into three different subcategories [23, 63, 82, 87, 115, 167]: Miniature Robots, Microelectromechanical Systems (MEMS) based Microrobots and Nanorobots. Miniature Robots have a size of the order of a few cubic centimetres, are fabricated by assembling conventional miniature components and generate forces comparable to those applied by human operators during fine manipulation. The size of Microrobots is of the order of a few cubic micrometers. Therefore, the structure of these vehicles can be conceived as a modified integrated circuit containing micro motors, sensors and processing circuitry. These type of robots may be as small as 60 x 250 x 10 μm [67]. Ultimately, Nanomachines and Nanorobots have sizes comparable to those of biological cells being in the order of several hundred nanometres.

For inspection of engineering structures, the dimensions of the robots of the miniature category are regarded as most appropriate. The main challenges of scaling down these vehicles emerge from space and power restrictions [48, 198, 210, 229] and have been resolved most successfully in the 'Alice' robot. Five years of development at the Institute of Robotics at the Swiss Federal Institute of Technology

Figure 2.1: Prototype evolution of miniature robot Alice [40].

and several iteration processes have led to the 20 x 20 x 20 mm small prototype shown in Fig. 2.1, which comprises two bidirectional watch motors with aluminium wheels and rubber tires, a PIC16F84 micro controller and three silver-oxide batteries, supported by a plastic frame. Interconnection of all the vital components is facilitated by a flexible PCB [40, 41, 42, 81]. The robots weigh 11 g, have a power consumption of 12–18 mW and several hundreds have been built so far and sold as a commercialised product.

A European consortium is currently developing a cluster of mobile miniature robots slightly smaller than the 'Alice' machines for micro- manipulation and assembly in a micro factory [6, 75, 301]. These vehicles comprise a piezo electric module for high velocity locomotion at nanometric resolution and an adhoc infrared link for wireless communication. Positioning control with micrometer accuracy is achieved utilising a Moiré Fringe based machine vision system. An induction coil provides power to the on board electronics during operation via a specially designed floor. The same application area has been targeted by other researchers using an 8 mm long, 6 mm wide and 6 mm high omni-directional miniature robot which is based on a novel castor structure and a 2.1 x 2.1 x 1.3 mm electromagnetic micromotor [130]. However, the main application areas of the 'Alice' robots are well-controlled indoor environments under laboratory conditions.

For real world applications, miniature robots are slightly larger: A prototype measuring 41 x 30 x 20 mm has been developed for investigation of the interaction between robots and animals in mixed societies [41], and a wireless miniature pipe robot with a diameter of 9.5 mm and a length of 66 mm is available from Denso Corporation [162, 167]. The latter features a total power consumption of 65 mW, transmits images from the inside of the pipe to an external host and employs a microwave module for energy supply and communication.

The field of military reconnaissance and surveillance completes the major application areas of miniature robots, although it must be born in mind that the number of application areas is continuously expanding: A set of cylindrical 'Scout' robots of 11 cm length and 4 cm diameter has been designed for independent exploration and mapping of unknown terrains by transmitting a video from a small on board camera to a remote human teleoperator [69, 187, 188, 211]. The small size of these robots is important to avoid detection, they use wheels to travel on smooth surfaces and have spring loaded tails which enable them to jump over over 30 cm high obstacles. Scouts are deployed by larger 'Ranger' robots, and may work together as described in the following section.

2.2   Groups and Teams of Robots

Collective autonomous agents can exploit information derived from multiple disparate viewpoints and simultaneously collect information from different locations [96, 161]. These multirobot systems display advantages in comparison to single units. For example, they offer simultaneous sensing and action from physically different positions, reconfigurability of the system, redundancy and the ability to achieve linear performances via division of labour, dynamic task allocation and adaptive behaviour approaches [7, 14, 89, 91, 125, 129].

In this context, large size robotic sensor agents for complex environmental monitoring have been developed [169, 170, 171] and cooperative repair capability in a team of two robots has been studied [17, 18]. The first results in the field of collaborating robots have been obtained by the 'Millibots' project [96, 97, 161, 222]: A team of heterogeneous centimetre scale robots exploits ultrasonic distance measurements from each moving robot to three stationary robots for collective mapping and exploration of unknown environments. In this leap-frogging approach, the stationary robots serve as beacons, and the position of the moving robot is obtained by trilateration. Hence, neither landmarks nor previously deployed beacons are required. The robots reach 20 cm/s on smooth surfaces, have a range of about 30-50 m per battery charge and a run time of 90 minutes. They comprise infra red sensors for short range obstacle detection, a miniature CMOS video camera with transmitter and pyro-electric sensors for detection of humans and other warm bodies. Heterogeneity of the Millibots arises from functional rather than physical differences.

Cooperation between robots has been developed at a higher level by establishing physical interconnections between team members [36, 68, 102, 103, 104, 156, 157,

163, 228]: the 'S-bots' are currently the state of the art of robots with self-assembling capabilities. They either act independently as a full autonomous mobile robot or self-assemble into a 'Swarm-bot' by using grippers to perform collective transportation when encountering larger obstacles. This 'Swarm-bot' concept is a compromise between collective and self-reconfigurable robotics. Similarly, a team of modular 'M-Tran III' robots has been developed that collectively assemble and disassemble into different shapes to move across rough terrain [178]. Each unit has a 6.5 cm x 6.5 cm footprint and consists of two motorised rounded blocks with a U-shaped cross section, connected by a rigid bar.

Swarm robotics, a subset of multi agent systems research, focuses on large teams of small robots working together towards a common goal [59, 60, 61]. Originally inspired by the capabilities of natural swarms such as termites, wasps, and ants, it is a novel paradigm for the coordination of multiple robots. The concept is aimed to find application in the inspection of complex engineered structures such as turbines: A simplified two dimensional turbine environment has been created by the Swarm-Intelligent Systems Group at the École Polytechnique Fédérale Lausanne for evaluation purposes. While neither the issue of actual flaw detection nor the problem of how to attach the vehicles on a real cylindrical structure have been addressed, focus has been on individual and group motion in the turbine scenario. The swarm for this study consisted of 40 'Alice' robots presented in Section 2.1, which were small enough to be released into a real turbine without disassembling it. The individual robots were able to discriminate between team mates, blades and external walls in the arena by utilising exclusively on board sensors. To understand general properties of the dynamics of the swarm engaged in an inspection task, the probabilistic population dynamics of the swarm, the average ratios of robots within a certain state, and the spatial distribution of the swarm in the environment in terms of a spatial probability density functions have been modelled.

However, issues involving how to coordinate a team of robots and how to represent the different capabilities of individuals are still open fields of research. There have been a variety of studies on efficient control and navigation of a group of mobile robots moving to target locations to achieve multiple tasks. Most algorithms are proposed for the task assignment problem in static environments, such as a dynamic tabu search algorithm [111], a neural network approach [260], the graph matching algorithm [127], a distributed auction algorithm [237], a network simplex algorithm [165], a genetic algorithm [53] and agent based algorithms [3]. Other studies have focused on collaboration and priority control of groups of robots [30, 47, 74, 154, 212]

and coordinated multirobot exploration and localisation [37, 96, 113, 179, 200, 137, 262].

2.3 Climbing Robots

Autonomous Non-destructive Testing is not restricted to pure horizontal applications. In fact there are many cases where the vehicle needs to be able to cope with different types of inclined, curved, and vertical surfaces. Even upside down operation would be envisaged, thus the robot requires climbing skills.

Climbing robots establish the connection between themselves and an engineering structure either by adhesive forces or by positive connections like grippers [13, 33, 34, 193]. Since the main applications involve smooth surfaces, predefined structural elements that support mechanical fasteners are not to be expected, the vehicle has to be attached by some kind of adhesive force. In this field state of the art climbing systems can be divided into four main types, and each is characterised by the adhesive force it employs. These four modalities are listed below:

- suction adhesion,

- magnetic adhesion,

- adhesion based on vortex regenerative air movement (VRAM) and

- dry adhesion.

These four different adhesion techniques constitute partial solutions to the climbing requirement and therefore represent one row of a morphologic box during the design process.

Suction adhesion offers the advantage of being independent of the surface material, as long as the surface structure is smooth, non porous and has no surface cracks [112, 166, 182, 250, 258, 276]. Recently passive elastic suction cups have been developed, which are evacuated simply by pressing them onto the surface. The suction is released by opening small valves to reinflate the cups [35]. In this way, they require only minimal energy for adhesion, which is important for an autonomous climbing robot. However, the main drawback of suction cups are their large size and high degree of complexity of the robots. This is due to multiple legs and the reduced travelling speed as developing appropiate vacuum requires time. The main

11

application for robots with suction adhesion is window- and facade cleaning in high-rise buildings, where big legged robots cover larger areas in less time and the smooth glass surfaces offer optimal conditions for suction cups [73, 153, 225, 226, 227]. In addition to climbing, the legged climbing robot RobugII with suction cups is also able to perform autonomous floor to wall transfers [133, 134, 240] and to seek and verify its own foot holds. This robot has an endoskeletal structure: An internal frame that provides the required strength and stiffness for locomotion as well as locations for the joints, whilst the external actuators act as the prime mover. It consists of two pivot-mounted modules with mechanical legs and a vacuum gripper feet powered by double acting pneumatic cylinders. The most recent design in the field of legged climbing robots is 'SkyCleaner 3' [255, 256], which comprises 14 suction cups and a novel movement mechanism. It is 113 cm long, 73 cm wide, 38 cm high, weighs 45 kg and can carry a payload of 15 kg. Like all robots of this kind, it requires a supporting vehicle and a hose.

A variation of suction adhesion has been employed at the Alicia[3] climbing robot, which is based on a large air aspirator and high airflow [132]. As aspirators have a lower vacuum level compared with vacuum pumps, they need to be of large diameter in order to provide sufficient adhesion force. Three modules of 30 cm diameter are combined with a linear actuator leading to an overall length of the robot of 1.3 m and a weight of 20 kg. When incorporating fewer actuators, in order to reduce size and weight, more compact underactuated kinematic designs have been proposed which comprise a self-contained smart robotic foot (SRF) [10, 124, 126, 246, 247, 248]. These feet are equipped with an integrated vacuum pump, a suction cup of 4 cm diameter, a micro-valve and a pressure sensor, which is used by the micro-controller on the robotic body to decide whether the SRF is firmly attached to the surface. In spite of the under actuated design robots containing two SRF need 123 cm space in flipping stride to pass through and 58 cm in crawling mode.

Due to the fact that the adhesive force provided is up to ten times higher than that delivered by suction grippers, magnetic adhesion is commonly employed on ferromagnetic surfaces. It allows for fast inspection, small robot size and is characterised by inherent reliability [204, 244, 245, 267, 282, 286, 294]. Crawlers exploiting this inspection technique have found application in pipework [52, 167, 194, 214, 253, 257, 261], storage tanks [58, 206] and on hulls of vessels [114, 189]. In general, they are significantly smaller than climbing robots with suction cups, down to a few centimetres overall size, and less complex. However, application is restricted to ferromagnetic structures.
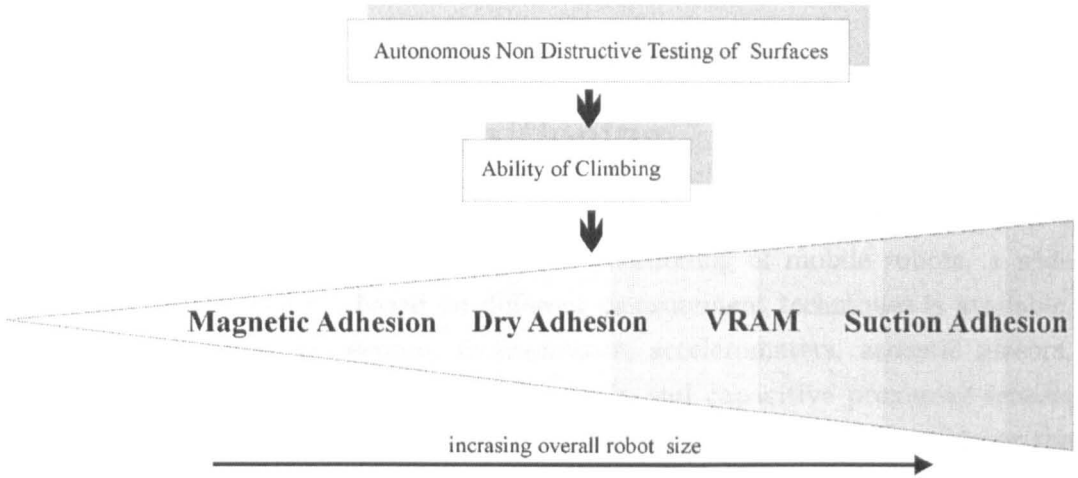
Figure 2.2: Robot size and complexity resulting from different climbing techniques.

Two innovative technologies in the field of climbing robots independent from the surface material are vortex regenerative air movement (VRAM) and dry adhesion. VRAM technology provides attraction in air and underwater by creating a local captive vortex, which is significantly more efficient than conventional vacuum [249, 271]. A vehicle of 18 x 12 x 6 cm is commercially available, which can carry a payload of 0.45 kg for approximately 45–60 minutes. Equipped with a video camera, it is mainly used for military surveillance and reconnaissance purposes.

Dry adhesion is the second novel adhesion technique. In contrast, it is biologically inspired and based on surface contact (van der Waals-) forces. These molecular forces result from a large number of artificially machined nano fibres [11, 149, 202, 203, 231] or from a special moulded structured polymer made of polyvinylsiloxane [62]. The nano fibres have a diameter of 4 μm and provide an adhesion force of up to 10N per 1cm^2 [150]. Both dry adhesion and VRAM are independent of the surface material and roughness, and in general result in more compact designs compared with robots equipped with suction cups, as illustrated in Fig. 2.2.

In addition to the above mentioned basic techniques for attaching robotic devices to engineering structures, there are research prototypes engineered for a specific application. E.g., a Stewart-Gough parallel platform with six degrees of freedom has been modified as a climbing robot to externally move along pipes, steel cables, electric posts and palm trunks [5, 242], and a novel omni-directional inspection robot has been presented which overcomes the limitations raised from pipe bends and pipe branches [49]. The latter comprises three sets of omni-directional wheels, symmetrically placed at 120° and evenly distributed along the total length of the

crawler.

2.4 Mobile Robot Positioning

Exact knowledge of the precise position of the vehicle is fundamental for navigation and localisation of the detected flaws. For positioning of mobile robots, a wide range of on board sensors based on different measurement techniques is available, including compasses, gyroscopes, inclinometers, accelerometers, acoustic sensors, laser and infra-red sensors, inductive, magnetic and capacitive proximity sensors and photoelectric proximity switches. The different principles for determining the position of a mobile robot in its environment are divided into two main groups — relative and absolute positioning systems. Further subdivision into the following categories is common [27]:

- **Relative Position Measurements (Dead Reackoning)**
  - Odometry
  - Inertial Navigation

- **Absolute Position Measurements (Reference-Based Systems)**
  - Active Beacons
  - Landmark Navigation
  - Model Matching

For wheeled mobile robots, the principle of utilising encoder measurements at the wheel shaft to ascertain the position of the vehicle is referred to as Odometry. Starting from a known reference point, the current position and orientation of the robot is obtained by time integration of the vehicles displacement. Similarly, integrating the information gathered from a combination of gyroscopes and accelerometers in order to determine the current position is deployed in inertial navigation: The linear acceleration of the robot in the inertial reference frame is determined by measuring both the current angular and linear acceleration. Performing integration on these inertial quantities and utilising the original velocity as the initial conditions yields the inertial velocities of the system, and integrating again utilising the original position as the initial condition yields the inertial position. Odometric and inertial navigation systems have the advantage of being totally self-contained, but both suffer from integration drift, as in particular, in Inertial Navigation systems small errors in the

measurement of acceleration and angular velocity are integrated into progressively larger errors in velocity and position.

These accumulated errors do not exist when measuring the absolute position of the system, most commonly facilitated by active beacons [27]. The Active Beacon method provides positioning information with minimal processing effort by carrying out angular and distance measurements. Two different types of active beacon systems are distinguished:

Trilateration: This type of beacon system determines the vehicle's position in 3D space based on distance measurements from an on board receiver to usually three known emitter locations. Alternatively, a method known as 'inverse GPS' is used whereby a small on board tag transmits a signal to multiple receivers.

Triangulation: Position and orientation of a vehicle in 2D is computed from the angles of three beacons relative to the vehicle's longitudinal axis.

Similarly, in Landmark Recognition artificial or natural landmarks in direct line of sight of the vehicle allow position estimation, as their locations in the environment are known, and in Model Matching the robot utilises on board sensors to create a map of its local environment. This local map is compared to a global map previously stored in memory.

Commercial absolute positioning systems based on the Active Beacon technique that utilise acoustic methods to determine the distances between emitter and receiver achieve accuracies up to $2 - 3$ cm [19, 109, 110, 289, 296]. Hybrid systems, which comprise inertial measurement units, provide additional orientation information, are immune to metallic, acoustic, and optical interferences, and do not suffer from line of sight obstructions [281]. The position and orientation of the tracking stations of these systems are preliminary obtained by accelerometers and gyroscopes, and to prevent position and orientation drift, this data is fused with range measurements from the ultrasonic components. This approach yields an accuracy of 3 mm and $0.5°$. The highest accuracy is achieved by systems based on optical techniques: the state of the art 'Indoor Laser GPS Constellation 3Di' from ArcSecond [265] utilises small infra red laser transmitters that emit laser pulses to provide their real-time coordinate location. Photo detectors pick up the signals and compute angle and positions based on the timing of the arrival of the light pulses. The system is designed so that the horizontal and vertical angles from the transmitter to

the receiver can be instantaneously measured, and this is accomplished by having each transmitter generating three signals: two infra red laser fanned beams rotating in the head of the transmitter and an infra red LED strobe. The accuracy of the system is less than 1 mm. In harsh indoor environments or wherever dust or physical contaminants could damage the sensitive laser optics the Partial Pulse Positioning (P^3) radio frequency carrier phase position tracking technology offers the most accurate alternative [106, 291]: A small transmitter tag transmits an RF signal that is received at a number of fixed receivers or at an array of two receiving antennas. P^3 achieves standard derivations of 7.1 mm, 5.7 mm and 33.0 mm in x-, y- and z-direction [106] and avoids errors caused by signal reflections that usually impairs RF position tracking.

There are numerous approaches to improving Relative Position Measurements of mobile robots. In [22, 45, 46, 123, 186, 219, 259] sensor-fusion techniques are proposed utilising odometry together with inertial measurements from gyroscopes and accelerometers. When fusing these data, Kalman Filtering techniques are commonly applied to improve accuracy [117, 128, 184, 197, 205]. In addition, efforts have been undertaken recently to establish collective or collaborative localisation [76, 79, 159, 185, 209]. For this purpose, an infrared localisation system based on inexpensive commercial transducers has been developed to detect both range and bearing of autonomous mobile robots. By measuring the strength of a modulated infrared signal, which is also utilised for communication between the robots, average standard deviations of 6–8° and of 3–18 cm have been achieved [120, 174].

The control and motion planning of multiple robots navigating in a terrain with obstacles while maintaining a desired formation and changing formations has been addressed in [64] and [72]. Based on Graph Theory, the robots follow a trajectory while maintaining a desired formation by designating a lead robot that directly and indirectly controls all the remaining vehicles in the formation.

2.5   Non-destructive Evaluation Methods

Non-destructive testing (NDT) as well as non-destructive inspection (NDI) and non-destructive evaluation (NDE) testing play key roles in the prevention of structural failures. An initial inspection of new structures, in order to detect manufacturing flaws, is usually followed by repeated inspections during service to locate fatigue cracks, corrosion or forms of accidental damage. General requirements for NDE are simplicity of application, sensitivity to small anomalies and reliability.

While destructive testing provides a more reliable assessment of the state of the test object, it is usually more costly and inappropriate in many circumstances, such as forensic investigation. The six primary methods for non-destructive testing of engineering structures as reported in literature are:

Visual Inspection: This is the most common procedure employed in practice and the majority of defects are detected in this way [208]. For this simple technique the human eye or a camera system acts as the inspection sensor and the inspection stimulus is visible light. Due to shadows and reflections lighting is critical, hence visual inspections are usually combined with other NDE methods.

Penetrant Inspection: Significant enhancement of visual inspection of surface breaking defects is achieved by applying dye penetrants. The penetrant, a solution of coloured or fluorescent dye in an oil based liquid, enters into cracks and tight crevices by capillary action. After thoroughly cleaning the surface a developer highlights remaining penetrant and thereby reveals the defective region.

Radiography: This classical NDE method can be used for detecting internal and external defects. Radiation passes through the test object and creates a shadow image of the internal structure on a recording plane. Usually X- or gamma rays are used in combination with photographic films, fluoroscent screens or electronic sensors acting as recording media. In particular, non-planar effects like voids and cavities are detected reliably using this method. However, this method may require a disassembly and there is a radiation hazard.

Ultrasonic Inspection: Soundwaves are introduced by transducers and propagate in the test material. The information regarding interactions of these sound waves with imperfections within the structure are recorded by ultrasonic sensors. Ultrasonic (US) Inspection is versatile, simple, safe and applicable for metallic and composite materials. It is widely used for locating and quantifying both surface and internal defects, but requires admissible surface conditions and usually a couplant [21].

Electrical Inspection: Electromagnetic Inspection is the process of inducing electric currents or magnetic fields or both inside a test object and observing the response. There are a number of electrical methods which can be used for NDE, such as resistance measurement, electrical conductive measurement and

17

the use of triboelectric, thermoelectric and exoelectron effects. The two groups of major relevance for automated inspection, however, are Alternating Current Field Measurement (ACFM) and Eddy Current (EC) Inspection. In both, an alternating current-carrying coil induces the eddy current in the metal under test. In the EC technique, the change in the impedance of the coil is exploited in order to detect a flaw, while in the ACFM technique the flaw is detected by directly measuring the magnetic field using a specialised probe [151].

Magnetic Inspection: The test piece is magnetized by magnets or electrical current. Anomalies cause flux leakage fields that are then detected by visual or electronic sensors on the surface. Subset of this technique are Magnetic Flux Leakage (MFL) Inspection and Magnetic Particle Inspection, where small particles migrate to the flux leakages associated with the flaws in the test piece. This method is restricted to ferromagnetic materials and surface or near surface defects. Magnetic Flux Leakage Inspection is commonly employed in pipelines, and can be further subdivided into the induction coil method and the Hall effect method.

Further details and an assessment of the usefulness of the various methods can be found in references [95] and [105]. In addition to the primary techniques, current research focusses on new methods based on acoustic emission, thermal imaging, advanced optical methods like holography, proton annihilation, neutron scattering, proton radiography, microwaves and nuclear magnetic resonance [32, 70, 95, 138, 140]. Depending on whether or not energy is introduced to the test object all techniques can be characterised as being either active or passive. In a similar manner there is the distinction between surface-, near surface- and volumetric methods.

2.6   Robots for NDE Tasks

As indicated in 1.1 in Section 1.3, there have been recent developments directed towards merging the fields of large scale robots, climbing robots and NDE equipment. Several prototypes based on Magnetic Adhesion have been presented for underwater reactor vessel inspection [121], in-pipe inspection [167, 194, 214], inspection of storage tanks [58, 206] and hulls of vessels [114, 189]. In general, the dimensions of inspection robots with climbing abilities are between 30 x 50 x 30 mm up to 640 x 400 x 180 mm [43, 98, 114, 134, 183, 189, 190, 191] and magnetic inspection with Hall sensors [207, 215], Eddy Current inspection [217] and automated Ultrasonic inspection [43, 134, 190] is applied.

The majority of the presented designs are specifically geared towards particular applications, such as the inspection of the fire side of water wall boiler tubes [207]. This system, effectively based on the MFL technique and the ultrasonic method, is able to identify 1.6 mm through hole and wall loss. The robot is 320 x 240 x 200 mm, its crawling speed is 5–15 m/min and apart from the NDE payload it includes a furnace wall cleaning apparatus. However, it requires external power via an umbilical, is restricted to one specific tube size and can only travel in one direction. Unfortunately however, the resulting NDE signal is seriously corrupted by noise. Similarly, the teleoperated mobile service robots SADIE and NERO [134] had been especially designed for non-destructive testing of welds on the main reactor cooling gas ducts in the nuclear power plant at the Trawsfynydd nuclear power station in Wales. Owing to the design of this reactor, which provides only limited access for engineering servicing, the vehicle is driven remotely by an operator and controlled via a 100 m umbilical. An additional operator is required to handle the cable.

Umbilicals of up to 150 m length have also found application in underwater inspection systems for hulls of marine vessels and floating units employed in the offshore oil industry [43, 44]. A remotely controlled mobile vehicle with magnetic wheels has been developed which carries ultrasonic transmit-receive apparatus involving immersioned transducers. However, due to its length, significant electronic noise is developed when the cable is entering the water, which affects the quality of the NDE signal. The inspection vehicle weighs 170 kg, and is 1.7 m long, 1 m wide and 0.5 m high.

A similar approach is employed for visual inspection of reactor vessels and in-service inspection of storage tanks. Inspection vehicles have been developed for operation within a fluid medium thus avoiding the inconvenience of emptying and cleaning the tanks [51, 58, 190, 191, 243]. These vehicles are 540 x 300 x 300 mm and 250 x 250 x 750 mm and generate adhesion force to the tank wall by means of thrusters. The motors and their drivers are sealed in a pressurised box with inert gas to ensure the vehicle complies with safety requirements. In cases where there is the possibility of emptying storage tanks, automated floor-inspection can be performed by a 1 x 1 x 0.75 m rugged four-wheel drive robot with laser range finders for mapping the environment [20]. The robot is equipped with a water-filled rubber wheel, which contains an ultrasonic sensor for measuring the thickness of the bottom plates, and a side-scanner with ACFM sensors and phased-array sensors for weld inspection.

In the field of miniature pipe inspection robots the most representative prototype

19

has been developed at Shanghai Jiaotong University, which includes a machine frame tooth gear, pressing force driving mechanism [215]. Three driving rubber wheels are installed equably around the pipeline by 120°, and can be adapted to suit pipeline diameters between 190 mm and 320 mm. 112 Hall sensors for MFL inspection are utilised on a separate sensing unit to detect defects of with a minimum area of 10 mm^2.

2.7 Probability of Detection and Receiver Operating Characteristic

Under specified inspection conditions and procedures and for a defect of a given type and size group, repeated inspections do not necessarily result in consistent hit or miss indications. In fact, the spread of detection results for each defect size and type is represented by the quantitative statistical parameter Probability of Detection (PoD) [90, 92, 164]. For a specific test method and test protocol, there are four possible outcomes for an inspection of a component:

- **True Positive:** a defect indication is reported and there is an actual defect present, equivalent to a hit

- **False Positive:** a defect indication is reported and there is no defect, equivalent to a false alarm

- **False Negative:** no defect is reported and an actual defect is present, equivalent to a miss

- **True Negative:** no defect is reported and no defect is present, equivalent to correct rejection

The bottom diagram in Fig. 2.3 shows the internal response probability of occurrence curves of an NDE instrument. The internal response may be the output voltage of a sensing element, and the vertical axis shows its probability of occurrence depending on whether a defect is present or not. Whenever the output voltage of the sensor is higher than the criterion indicated in Fig. 2.3, the device will detect a defect. The criterion divides the graph into four sections that correspond to the True Positives (TP), False Positives (FP), False Negatives (FN) and True Negatives (TN) as described earlier.

In signal detection theory, a Receiver Operating Characteristic (ROC) is a graphical plot of sensitivity for a binary classifier system as its discrimination threshold is
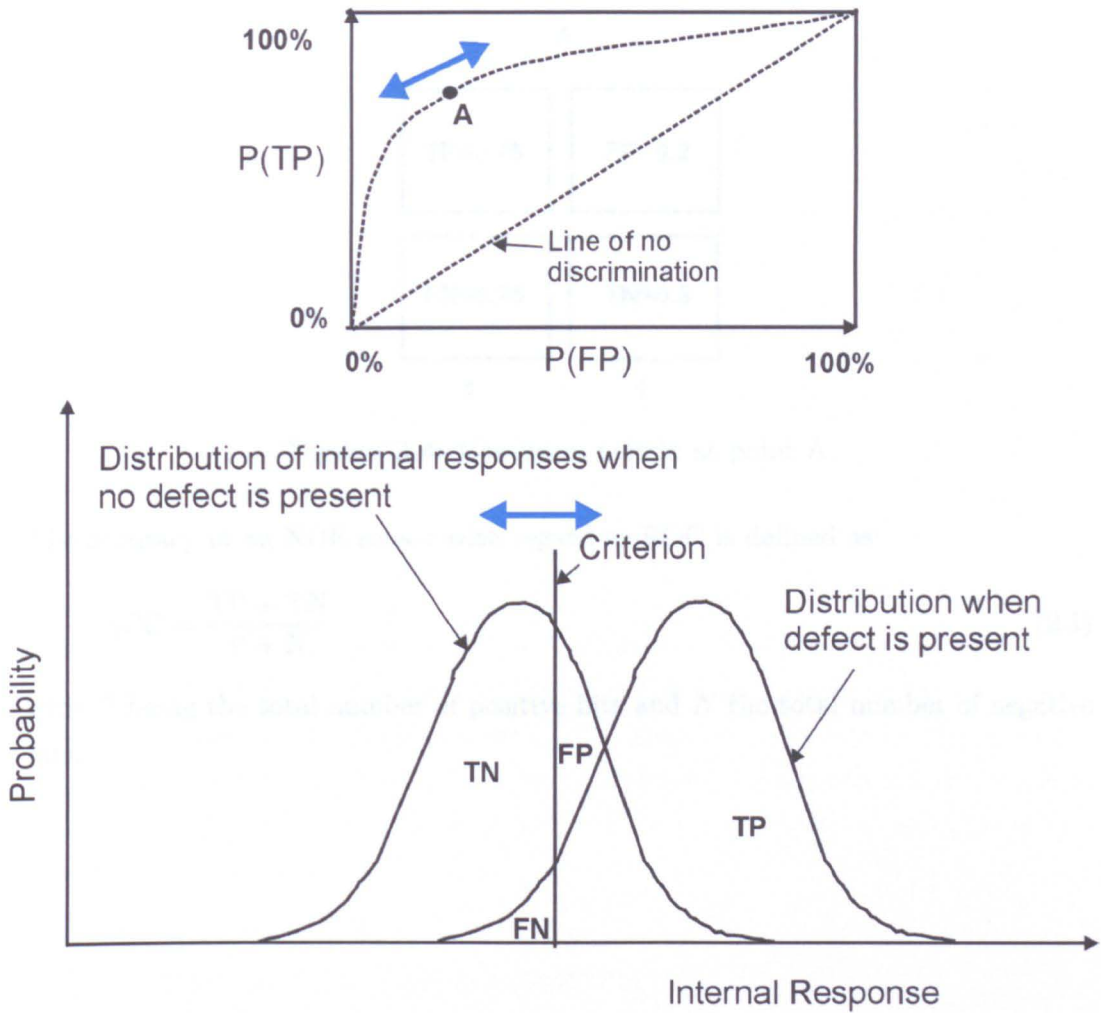
Figure 2.3: Internal response probability of occurrence and ROC curves of an NDE device.

varied. The ROC curve is obtained by plotting the fraction of True Positives over the fraction of False Positives. The best possible detection method would yield a point in the upper left corner or coordinate [0; 1] of the ROC plane with 100% sensitivity and no False Positives. The top diagram in Fig. 2.3 shows the ROC curve for the NDE sensor describing the effect of different values for the criterion and giving an indication about the quality of the device. If the inspection method is represented by Point A with a True Positive rate of 0.75 and a False Positive rate of 0.2, the four outcomes can be formulated in a 2×2 contingency table or confusion matrix, with the columns adding to unity as illustrated in Fig. 2.4.

A

Figure 2.4: Confusion matrix at point A.

The accuracy of an NDE sensor with regard to ROC is defined as:

$$ACC = \frac{TP + TN}{P + N} \tag{2.1}$$

with P being the total number of positive hits and N the total number of negative hits.

Chapter 3

System Design

3.1 Introduction

This Chapter covers the design and development of the inspection system, which apart from the vehicles, also includes the positioning equipment and the host computer. Advantages and disadvantages of different design aspects in respect of the requirements for non-destructive testing applications are discussed and the design based on magnetic wheels is justified, followed by a description of the software running on the host and the vehicles' on board controller.

3.2 Prototype Development

3.2.1 Locomotion Mechanism and Climbing Technique

The design decision regarding which of the climbing mechanisms presented in Section 2.3 to adopt and how to attach the robot to the structure for inspection, is determined from the performance specifications and the particular requirements for the autonomous vehicle. As magnetic devices generate more than ten times higher [189] adhesive force per unit area on ferromagnetic surfaces and the aspect of miniaturisation is of particular importance, the most compact design based on magnetic adhesion is chosen for the miniature vehicles. This magnetic function can also be integrated into already existing robot components like wheels to reduce the size even further. They are replaced, if necessary, in later design stages by one of the alternative adhesion techniques presented in Section 2.3 for non-ferromagnetic structures.

The second fundamental design decision is related to the locomotion mechanism, as this directly affects the general structure and the final performance of the robots.

Shortcomings at this point, at the foundation of the design, are directly related to greater demands at the control- and positioning system in later design stages. In general, for autonomous vehicles there are a variety of possible ways to move through their environment. The different motion mechanisms have been partly inspired by nature: crawling, sliding, running, jumping and walking [192, 199, 216]. Additionally, mobile robots may benefit from human inventions like the actively powered wheel or tracks. Due to the still existing limitations of human fabrication techniques and the advantageous cell-structure of biological systems, artificial mechatronic systems in general are in a significantly inferior position to biological systems in the important areas of torque to weight ratios, energy storage, complexity and miniaturisation. For this reason small state of the art autonomous research robots are either wheeled or use a small number of articulated legs. Legged locomotion offers high manoeuvrability and adaptability in difficult terrains with major vertical variation in ground height and on soft ground. However, it requires higher degrees of freedom and therefore greater mechanical complexity and electrical power. Compared with legs and tracks, wheels have a relatively simple mechanical implementation while being well suited for flat surfaces. They consume less energy as there is only negligible rolling friction, which is of major relevance taking the limited on board energy supplies of autonomous robots into account. Furthermore, wheeled designs do not encounter challenges in respect of stable balance, given that the number of wheels is greater than one.

In conclusion, as the robots are aimed to be small and employed within the scope of structural condition monitoring where hard surfaces are to be expected, a locomotion mechanism based on magnetic wheels is regarded as being most suitable.

3.2.2 Wheel Types

Having elucidated the advantages of a wheeled design in the previous section, further specification is necessary at this point to decide on the design of the wheel itself and the overall wheel arrangement. Considering the requirements of the vehicle kinematics according to McKerrow [147] and Siegwart [199], when designing complex systems, a common method to visualise the numerous requirements and their possible partial solutions is to list them in Morphologic Boxes. In terms of the wheel arrangement, the different partial solutions are listed in Figures 3.2 and 3.3 and can be interpreted as a row within such a Morphologic Box. The main benefit from using this technique in the design process is the possibility of arbitrarily combining different partial solutions to the final design and thereby finding solutions
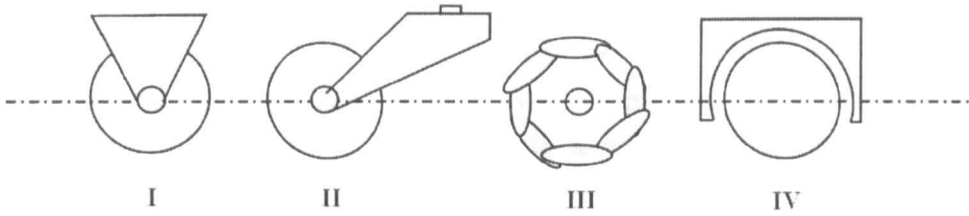
Figure 3.1: Different wheel types: I) Fixed Standard Wheel, II) Steered Standard Wheel, III) Swedish wheel, IV) Spherical Wheel.

that are not obvious in the first instance.

The four major wheel types are illustrated in Fig. 3.1: A steered standard wheel is characterised by a primary axis of rotation that intersects with the wheel axle, so the wheel must be steered firstly along this vertical axis before moving it in different directions. It has two degrees of freedom: the rotation about the wheel axle and the vertical rotation about the contact point. This is the main difference to the castor wheel, where this vertical axis of rotation is situated with an offset from the horizontal one and not passing through the contact patch with the ground. Accordingly, steering motions of castor wheels involve side effects to the chassis of the vehicle. The two remaining wheel types, Swedish wheels and Spherical wheels, constrain the vehicle motions less as they allow sideways motion. Swedish wheels consist of a circular hub surrounded by rollers, the angle between the rollers and the hub is either 90° (Stanford Wheels) or 45° (Illanator wheels). In that way they not only move forwards and backwards but along various possible other trajectories along the surface. Spherical wheels possess the lowest constraints regarding directionality since they spin in any direction.

3.2.3 Number of Wheels

The design decision regarding the four different wheel types in the previous section is linked to the choice of the wheel arrangement and the number of wheels. Figures 3.2 and 3.3 provide an overview about the different wheel arrangements. A wheel configuration based on two wheels offers the potential of small overall size, however, for reasons of stability, two-wheeled designs are inappropriate due to the fact that the centre of gravity has to be situated below the wheel axle, which in turn requires impractically large wheel diameters. Moreover, there is no dynamic stability, since the absence of a counter torque results in rotational movements of the chassis during rapid motor accelerations. In combination with the restoring gravitational force at the centre of gravity, the chassis performs uncontrolled swinging movements — an

25

unacceptable condition for obtaining precise NDE sensor readings.

In contrast, static and dynamic stability pose no problems with vehicles having three wheels. Providing the centre of gravity is within the circle defined by the three points of contact on the surface, the vehicle is in balance at any time. Three points of support are also advantageous for operating on curved surfaces. When using more than three wheels, suspension systems have to be integrated in order to maintain continuous wheel-to-ground contact. Miniaturisation is more difficult and maneuverability of four-wheeled constructions is limited, hence a three-wheeled design is most appropriate for the vehicle.

3.2.4   Wheel Kinematic Constraints

The vehicle's driving performance depends mainly on the wheel types, as described in Section 3.2.2. The different three-wheeled variations [3.1] to [3.6] in Fig. 3.2 are evaluated utilising the concept of holonomy, which describes the path space of mobile robots and refers to the kinematic constraints of the robot chassis [199]. For describing a holonomic robot it is necessary to distinguish between its degrees of freedom (DOF) and its differentiable degrees of freedom (DDOF): the DOF is equal to the number of independent coordinates that a robot can attain on a two-dimensional surface. Vehicles that can be positioned at any (x, y, Θ) in the global reference frame have a DOF = 3. In contrast, a robot with only two fixed standard wheels would have a DOF = 1, since it can only be positioned along the axis that runs through the wheel planes. The DDOF of a mobile robot is equal to the number of independently achievable robot velocities $(\dot{x}, \dot{y}, \dot{\Theta})$ that arise from the kinematic constraints of the wheels, also denoted as the components of robot motion that are independently controllable, or the number of dimensions of the admissible velocity space of a robot [199]. It is always equal to the number of degrees of freedom that can be immediately manipulated by changes in wheel velocity. A bicycle-type vehicle therefore has a DDOF of 1 – it can only directly control its forward and reverse speed rather than its entire global position and orientation at a certain point in time. Vehicles with DOF = DDOF are holonomic and vehicles with DOF > DDOF are referred to as nonholonomic. The kinematic constraints of the four different wheel types arise from restricting free two-dimensional vehicle movements due to:

- the rolling movement of the wheel – in order to allow for pure rolling at the contact point all motion along the direction of the wheel plane must be accompanied by the appropriate amount of wheel spin,

- no lateral slippage on the contact point, wheels do not slide orthogonal to the wheel plane.

As shown in Fig. 3.4, the position and orientation of a fixed standard wheel within the chassis is described by $\alpha, \beta, \phi, r, l, A$ and v in the body-fixed reference frame X_r, Y_r. β denotes the angle of the wheel plane relative to the chassis and α describes the position of the wheel [38]. The rolling constraint for a fixed standard wheel therefore is:

$$[\sin(\alpha + \beta) \quad -\cos(\alpha + \beta) \quad (-l)\cos\beta] \quad R(\Theta)\dot{\xi}_I = r\dot{\phi} \tag{3.1}$$

The term $R(\Theta)\dot{\xi}_I$ transforms the motion parameters $\dot{\xi}_I$ from the global reference frame into the local reference frame $\{X_r, Y_r\}$. Furthermore, taking the sliding constraint into account, wheel movements orthogonal to the wheel plane of standard wheels must be zero, and thus:

$$[\cos(\alpha + \beta) \quad \sin(\alpha + \beta) \quad l\sin\beta] \quad R(\Theta)\dot{\xi}_I = 0 \tag{3.2}$$

If the rank of a matrix is defined as the maximal number of linearly independent rows and C_1 denotes a matrix whose rows consist of Equations (3.1) and (3.2) applied to all standard wheels of the vehicle, the DDOF is:

$$DDOF = 3 - rank[C_1]. \tag{3.3}$$

Three is the maximum number of degrees of freedom in the plane, and the rank of C_1 is equal to the number of linear independent sliding constraints. Vehicles with $rank[C_1] > 1$ are consequently restricted to movements along a straight line or a circle. The wheel types castor wheel, swedish wheel and spherical wheel do not impose kinematic constraints on a robot chassis since they do not constrain vehicle movements in terms of Equations (3.1) and (3.2).

These considerations regarding holonomy and kinematic constraints of different wheel types are the base for evaluation of the configurations [3.1] to [3.6] in Fig. 3.2. For the inspection of surfaces vehicles have to accomplish a search pattern — a typical path is shown in Fig. 3.5. The main requirements for the wheel configuration are the provision of high directional stability for accurate straight line movements between AA and BB as well as the ability to perform turning-over manoeuvres neatly on the locus between AB and BA. So, evidently, the DOF of the vehicle has to be three. However, the appropriate value for the DDOF is two: In order to allow

for directional stability the vehicle should physically be incapable of immediately changing its position orthogonal to the current moving direction. Due to the wheel constraints, accurate straight line movements are possible while providing for sufficient manoeuvrebility for turn-overs on one spot. The holonomic configurations [3.5] and [3.1], based on three spherical/swedish wheels therefore are not suitable, as they lack the mechanical prerequisites for directional stability. It is not essential to follow an arbitrary path while maintaining a certain orientation in that application, therefore these two omnidirectional holonomic configurations with DOF = DDOF = 3 provide a degree of manoeuvrebility, that is not required. In contrast, the DDOF of configurations [3.3], [3.4] and [3.6] is one: there are no two robot motions ($\dot{x}, \dot{y}, \dot{\Theta}$) that are independently controllable in these configurations. Consequently, the manoeuvrebility in respect of turning-over performance at the end of each straight line between AB and BA in Fig. 3.5 is restricted. This is a major disadvantage compared with the differential drive of configuration [3.2]. Here DDOF = 2 and $rank[C_1] = 1$, since the two fixed standard wheels share a common horizontal axle and the second wheel adds no additional kinematic constraints. Thus only in this three-wheeled nonholonomic configuration does the vehicle meet the requirements of sufficient manoeuvrebility and directional stability. Further advantages of a two-wheel centred differential drive with an unpowered omnidirectional wheel are:

- climbing performance and automated floor to wall transfer capability: integration of two magnetic wheels of sufficient size and a magnetic castor wheel as omnidirectional third wheel,

- no steering errors due to a combined drive and steering mechanism,

- no jamming rollers, characteristic of Swedish wheels, leading to immobilisation of the vehicle,

- no complex and fault-prone mechanical design of spherical wheels,

- no off-directional forces of Swedish wheels — higher efficiency,

- flexible adjustment of wheel size depending on surface irregularities and expected obstacles,

- reliable odometric pose estimates for dead reckoning positioning possible due to reduced slippage of magnetic wheels,

- shorter transmission change – minimisation of probability of failure,

Concluding the considerations in respect of wheel design, number of wheels and wheel kinematic constraints, a mechanical structure based on on a differential drive and a passive castor wheel proves to be most appropriate for an autonomous NDE vehicle.

			DOF	DDOF	
2.1		One steering wheel in the front, one traction wheel in the rear	3	1	2 wheels
2.2		Two-wheel differential drive with COM below the axis	3	2	
3.1		Three motorised spherical wheels,omnidirectional movement possible	3	3	3 wheels
3.2		Two independently driven wheels in the rear/front, 1 unpowered omnidirectional wheel in the front/rear	3	2	
3.3		Two connected traction wheels (differential) in rear, 1 steered traction wheel in front	3	1	
3.4		Two wheels in rear, 1 steered traction wheel in front	3	1	
3.5		Three motorised swedish wheels arranged in a triangle; omnidirectional movement possible	3	3	
3.6		Three synchronosly motorised and steered wheels; orientation not controllable	3	1	
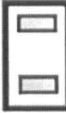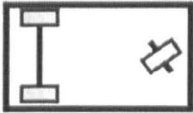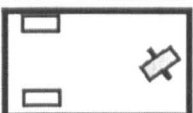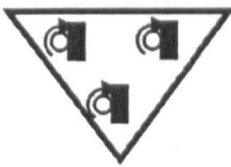
○ Unpowered omnidirectionl wheel (spherical, castor, Swedish)

▭ Unpowered standard wheel

▭ Motorised standard wheel

▨ Motorised Swedish wheel (Stanford wheel)

⊟ Connected wheels

⊥ Steered standard wheel

▭○ Motorised and steered castor wheel

Figure 3.2: Wheel configurations for rolling vehicles with two and three wheels based on [199].
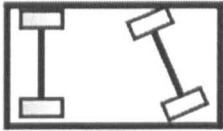
4.1		Two motorised wheels in the rear, 2 steered wheels in the front, steering has to be differential for the 2 wheels to avoid slipping / skidding	
4.2		Two motorised and steered wheels in the front, 2 free wheels in the rearsteering has to be differential for the 2 wheels to avoid slipping / skidding	4 wheels
4.3		Four steered and motorised wheels	
4.4		Two traction wheels (differential) in the rear/ front, 2 omnidirectional wheels in the front/ rear	
4.5		Four omnidirectional wheels	
4.6		Two-wheel differential drive with 2 additional points of contact	
4.7		Four motorised and steered castor wheels	
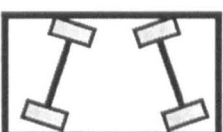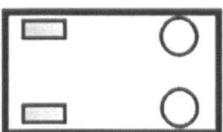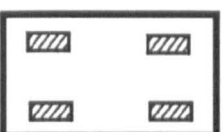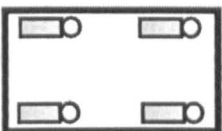
Figure 3.3: Wheel configurations for rolling vehicles with four wheels based on [199].

31
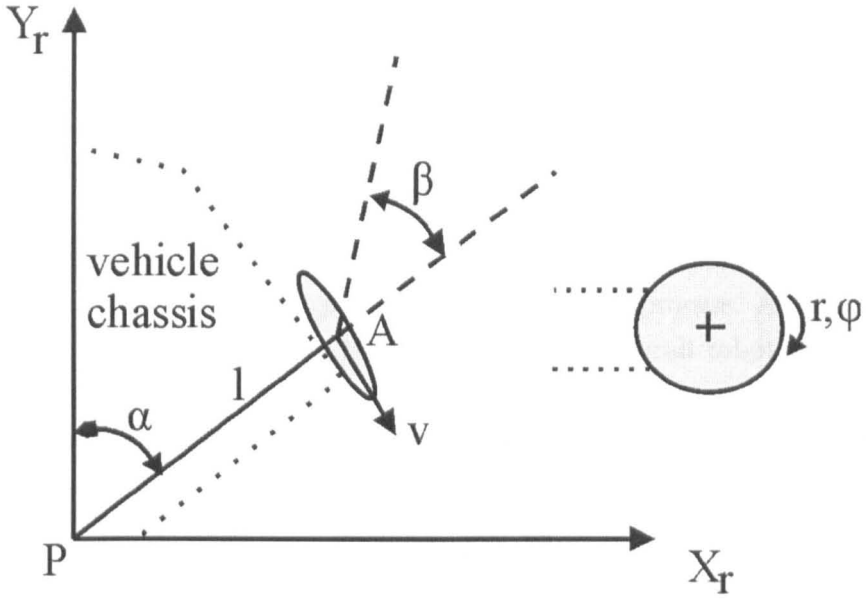
Figure 3.4: Parameters of a fixed standard wheel.
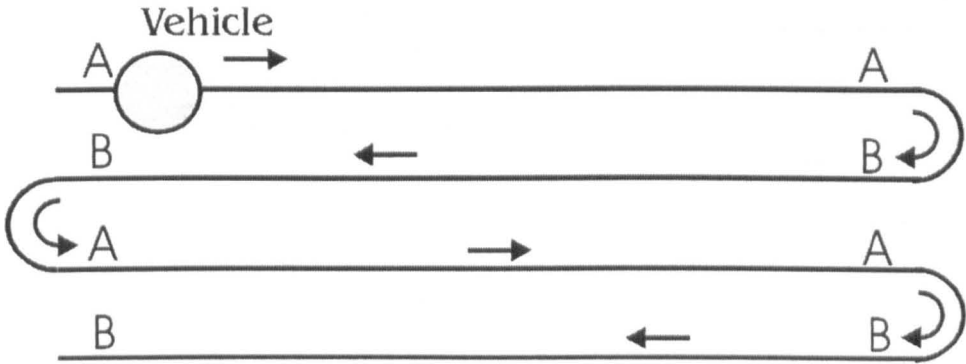
Figure 3.5: Search pattern.

3.2.5 Modular Components

To allow for future modifications and to incorporate a wide range of NDE inspection equipment for different test objects, materials and surface conditions, modularity has long been recognised as a concept for attaining robot specialisation without creating an unacceptably large pool of robots [49, 78, 80, 169, 170, 178, 234]. This section presents the different modules for propulsion, power, sensing, communication and computation that are combined with the different NDE payloads to construct vehicles specialised for detection of certain types of defects. Restricting the supply voltages to 12V and 5V and utilising a common connector system allows for easy replacement of components as a part of the development process. As size is crucial and standard crimps and sockets tend to increase the overall robot size unacceptably, the components are connected utilising a special compact system for wire sizes between 28 and 32 AWG. Fig. 3.6 shows the different modules in a block diagram:
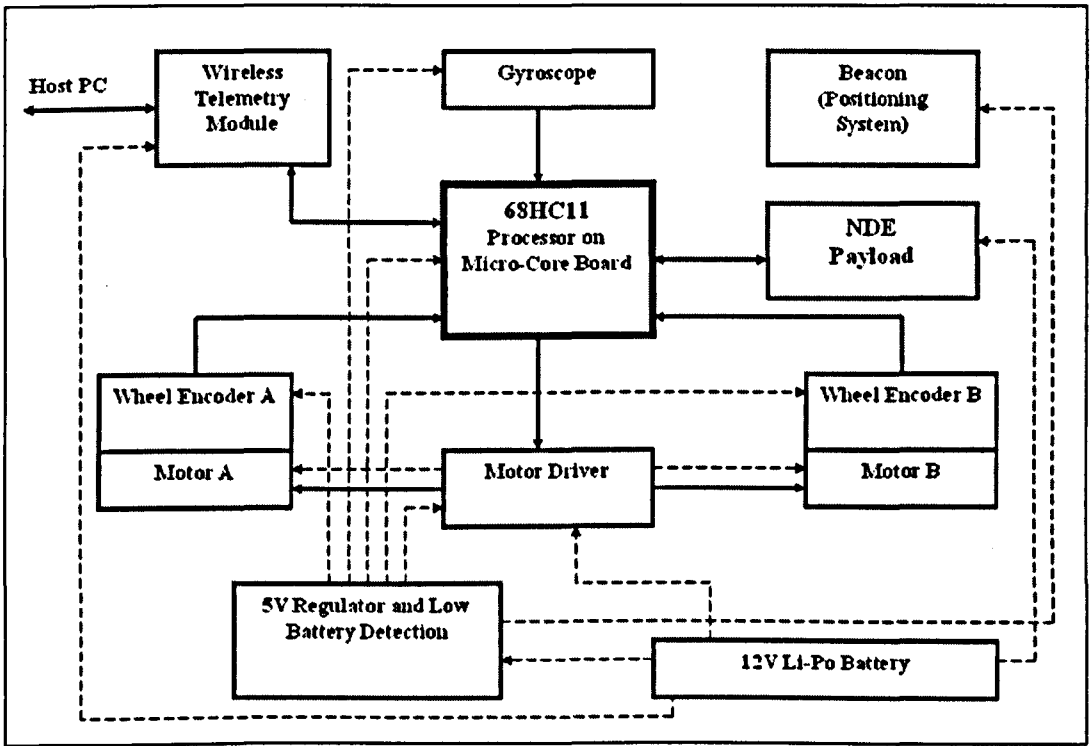
Figure 3.6: Block diagram.

the full arrows represent data flow, while the dashed lines indicate the flow of energy. The pivotal component is the micro controller, which is described in the next subsection, followed by a brief discussion of the remaining components.

33

3.2.5.1 The Microcontroller Module

The process of designing embedded microprocessor systems starts with defining the requirements and specifications and generally follows the steps presented in [15], which includes processor selection, system evaluation and firmware design. This is crucial, since all modules have to be interfaced to the micro controller unit (MCU) and for preventing long term shortcomings like insufficient RAM or speed. For the team of miniature robots these main requirements are:

- small board size and potential of miniaturisation,

- 8-bit based processor (sufficient computing power and low cost),

- multichannel AD converters for evaluation of analogue NDE signals,

- flexibility of interfacing both standard and non standard sensors and actuators,

- on board communication interface,

- low current operation and noise immunity,

- low cost, especially with regard to a swarm of inspection robots,

- mounting holes, standard connectors and robustness,

- 32K RAM program storage capacity,

- programmable in C.

The 5 cm x 5 cm square Microcore-11 board which includes an M68HC11 processor from Motorola meets these requirements most closely. It is the most versatile general purpose controller at the higher end of the 8-bit market and there is an extensive range of documentation and software tools available. In respect of further miniaturisation, it offers the option of implementing the 2.5 cm^2 Microstamp-11 in a second design stage as described in Section 7.6, the smallest M68HC11 module available. The necessary programming environment and compiler are identical and only minimum change of code is required to change the programs from the Microcore to the Microstamp board. Both controllers are programmed in C utilising the ImageCraft ICC11 integrated development environment [279] as a cross compiler and the final assembler files are downloaded with the free software MicroLoad [297].

3.2.5.2 The Power- and Motor Driver Module

Figure 3.7: Power- and motor driver module circuit diagram.

35

Figure 3.8: 3D Model of module for 5V generation, low battery detection circuit, gyroscope and motor driver.

As all robots require regulated +5V and –5V, a motor driver, a battery low detection circuit and a gyroscope, these functions are integrated on a single common power- and motor driver module. This compact double sided board, the circuit diagram of which is shown in Fig. 3.7, is designed to be of identical dimensions as the micro controller and has the same configuration of mounting holes to allow for a stacked board arrangement on threaded studs. A MAX638 step-down switching regulator with external inductor, a catch diode and filter capacitors, generates regulated +5V with an efficiency of 85%. The circuit also contains a low battery detection function: The LBO pin sinks current when the input voltage at LBI is less than the 1.31V internal bandgap reference. LBO is connected to a pull up resistor and a pnp transistor for switching the battery low Light Emitting Diode (LED) D1. A voltage divider consisting of a 100 kΩ and a 650 kΩ resistor creates the input voltage at LBI from the main battery supply to switch the LED on whenever the battery voltage is below 10.4V, thus indicating the critical discharge point. As visible in Fig. 3.8, the gyroscope is located in the centre of the board close to the centre of rotation of the robot. The output of is device is a voltage proportional to the angular rate about the axis normal to the top surface of the package, in this way providing a measure of how fast the robot is turning. The remaining space on the board is occupied by the L293D four channel driver and a 74HC04 CMOS inverter IC. Both constitute part of an H-Bridge for driving the two DC-Motors with the L293D providing up to 600 mA output per channel and accepting standard Transistor-Transistor Logic (TTL) signals from the micro controller on the enable inputs. The motor driver and the gyroscope require -5V, which is generated by a MAX660 charge-pump voltage

36
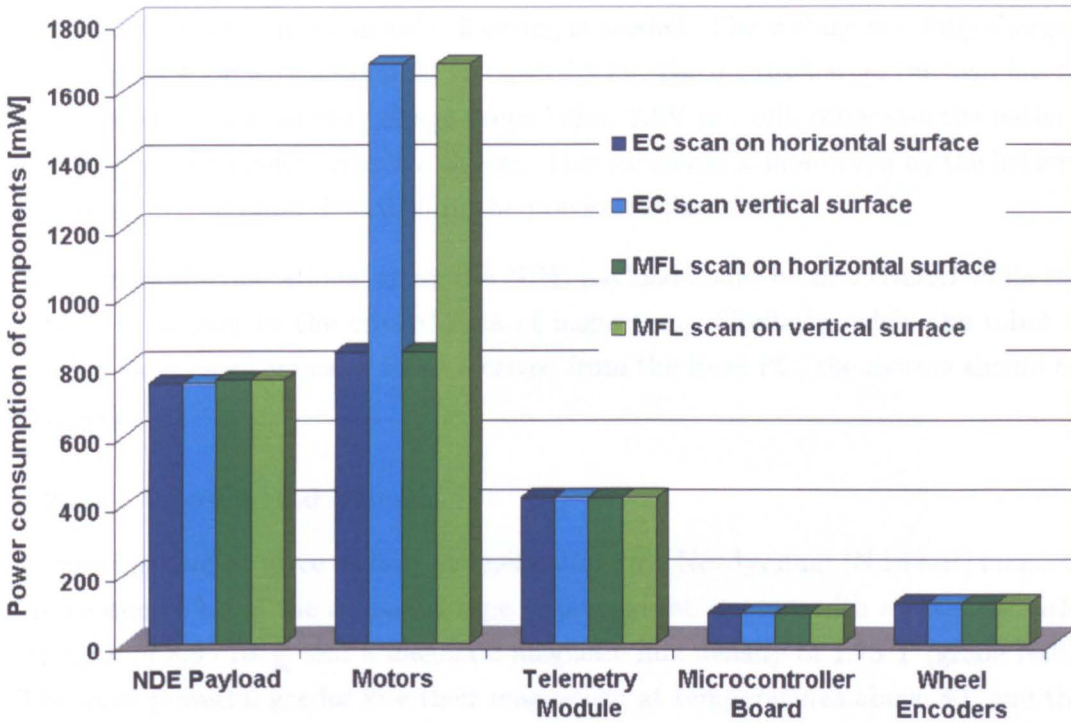
Figure 3.9: Power consumption of components.

inverter and two external capacitors. This inverter offers an efficiency of more than 90% and is capable of sourcing a current of up to 100 mA although operating at 120 μA.

3.2.5.3 Battery

The overall power consumption during operation, taking into account that the regulated 5V is generated with an efficiency of 85% as described in the previous subsection, is between 2200 mW and 3070 mW, depending on the inclination of the test surface. Fig. 3.9 illustrates the contribution of the different components. Main energy source of the robot is a three-cell Lithium-Polymer (Li-Po) battery with 910 mAh, which yields a theoretical minimum operating time of 3.3 hours. However, due to the discharge rate characteristics, the total battery voltage drops below 12V already after approximately 25 minutes.

Considering that the battery volume of centimetre-scale robots usually reaches upwards of one third of their volume [161], Li-Po technology offers currently the highest volumetric capacity among rechargeable batteries [41]. The energy density of Li-Po batteries is over 20% higher than Lithium-Ion batteries and three to four times better than Nickel-Cadmium and Nickel-Metal-Hydride batteries, while also being

significantly lighter, as no metal cell casing is needed. The voltage of a fully charged Li-Po cell is 4.2V with a nominal voltage of 3.7V. During discharge, the load has to be removed as soon as the voltage drops below 3.0V per cell, otherwise the battery subsequently no longer accepts a charge. This threshold is monitored by the battery low detection function described in the previous subsection.

To increase the operational time, the NDE payload could be deactivated while the vehicle is moving to the critical area of inspection. Similarly, while the robot is waiting for a new command to be received from the Host PC, the motors should be stopped.

3.2.5.4 Chassis and Wheels

To provide holding force on ferromagnetic material, Neodymium (Nd-Fe-B) magnets are chosen. This is the strongest type of permanent magnet with a magnetic field strength of $8.9 \cdot 10^5 \frac{A}{m}$ and a magnetic magnetic flux density of 1.23 T (grade N40). The most powerful grades lose their magnetism at temperatures above 80° and the material is extremely brittle. For this reason initial attempts to build wheels out of disc magnets, by drilling a central hole to fit the shaft extension for the motors failed, and 6.35 mm thick ring magnets with an outer diameter of 38 mm and inner diameter of 12.7 mm were utilised for the final design. As both magnetic wheels together provide a high holding force of 30 N, the main chassis is made from aluminium to allow for a robust base and the motors and the castor wheel are mounted directly, as the main load is on these components when the vehicles are attached or released from a ferromagnetic surface. The frame consists of four bolted plates which support the threaded rods that hold the square shaped electronic boards and the screws for the main power switch and the NDE payload, as visible in the technical drawings A.3, A.4 and A.5. However, due to this rigidity the chassis contributes a major part of the overall robot weight, as shown in Fig. 3.10.

The third point of support is established by the omnidirectional castor wheel. Since the wheel has to rotate freely 360° about the steering axis, a significant amount of space in the rear end of the vehicle is required. Attaching the support for this castor wheel at the outside of the main frame and leaving a major cut-out in the rear lateral block, as visible in drawing A.3, provides sufficient space for these free rotations about the steering pivot. The wheel itself is a Nd-Fe-B ring with an outer diameter of 12 mm and a thickness of 3 mm, pivot-mounted on a 3 mm brass shaft which is secured on the hold by miniature circlips. A significant challenge here is the correct height of the castor wheel to ensure a constant horizontal level of
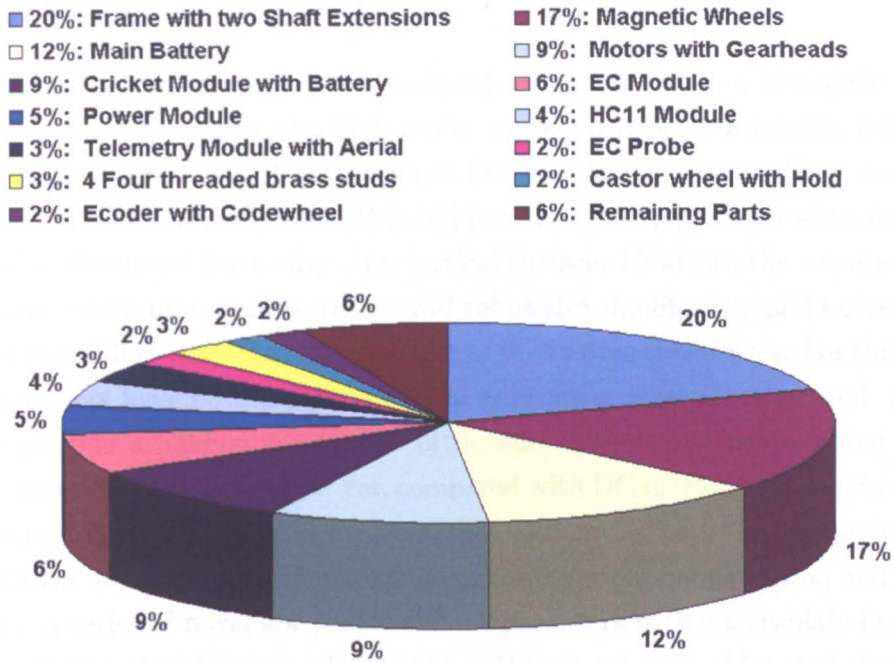
Figure 3.10: Weight distribution.

the vehicle frame. As there is only a limited selection of Nd-Fe-B rings with fixed outer diameters commercially available, the hold of the wheel is designed so that the exact vertical position is adjustable by a brass distance piece of variable thickness, as shown in drawing A.12. Similarly, the inner diameter of the magnetic wheels cannot be chosen arbitrarily by drilling a hole into a disc magnet due to the brittleness of the material. Hence, the brass shaft extension in drawing A.13 has been designed to fit both the main wheel and the encoder code disc of inner diameters of 12.7 mm and 5 mm respectively on the 3 mm output shaft of the motor-gearhead units. This shaft extension also solves the problem of limited length of the output shaft of 10 mm, taking into account a minimum required shaft length of 6 mm for the encoder code disc, a frame width of 3 mm, a 2 mm thick encoder hold, a wheel thickness of 6.35 mm and 2 mm clearance between the wheel and the frame and the wheel and the encoder hold. To decouple the DC motors magnetically from the neodymium wheels the shaft extension is made of brass. It is secured on the output shaft by 1 mm grub screws.

3.2.5.5 Motors

An initial test prototype vehicle was designed, comprising a set of ultrasonic motors, which offer the advantages of a high power to weight ratio, low inertia, a compact design, high precision and high torque at low angular velocities. They may be as small as 1 mm in outer diameter [254] and provide a holding torque when not being supplied with current for a stop on a vertical surface. However, the required drive- and power electronics increase the overall robot size significantly and outweigh the benefits that follow from the miniature size of the motors themselves. For this reason stepper motors have been considered as an alternative propulsion method. Stepper motors provide a holding torque like ultrasonic motors, are compact and require neither encoders nor gear heads. Yet, compared with DC motors they require greater complexity in terms of power electronics, they also have a worse weight-performance ratio, do not support continuous rotation in the standard configuration and are less efficient. A series of novel low profile DC micro motors with encapsulated precision gear heads was therefore regarded as the optimum solution. Mounted directly on the chassis, no bevel gears or additional transmission is necessary, and they can be driven with minimum electronic effort via an H-Bridge as described in section 3.2.5.2.

Motor dimensions are of particular importance, as experience has shown that the propulsion system consumes the major part of the on board energy. Standard dimensioning criteria for motors are maximum power, maximum torque, angular velocity and motor size. The highest demand for long term operation is when the vehicle is driving straight up a vertical wall. With a weight of 500 g and a wheel diameter of approximately 40 mm, this requires a torque per shaft of 50 mNm. Hence, the necessary gear reduction is 207:1 [277], which corresponds to a gearbox output speed of 24 rpm and a maximum inspection speed of 5 cm/s. With this gear ratio the units also provide sufficient holding torque for a stop on vertical walls with switched off motors.

3.2.5.6 Wheel Encoders

For relative position measurement and velocity control, wheel encoders provide feedback from the motor shafts. The smallest overall size use magnetic encoders, which are commonly used with standard DC motors mounted directly on the drive unit increasing its overall length by only 1.4 mm [277]. However, implementation of this encoder type, in combination with the novel low profile motors, is not feasible due to the internal coil arrangement and larger optical encoders have to be utilised instead. Optical incremental encoders use a disc attached to the shaft which contains
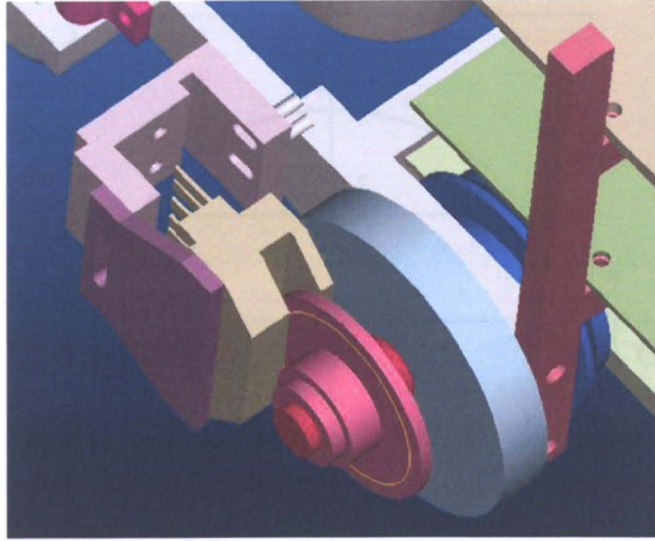
Figure 3.11: Initial Encoder design with separate codewheel and sensing unit.

a multitude of radial marks. A photo diode working as an optical switch gener-
ates an electrical pulse whenever one of the radial marks on the code wheel passes
through its sensing region. Initially, a design based on a thin aluminium disc with
machined radial slots and a separate sensing unit as illustrated in Fig. 3.11 was
tested. However, alignment of the two components has proven to be difficult due
to low shaft axial- and off-axis tolerances and the position on the outer sides of
the robot exposed to mechanical impacts. Significantly greater robustness is offered
by encapsulated encoders, where the precision machined aluminium hub and the
encoder circuit board module are protected by a plastic cover, these are also more
tolerant to misalignment. The smallest of such units, which is used for the final
design, is 13 mm high and has an overall outer diameter of 20 mm [284, 299]. It
requires a single +5V power supply and has a low power option as well as provision
of a simplified adjustment of code wheel and diodes. The resolution r is 300 pulses
per revolution, but as the motor- gearhead units only have a single output shaft, it
measures the gear-reduced output directly on the wheel hub.

For spot turning manoeuvres of differential drive robots with two independently
driven propulsion wheels and an unpowered omnidirectional third wheel, the centre
of rotation of the robot is located exactly in the centre between the two wheels as
indicated in Fig. 3.12. Hence, with a wheel diameter d of 38.1 mm and a distance
f between the centre of gravity of both wheels, the corresponding number of pulses
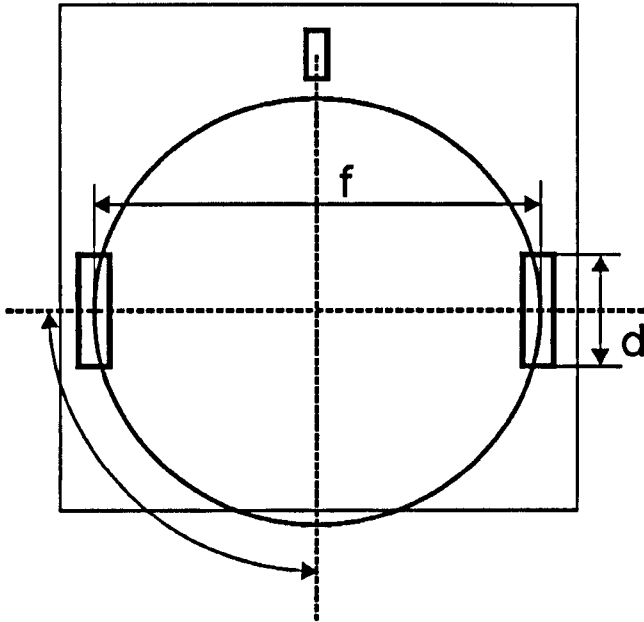
Figure 3.12: Ascertaining maximum turning speed and number of encoder pulses for 90° turns.

per shaft p for a 90° turn is:

$$p = 75 \, \frac{f}{d}. \tag{3.4}$$

f for the vehicles carrying MFL payload is 42.5 mm while the distance between the centre of gravity of the main wheels of the remaining robots is 64 mm. The theoretical accuracy for spot turns, $\Delta\alpha$, is hence

$$\Delta\alpha = \frac{f}{dr} \, 360°, \tag{3.5}$$

which yields 1.3° for a wheel distance of 42.5 mm and 2° for a wheel distance of 64 mm.

3.2.5.7 Gyroscope

The most critical disadvantage of the odometry-based positioning method described in the previous subsection is that small momentary orientation errors cause a constantly growing lateral position error. For this reason the encoder data is supplemented by angular rate information provided by a ADXRS150 micromachined angular rate sensor from Analog Devices. The device operates on the principle of a resonator gyroscope: two polysilicon sensing structures each contain a dither frame,

which is electro statically driven to resonance. This produces the velocity element to produce a Coriolis force during angular rate. At two of the outer extremes of each frame, orthogonal to the dither motion, are movable fingers that are placed between fixed pickoff supports to form a capacitive pickoff structure that senses Coriolis motion. The resulting signal is fed to a series of gain and demodulation stages that produce the electrical rate signal output on the printed circuit board — a voltage proportional to the angular rate about the axis normal to the top surface of the board (yaw rate). An on-chip charge pump provides the 14V – 16V for the electrostatic resonator, so that, in keeping with the concept of modularity, only a single +5V supply is required for operation. The device is suitable for operation between 55°C and +125°C and has a sensitivity of 12.5 mV/°s. Orientation changes up to 150°/s are detected, which is adequate considering the maximum turning rate $\dot{\alpha}$ of the vehicle:

$$\dot{\alpha} = \frac{n\,d}{f}\,360°. \tag{3.6}$$

With n being the gearbox output speed of the motor units and f the distance between the wheels according to Fig. 3.12, Equation 3.6 yields a maximum turning speed of 130°/s for the robots with the closer wheels for MFL inspection and 86°/s for the remaining vehicles.

3.2.5.8   Communication Link

The vehicles comprise a miniature RF module to access the RS-232 interface of the micro controller board wirelessly. Working at 10 selectable spot frequencies between 433 and 434 MHz communication is possible up to a distance of 250 m line of sight. The size of the units without the aerial is 53 mm x 20 mm x 5 mm, they operate at the battery voltage of 12V and have a selectable power output to reduce energy consumption. The turbo version of the Microcore-11 board contains a 9.8304 MHz crystal, which provides an increased Baud rate from 9600 bits/s to the maximum speed of these telemetry modules of 38400 bits/s.

3.2.5.9   Hall Sensor Array for MFL Inspection

For detection of corrosion pits and thickness loss a linear array of Honeywell SS94A2 Hall sensors is mounted on a spring loaded lever underneath the vehicle for MFL inspection in the centre between the two magnetic wheels, as shown in Fig. 3.13. These ceramic based linear Hall effect devices produce an output voltage proportional to the intensity of the magnetic field to which they are exposed. Their sensitivity is

43
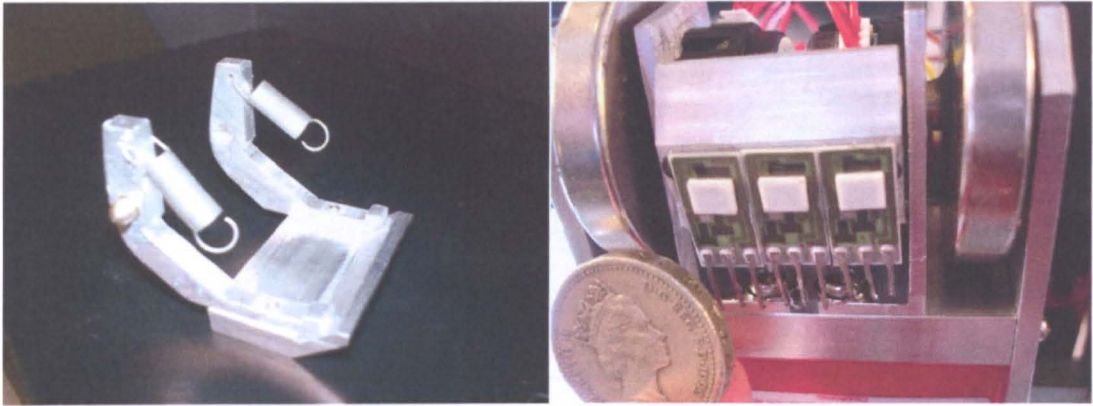
Figure 3.13: Linear Hall array on spring loaded lever for constant lift-off distance of Hall elements from surface.

5 mV/Gauss, they require 30 mA current at regulated +12V, have an effective area of 1 mm^2 and operate between –40 to +125°C. In order to insulate the array from external magnetic fields the central plate of the lever is made of steel, and the motors of the vehicles that carry this NDE payload are located at the outer side of the chassis, while the wheels and the separate optical encoders are positioned inside. Thus, with the wheels being closer together, the magnetic field strength in the sensor area is increased which leads to an improvement of defect sensitivity.

The spring loaded lever maintains a constant minimum distance between the array and the inspection surface, as the Hall sensor readings are highly sensitive to changes in stand off and the signal is proportional to $1/d^4$ [54]. Two 1.25 mm high shoulders, shown in Fig. A.25, along the sides of the bottom plate ensure that there is no physical contact between the 1 mm thick Hall plates and the specimen and avoid attrition of the sensing elements when the vehicle is moving. Electrical insulation of sensor connectors from the conducting surface is essential, and for obtaining high quality array data it is important that the thickness of the glue layer underneath the elements is uniform across the plate to provide for equal height of all Hall Sensors. Chapter 5 gives a more detailed description of the payload for MFL inspection.

3.2.5.10 Eddy Current Sensing

For inspection of conducting material, vehicles are equipped with an EC sensor which consists of a pair of coils as shown in Fig. 3.14. The probe is located at a maximum distance from the motors to avoid electrical interference, and, like the linear Hall array described in the previous subsection, they are mounted on a spring loaded lever that holds the probe in firm contact with the surface to maintain minimum stand off.

44

Figure 3.14: Eddy Current coils on spring loaded lever.

Different coils have been designed in order to optimise both defect sensitivity and the discrimination between flaws and stand off. Coils with 10 – 400 windings with wire sizes varying from 27 – 34 SWG have been tested at frequencies between 100 Hz and 40 MHz. The coil core is a 1.5 mm ferrite rod, a ferrimagnetic ceramic sintered compound material consisting of various mixtures of iron oxides, commonly used for antenna applications and Radio Frequency Identification (RFID) devices. Due to the small particle size of $< 2\mu m$ and the resulting high electrical resistance, eddy current losses are minimised while offering a relative permeability of 48. Chapter 4 gives a more detailed description of the payload for EC inspection.

3.2.5.11 Transducers for Ultrasonic Inspection

For US inspection, the vehicle carries a pair of air coupled piezoelectric transducers. Working as transmitter and receiver in pulse echo mode, they generate a local zeroth order anti-symmetric (A_0) Lamb wave in thin, planar structures. As the angle to the test specimen needs to be variable to adjust the required angle of incitation for the specific test frequency, the transducers are pivoted and clamped between two thin parallel beams, illustrated in drawing A.31, which constitute the main sensor bar. The height can be changed by varying the position of the threaded support rod by which each transducer is attached to the pivotal cube between the beams. Both rod and bar are made of acoustically lossy plastics and feature multiple cut-outs in order to minimise crosstalk between the transmitting and the receiving transducer via the clamp. For adjusting the transducer angle, two tensioning screws between the two beams have to be released and tightened respectively.

3.2.5.12 Wireless Camera for Visual Inspection

A miniature camera based on a Sharp CMOS Sensor with a resolution of 380 lines is integrated for visual inspection and machine vision for automated weld imaging.

45

| Wireless Telemetry Module | Acoustic Positioning Module | 68HC11 Processor | Micro Gyroscope | Motor Driver |

| 12V Li-Po Battery |
| NDE Payload |
| Power Module |
| Low Battery LED |

| Miniature DC FTB-Flatmotors | Encapsulated Gearheads | Magnetic Wheels (NeFeB) | Optical Shaft Encoders | Wireless Camera |
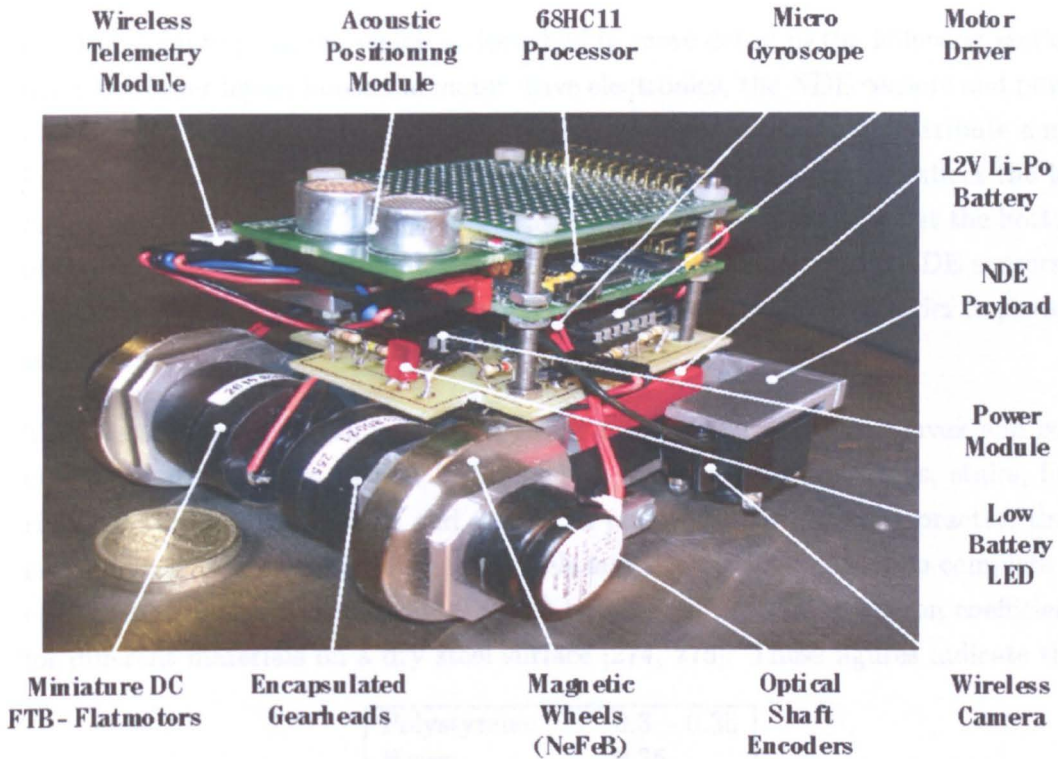
Figure 3.15: Prototype vehicle.

This module weighs 20 g, measures 19 x 19 x 16 mm and has a power consumption of 50 mW. The focal lens is adjustable to allow for closeup views of surfaces from less than 1 cm. Four infra-red LEDs switch on automatically below 3 Lux and the camera switches into night mode for operation inside pipes independent from ambient light conditions. The picture is transmitted wirelessly to the receiver unit up to a distance of 100 m.

3.2.6 Vehicle Design

Based on the considerations of the previous five subsections of this chapter, a three wheeled vehicle has been designed utilising the three dimensional design software package Pro Engineer Wildfire [292] and four prototypes with different NDE payloads have been built. A sequence of iterative steps eventually led to the design shown in Fig. 3.15. The dimensions are 7 x 7 x 8 cm and the vehicle weighs 580 g. The open architecture and the identical configuration of mounting holes of all boards allows for a stacked board arrangement on threaded studs and the possibility of employing backplane adaptors, thus enabling fast module replacement and adaptation to different inspection requirements. The top layer board in Fig. 3.15 manages the

46

robot's absolute position, which is described in more detail in the following section, while the lower layers house the motor drive electronics, the NDE sensors and power management. As illustrated in Fig. 3.10, these components do not contribute a major part of the overall weight, so locating them at the top does not affect the low centre of gravity of the robot. In contrast, the main battery is placed at the bottom of the vehicles. The pivot of the spring loaded levers that carry the NDE sensors is located in the front of the vehicle with the lever facing backwards in order to prevent self locking.

The overall vehicle length is kept short enough to cope with 90° convex and concave corners, as shown in Fig. 3.16 and Fig. 3.17, to overcome steps, stairs, fins, ripplings, bulges, depressions and flanges in pipework. However, in practice there is not sufficient friction between the wheels and the surface in order to complete all of the transitions autonomously. Table 3.1 shows a selection of friction coefficients for different materials on a dry steel surface [274, 275]: These figures indicate that

Polystyrene:	0.3 – 0.35
Brass:	0.35
Copper:	0.53
Leather (clean):	0.6
Aluminium:	0.61
Steel:	0.78
Rubber:	0.6 – 0.9

Table 3.1: Static friction coefficients steel

a thin rubber belt fitted to the outer surface of the wheels could improve traction, but neither this nor a layer of sandpaper or a toothed timing belt on the wheels with rubber studs provide sufficient friction, thus radii of more than twice the wheel radius on the test structure are required for autonomous transition between different surfaces.
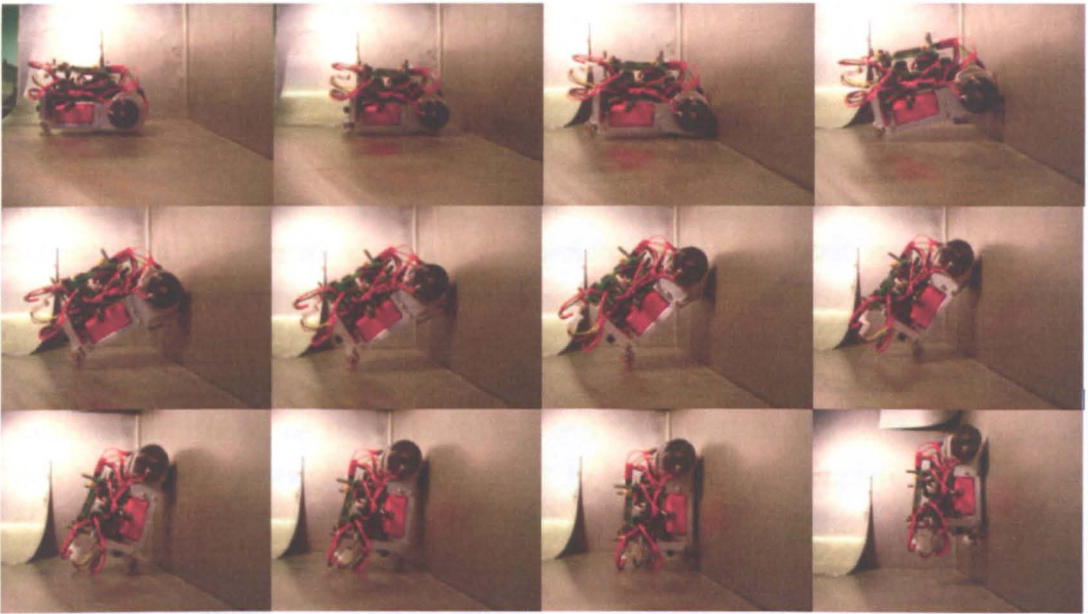
Figure 3.16: Transfer from non-ferromagnetic floor to steel wall.

Figure 3.17: Vehicle temporarily sliding on frame on 90° convex corners.

3.3 Vehicle Positioning

3.3.1 Introduction

For implementation of an automated scan pattern, the vehicles need to be continuously driven in order to closely follow the previous swath and to be quickly repositioned at the end of each cut. Deviating from the path leaves a band of missed surface area, while overlapping leads to longer inspection times. In general, none of the methods listed in Section 2.4 are utilised exclusively for reliable mobile robot positioning, but two or more methods are combined to overcome individual weaknesses. Hence, as there is also not only the position of a single robot to be determined, but a swarm of vehicles needs to be controlled, complete direct control of each individual robot's position by a host in real-time appears to be intricate and fault-prone. Thus, each inspection vehicle comprises an independent relative positioning system.

Starting from the overview about the different techniques for mobile robot positioning presented in Section 2.4, a trilateration type system with portable emitters carried by the vehicle and beacons which have been previously installed in the local environment, is considered as the most suitable absolute positioning system. A major advantage, given the severe power and weight restrictions, is the minimal number of sensors required on board the individual robots, which can be of much smaller and lighter construction. The following sections describe the positioning system which combines relative and absolute position measurements.

3.3.2 Relative Position Measurement

3.3.2.1 Introduction

The vehicles comprise a set of two wheel encoders and a gyroscope which provide incremental motion information with excellent short term accuracy. During normal driving, both motors receive a pulse width modulated signal according to the encoder output, and depending on the surface condition and the slope. The length of this duty cycle and consequently the efficient motor power, is adjusted to maintain vehicle velocity and current travelling direction. This is of particular importance when performing NDE on structures, as the sensor signals are affected by the vehicle's travelling speed.
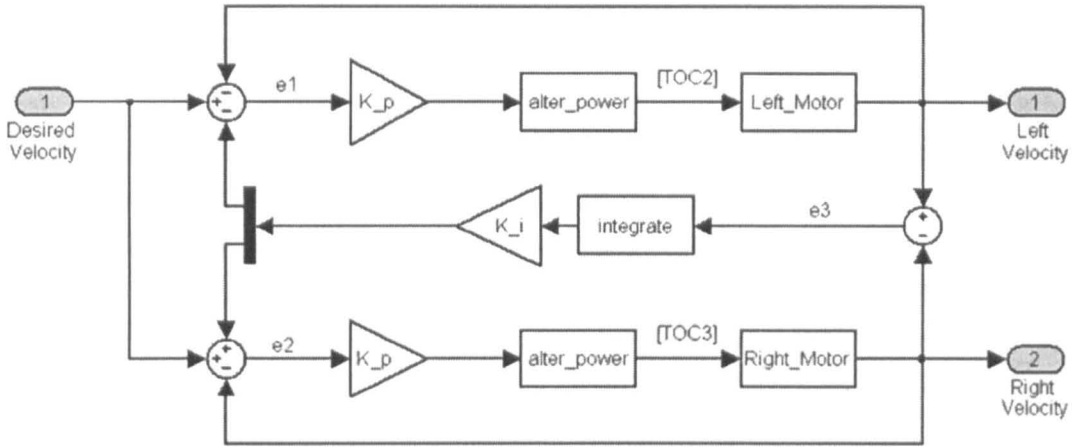
Figure 3.18: PI-control for accurate straight line behaviour and constant inspection velocity.

3.3.2.2 Local PI-Control

The encoder output is fed back to the micro controller to establish a local Proportional-Integral (PI) control loop. Due to the differential steering design, both motor speeds are monitored and updated continuously to achieve accurate straight line driving: The two separate feedback paths at the top and the bottom in Fig. 3.18 maintain the desired velocity, while the central feedback path secures synchronisation of the two wheels. Implementing additional derivative and integral controls within the two separate paths for velocity control of the motors has been tested, but did not lead to improvements in driving performance.

As the encoders are measuring the gear-reduced output directly on the wheel hub as described in section 3.2.5.6, the motor's speed is updated every 500 ms. The experimentally obtained gain for optimal response is:

$$K_p = 1 \quad \text{and} \quad K_i = 0.8. \tag{3.7}$$

Normal driving on flat ground is based on 70 encoder pulses per control interval and 40% pulse width, which leaves sufficient reserves for maintaining the same travelling speed for inspection up vertical walls.

3.3.2.3 Calibration of Odometry System and UMBmark Experiment

Odometry is based on integration of incremental motion information over time and the assumption that wheel revolutions can be translated into linear displacement relative to the floor. Reasons for inaccuracies in the translation of wheel encoder

readings into linear motion can be categorised as systematic errors and non systematic errors [9]. Non systematic errors are not directly caused by the kinematic inaccuracies of the vehicle's propulsion system, but arise through factors such as wheel slippage, floor irregularities, external forces, internal forces resulting from castor wheels and non-point wheel contact with the floor. Systematic errors, in contrast, build up because of the modelling error due to the parameter uncertainties in the kinematics equations which are used to convert the wheel's displacements into vehicle's displacements: They can arise from unequal wheel diameters, differences between left and right wheel diameter and nominal wheel diameter, misalignment of wheels, limited encoder resolution and limited encoder sampling rate [25]. Systematic errors are particularly grave, because they accumulate constantly and therefore, for inspection of smooth surfaces, they make the major contribution to the overall odometry error. Careful mechanical design and the most common calibration methods based on Least Square techniques [8, 9] and the University of Michigan Benchmark (UMBmark) procedure [24] reduce these systematic errors significantly. As the calibration procedure proposed by Borenstein and Feng [26] claimes to be capable of isolating and identifying minute mechanical inaccuracies such as wheel diameters that differ as little as 0.1%, this method was selected and applied.

For differential drive mobile robots, the two dominant systematic error sources are unequal wheel diameters and the uncertainty about the effective wheelbase [27]. These two errors, E_d and E_b respectively, are dimensionless vehicle specific values defined as:

$$E_d = \frac{D_R}{D_L} \qquad \text{and} \qquad E_b = \frac{b_{actual}}{b_{nominal}}, \qquad (3.8)$$

where b is the wheelbase of the vehicle and D_R and D_L are the actual wheel diameters of the right and left wheel, respectively. E_b only affects turning manoeuvres while E_d has an effect only on straight line motion. By measuring the individual contribution of these two dominant errors, their effect can be compensated for by the on board software. Therefor the inspection vehicles complete a variation of the University of Michigan Benchmark (UMBmark) test for mobile robots, a set of well defined experimental runs where each vehicle is programmed to traverse the four legs of a 4x4 m square path. As the subject of investigation are vehicles of miniature size and due to the size of the available test specimens, this path was reduced to 0.75 x 0.75 m. The experiment was performed five times in clockwise (cw) and counter clockwise (ccw) directions and yielded five sets of return position errors ($\varepsilon x_i, \varepsilon y_i,$). Averaging reduces the random effect of non-systematic errors and yields the centre

of gravity of the cluster of return positions for each cw and ccw test:

$$x_{c.g.} = \frac{1}{n} \sum_{i=1}^{n} \varepsilon x_i \qquad\qquad y_{c.g.} = \frac{1}{n} \sum_{i=1}^{n} \varepsilon y_i \qquad\qquad (3.9)$$

For deriving correction factors from the error distribution pattern, two odometry error characteristics in orientation, Type A and Type B, are defined. As illustrated in Fig. 3.19, orientation errors which reduce or increase the total amount of rotation of the robot during the square path experiment in both cw and ccw direction are of Type A, and Type B errors in orientation are defined as reducing or increasing the total amount of rotation of the robot during the square path experiment in one direction, but increasing or reducing the amount of rotation when going in the other direction. Type A errors are caused only by the wheelbase error while Type B errors result from unequal wheel diameters. Both can be calculated as follows, utilising expressions for α and β derived from the geometric relationships in Fig. 3.19:

$$\alpha = \frac{x_{c.g.,cw} + x_{c.g.,ccw}}{-4L} \frac{180°}{\pi} \qquad\qquad (3.10)$$

$$\beta = \frac{x_{c.g.,cw} - x_{c.g.,ccw}}{-4L} \frac{180°}{\pi} \qquad\qquad (3.11)$$

$$E_d = \frac{R + \frac{b}{2}}{R - \frac{b}{2}} \qquad\qquad (3.12)$$

$$E_b = \frac{90°}{90° - \alpha} \qquad\qquad (3.13)$$

with R being the the curvature of the path of Fig. 3.19b

$$R = \frac{\frac{L}{2}}{\sin\frac{\beta}{2}} . \qquad\qquad (3.14)$$

Compensating for these errors in software is achieved by defining the two correction factors

$$c_l = \frac{2}{E_d + 1} \qquad\qquad (3.15)$$

and

$$c_r = \frac{2}{\frac{1}{E_d} + 1} , \qquad\qquad (3.16)$$

52
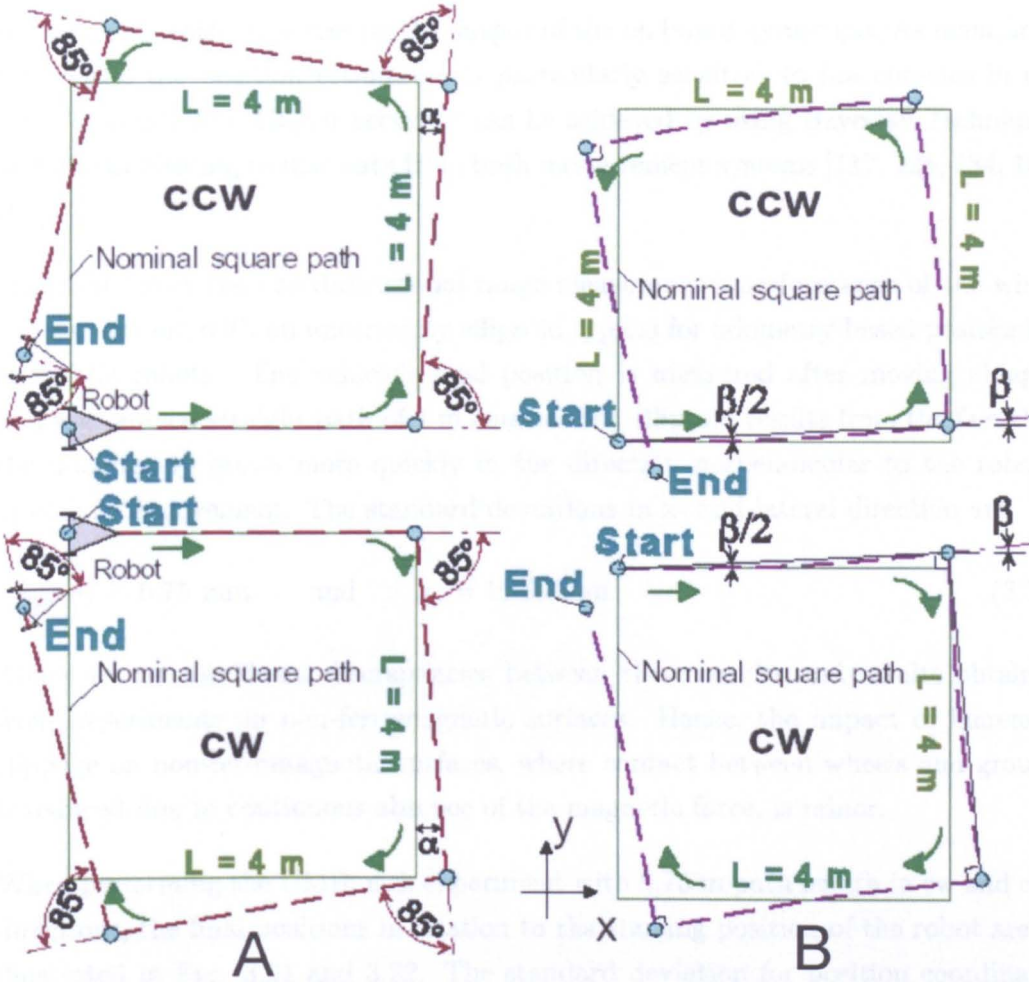
Figure 3.19: UMBmark Eperiment – Type A and Type B errors in orientation in ccw and cw direction [26].

which are implemented in the calculation of the travelled distance per wheel as:

$$\delta U_{L/R} = c_{L/R} c_m N_{L/R} ,$$ (3.17)

where c_m is a conversion factor to translate encoder pulses into linear wheel displacement:

$$c_m = \frac{\pi D_n}{C_e} .$$ (3.18)

$N_{L/R}$ is the pulse increment of the encoder, D_n the nominal wheel diameter and C_e is the encoder resolution in pulses per revolution.

For this experiment, information about the robots orientation is solely based on the

encoder data without accessing the output of the on board gyroscope. As mentioned previously, the position estimation is particularly sensitive to inaccuracies in the robot's orientation. Higher accuracy can be achieved by using Bayesian Techniques or Kalman filtering to fuse data from both measurement systems [117, 128, 184, 197, 205].

Fig. 3.20 shows the one dimensional range measurement performance of the wheel encoder system with an uncertainty ellipsoid typical for odometry based positioning of mobile robots. The vehicle's final position is measured after moving along a preprogrammed straight path of 1 m length. The ellipsoid results from the fact that the uncertainty grows more quickly in the direction perpendicular to the robot's direction of movement. The standard deviations in x- and lateral direction are:

$$\sigma_x = 0.75 \text{ mm} \qquad \text{and} \qquad \sigma_y = 10.69 \text{ mm}. \tag{3.19}$$

There are no significant discrepancies between these results and results obtained from experiments on non-ferromagnetic surfaces. Hence, the impact of increased slippage on non-ferromagnetic surfaces, where contact between wheels and ground is reduced due to continuous absence of the magnetic force, is minor.

When performing the UMBmark experiment with 0.75 m path length in cw and ccw directions, the final positions in relation to the starting position of the robot are as illustrated in Fig. 3.21 and 3.22. The standard deviation for position coordinates before calibration in two dimensions is

$$19.74 \text{ mm} < \sigma_{x/y} < 22.8 \text{ mm}. \tag{3.20}$$

This changes to

$$6.08 \text{ mm} < \sigma_{x/y} < 28.15 \text{ mm} \tag{3.21}$$

after calibration, and the centre of gravity of the cluster of cw turns improves from [-65 mm; -49 mm] to [-3 mm; 9 mm], as shown in Fig. 3.21.
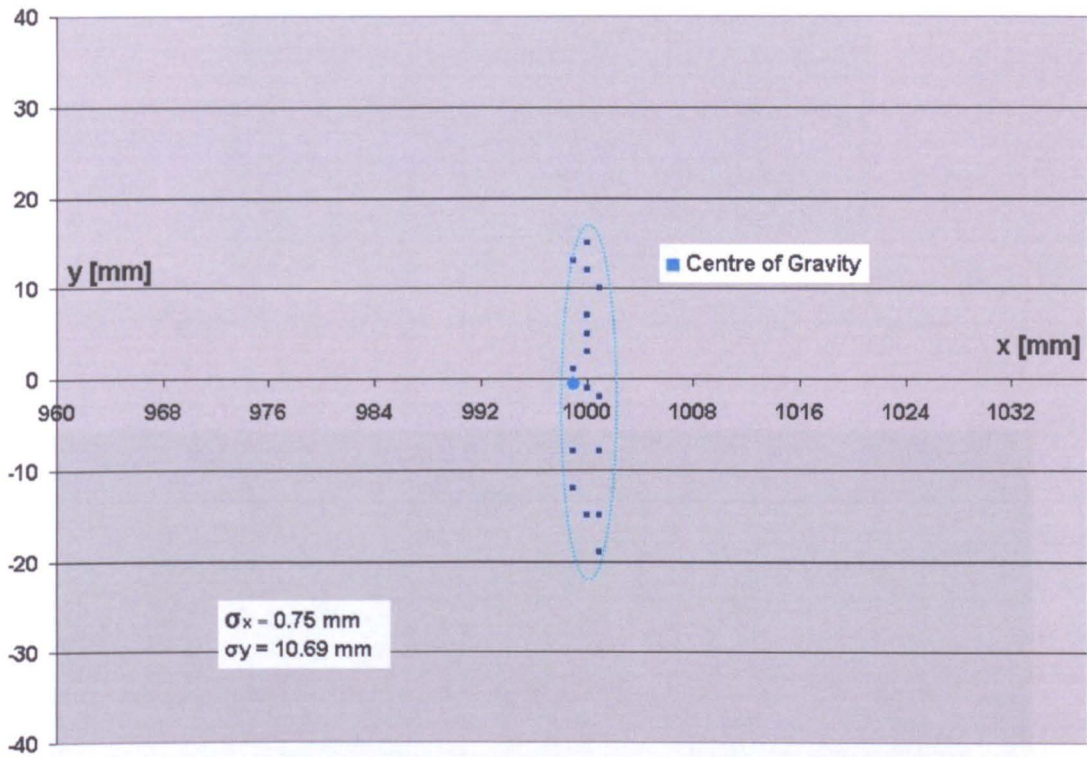
Figure 3.20: Results of linear position experiment, uncertainty ellipsis.
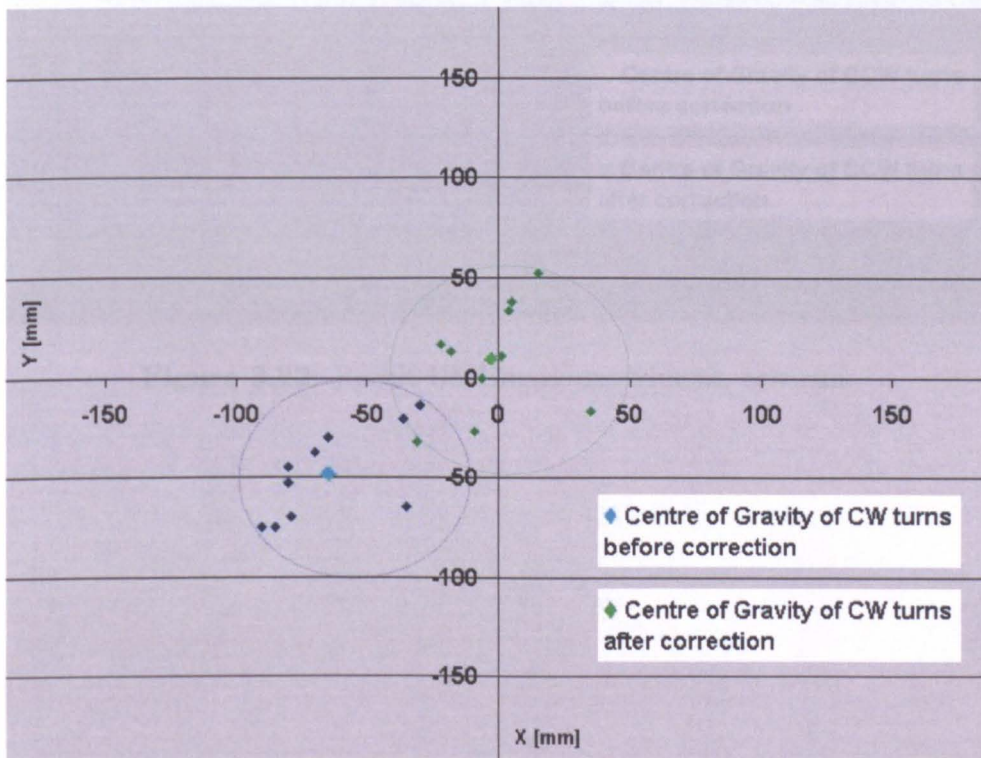
Figure 3.21: Result UMBmark experiment, cw run.
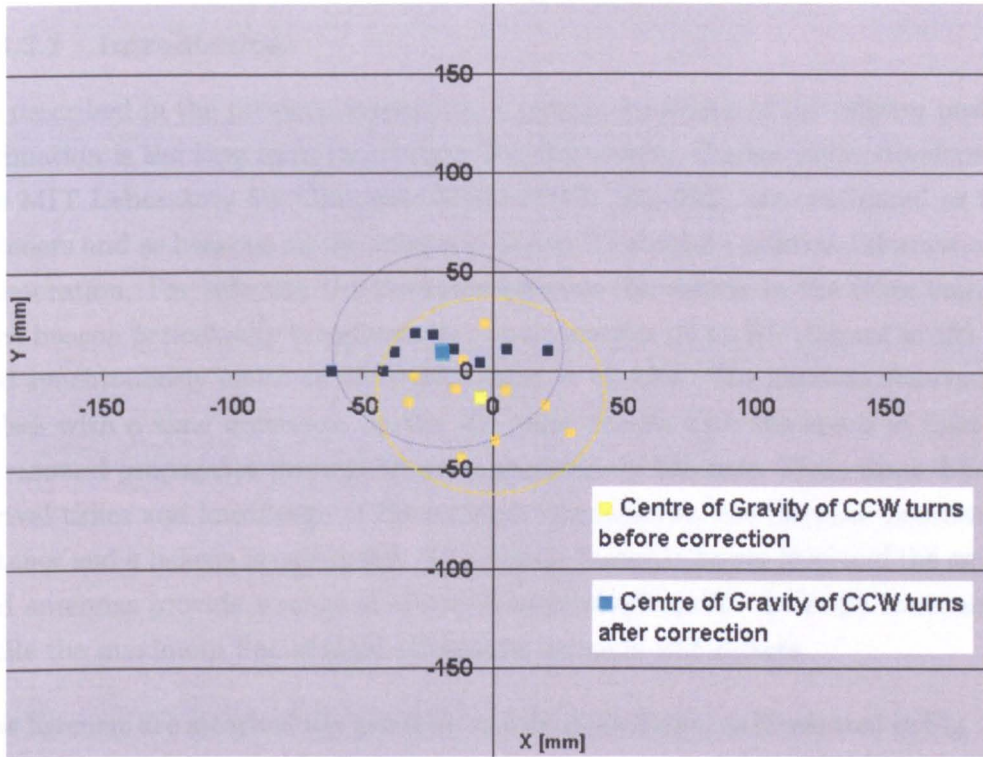
Figure 3.22: Result UMBmark experiment, ccw run.
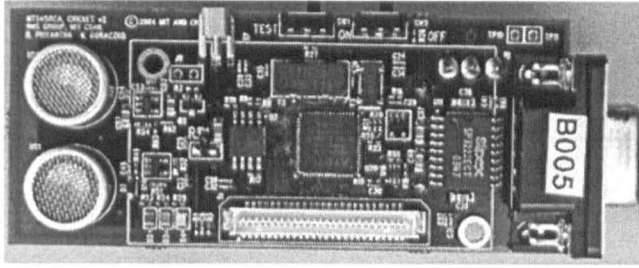
Figure 3.23: Cricket unit, configurable as listener or beacon.

3.3.3 The Absolute Positioning System

3.3.3.1 Introduction

As described in the previous subsection, the main drawback of the relative position estimation is the long term inaccuracy. For this reason, Cricket units, developed at the MIT Laboratory for Computer Science [173, 205, 289], are configured as fixed listeners and as beacons on the robots to derive 3D absolute position information by trilateration. For inferring the distances between the vehicle to the three listeners, each beacon periodically broadcasts its space identifier on an RF channel at 433 Mhz and synchronously emits an ultrasonic pulse at 40 kHz. The listeners receive both pulses with a time difference, as the RF pulse travels with the speed of light and ultrasound propagates through air at approximately 343 m/s. From these different arrival times and knowledge of the ambient temperature, the distance between one listener and a beacon is calculated. The default transmit power level and the embedded antennas provide a range of about 30 meters indoors for the radio transmission while the maximum line of sight ultrasound range is 10.5 meters.

The listeners are attached to a portable and foldable frame, as illustrated in Fig. 3.24. Assigning coordinates to the listeners, the beacons are localised with reference to the local coordinate system of the frame. In this way, the system is kept versatile and mobile for a wide range of applications. Denoting the position of listener 1 on the frame as the origin of this reference system and placing the remaining listeners at $L_2 = (r, 0, 0)$ and $L_3 = (0, r, 0)$, the position of the robots in Cartesian coordinates (x_r, y_r, z_r) is calculated by simultaneously solving the set of three equations

$$d_i^2 = (x - x_i)^2 + (y - y_i)^2 + (z - z_i)^2 \quad \text{for} \quad i = 1, 2, 3 \tag{3.22}$$
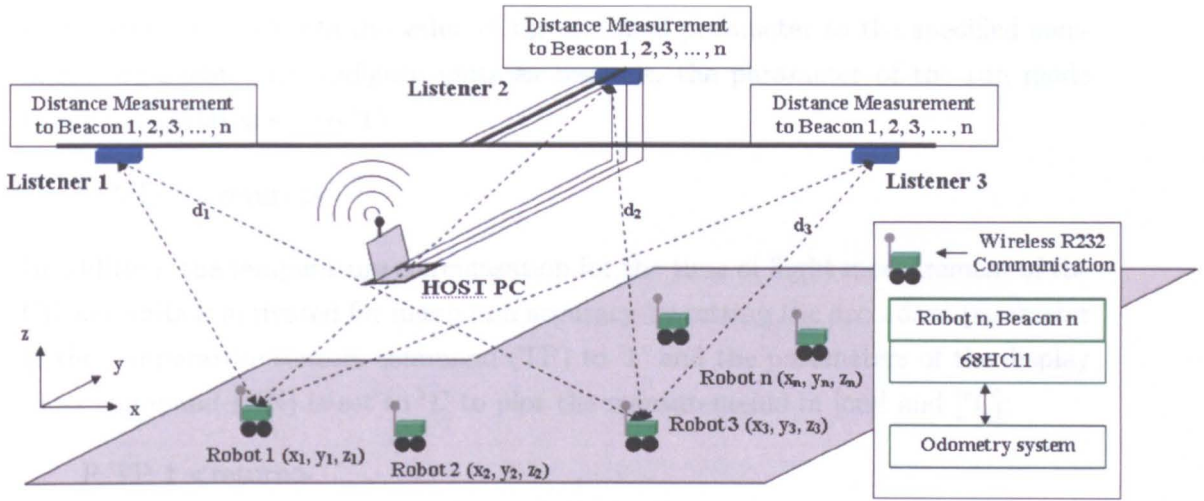
Figure 3.24: Overall system concept - position estimation by trilateration.

to

$$x_r = \frac{1}{2r}(-d_2^2 + r^2 + d_1^2), \tag{3.23}$$

$$y_r = \frac{1}{2r}(-d_3^2 + r^2 + d_1^2) \quad \text{and} \tag{3.24}$$

$$z_r = \pm\frac{1}{2r}\sqrt{(-d_2^4 + 2d_2^2 r^2 + 2d_2^2 d_1^2 - 2r^4 - 2d_1^4 - d_3^4}$$
$$\overline{+2d_3^2 r^2 + 2d_3^2 d_1^2)}. \tag{3.25}$$

If the portable frame is installed above the area of interest, only the negative solution
of Equation 3.25 has to be considered.

3.3.3.2 Configuring Cricket Units

The Cricket Command Interface serves for configuring the Crickets and is accessible
via the standard communication utility HyperTerminal [278]. The parameters for
this serial command interface are:

Transmission speed:	115200 bits/second
Data format:	8 bits, no parity
Flow control:	Xon/Xoff
Stop bits:	1

Figure 3.25: Parameters for Cricket serial interface

All commands have identical general formats and utilise one of two directives [263]:
'Get' (G) returns the values corresponding to the parameters specified in the com-

mand and 'Put' (P) sets the value of the specified parameter to the specified command argument. To configure units as beacons, the parameter of the run mode command (MD) is set to '1':

    P MD 1 <return>

In addition, the temperature compensation for the time of flight measurement of the Cricket units is activated for maximum accuracy by setting the accordant parameter of the temperature sensors command (TP) to '1' and the parameters of the display units command (UN) is set to '1' to plot the measurements in [cm] and [°C]:

    P TP 1 <return>
    P UN 1 1 <return>

For the listeners, the parameter of the output format command (OU) is set to '0' to switch off the automated listings and restrict the output to responses to the beacon listing (LS) command:

    P OU 0 <return>

Eventually, the above settings have to be saved to flash memory to be active the next time the beacon is powered up:

    P SV <return>

In order to reduce energy consumption, the on board RS-232 chip of the beacons is disabled by placing the test switch of the modules in the 'off' position.

3.3.3.3   Error Propagation

The accuracy of distance measurements between two Cricket units is stated to be between 1 cm and 3 cm [289]. However, the variance of this error is ascertained more precisely by linear displacement experiments and found to be proportional to the absolute value of the measured distance:

$$u(d_1) = u(d_2) = u(d_3) \approx 1\,\frac{\text{cm}}{\text{m}}. \tag{3.26}$$

Three of these measurements are necessary to extract a single space coordinate. The probability distribution of the three coordinates x_r, y_r and z_r, each of them depending with known functions f_i on the three input signals d_1, d_2 and d_3 according

59

to Equations (3.23), (3.24) and (3.25) can be described with the output covariance matrix C_p given by the error propagation law:

$$C_P = F_D C_D F_D^T \tag{3.27}$$

where C_P is the covariance matrix representing the propagated uncertainties for the position coordinates, C_D is the covariance matrix representing the uncertainties of the individual distance measurements and F_D is the Jacobian matrix defined as

$$F_D = \nabla f = \left[\nabla_D \cdot f(D)^T \right]^T = \begin{pmatrix} f_1 \\ f_2 \\ f_3 \end{pmatrix} \begin{pmatrix} \dfrac{\delta}{\delta d_1} & \dfrac{\delta}{\delta d_2} & \dfrac{\delta}{\delta d_3} \end{pmatrix}. \tag{3.28}$$

The three distance measurements between the robot and the listeners can be regarded as being independent from each other, hence

$$C_D = \begin{pmatrix} u(d_1) & 0 & 0 \\ 0 & u(d_2) & 0 \\ 0 & 0 & u(d_3) \end{pmatrix}. \tag{3.29}$$

This yields the covariance matrix C_P which represents the propagated uncertainties for the 3D space coordinates according to Equation 3.27:

$$C_P = \begin{pmatrix} (\frac{\delta x_r}{\delta d_1})^2 u(d_1) + (\frac{\delta x_r}{\delta d_1})^2 u(d_2) & \frac{\delta y_r}{\delta d_1}\frac{\delta y_r}{\delta d_1} u(d_1) \\ \frac{\delta x_r}{\delta d_1}\frac{\delta y_r}{\delta d_2} u(d_1) & (\frac{\delta y_r}{\delta d_1})^2 u(d_1) + (\frac{\delta y_r}{\delta d_3})^2 u(d_3) \\ \frac{\delta z_r}{\delta d_1}\frac{\delta x_r}{\delta d_1} u(d_1) + \frac{\delta x_r}{\delta d_2}\frac{\delta z_r}{\delta d_2} u(d_3) & \frac{\delta y_r}{\delta d_1}\frac{\delta z_r}{\delta d_1} u(d_1) + \frac{\delta y_r}{\delta d_3}\frac{\delta z_r}{\delta d_3} u(d_3) \end{pmatrix}$$

$$\begin{pmatrix} \frac{\delta z_r}{\delta d_1}\frac{\delta x_r}{\delta d_1} u(d_1) + \frac{\delta z_r}{\delta d_2}\frac{\delta x_r}{\delta d_2} u(d_2) \\ \frac{\delta y_r}{\delta d_1}\frac{\delta z_r}{\delta d_1} u(d_1) + \frac{\delta y_r}{\delta d_3}\frac{\delta z_r}{\delta d_3} u(d_3) \\ (\frac{\partial z_r}{\partial d_1})^2 u(d_1) + (\frac{\partial z_r}{\partial d_2})^2 u(d_2) + (\frac{\partial z_r}{\partial d_3})^2 u(d_3) \end{pmatrix}, \tag{3.30}$$

since

$$\frac{\partial x_r}{\partial d_3} = \frac{\partial y_r}{\partial d_2} = 0$$

and with the partial derivations as in Equations 3.32 — 3.37.

Figures 3.26, 3.27 and 3.29 visualise the propagated uncertainties at different positions employing Gauss' law of error propagation. For a measurement result $y =$

$f(A, B, C, ...)$ derived from different independent measurands A, B and C, the resulting measurement uncertainty $u(y)$ in dependence on the measurement uncertainties of the individual measurands $u(A)$, $u(B)$ and $u(C)$ is given by:

$$u(y) = \sqrt{\left(\frac{\partial f}{\partial A}u(A)\right)^2 + \left(\frac{\partial f}{\partial B}u(B)\right)^2 + \left(\frac{\partial f}{\partial C}u(C)\right)^2 + \cdots}. \qquad (3.31)$$

With

$$\frac{\partial x_r}{\partial d_1} = \frac{\partial y_r}{\partial d_1} = \frac{d_1}{r}, \qquad (3.32)$$

$$\frac{\partial x_r}{\partial d_2} = -\frac{d2}{r}, \qquad (3.33)$$

$$\frac{\partial y_r}{\partial d_3} = -\frac{d3}{r}, \qquad (3.34)$$

$$\frac{\partial z_r}{\partial d_1} = \frac{d_1(d_2^2 - 2d_1^2 + d_3^2)}{r\sqrt{-d_2^4 + 2d_2^2 r^2 + 2d_2^2 d_1^2 - 2r^4 - 2d_1^4 - d_3^4 + 2d_3^2 r^2 + 2d_3^2 d_1^2}}, \qquad (3.35)$$

$$\frac{\partial z_r}{\partial d_2} = \frac{d_2(d_2^2 + r^2 + d_1^2)}{r\sqrt{-d_2^4 + 2d_2^2 r^2 + 2d_2^2 d_1^2 - 2r^4 - 2d_1^4 - d_3^4 + 2d_3^2 r^2 + 2d_3^2 d_1^2}}, \qquad (3.36)$$

$$\frac{\partial z_r}{\partial d_3} = \frac{-d_3(d_3^2 - r^2 - d_1^2)}{r\sqrt{-d_2^4 + 2d_2^2 r^2 + 2d_2^2 d_1^2 - 2r^4 - 2d_1^4 - d_3^4 + 2d_3^2 r^2 + 2d_3^2 d_1^2}}, \qquad (3.37)$$

and Equation 3.26 this yields the measurement uncertainties of the positioning coordinates:

$$u(x_r) = \sqrt{\left(\frac{d_1}{r}u(d_1)\right)^2 + \left(-\frac{d_2}{r}u(d_2)\right)^2}, \qquad (3.38)$$

$$u(y_r) = \sqrt{\left(\frac{d_1}{r}u(d_1)\right)^2 + \left(-\frac{d_3}{r}u(d_3)\right)^2}, \qquad (3.39)$$

$$u(z_r) = \sqrt{\left(\frac{\partial z_r}{\partial d_1}u(d_1)\right)^2 + \left(\frac{\partial z_r}{\partial d_2}u(d_2)\right)^2 + \left(\frac{\partial z_r}{\partial d_3}u(d_3)\right)^2}. \qquad (3.40)$$

For a plane parallel to the plane defined by the portable frame this yields the average positioning accuracy in x-, and y-direction visualised in Fig. 3.26: As expected, highest accuracy is at $P_0 = [20; 160]$ in the central area between listeners on the frame in the first quadrant, and with an inter-listener distance of 300 cm the error increases as shown. To optimise positional accuracy for inspection of two dimensional surfaces, the parameters frame distance h and inter-listener distance r are determined analytically. For re-initialisation of the odometry system, a high local accuracy in a single point is vital and is achieved by choosing low values for r and h, as visible in Fig. 3.29. By contrast, as can be seen in Fig. 3.27, reasonable accuracy over a larger surface results from greater values for r and h. A C-algorithm has

been developed to determine those values for r and h that yield the largest surface coverage for a given threshold in the point of highest accuracy. For example, placing the beacon at

$$P_t = \begin{pmatrix} 30 \\ 30 \\ -80 \end{pmatrix} \text{cm} \tag{3.41}$$

with a listener distance r of 50 cm yields an accuracy, according to equations 3.38, 3.39 and 3.40, of:

$$u(x_r) = 3,4\,\text{cm} \qquad u(y_r) = 5,2\,\text{cm} \qquad u(z_r) = 7,6\,\text{cm}. \tag{3.42}$$

This theoretical error propagation is validated experimentally by positioning the beacon at different locations within the observation space and determining the Cartesian coordinates with the implemented C-routine for trilateration. The result is displayed in Fig. 3.28: The colour marks indicate the position estimation derived from trilateration while the bold marks each represent the true position of the beacon. As shown, the measured position is within the previously ascertained tolerances.
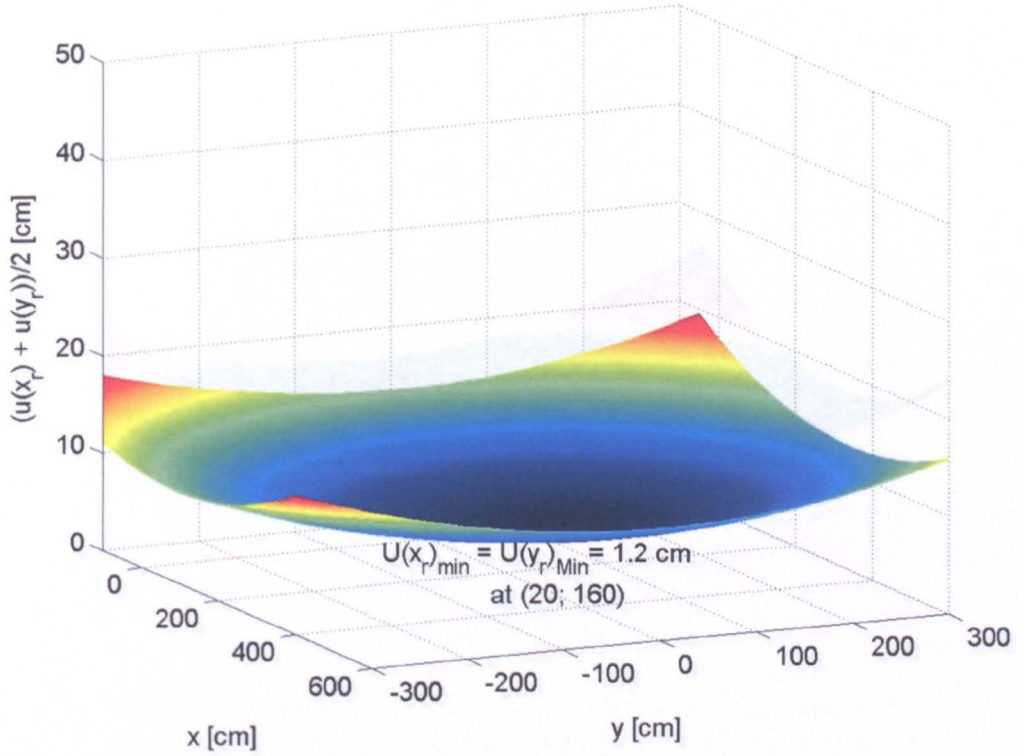
Figure 3.26: Propagated uncertainties for x- and y- according to Gauss' law of error propagation, frame distance from surface = 50 cm, inter-listener distance 300 cm.

Frame Distance from surface h = 200cm; Inter-Listener Distance r = 200cm

$U(x_r)_{min} = U(y_r)_{Min} = 3.5$ cm
at (20; 120)
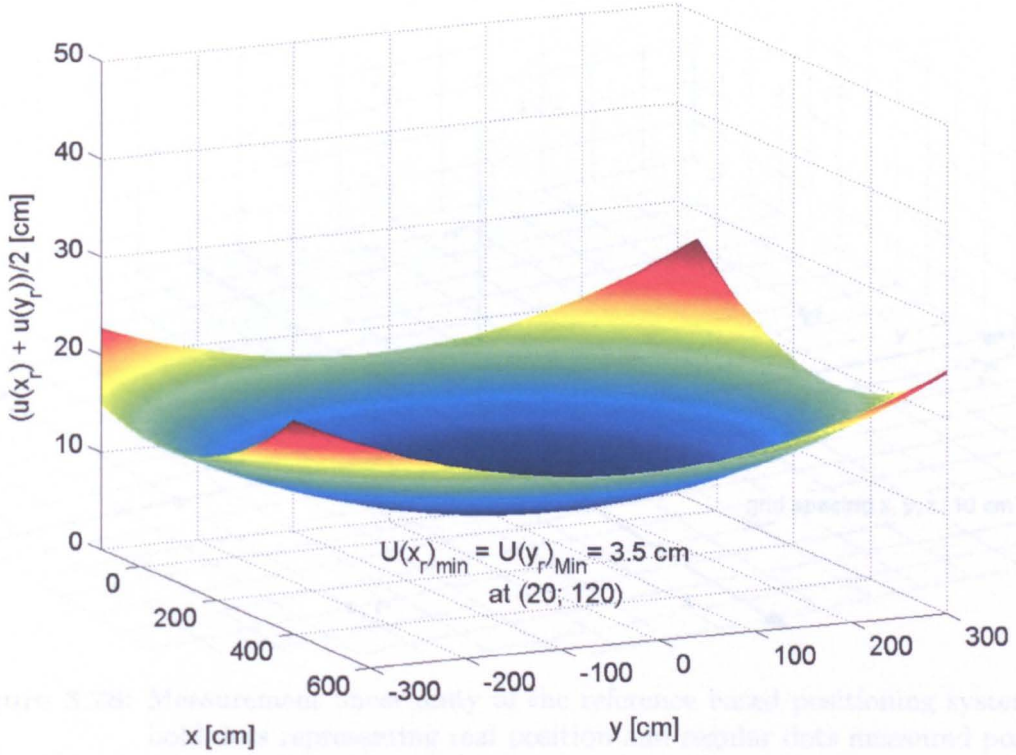
Figure 3.27: Propagated uncertainties for x- and y- according to Gauss' law of error propagation, frame distance from surface = 200 cm, inter-listener distance 200 cm.
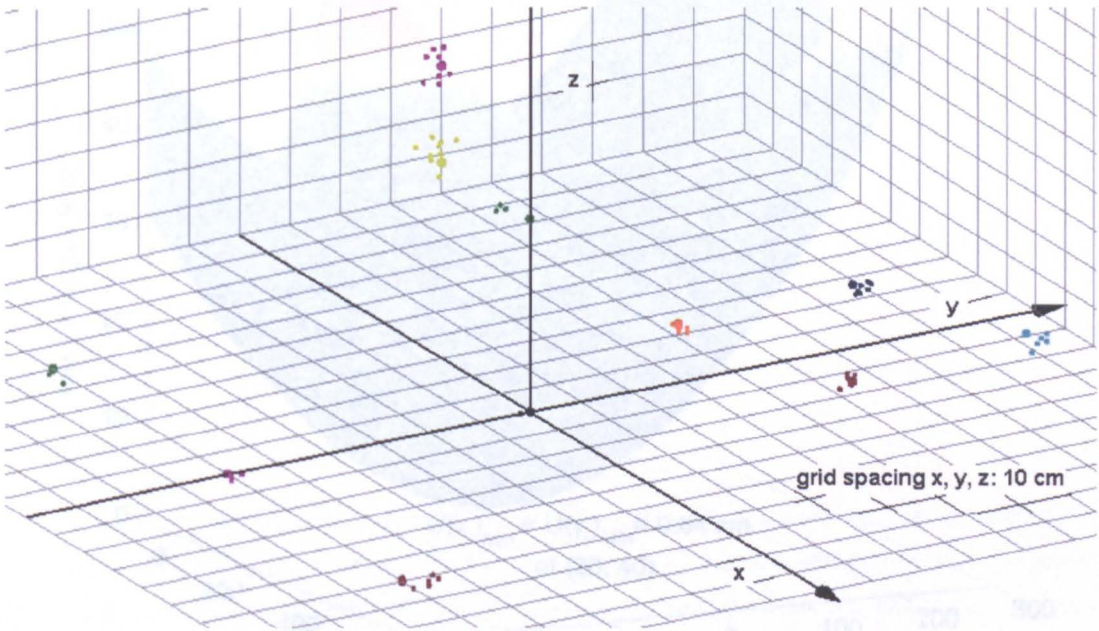
Figure 3.28: Measurement uncertainty of the reference based positioning system, bold dots representing real position and regular dots measured position of beacon ('3D Grapher').

Frame Distance from surface h = 40cm; Inter-Listener Distance r = 50cm
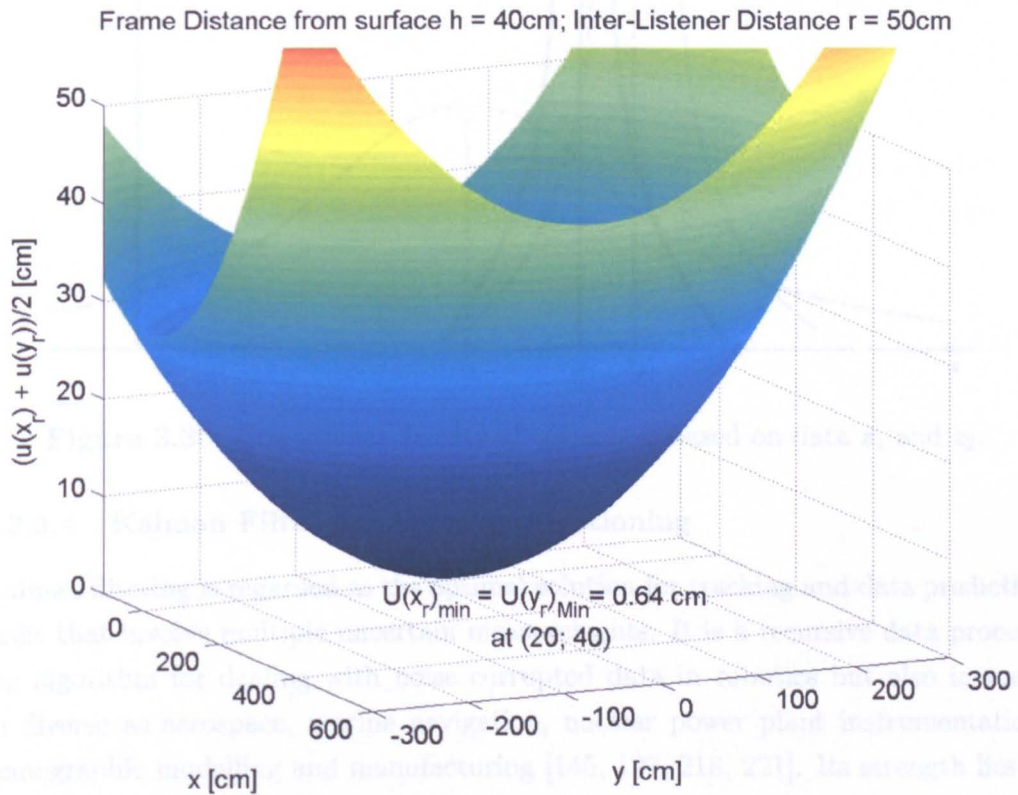
Figure 3.29: Propagated uncertainties for x- and y- according to Gauss' law of error propagation, frame distance from surface = 40 cm, inter-listener distance 50 cm.
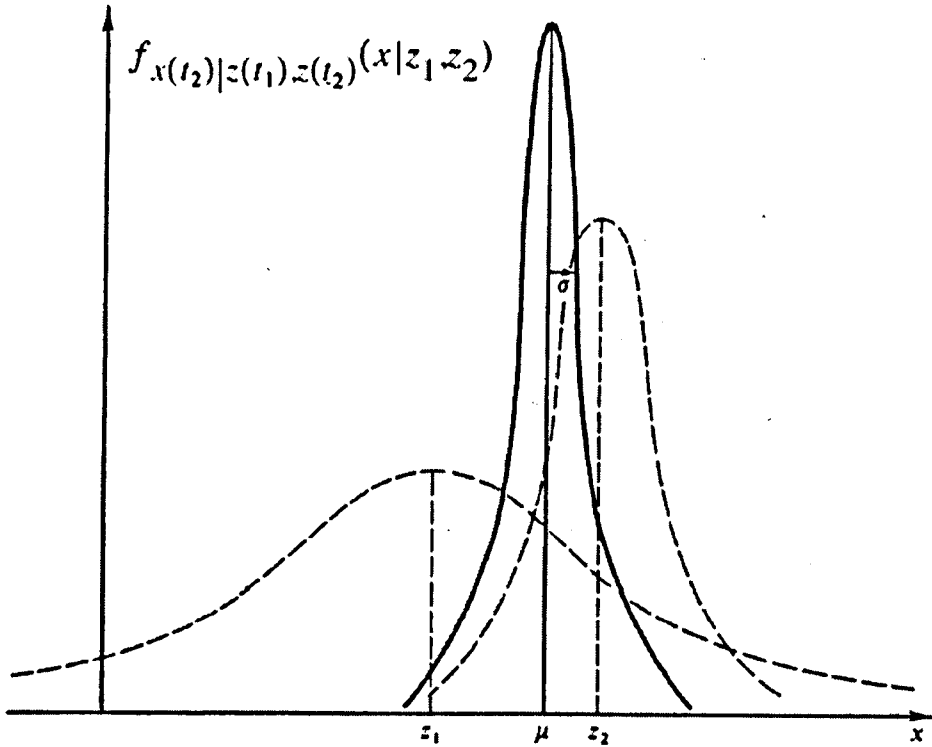
Figure 3.30: Conditional density of variable x based on data z_1 and z_2.

3.3.3.4 Kalman Filter for Absolute Positioning

Kalman filtering is regarded as the optimal solution for tracking and data prediction tasks that involve multiple uncertain measurements. It is a recursive data processing algorithm for dealing with noise corrupted data in robotics but also in areas as diverse as aerospace, marine navigation, nuclear power plant instrumentation, demographic modelling and manufacturing [145, 197, 218, 221]. Its strength lies in its simplicity and computational efficiency. A Kalman filter processes all available measurements, regardless of their precision, to estimate the current value of the variables of interest utilising knowledge of:

- the system and measurement device dynamics

- the statistical description of the system noises

- measurement errors

- uncertainty in the system models

- any available information about initial conditions.

67

For this, the confidence in the measurement is balanced against the confidence in the state estimate to determine the amount by which the state estimate should change [145]. As illustrated in Fig. 3.30, the best estimate of a variable x based on the two measurements (or a measurement and an estimate) z_1 and z_2 is μ. z_1 and z_2 have the standard deviations σ_1 and σ_2 and are taken at t_1 and t_2. The probability of x being a certain value based on z_1 and z_2 is represented by $f_{x(t_2)|z(t_1,t_2)}(x|z_1, z_2)$. σ_2 in Fig. 3.30 is smaller than σ_1, hence the second measurement or estimate is more accurate than the first one and the optimal estimate μ at time t_2 is closer to z_2. Although σ_1 is large, the standard deviation σ of this optimal estimate μ is still less than σ_2, which shows that even poor quality data can provide additional information and increase the precision of the filter output.

The Kalman Filter addresses the general problem of estimating the state $x \in \Re^n$ of a discrete time controlled process that is governed by the linear stochastic difference equation

$$x_k = Ax_{k-1} + Bu_{k-1} + w_{k-1} \tag{3.43}$$

with a measurement $z \in \Re^m$

$$z_k = h(x_k) + v_k. \tag{3.44}$$

$h(x_k)$ is the observation model relating the state x_k to the measurement z_k according to Equation 3.22:

$$h(x) = \begin{pmatrix} \sqrt{x^2 + y^2 + z^2} \\ \sqrt{(x - r)^2 + (y)^2 + z^2} \\ \sqrt{x^2 + (y - r)^2 + z^2} \end{pmatrix} \tag{3.45}$$

The random variables w_k and v_k in Equations 3.43 and 3.44 represent white process and measurement noise. They are assumed to be independent of each other and normally distributed as illustrated below:

$$p(w) \sim N(0, Q) \tag{3.46}$$
$$p(v) \sim N(0, R) \tag{3.47}$$

Q and R are referred to as the process and measurement noise covariance matrices:

$$Q = E[w_k w_k^T] \tag{3.48}$$

$$R = E[v_k v_k^T] . \tag{3.49}$$

Both might change with each time step. The n × n matrix A in the difference Equation 3.43 is the transition model relating the state at the previous time step *k-1* to the state of the current step *k* in the absence of both a driving function and process noise. The n × 1 matrix B is the control input model relating to optional control input $u \in \Re^l$ to the state x. As mentioned previously, Kalman filters use the most recent sample and its internal state to project ahead and produce an estimate of the state vector for the next time step. If $\hat{x}_k \in \Re^n$ is the a priori state estimate at step k, given knowledge of the process prior to step k, and $\hat{x}_k^- \in \Re^n$ the a posteriori state estimate at step k given measurement z_k, the a priori and a posteriori estimate errors e_k^- and e_k are defined as

$$e_k^- = x_k - \hat{x}_k^- \tag{3.50}$$

$$e_k = x_k - \hat{x}_k. \tag{3.51}$$

The a priori and a posteriori covariance matrices are then

$$P_k^- = E[e_k^- e_k^{-T}] \tag{3.52}$$

$$P_k = E[e_k^- e_k^T]. \tag{3.53}$$

P_k can be interpreted as a measure for the estimated accuracy of the state estimate.

Recursive Kalman filter algorithms start with initial values for $\hat{x}_{k-1}$ and P_{k-1} and recursively condition the current estimate on all of the past measurements in a feedback loop [238]:

$$\hat{x}_k^- = A\hat{x}_{k-1} + Bu_{k-1} \tag{3.54}$$

$$P_k^- = AP_{k-1}A^T + Q \tag{3.55}$$

$$K_k = \frac{P_k^- H^T}{HP_k^- H^T + R} \tag{3.56}$$

$$\hat{x}_k = \hat{x}_k^- + K_k(z_k - h(\hat{x}_k^-)) \tag{3.57}$$

$$P_k = (I - K_k H)P_k^- \tag{3.58}$$

Where H is the Jacobian of the observation model $h(x_k)$:

$$\tilde{H}_{[i,j]} = \frac{\partial h_{[i]}}{\partial x_{[i]}}(x_k, 0). \tag{3.59}$$

The term $HP_K^- H^T$ in Equation 3.56 corresponds to the covariance matrix C_P of Equation 3.27 in Section 3.3.3.3, though a different observation model is utilised here.

The filter algorithm thus has two stages: time update and measurement update. The time update equations project the current state and error covariance estimates to obtain the a priori estimates for the next time step, while the measurement update equations provide feedback by incorporating a new measurement into the a priori estimate. Equations 3.54 and 3.55 are also referred to as predictor equations and the measurement update equations 3.56 – 3.58 as corrector equations. As the measurement error covariance R in equation 3.56 approaches zero, the residual is weighted more heavily. That is, more confidence is put into highly accurate measurements of z_k. The noiseless connection H between the state vector and the measurement vector serves for correctly propagating only the relevant component of the measurement information and magnifies only the proportion of the residual that does affect the state. Equation 3.57 computes the a posteriori state estimate as a linear combination of the a priori state estimate a weighted difference between the actual measurement z_k and a measurement prediction $h(\hat{x}_k^-)$. The difference $z_k - h(\hat{x}_k^-)$ in Equation 3.57 is referred to as measurement innovation or residual and K_k is the Kalman gain. If Q and R are constant, both the estimation error covariance and the Kalman gain will stabilise quickly and then remain constant. These parameters can then be precomputed by either running the filter off-line or by determining the steady-state value of P_k.

The position-velocity filter model of the inspecting robots is based on straight movements with a constant velocity along the surface of the test specimen and the discrete absolute position measurements. The filter utilises the most recent distance sample to project ahead and produce an estimate where the vehicle should be in the next time step. When the next distance sample arrives, the Kalman filter corrects its internal state taking into account the difference between where the vehicle would have been had the prediction been accurate and the actual distance sample. The state vector x_k^- in Equations 3.54 — 3.58 contains the x-, y- and z- coordinates of the vehicles. The process noise variance is assumed to be 1 cm and the measurement
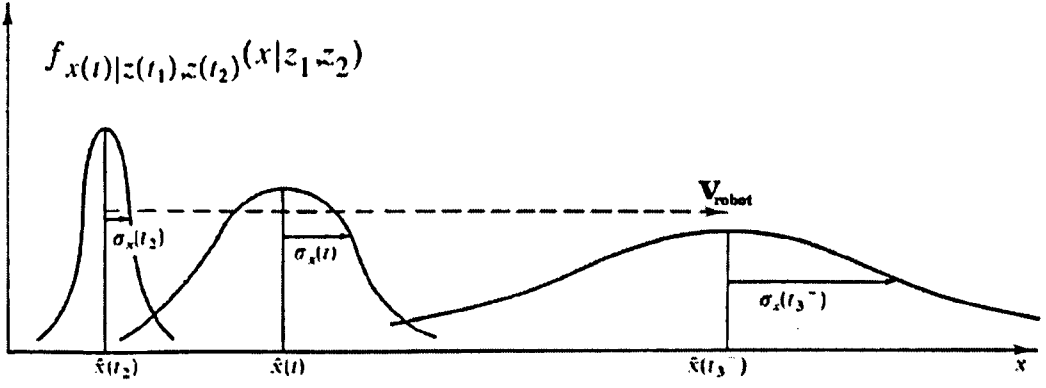
Figure 3.31: Propagation of conditional probability density.

noise covariance R is measured prior to operation of the filter:

$$R = \begin{pmatrix} \sigma_x^2 & 0 & 0 \\ 0 & \sigma_y^2 & 0 \\ 0 & 0 & \sigma_z^2 \end{pmatrix} = \begin{pmatrix} u(d_1)d_1 & 0 & 0 \\ 0 & u(d_1)d_2 & 0 \\ 0 & 0 & 0 \end{pmatrix} \tag{3.60}$$

for a measurement in two dimensions with known horizontal position z and with a standard derivation according to Equation 3.26. The impact of Q is clarified in Fig. 3.31. The robot is travelling with a constant velocity

$$\frac{d_x}{d_t} = v_{robot} + w, \tag{3.61}$$

with w being a noise term which represents the uncertainty in the knowledge of the actual velocity due to disturbances and effects not regarded in the first order equation above. The conditional density of the robot position travels along the abscissa at nominal speed v_{robot} while simultaneously spreading out about its mean.

The resulting performance of the implemented filter is shown in Figure 3.32: The red line is a simulated circular path of an inspection vehicle and the blue marks represent the noise corrupted measurements of the beacon system. Applying the filtering technique described above yields the smooth estimated robot path plotted in green. Also, clearly visible is the reduced accuracy in the third quadrant resulting from greater beacon-listener distances, as described in Section 3.3.3.3. Figure 3.33 shows the performance of the filter on a simulated straight path.

71
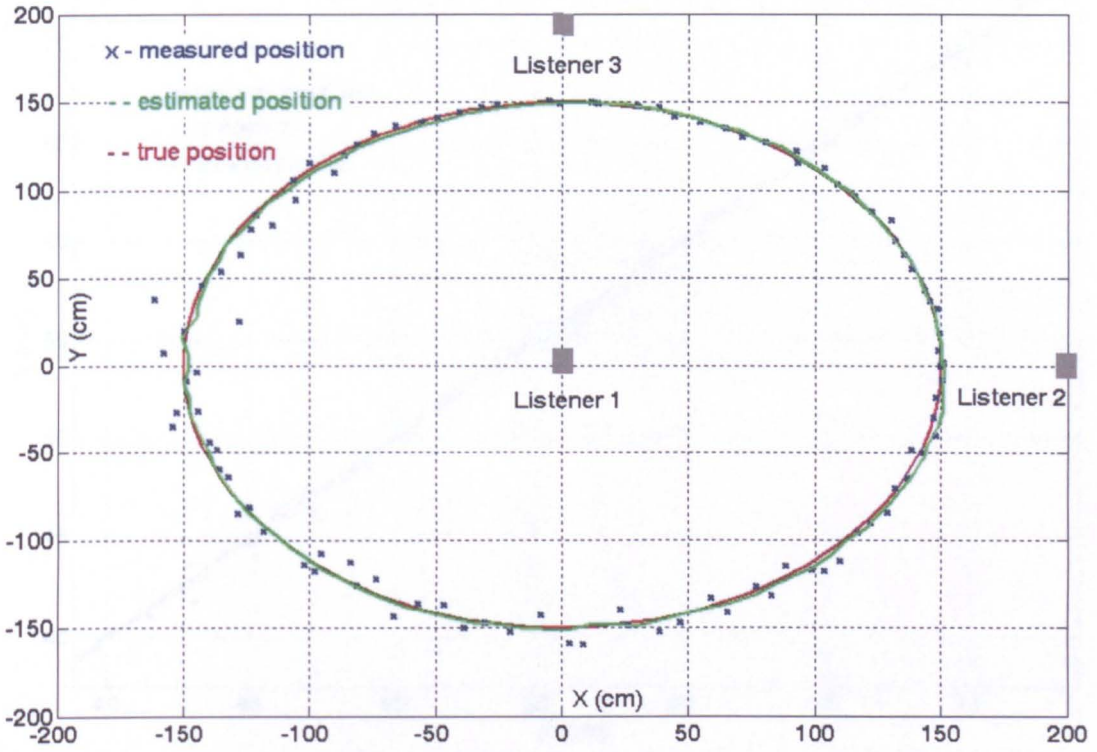
Figure 3.32: Performance of the Kalman Filter on a simulated circular path.
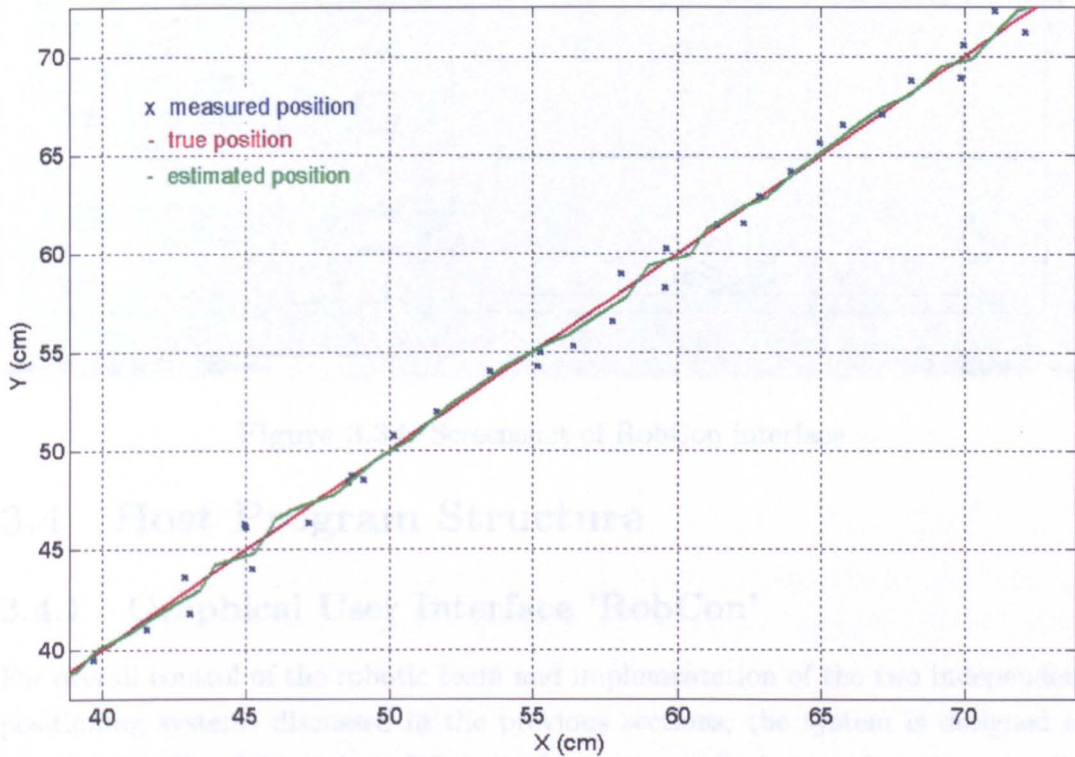
Figure 3.33: Performance of the Kalman Filter on a simulated straight path.

Figure 3.34: Screenshot of RobCon interface.

3.4 Host Program Structure

3.4.1 Graphical User Interface 'RobCon'

For overall control of the robotic team and implementation of the two independent positioning systems discussed in the previous sections, the system is designed as visualised in Fig. 3.24: A host PC controls the team of robots and receives the distance measurements between the beacons on each robot and the three listeners on the portable frame for calculating the position of the robots in Cartesian coordinates as described in Section 3.3.3. For this purpose, the MS-Windows application 'Rob-Con' has been developed utilising the Microsoft Foundation Class (MFC) to create the Graphical User Interface shown in Fig. 3.34. In addition to the RobCon C++ class, this dialog based application comprises 'CSerialPort' for serial communication and the library class 'DrawWindow' for visualisation of the robot positions. The window in the top left corner of this interface displays the 3D-coordinates of each vehicle if the Cricket system is activated beforehand, by pushing the corresponding radio buttons. With the two radio boxes below, the user is able to address spe-

cific robots and switch between 'manual mode', 'target mode' and 'automated scan mode'. The box for manual control contains push buttons for forward and backward vehicle movements, left and right turns, a vehicle stop and buttons that initiate 90° and 180° turns. Depending on the ID of the vehicle that the user wants to address, a corresponding command is sent via the serial port. The editable text area for setting the target position is active in 'target mode', while the search pattern and clockwise or counter clockwise scanning direction can only be set in 'automated scan mode'. An emergency stop button is active at all times. On the right hand side of the interface the 3D position of the vehicles, with reference to the absolute coordinate system, is displayed, with yellow boxes representing the listeners on the frame. Each robot is marked as a red dot and its path is plotted in blue.

3.4.2   Interfacing the Cricket Units

The main program consists of an event-driven thread for vehicle control and a parallel timer thread for position estimation and plotting. This timed thread accesses the listeners by opening the accordant COM port every 1000 ms, which is the average interval between beacon messages [263]. The output format of each listener is set to 'no output' to switch off the automated reports, as described in Section 3.3.3.2. Instead, the timed thread of the application is sending a listing command:

G LS <return >

and each listener lists the unique ID of all beacons that signals have been received within the past 15 seconds and the last five distance measurements received for these beacons. The listener ID is a permanent 64-bit number that is returned in the form of 8 hexadecimal numbers and cannot be changed. The output is a string in ASCII format, a typical listing of three beacons in range is:

LS 0: 5:f2:66:b1:a:0:0:df 211 213 212 211 211
LS 1: 3:f2:32:67:a:0:0:45 156 156 156 156 156
LS 2: a:42:0:b4:a:0:0:21 91 91 92 92 91

To convert the distances of the string above into integers, a subroutine extracts the relevant three-, two- or single digit numbers by searching within the string for both space and control characters which separate the individual measurements and mark the line feed.

As Ultrasound-based sensors suffer from specular and multi-path reflection from multiple objects [27, 96], the average distance of the previous four measurements

is utilised to detect and compensate erroneous readings: In case the latest distance sample exceeds a previously defined range of tolerance, it is regarded as an outlier and replaced by the average distance. This feature is of particular importance for the path plotting feature of the program, where a single wrong set of positioning coordinates results in a corrupted plot. The new distance sample then serves as the base for the the trilateration equations with the inter-listener distance r as a parameter. To establish the hardware connection between the host and the listeners, a USB Hub and Serial to USB adaptors are required to interface each Cricket unit. The baud rate for this connections is 115200 $\frac{bits}{s}$, while communication between the robots and to the host is established at 38400 $\frac{bits}{s}$ as described in Section 3.2.5.8.

3.4.3 Target Mode

For automatically directing a vehicle to a certain x-y position in 'target mode' without orientation information and to establish basic position control, an estimate of the robot's driving direction is derived from the latest two consecutive sets of co-ordinates at t_1 and t_2. The target position and the current vehicle position are compared as shown in the structogram in Fig. 3.35 and visualised in Fig. 3.36. A general description of structograms is given in Section 3.5.2. Depending on the quadrant and the driving direction, a 'correct-left' or 'correct-right' command according to the command protocol in Table 3.2 is sent to the vehicle, which reacts with a minor heading change into the direction of the target. If the robot is driving straight away from or towards the target, within a corridor between quadrants of width d, as illustrated in Fig. 3.36, the host is sending no command or a command for a 180° turn respectively. The routine is completed once the vehicle position equals the target position plus a selectable tolerance. The smaller this tolerance, the longer the routine takes for completion. In this way it is possible to navigate the vehicle up to 5 cm close to the target position, if it is located at the point of highest accuracy described in Section 3.3.3.3.

While not at target position																
Steering towards –x direction ?																
true				false												
Yr > Yt ?				Steering towards +x direction ?												
true		false		true				false								
		Yr < Yt ?		Yr > Yt ?				Steering towards –y direction ?								
	true		false	true		false		true				false				
		Xr < Xt ?				Yr < Yt ?		Xr > Xt ?				Steering towards +y dir. ?				
		true	false		true		false	true		false		false		true		
						Xr > Xt ?				Xr < Xt ?				Xr > Xt ?		
						true	false		true		false		true		false	
											Yr < Yt ?				Xr < Xt ?	
										true	false			true		false
																Yr > Yt ?
															true	false
Left	Right	Turn	Str.	Right	Left	Turn	Str.	Right	Left	Turn	Str.	Str.	Left	Right	Turn	Str.

(Xr; Yr): Current Position of Robot (Xt; Yt): Desired Target Position

Left: Minor heading change to left **Turn:** 180° Turn
Right: Minor heading change to right **Str.:** Straight, maintain heading

Figure 3.35: Structogram Target Mode.

Figure 3.36: Schematic of target algorithm.

Command	All	Robot 1	Robot2	Robot3	Robot4
left	1	a	A	n	N
right	2	b	B	o	O
back	3	c	C	p	P
forward	4	d	D	q	Q
left90	5	e	E	r	R
right90	6	f	F	s	S
scan_ccw	7	g	G	t	T
scan_cw	8	h	H	u	U
go_1m	9	i	I	v	V
correct_right	0	j	J	w	W
correct_left	\	k	K	x	X
stop	!	l	L	y	Y
start_nde	[	{	£	%	&
stop_nde	]	}	$	^	*
acknowleged	#	-	+	=	?

Table 3.2: Command protocol for serial communication.

3.5 Onboard Program Structure

3.5.1 Introduction

The Microcore-11 MCU offers 18 interrupt vectors supporting 22 interrupt sources. Interrupts are a common technique for multitasking. They are asynchronous signals from hardware indicating the need for attention or synchronous events in software reporting the need for a change in execution. A hardware interrupt causes the processor to save its state of execution, the contents of all registers, via a context switch, and begin execution of an interrupt handler. Software interrupts are usually implemented as instructions in the instruction set, which cause a context switch to an interrupt handler similar to a hardware interrupt. In both cases, the program counter is loaded with a vector that points to the new location from which instructions are to be fetched. The interrupts utilised in the programs running on the HC11 are recognised when the global interrupt mask bit in the condition code register (CCR) is clear. For some interrupt sources, such as the Serial Communications Interface (SCI) interrupt, the flags are automatically cleared during the normal course of responding to the interrupt requests.

In a computer architecture, a register is a small amount of fast memory providing quick access to commonly used values. The micro processor moves data from the memory into its internal registers for processing, operates on them, and moves the result back into the main memory. There are two different types of registers: accumulators, and index registers. While accumulators are utilised to perform arithmetic or logical and bit operations, index registers point at data that is located in memory. At the start of the main program running on the HC11, the relevant registers for serial communication, A/D conversion, timers and counters input capture- and timer functions and interrupts are set initially and configured continuously during execution depending on the different operations.

The analog input port, which interfaces the gyroscope and the NDE payload, is configured by the System Configuration Options (OPTION) and the A/D Control Status (ADCTL) registers. In order to use the A/D converter, the system has to be powered-up initially by setting the corresponding bit in the OPTION register. There are two banks of four analog channels each, and during normal operation only values from either of these four-channel banks are converted. The channels and the sampling mode are selectable via the ADCTL register. Since sampling a channel takes a significant amount of time, it is possible to repeatedly sample only a single channel for close monitoring of a particular signal. The HC11 timing system is
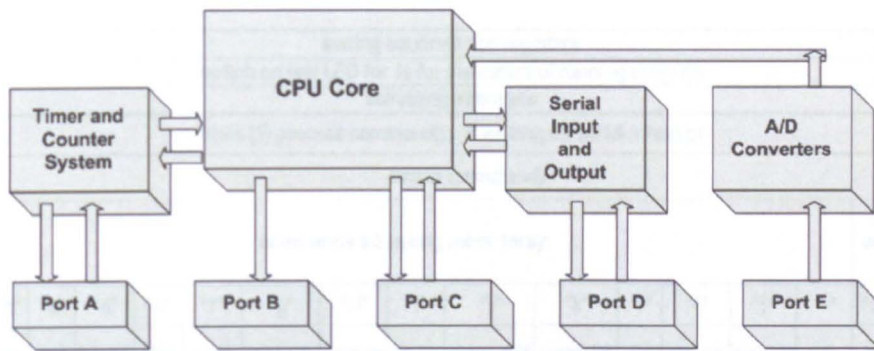
Figure 3.37: Simplified 68HC11 architecture.

composed of five clock divider chains, the main one of which includes a 16-bit free-running counter (TCNT) which is driven by a programmable prescaler controlled via the Timer Interrupt Mask Register 2 (TMSK2). There are four timers, each with its own output compare register which is compared against TCNT, and the programmed action is started as soon as the value of TCNT matches the value in the timer's output compare register. Furthermore, the HC11 supports a pulse accumulator that operates either as a simple event counter or for gated time accumulation. In event counting mode, this 8-bit counter increments when a specified edge is detected on an input pin, and during gated time accumulation an internal clock source increments the counter while an input signal has a predetermined logic level. In addition to the pulse accumulator, there are three input capture registers at port A. These store the time an external event occurs at the associated input pin by transferring the value of TCNT into the input capture register pair as a single 16-bit parallel transfer.

As mentioned previously and illustrated in the simplified block diagram in Fig. 3.37, the HC11 includes features for serial line input and output, A/D converters, programmable timers and counters. While Port C is a bidirectional digital port, Port B is unidirectional and for output only. The data direction of Port C is configured via the data direction C (DDRC) register. Port E is the analog input port, Port A implements special timer and counter circuitry and port D is dedicated to serial input and output functions.

3.5.2 Serial Communications Interface Interrupt and Main Subroutines

In computing, a structogram, also referred to as Nassi-Shneiderman diagram, is a graphical design representation for structured programming. Algorithms and program functions are illustrated as a flowchart to visualise the logical structure follow-

setting baudrate and registers																	
switch on test LED for 1s for indication of running program																	
activating interrupts																	
while (1) process command(); // waiting for serial interrupt																	
switch (command)																	
commands adressing robot 1only															commands adressing all robots		
"a"	"b"	"c"	"d"	"e"	"f"	"g"	"h"	"i"	"j"	"k"	"l"	"t"	"y"	"."	"1"	"2"	...
left	right	back	forward	left90	right90	scan_ccw	scan_cw	go_1m	correct_right	correct_left	stop	start_nde	stop_nde	ackn.	left	right	...

Figure 3.38: Top level structogram of on board program.

ing a top-down design: the problem at hand is reduced into smaller subproblems, represented as nested boxes, until only simple statements and control flow constructs remain. Hence, consistent with the philosophy of structured programming, structograms have no representation for a 'goto' statement.

The basic elements of structograms are processes desribing a program function as pseudocode. For instance, the first line in the structogram in Fig. 3.38 represents the set of commands for the initial set up of the baudrate and registers at the beginning of the on board programs of the robots. In the case where the process is an elementary command directly translated from the source code, this is marked by a semicolon. Loop notations are utilised when processes are repeated until a certain condition is met while a double forward slash is indicating comments for a more detailed description, as shown in line four of Fig. 3.38. The selection symbol, a rectangle divided into three parts by diagonal lines, marks decisions with the condition or decision in the uppermost triangle and the two possible outcomes on either side of the decision. For a Case statement, the multiple cases are listed next to each other in a table format, as illustrated in lines seven and eight of Fig. 3.38.

The programs running on the individual controllers of each robot utilise the SCI interrupt handler to respond to incoming commands on the serial port. As shown in the top level structogram in Fig. 3.38, the program stops until a character from either the main host or another team member is received. According to the command protocol in Table 3.2, the vehicle then starts the requested subroutine. Each team member can be addressed either individually by its own unique set of characters or by the set which is shared by all robots. The Serial Peripheral Interface Status Register (SPCR) for this purpose has to be set to 0b01010000 and the Serial Communications Interface Control Register 2 (SCCR2) to 0b00101100. As the Turbo version of the

81

Microcore-11 board contains a 9.8304 MHz crystal which supports a Baud rate of 38400 bits/s, the Baud Rate Control Register (BAUD) has to be set to 0b00100000 and the Highest Priority I Bit of the Interrupt and Miscellaneous Register (HPRIO) to 0bxxxx0100 (x - arbitrary) in order to elevate the SCI system above all other interrupt sources.

With the corresponding character on the serial port, the subroutine 'forward' is started: Motors, variables and counters are initialised, the encoder readings are reset and the vehicle starts the scan. The ADCTL Register is set to 0b00110000 and the OPTION Register to 0b10000000 to enable A/D conversion on pin AN0 and sample the input from the NDE sensor. As shown in the structogram in Fig. A.44 and Fig. A.45 and described in Sections 4.5.3 and 5.4.1, different algorithms, depending on the vehicle payload, are utilised for reliable defect detection.

As illustrated in Fig. A.46 and Fig. A.47, the subroutines for minor corrections to left and right for the operation in 'Target' mode, for a straight line movement of 1 m and the subroutines for 90° turns comprise a while loop that monitors the encoder output. In contrast, the structograms of the subroutines for basic left, right and back movements and stopping are of plain structure, as shown in Fig. A.47, Fig. A.48 and Fig. A.49. A combination of these elementary routines build the subroutines 'scan-ccw' and 'scan-cw' for initiation of a counter clockwise or clockwise scan respectively. The subroutines 'start-nde', 'stop-nde' and 'acknowledged' only consist of setting the accordant flag, which is utilised in the 'forward' routine described above and for organisation of communication between multiple vehicles.

The software structure described is predictable according to the hierarchical model, also referred to as the classical, functional or engineering model with three levels of abstraction and a top-down implementation [31]. The highest level takes the driving decisions, in this case the main routine of the top level structogram in Fig. 3.38, which responds to commands from the main host by starting one of the requested subroutines of the medium level. Execution of the actual driving commands and raw data processing of the sensors is left to the bottom layer, the actual interface to the vehicle. In contrast, a program architecture based on a behaviour-based model is bottom-up designed and less predictable: Each robot's functionality is encapsulated in a small self-contained modules, behaviours, which run as parallel processes while an overall controller coordinates the activation of behaviours at appropriate times to achieve the desired objective.

3.5.3 Shaft Encoder Pulse Accumulator Software Driver and Input Capture Registers

As the HC11 comprises only one pulse accumulator, the right wheel encoder output on pin PA0 is monitored by the IC3 interrupt handler and the accumulated pulses are fed into the input capture register three (IC3). To configure the register for this operation, the Timer Control Register 2 (TCTL2) is set to 0b00000001 and the Timer Interrupt Mask Register 1 (TMSK1) to 0bxxxxxxx1. The IC3F flag is cleared by setting the Timer Interrupt Flag 1 Register (TFLG1) to 0bxxxxxxx1 at the start of the program and after every interrupt. By contrast, for the left encoder the internal 8-bit counter associated with port A pin PA7 and the pulse accumulator register PACNT is utilised for counting the rising edges. The pulse accumulator control register (PACTL) is therefore set to 0b01011000 to declare port PA7 as input, PA3 as output and set the Real-Time Interrupt Rate (RTI). Both left and right encoder readings provide the required input for the pulse-width modulation software driver described in the following section.

3.5.4 Pulse-Width Modulation Software Driver and Output Compare Registers

The motor speed in the PI-loop of Fig. 3.18 described in Section 3.3.2.2 is set by sending a pulse width modulated signal exploiting the latency of the mechanical motor system: instead of generating an analogue output signal with a voltage proportional to the desired motor speed, it is sufficient to generate digital pulses of amplitude equal to the system voltage. Varying the pulse width changes the effective analogue motor signal. The three output compare registers OC1, OC2 and OC3 determine the length of this duty cycle and are compared with TCNT. Both the Output Compare 1 Data Register (OC1D) and the Output Compare 1 Mask Register (OC1M) are set to 0b0110000 to enable the motors on PA5 and PA6 via the H-bridge and to specify the action of disabling both motors after each duty cycle, the Timer Control Register 1 (TCTL1) is set to 0b1x1xxxxx.

3.5.5 Gyroscope Software Driver

For deriving the orientation information, the gyroscope output is integrated over time:

$$\Theta_g(k) = \Theta_g(k-1) + \int_{k-1}^{kT} \dot{\Theta}(t)\mathrm{d}t + \nu_g(k) \tag{3.62}$$

The sampling time is 10 ms. Before each turn, the gyroscope is initialised by taking 20 readings which are stored into an evaluation vector. The arithmetic mean of this vector, as well as the largest and smallest reading, are determined, and the difference between the sample and the arithmetic mean is utilised for integration. Only those values contribute, that are outside the previously defined span. After ascertaining the exact threshold for 90° turns by calibration experiments, $\Theta_g(k)$ serves as the terminating condition for the main while loop in the corresponding subroutine.

Chapter 4

Eddy Current Inspection

4.1 Introduction

For inspection of electrically conducting material, Eddy Current (EC) Inspection is one of the most widely used and well-understood NDE techniques, which is particularly sensitive to service induced fatigue cracks and stress corrosion cracks of 0.1 mm depth and less [28, 65, 107, 122, 252]. It gives an instantaneous indication and offers high reliability and potential for miniaturisation. In general, EC sensors provide the most reliable results for NDE [21, 94, 152, 195, 239].

4.2 Theory

According to [107] any practical eddy current test requires the following:

- a suitable probe,

- an instrument with the necessary capabilities,

- an approximate idea of size, location and type of the flaws it is desired to find,

- a knowledge of the material conductivity and whether it is magnetic or not,

- a suitable test standard to set up the equipment and verify correct operation,

- a procedure for accept/reject criteria based on the above,

- the necessary operator expertise to understand and interpret the results.

EC testing is based on generating alternating currents in a test coil with frequencies between 100 Hz and 10 MHz which induce eddy currents in conducting material
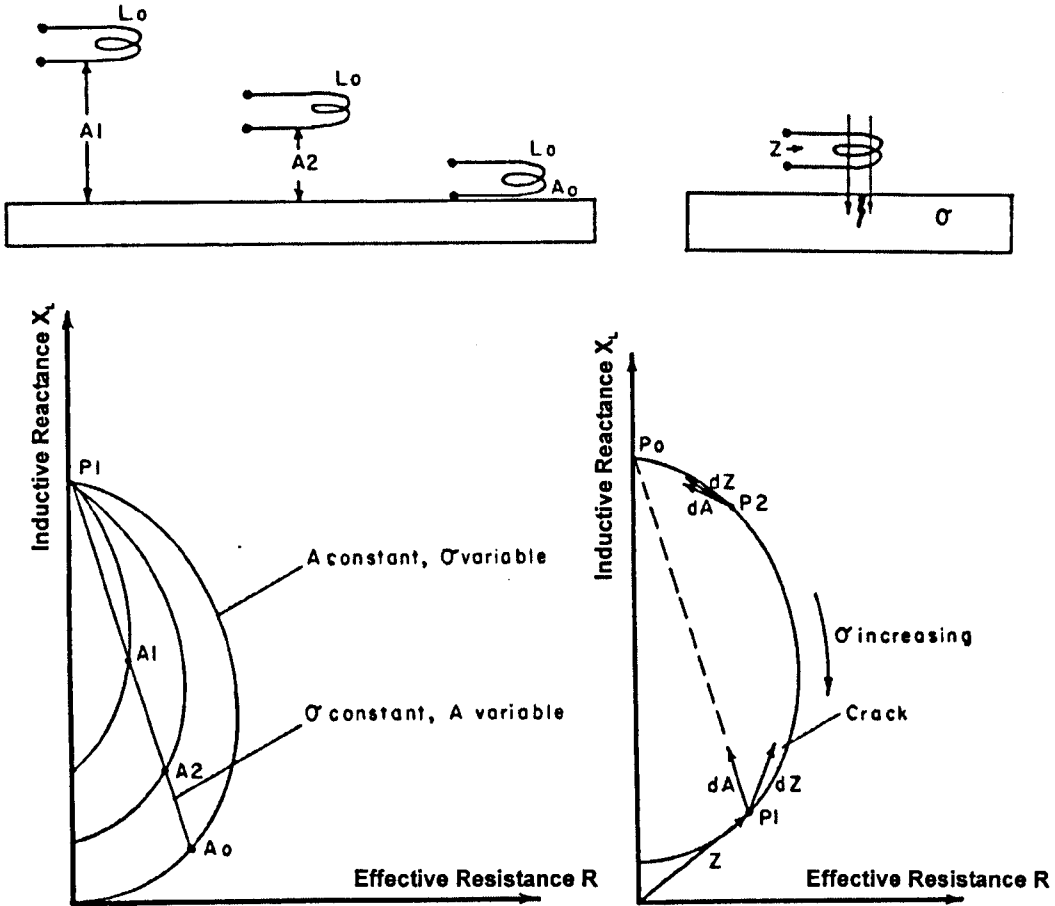
Figure 4.1: Effect of lift-off, conductivity and crack on coil impedance [155].

in close proximity [105]. The ECs generate a reverse magnetic field, that affects the loading on the coil which leads to changes in its impedance. A crack in the surface immediately underneath the test coil interrupts or reduces the EC flow, thus decreasing the loading on the coil and increasing its effective impedance. Fig. 4.1 shows the effect of lift-off A and conductivity σ: The inductive reactance of the coil increases for higher values of A and lower values of σ as shown. The effect of a crack on coil impedance is represented by the vector in P_1. With the conductivity being as low as in point P_2, discrimination between impedance change caused by probe clearance and impedance change caused by a crack requires higher accuracy. Apart from lift off, cracks and conductance the change of the test coil impedance is affected by:

- magnetic permeability in a ferromagnetic specimen μ

- metallurgical variables in the specimen

86

- primary coil size

- test frequency

- dimensions of the specimen

- the orientation of the crack

Furthermore, the density of ECs within a material decreases monotonously in thickness direction, which is referred to as skin effect. Pivotal to efficient EC inspection is good probe design. Particularly, the probes ability to induce and detect ECs in the material under test. The coil usually contains a ferrite core, a rod of electrically non-conductive ferromagnetic ceramic compound material consisting of iron oxide, to focus the magnetic fields into the work piece, thereby increasing the probe sensitivity to the defect.

Three different probe types are distinguished: Absolute EC probes probes consist of a single coil and do not compensate for material variations, non planar orientation (wobble) and temperature changes. In contrast, differential probes consist of two sensing elements which are placed at different locations of the test material. Compensation is achieved as the instrument responds to the difference between the EC conditions at the two points. The third probe type is the reflection or driver-pickup probe, which has a primary winding driven from an oscillator and one or more sensor windings connected to the measurement circuit. Depending on the configuration of the sensor windings reflection probes give a response equivalent to either an absolute or differential probe.

Surface crack detection is normally carried out with pencil probes with the probe axis normal to the surface at frequencies from 100 kHz to a few MHz. Depending on the surface condition cracks up to 10 μm depth are detectable [105, 160, 217, 232]. The following sections describe the development of the EC test equipment which incorporates two sensing differential coils for autonomous operation on a miniature inspection robot.

4.3   Simulation

Prior to the actual design of the probe, the induction of eddy currents in a metallic test sample is simulated with Femlab. The coils for this simulation are based on an array instrument for offshore applications developed earlier [220] and consist of 30 windings of 31 SWG wire around a 15 mm x 1.5 mm ferrite core with a relative
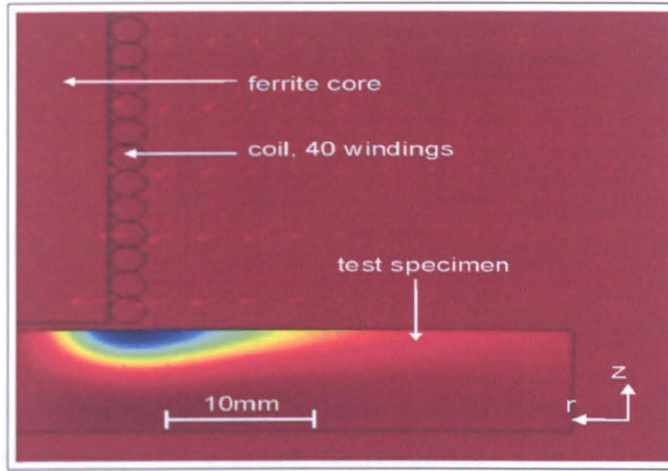
Figure 4.2: Qualitative distribution of induced eddy currents and magnetic field, blue areas indicating high eddy current density within the material.

permeability of $\mu_r = 48$. Fig. 4.2 shows a cross section of the model through the r-z plane, using the axisymmetric quasi-statics azimuthal currents application mode and a time-harmonic formulation. The dependent variable in this mode is the azimuthal component of magnetic vector potential A which obeys the relationship:

$$J_\varphi{}^e = (j\omega\sigma - \omega^2\varepsilon)A_\varphi + \nabla \times (\mu^{-1}\nabla \times A_\varphi) \qquad (4.1)$$

where ω is the angular frequency, σ is the conductivity, μ is the permeability, ε is the permittivity, and J_φ^e denotes the current density due to an external source. The boundary conditions for this model for the exterior surroundings correspond to zero magnetic flux, the coil is modelled without skin effect. The simulation shows the direction of the eddy currents within the material. As defects must interrupt the surface eddy current flow, thin cracks parallel to the eddy currents do not cause significant interruption of these and may remain undetected. However, Fig. 4.2 indicates general suitability of the coil design for the intended application. The following section describes the development of the required drive electronics.

4.4   Coil and Circuit Design

For simplifying on-board interpretation of sensor data while compensating for any irregularities within the test material, inspection is performed with a differential probe. The two coils form the legs of a bridge, as shown in Fig. 4.3. When the bridge is balanced, the measured voltage is zero while any change in the condition of either coil results in an unbalanced bridge. The degree of imbalance corresponds
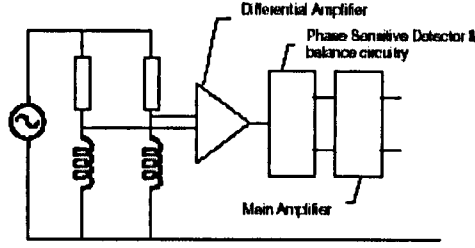
Figure 4.3: Bridge circuit of two differential coils.

to the change in coil impedance, it is measured by determining the phase angle between the two signals with a phase discriminator. The two coils are positioned on a vertically adjustable spring loaded lever, as shown in Fig. 3.14. This maintains a constant minimum sensor lift off by holding the probe in firm contact with the surface. The probe is located at a maximum distance from DC motors to avoid electro magnetic interference. The initial coil design is based on the work of Thomson [220] as described in the previous section. The probe consists of two coils 1 cm apart. The inductance of each coil is directly proportional to the square of the coil diameter d and the number of windings N:

$$L = \frac{\mu_0 \mu_r N^2 A}{l}, \tag{4.2}$$

with μ_0 being the the permeability of free space ($4\pi \cdot 10^{-7} \frac{H}{m}$), μ_r the dimensionless relative permeability of the ferrite core (48), A the cross sectional area of the coil in square metres and l the length of the coil in metres. This yields a theoretical inductance of 16 μH, which is in compliance with the experimentally determined values of 15.8 μH for coil 1 and 14.2 μH for coil 2. The DC resistance of the coils is

$$R = \frac{\pi \rho d N}{A}, \tag{4.3}$$

which yields $\approx 0.1 m\Omega$ and can be disregarded. For accurately detecting a change of inductance, the two coils are driven in a series resonant circuit with two 100 pF capacitors and two additional resistors. Equation 4.4 gives a theoretical resonant frequency of 3.97 MHz.

$$f = \frac{1}{2\pi\sqrt{LC}} \tag{4.4}$$

$$\tan\varphi = \frac{\omega L - \frac{1}{\omega C}}{R} \tag{4.5}$$

According to Equation 4.5 the theoretical phase angle at resonance is zero, and marginal changes in the inductance of either of the coils will therefore cause a significant change of the phase angle between them.

In order to improve the sensitivity of the sensor further, the coil diameter and the number of windings are increased in a second design step to achieve a higher coil inductance of 1.2 mH on a flawless mild steel surface. With two 1 nF capacitors these coils work close to the optimum operational frequency of the ferrite cores at approximately 145 kHz at resonance, depending on the exact inductance of the manufactured coils. The inner and outer diameter are increased to 5 mm and 10 mm respectively, and thinner 34 SWG wire allows for 400 windings.

Fig. 4.4 shows the circuit diagram of the eddy current module. The MAX660 monolithic charge-pump voltage inverter converts the regulated 5V from the motor driver board into -5V which is needed for operation of the remaining ICs. The high frequency function generator MAX038 produces a sine wave signal, which is selected via A_0 and A_1 in Fig. 4.4. The output frequency is inversely proportional to the capacitor C_f and can be set manually by the variable resistor R_{in} to adjust the exact resonance frequency of the coils. In this way, compensation for both deviations of coil and material properties of the test specimen is achieved. The internal frequency adjust circuit of the function generator, intended for fine frequency control inside phase-locked loops, adds a temperature coefficient to the output frequency, and as it is not required for this application, this feature is disabled by connecting the *FADJ* pin to ground through R_3. However, in this configuration the oscillator frequency doubles, which changes the formula for the output frequency to

$$f_0 = \frac{2V_{ref}}{R_{in}C_f},$$
(4.6)

with V_{ref} being the internal reference voltage of 2.5 V on pin 1. The generated signal is fed into a high speed unity-gain open-loop buffer BUF634, which provides 250 mA output current for driving the two coils. As at resonance the coil impedance is minimal, the current limiting variable resistors R_{in1} and R_{in2} are used to adjust the maximum available current through the coils. The higher the current through the coils, the higher the induced eddy currents and consequently the greater the probe sensitivity. Both AC signals are connected to the non-inverting input of LM311 voltage comparators which work as zero crossing detectors and provide two square waves with a phase difference equivalent to the phase difference between the two eddy current coils. These signals are the input for the balanced phase comparator

of the XR-215A phase-locked loop system, the DC voltage between pins 2 and 3 of which corresponds to the phase difference between the signals on pins 4 and 6. Adjustable voltage dividers consisting of R_8, R_9, R_{in3} and R_{in4} scale the output of the phase comparator to a range of 5V for the following instrumentation amplifier. This differential amplifier is adjustable via R_{in5} and R_{in6} to provide appropriate gain of the phase difference signal:

$$U_{out} = \frac{R_2}{R_1}(U_2 - U_1). \tag{4.7}$$

The output of the instrumentation amplifier is subsequently connected to one of the analog input pins of the micro controller.

Figure 4.4: Circuit diagram eddy current board.
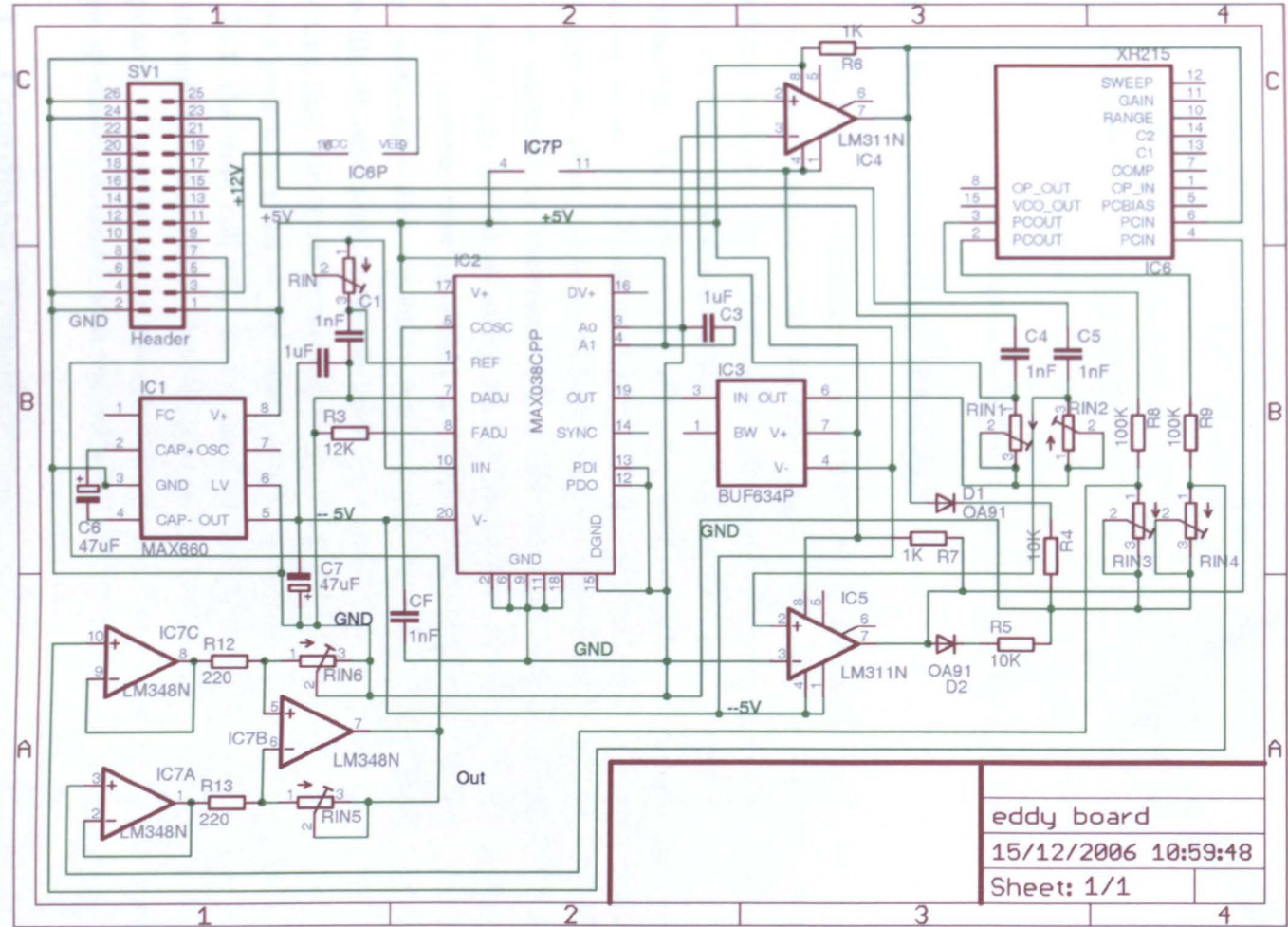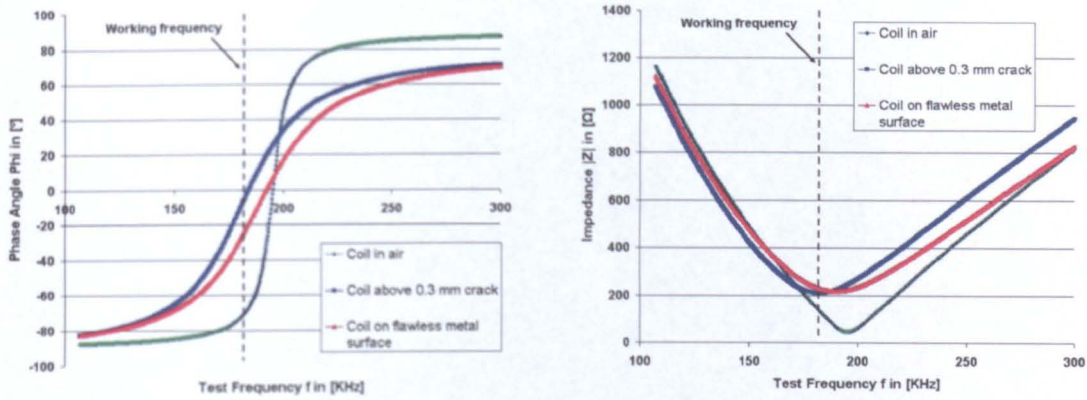
Figure 4.5: Effect of Lift-off and Crack on $\|Z\|$ and Phi.

4.5 Experimental Results

The resonant circuit consisting of a coil of the second design step and a 1 nF capacitor was tested separately from the drive circuit with a Hewlett Packard HP4194A impedance analyser. Fig. 4.5 shows the phase angle and the impedance against frequency for different positions of the test coil in reference to a 0.3 mm defect in the test specimen. The eddy currents affect the coil impedance which shifts the resonant frequency in air, on a flawless metal surface and above a the crack as illustrated. In particular, the phase angle shows high sensitivity towards defects and lift off. Moreover, as suggested by Thomson [220], a discrimination between impedance changes that result from variations in lift off and those that are caused by the presence of a crack is possible when operating at the indicated working frequency. This offers many advantages with regard to automated scans, where maintaining a constant probe lift off, especially on uneven surfaces, constitutes one of the major problems. Providing that the probe is orientated so that the connecting line of the centre of the two coils is parallel to the main driving direction of the robot, as shown in Fig. 3.14, the front coil will cross a crack or an indentation before the back coil, and the algebraic sign of the phase change gives a clear indication about the type of irregularity. The following sections present results of autonomous scans of a variety of test specimens obtained with the on-board EC test equipment described above.

4.5.1 Coordinate Transformation and Euler Angles

When determining the exact location of a defect it has to be taken into account that the coordinates of the positioning module may well be different from the position of the actual NDE sensor which depends on the orientation of the robot-fixed reference
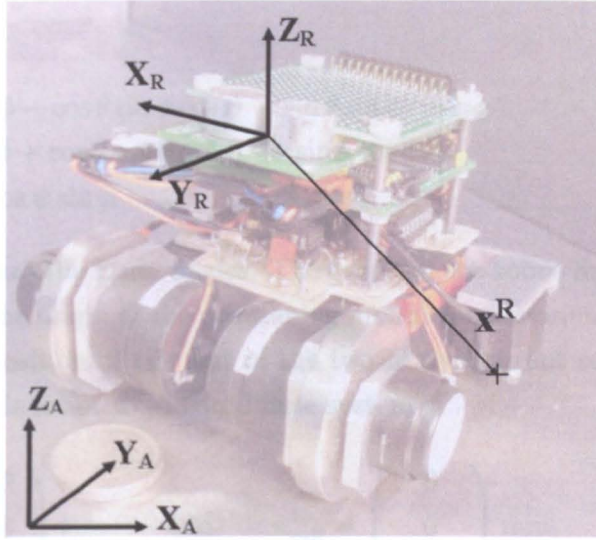
Figure 4.6: Absolute reference frame A and robotfixed reference frame R.

frame within the global absolute reference frame. Coordinates can be transformed from this robot-fixed reference frame R into the absolute coordinate system A by a sequence of three successive rotations. Engineering and robotics communities typically use Euler angles to describe these rotations. The z-x-z form (x-convention) of Euler angles is defined as:

1. Rotation over angle ψ about z-axis of the laboratory (absolute) reference frame

2. Rotation over angle θ about the new x-axis

3. Rotation over angle ϕ about z-axis which has been obtained as a result of the previous two rotations.

The rotations are not commutative. Hence, the transformation matrix that transforms coordinates of a frame R into coordinates of a frame A is:

$$\mathbf{R}_A^R(\Theta) = \mathbf{R}_{z,\psi}\, \mathbf{R}_{y,\theta}\, \mathbf{R}_{z,\phi} \tag{4.8}$$

$$\mathbf{R}_A^R(\Theta) = \begin{bmatrix} \cos\psi\cos\theta - \cos\theta\sin\phi\sin\psi \\ \cos\psi\sin\phi + \cos\theta\cos\phi\sin\psi \\ \sin\psi\sin\theta \end{bmatrix}$$

94

$$\left.\begin{array}{cc} -\sin\psi\cos\phi - \cos\theta\sin\phi\cos\psi & \sin\theta\sin\phi \\ -\sin\psi\sin\phi + \cos\theta\cos\phi\cos\psi & -\sin\theta\cos\phi \\ \cos\psi\sin\phi & \cos\theta \end{array}\right] \qquad (4.9)$$

where ϕ, θ and ψ are the Euler angles. The origin of the robot fixed reference frame R coincides with the origin of the positioning module and is orientated as illustrated in Fig. 4.6. The position of the first of the two Eddy Current coils and the middle Hall element in this robot fixed coordinate system is

$$\mathbf{x_{ec}^R} = \begin{pmatrix} -52 \\ -68 \\ -85 \end{pmatrix} \text{mm} \qquad \text{and} \qquad \mathbf{x_{mfl}^R} = \begin{pmatrix} 0 \\ 0 \\ -85 \end{pmatrix} \text{mm}, \qquad (4.10)$$

as the position of the middle Hall element in the robot fixed coordinate system is directly below the origin of the positioning module. The vectors in the absolute coordinate system for compensation of the offset between positioning module and actual NDE payload are thus:

$$\mathbf{x^A} = \mathbf{R_A^R(\Theta)x^R}, \qquad (4.11)$$

and the corrected position of the defect in absolute coordinates

$$\mathbf{x_{corr}} = \mathbf{x_{meas}} + \mathbf{x^A}. \qquad (4.12)$$

4.5.2   Upside Down Inspection of an Inclined Steel Plate

For a first test of the overall system the bottom side of an inclined plate of mild steel was scanned by an autonomous vehicle equipped with an EC probe, with the top of the robot facing towards the lab floor. During turning manoeuvres, between AB and BA of Fig. 3.5, the scan is interrupted. The plate has an inclination of 42° and a 2 mm through hole at an arbitrary position. The distance between the three listeners according to Fig. 3.24 for this experiment is 500 mm and the frame has been positioned with reference to the plane defined by the plate as shown in Fig. 4.7. Following the right-hand rule for the algebraic sign of the rotations, the Euler angles for the robots scanning the plate are

$$\phi = 180°, \qquad \theta = 132° \qquad \text{and} \qquad \psi = 0° \qquad (4.13)$$

95

for scanning in direction 1 and

$$\phi = 0°, \qquad \theta = -132° \qquad \text{and} \qquad \psi = 0° \tag{4.14}$$

for direction 2. The rotary matrices according to Equation 4.9 hence are

$$R_A^R(\Theta)_1 = \begin{bmatrix} -1 & 0 & 0 \\ 0 & -\cos\theta & \sin\theta \\ 0 & \sin\theta & \cos\theta \end{bmatrix} \tag{4.15}$$

and

$$R_A^R(\Theta)_2 = \begin{bmatrix} 1 & 0 & 0 \\ 0 & \cos\theta & -\sin\theta \\ 0 & \sin\theta & \cos\theta \end{bmatrix}, \tag{4.16}$$

which yield the vector for taking the offset between positioning module and actual NDE payload into account:

$$x_{ec}^A = \begin{pmatrix} 52 \\ -108 \\ 6 \end{pmatrix} mm \qquad x_{mfl}^A = \begin{pmatrix} 0 \\ 63 \\ 57 \end{pmatrix} mm \tag{4.17}$$

for direction 1 and

$$x_{ec}^A = \begin{pmatrix} -52 \\ -18 \\ 107 \end{pmatrix} mm \qquad x_{mfl}^A = \begin{pmatrix} 0 \\ -63 \\ 57 \end{pmatrix} mm \tag{4.18}$$

for direction 2. Comparing the vectors of Equations 4.17 and 4.18 with the true position of the defect $[-125; 182; 585]^T$ mm shows a deviation of up to 18% between the uncorrected and corrected position.
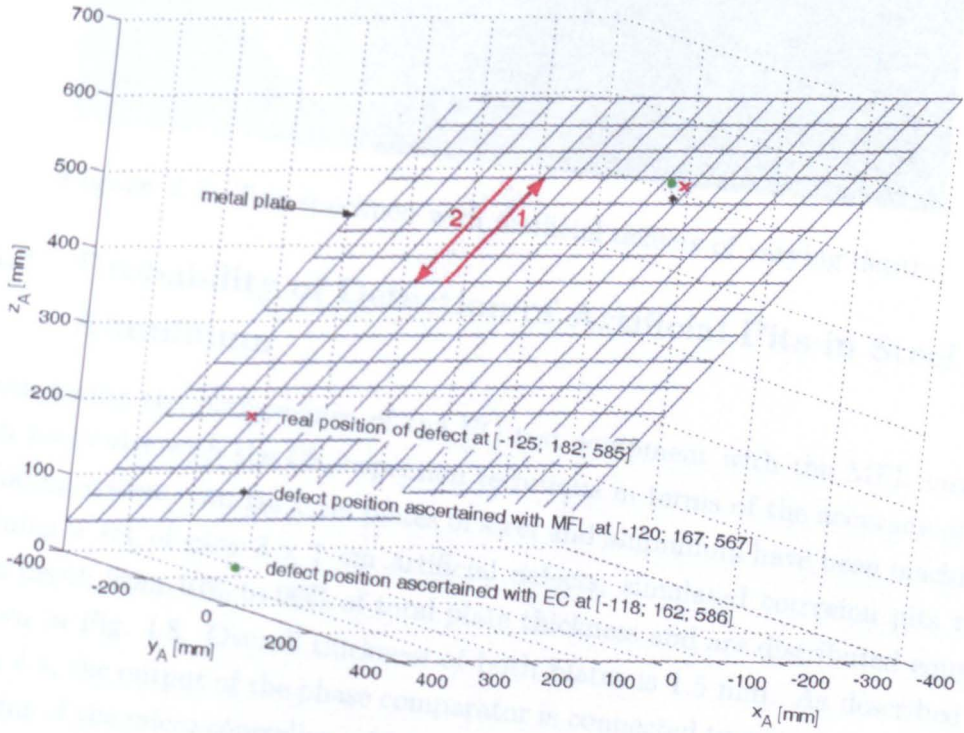
Figure 4.7: Detected defect at bottom side of inclined steel plate.
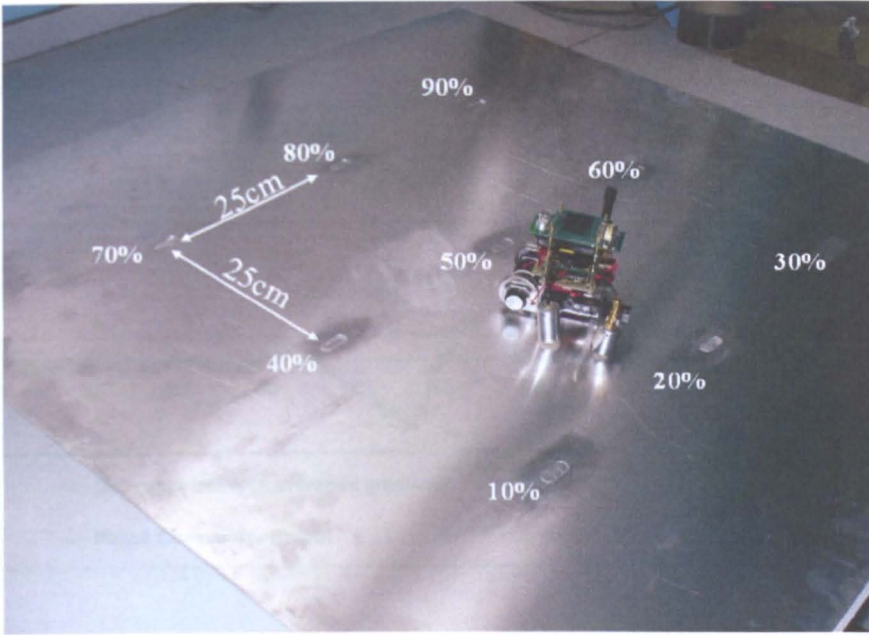
Figure 4.8: Test specimen with artificial defects of varying depths.

4.5.3 Probability of Detection of Artificial Pits in Steel and Aluminium

For comparing the performance of the EC test-equipment with the MFL method and in particular with the US inspection technique in terms of the accuracy of the positioning system, two 1m x 1m plates of steel and aluminium have been machined containing a set of nine 3 x 1 cm artificial defects, simulated corrosion pits that vary in depth from 10% to 90% of total plate thickness and are distributed equally as shown in Fig. 4.8. Overall thickness of both plates is 1.5 mm. As described in Section 4.4, the output of the phase comparator is connected to one of the analogue input pins of the micro controller, which is continuously sampled while the vehicle is scanning the surface. For evaluation, the following algorithm is implemented in the scanning routine of the robot: The average over 20 samples is taken for analysis to reduce the influence of random noise. A sequence of 40 of these average readings is stored in a vector e with old readings being replaced by new ones by a first-in-first-out (FIFO) principle. With every new averaged measurement, the average gradient of the left 20 values of e is compared with the gradient of the right 20 values. The difference of these gradients indicates a defect, as shown in Fig. 4.9. The robot stops as soon as the difference exceeds a threshold and sends the measurement of the phase difference to the host where it is stored together with the positioning information. Plotting these data, assuming a value below the threshold at all remaining positions,
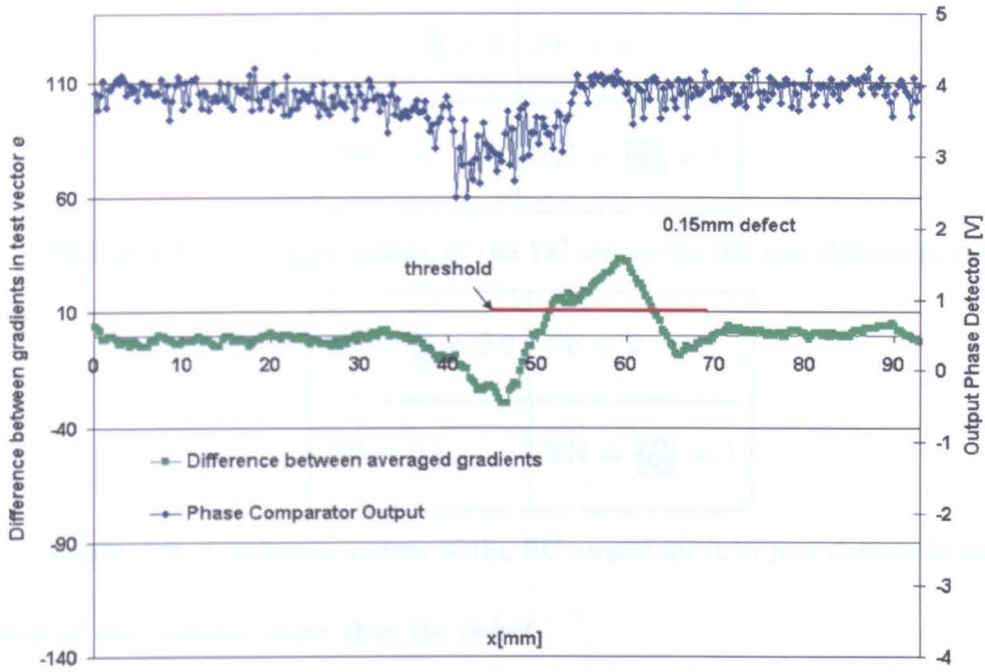
Figure 4.9: Typical signal resulting from 0.15 mm deep defect on a plate of mild steel.

an autonomous scan produces the C-scan image of the inspected metal plate shown in Fig. 4.10. The critical threshold corresponds to the ROC criterion in Fig. 2.3 and can be varied in the on-board program to achieve the desired ratio of True Positives to False Positives. Experimental investigations have shown that the accuracy of the EC sensor is close to 100%. For defects down to 0.3 mm depth located at the end of a 50 cm test path, in 20 out of 20 attempts the robot detected the defect at its correct position at the end of the path. The analog input of the microcontroller, which is connected to the NDE sensor, is sampled approximately every 100 ms while the robot is scanning. That is, by the time the robot reaches the defect there has already been a high number of True Negative detections at each attempt. Thus, assuming a number of 50 True Negative detections per attempt, this yields an ROC curve which runs close to the coordinate [0; 1] of the ROC plane. The confusion matrix for the EC sensor is shown in Table 4.1. The criterion can be set so that the number of false positive and false negative hits, according to Section 2.7, is close to zero for defects down to 0.3 mm depth and the probability of detection (PoD) for this defect size is 100%. In the experimental setup described earlier, the robot stops in 18 out of 20 attempts at the end of the scanning path for defects with 0.15 mm depth. This yields the confusion matrix shown in Table 4.2, as the robot does not

TP = $\frac{20}{20}$ = 1	FP = 0
FN = 0	TN = $\frac{1000}{1000}$ = 1

Table 4.1: Confusion matrix of the EC sensor for 0.3 mm defects in steel

TP = $\frac{18}{20}$ = 0.9	FP = 0
FN = 0.1	TN = $\frac{1000}{1000}$ = 1

Table 4.2: Confusion matrix of the EC sensor for 0.15 mm defects in steel

stop at any position other than the defect.

Experiments on an aluminium plate have shown, that the confusion matrix for defects down to 0.45 mm depth is identical to Table 4.1 and for 0.3 mm defects a confusion matrix identical to Table 4.2 was obtained.
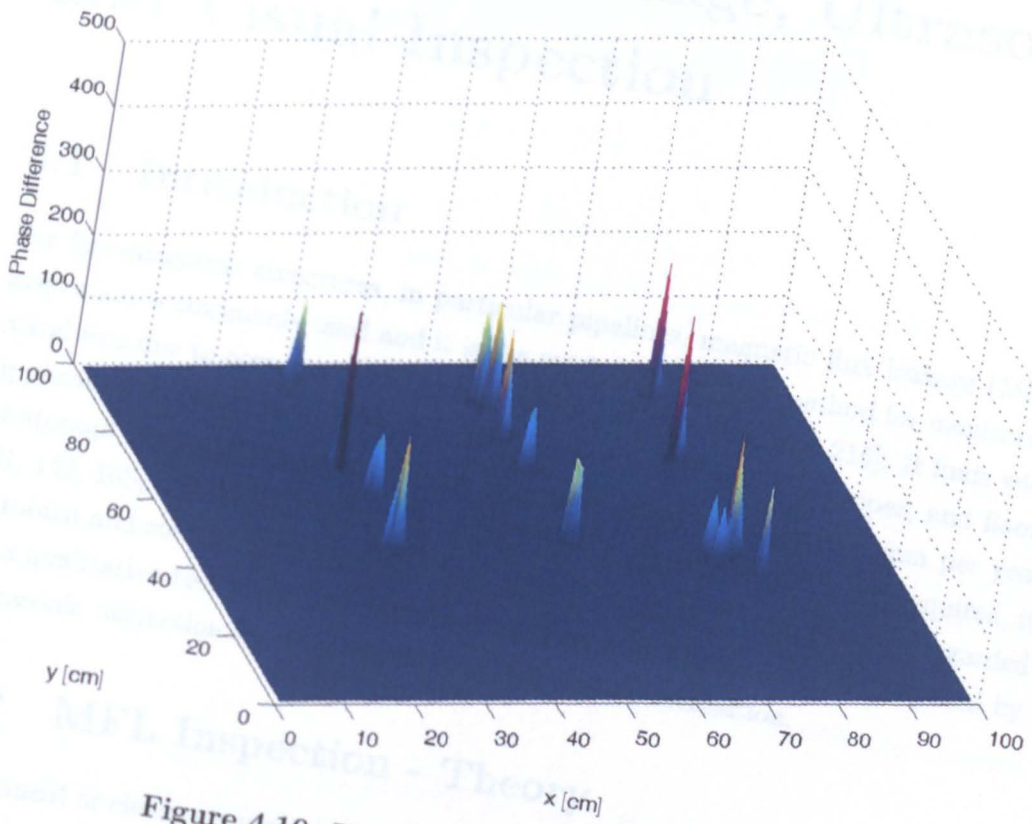
Figure 4.10: Eddy Current scan of metal plate.

Chapter 5

Magnetic Flux Leakage, Ultrasonic and Visual Inspection

5.1 Introduction

For ferromagnetic structures, in particular pipelines, magnetic flux leakage (MFL) inspection is commonly used and it is the most cost effective method for monitoring metal loss due to corrosion, pitting or gouging [20, 141, 143, 177, 215]. It finds wide application for in-service inspection of oil and gas pipelines, wire ropes, and floors of storage tanks, where corrosion pits can develop up to a rate of 5 mm per year [21, 142, 168, 236, 190]. Since direct contact with the test material is not required, it is robust and suitable for automated high speed testing. MFL inspection is regarded as a qualitative technique and largely a screening tool, which is usually followed by ultrasonic inspection for determination of defect characterisation.

5.2 MFL Inspection - Theory

Permanent or electromagnets magnetise the specimen to near saturation flux density and the magnetic flux lines, the magnetic lines of force, are uniform and unperturbed
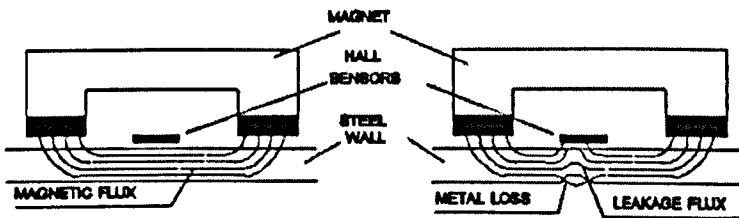
Figure 5.1: Principle of Magnetic Flux Leakage inspection.
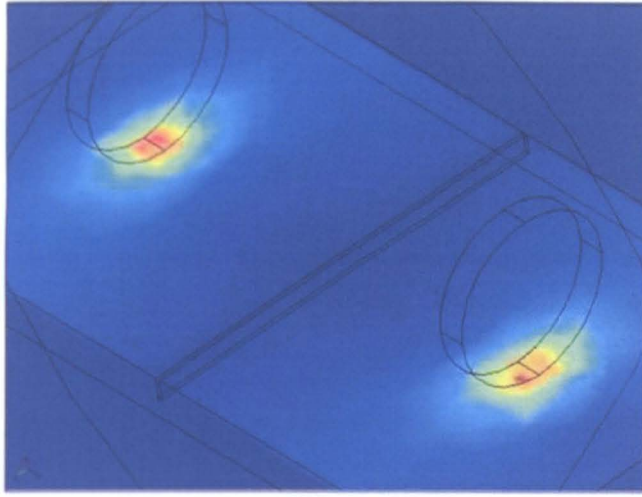
Figure 5.2: Wheels as the source of the magnetic field for inspection.

inside the ferromagnetic material [105]. If there is a surface-breaking or a subsurface flaw, there is a local change in permeability ν, and the field is distorted causing local magnetic flux leakage fields. A sensor is placed between the poles of the magnet to detect the leakage field, identify damaged areas and estimate the depth of metal loss. Fig. 5.1 illustrates the general principle of MFL inspection. The magnitude change of the magnetic field can be detected by miniature Hall sensors, which detect changes of magnetic fields up to 0.02 mT and achieve a spatial resolution of up to 1 mm [55, 136, 141, 142, 168, 195, 268]. Experiences with a single scanning-type Hall sensor for evaluation of weld quality in automotive tailor-welded blanks indicate excellent potential of the inspection method based on a moving Hall sensor and an inspection apparatus that creates the magnetic field by fixed permanent magnets [55, 142].

As described in Section 3.2 miniaturisation has high priority during the design process. Hence, the prototype vehicle for MFL inspection utilises the field created by the two magnetic wheels as the source field, as illustrated in Fig. 5.2 and Fig. 5.3. The contact area of the longitudinal magnetised magnets with the ferromagnetic test object then can be approximated as a thin line of length l. Fig. 5.3 shows the distribution of the flux lines on the plane surface of a ferromagnetic test material: with the north pole of the left wheel facing the south pole of the right wheel this arrangement is characteristic of standard MFL inspection principles. The following sections cover the simulation of this magnetic field and investigate the theoretical interaction with flaws and imperfections.
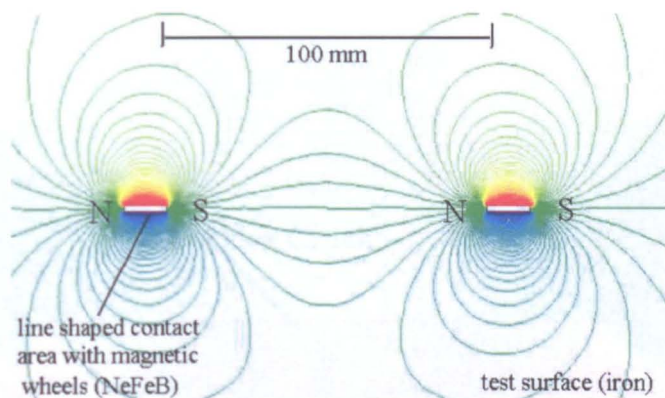
Figure 5.3: Qualitative distribution of flux lines on surface of ferromagnetic material.

5.3 MFL Inspection - Simulations

5.3.1 2D Magnetic Field Modelling

The change of the magnetic field above the surface due to imperfections in the test material can be simulated by a variety of software packages such as Maxwell 2D [269], Ansys [270], Femlab [272], Cosmos [273], MagNet [280], QuickField [293] or Vector Fields [300]. These tools, for general electromagnetic field modelling, simulate static magnetic fields in cross-sections of structures by employing finite element analysis. After specifying geometries and material properties the field strength and the magnetic flux density at arbitrary locations of the highly non linear magnetostatic system are calculated utilising Maxwell's equations:

$$B = \mu_0 (H + M) \tag{5.1}$$

$$B = \nabla \times A \tag{5.2}$$

$$J = \nabla \times H \tag{5.3}$$

with B being the magnetic flux density, H the magnetic field strength, M the intensity of magnetisation in the material, μ_0 the magnetic susceptibility, J the current density and A the magnetic potential.

Figure 5.4, generated with Maxwell 2D, shows the distribution of flux lines within the test object and the surrounding air. The cross-section runs through the supporting points of the magnetic wheels on the test surface. A thin crack is situated in the material centrally between both wheels, which are assumed to be 100 mm apart and have a diameter of 38 mm and a thickness of 6 mm. The relative permeablity μ_r of the testsurface is 4000 for iron, the magnetic field strength H of the Nd-

104
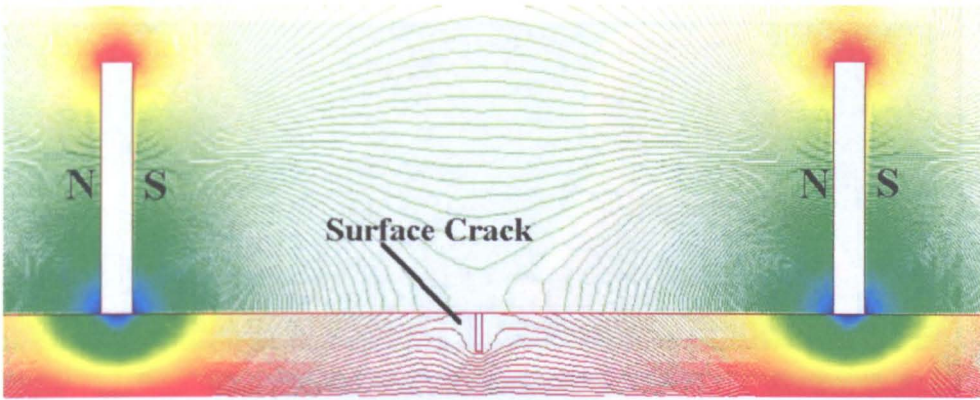
Figure 5.4: Fluxlines within the test material and the surrounding air.

Fe-B permanent magnets is $8.9 \cdot 10^5$ A/m and the magnetic flux density is set to 1.23 T [269]. The simulated gap, 1 mm wide and 4 mm deep, is filled with air with a relative permeability μ_r of 1. The surfaces of all objects are modelled with Neumann boundaries: the magnetic field is perpendicular to the edges of the problem space and continuous across all object interfaces. After specifying these parameters, the
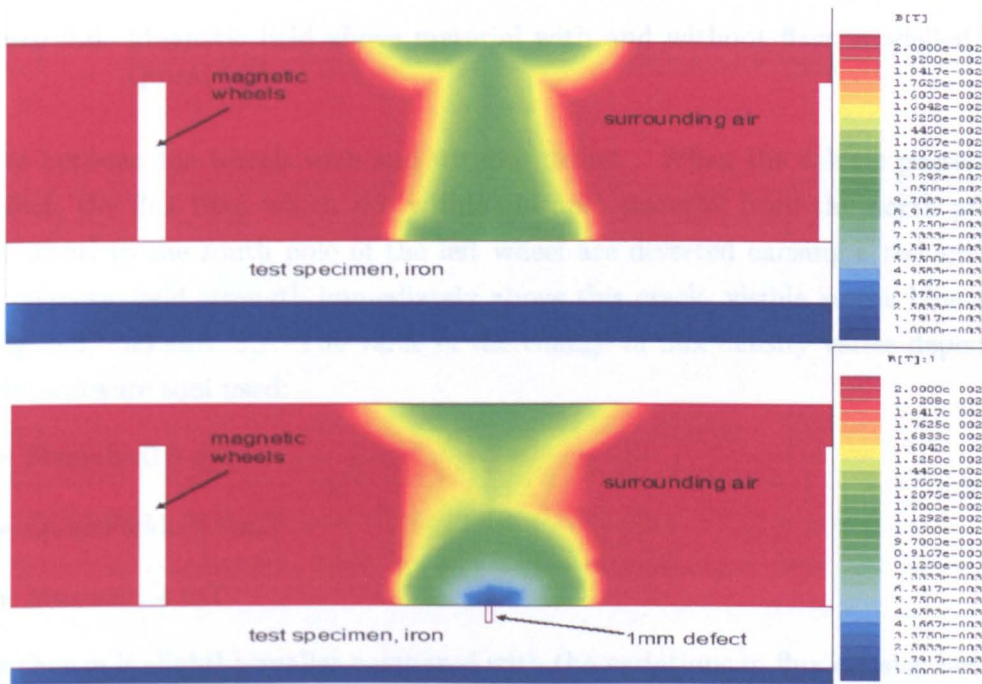
Figure 5.5: Magnetic field above material with and without flaw, modelled with Maxwell 2D.

software packages automatically create the finite element mesh and calculate the desired magnetic field solution. Fig. 5.5, 5.6 and 5.7, generated with Maxwell 2D, QuickField and Femlab, show a comparison of the magnetic field strength B in the
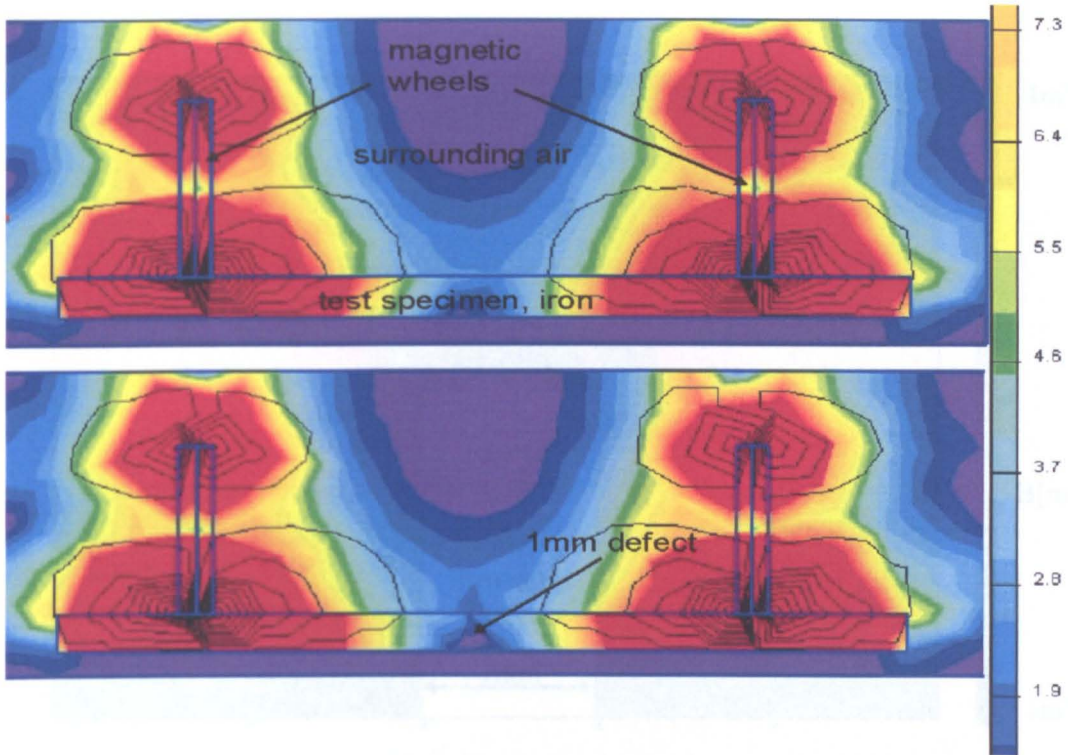
Figure 5.6: Magnetic field above material with and without flaw, modelled with QuickField.

centre between the wheels with and without defect. When the vehicle passes over a defect, the flux lines which run within the test material from the north pole of right wheel to the south pole of the left wheel are diverted causing a reduction of the magnetic field strength immediately above this crack, visible as the blue areas in Fig. 5.5, 5.6 and 5.7. The value of the change in flux density varies depending on the software tool used:

- Femlab: 0.3 mT

- QuickField: 0.7 mT

- Maxwell: 4 mT

This change is slightly smaller compared with the variations in flux density between 1 mT and 10 mT which are common for standard large scale NDE equipment [142, 236]. However, as further simulations show, the change of the magnetic field above a defect increases significantly when the wheels of the robots are closer together and thus create a stronger magnetic field in the sensing area. For this reason, the design of the vehicles carrying the MFL test equipment is different from the other vehicles by having a reduced wheel to wheel distance of 42 mm, as described in Section 3.2.

106
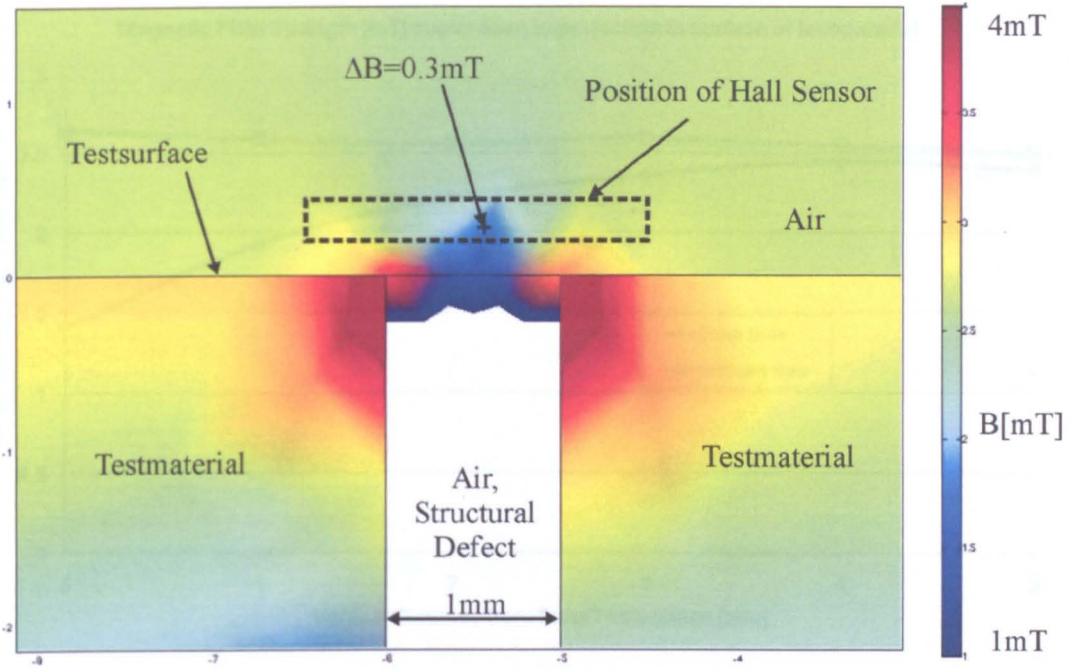
Figure 5.7: Detail view of magnetic field above material with flaw, modelled with Femlab.

The optical encoders of these inspection vehicles are located above the sensing Hall plates while the motor units are attached at the outside of the frame in order to avoid magnetic interference.

5.3.1.1 Effect of Lift-off

As visible Figures 5.5, 5.6 and 5.7, the change of flux density is limited to the region directly above the defect. Hence, the impact of lift-off distance is investigated closer: Fig. 5.8 and 5.9 show the field strength with and without a flaw being present as a function of surface distance based on simulations with the software package Femlab. While the height of the sensing Hall element is less crucial at large area defects, small deep defects cause measurable field changes only directly above the surface, as clearly visible when comparing these two plots. Hence, the sensing Hall elements are mounted on a spring loaded lever, as described in Section 3.2.5.9, to maintain a constant minimum distance between the array and the inspection surface.

Magnetic Field Strength [mT] above 5mm imperfection in surface of testmaterial

Figure 5.8: Magnetic field strength vs. height above a 5 mm wide and 2 mm deep defect, material: iron.

Magnetic Field Strength [mT] above 1mm flaw in surface of testmaterial
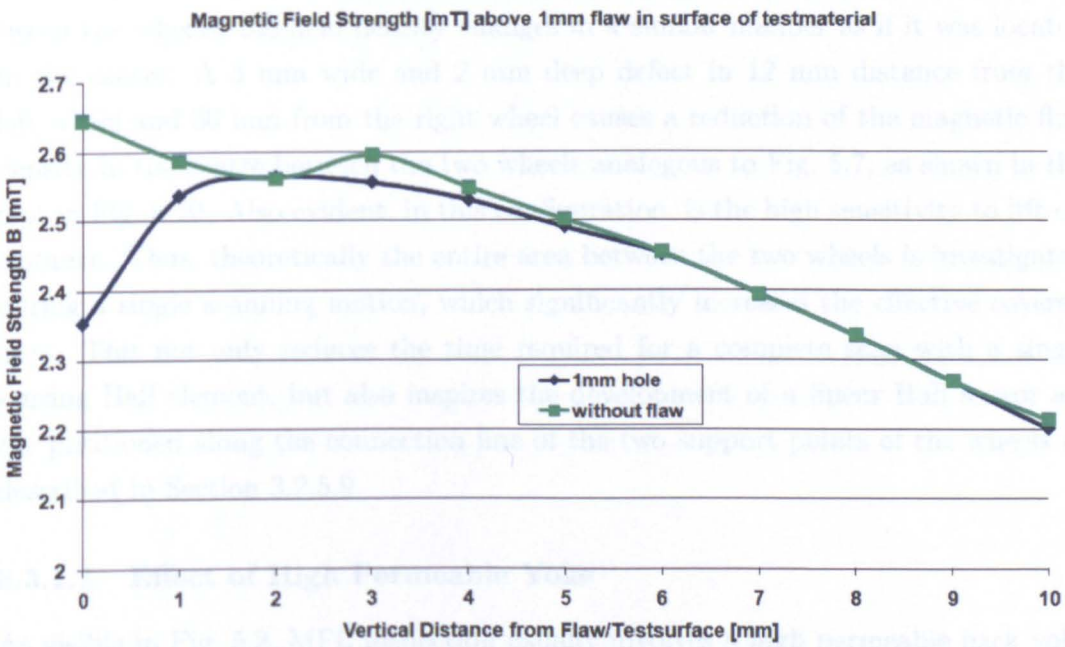
Figure 5.9: Magnetic field strength vs. height above a 1 mm wide and 4 mm deep defect, material: iron.

108
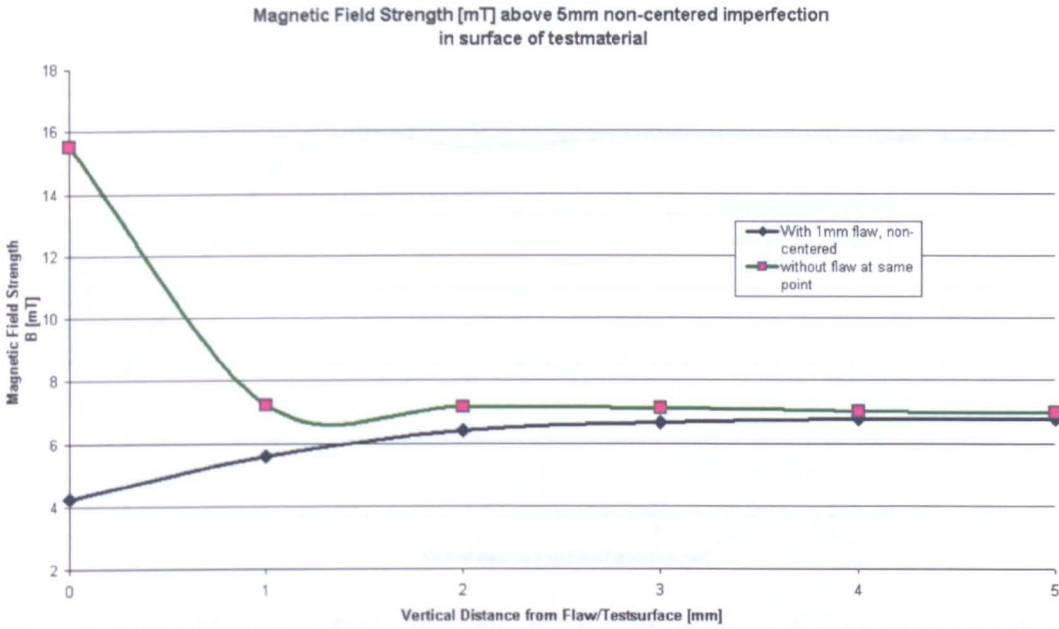
Figure 5.10: Magnetic field strength vs. height above a 5 mm wide and 2 mm deep non-central crack in an iron test surface.

5.3.1.2 Non-central Defects

According to simulations where the defect is located at a non-central position between the wheels, the field density changes in a similar manner as if it was located in the centre: A 5 mm wide and 2 mm deep defect in 12 mm distance from the left wheel and 30 mm from the right wheel causes a reduction of the magnetic flux density in the centre between the two wheels analogous to Fig. 5.7, as shown in the plot in Fig. 5.10. Also evident, in this configuration, is the high sensitivity to lift-off distance. Thus, theoretically the entire area between the two wheels is investigated during a single scanning motion, which significantly increases the effective covered area. This not only reduces the time required for a complete scan with a single sensing Hall element, but also inspires the development of a linear Hall sensor array positioned along the connection line of the two support points of the wheels as described in Section 3.2.5.9.

5.3.1.3 Effect of High Permeable Yoke

As visible in Fig. 5.2, MFL inspection usually involves a high permeable back yoke for closing the magnetic loop, which increases the sensitivity of the system up to 200% [21, 136, 168]. Since in the case of the inspection vehicles, the magnetic wheels
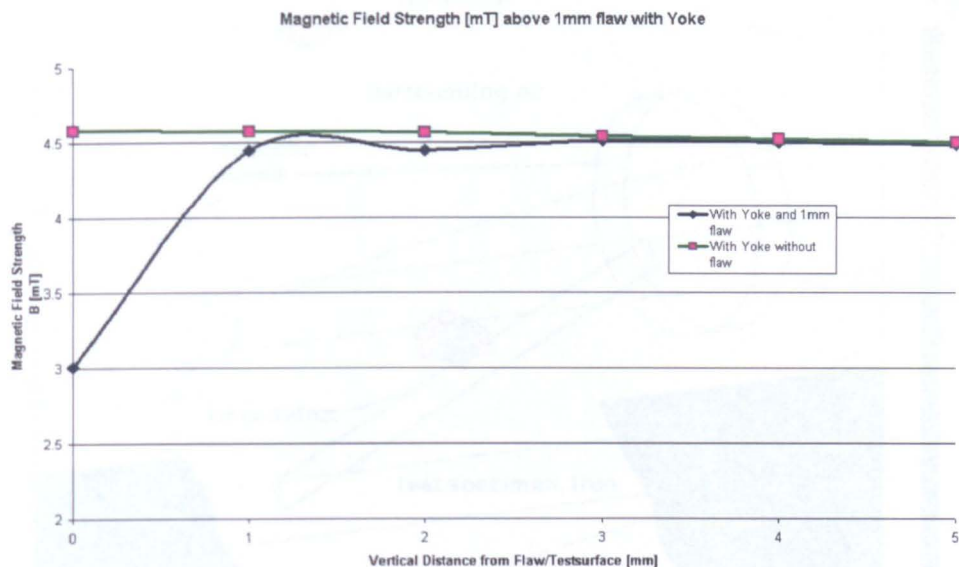
Figure 5.11: Magnetic field strength vs. height above a 1 mm wide and 4 mm deep crack in an iron testsurface, vehicle design with yoke.

create the source field for inspection, a flexible connection between the inner side of the wheels and such a yoke is required. In practice, carbon brushes could establish this connection, and with an iron back yoke, the theoretical change in field density in the centre of the wheels increases from 0.2 mT to 1.5 mT, as can be seen when comparing Fig. 5.9 with Fig. 5.11.

110
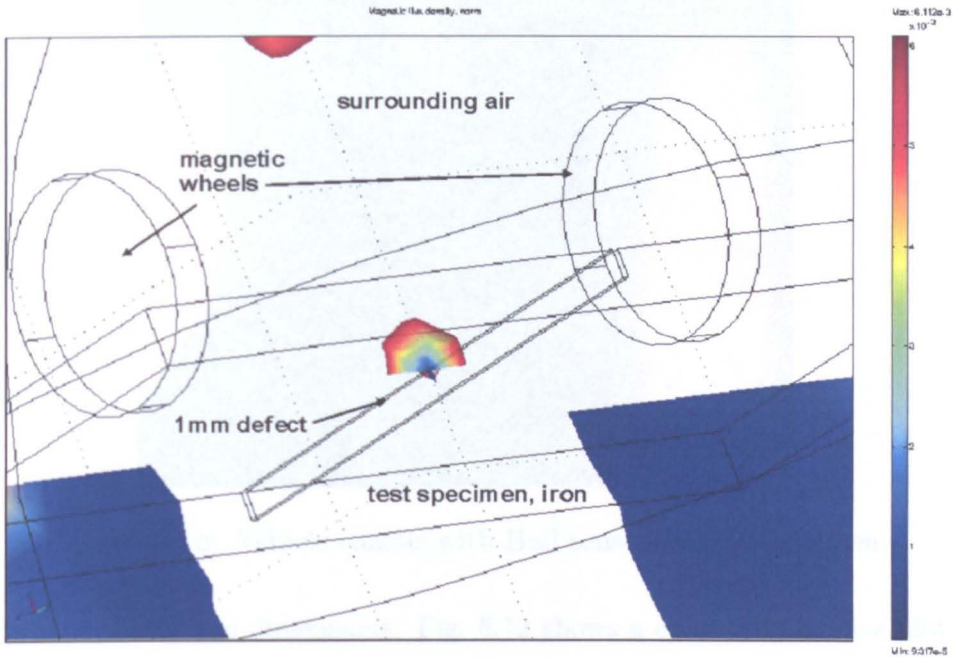
Figure 5.12: 3D plot of magnetic field, Femlab.

5.3.2   3D Magnetic Field Modelling

To support the results of the two dimensional simulations of the previous sections, the wheel-specimen-defect configuration was modelled in three dimensions with the electro magnetics add-on module of Femlab: An iron plate with two Ne-Fe-B disc magnets is located within a sphere of air. The boundary conditions of the sphere are set to magnetic insulation and for all remaining surfaces within the sphere continuity is assumed:

$$n \times A = 0 \tag{5.4}$$
$$n \times (H_1 - H_2) = 0 \tag{5.5}$$

The domain within the NeFeB magnets and the test specimen is governed by Equations 5.6 and 5.7, as the iron is not magnetised ($\mu_r = 4000$):

$$\nabla \times (\mu_0^{-1} \nabla \times A - M) - \sigma v \times (\nabla \times A) = J^e \tag{5.6}$$
$$\nabla \times (\mu_0^{-1} \mu_r^{-1} \nabla \times A) - \sigma v \times (\nabla \times A) = J^e \tag{5.7}$$

The subdomain settings for conductivity and magnetisation of the magnets are $\sigma_m = 1.12 \cdot 10^7$ and $M = 8.9 \cdot 10^5 \frac{A}{m}$, the velocity v and the external current density J^e are zero. The width of the simulated crack and the wheel distance are identical

111
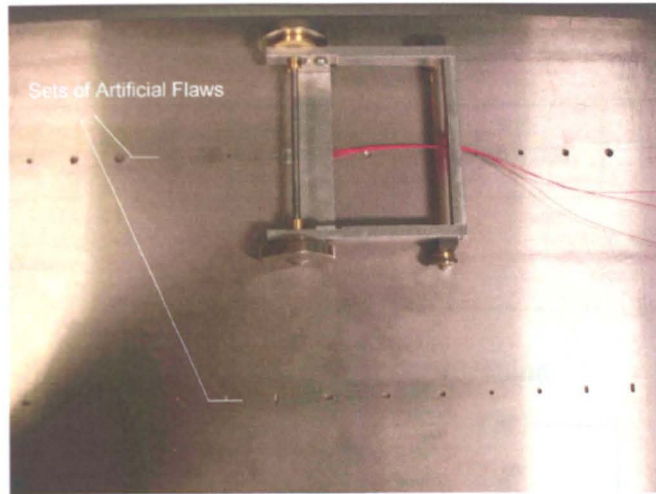
Figure 5.13: Vehicle chassis with Hall sensor on test specimen.

to the simulation in two dimensions. Fig. 5.12 shows a cross section slice plot perpendicular to the test surface and the moving direction of the vehicle. The result is identical to the one obtained with the simulation in two dimensions: a reduction of the magnetic field strength directly above the imperfection. For this purpose the plot is manually scaled to highlight a linear distribution between $B_{min} = 9.317 \cdot 10^{-5}$ T and $B_{max} = 6.112 \cdot 10^{-3}$ T, which leads to extensive white areas of regions that are out of range.

5.4 MFL Inspection - Experimental Results

To validate the theoretical simulations of the previous chapter, a large scale version of the vehicle chassis was constructed with a wheel distance of 100 mm and equipped with a Honeywell SS94A2 Hall effect probe to prove the concept of utilising the magnetic field of the wheels for surface inspection. Three sets of holes, varying from 5 mm to 1 mm in diameter and depths of 5 mm, 3 mm and 1 mm, are investigated as shown in Fig. 5.13. With the vehicle moving along the test surface the Hall probe detects changes of magnetic flux density above the artificial flaws. The level shifting and scaling circuit of Fig. 5.15 amplifies the output signal and compensates for the bias of the sensor. 10-bit A/D conversion of this signal takes place on a 16-bit Renesas M16-C micro controller, as shown in Fig. 5.14. A protection circuit consisting of a rectifying and a zener diode constrains the output voltage within 0V

112
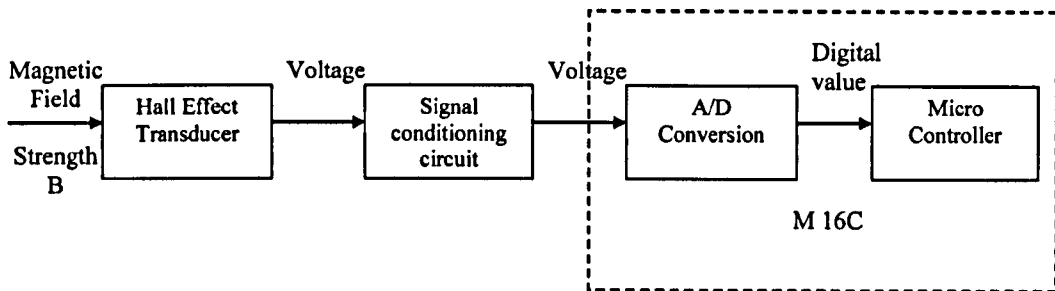
Figure 5.14: Signal conditioning.
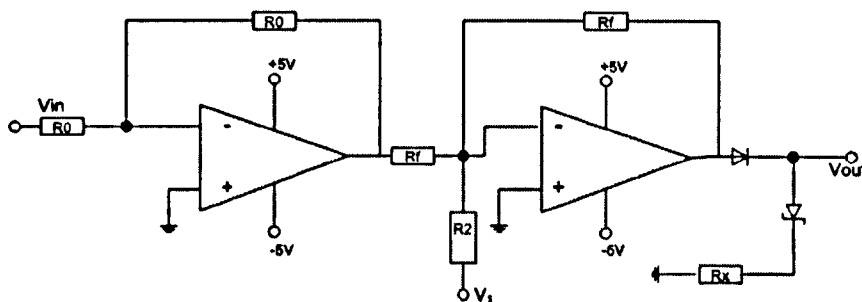
Figure 5.15: Level shifting and scaling circuit with additional diodes for limiting the overall voltage range.

and 5V. The output voltage in Fig. 5.15 is:

$$U_{out} = \frac{R_f}{R_1}U_{in} - \frac{R_f}{R_2}U_1 - U_{diode}. \tag{5.8}$$

This can be shifted from $U_{min_{in}} \sim U_{max_{in}}$ to $U_{min_{out}} \sim U_{max_{out}}$ by varying R_f and R_2 according to Equations 5.9 and 5.10. The voltage drop at the rectifying diode is $U_{diode} = 0.6V$, $U_1 = 12V$, $R_0 = 100K\Omega$ and $R_2 = 20K\Omega$.

$$R_f = R_1\frac{U_{max_{out}} - U_{min_{out}}}{U_{max_{in}} - U_{min_{in}}} \tag{5.9}$$

$$R_2 = R_1 U_1 \frac{U_{max_{out}} - U_{min_{out}}}{U_{min_{in}}(U_{max_{out}} + U_{diode}) - U_{max_{in}}(U_{min_{out}} + U_{diode})} \tag{5.10}$$

The measured Hall sensor output on an even flawless surface changes periodically with low frequency periodic background noise, as shown in Fig. 5.16. This periodic change of the magnetic field results from inhomogeneous magnetisation of the disc magnets and has to be taken into account when interpreting the sensor data. The frequency depends on the vehicle's travelling speed.
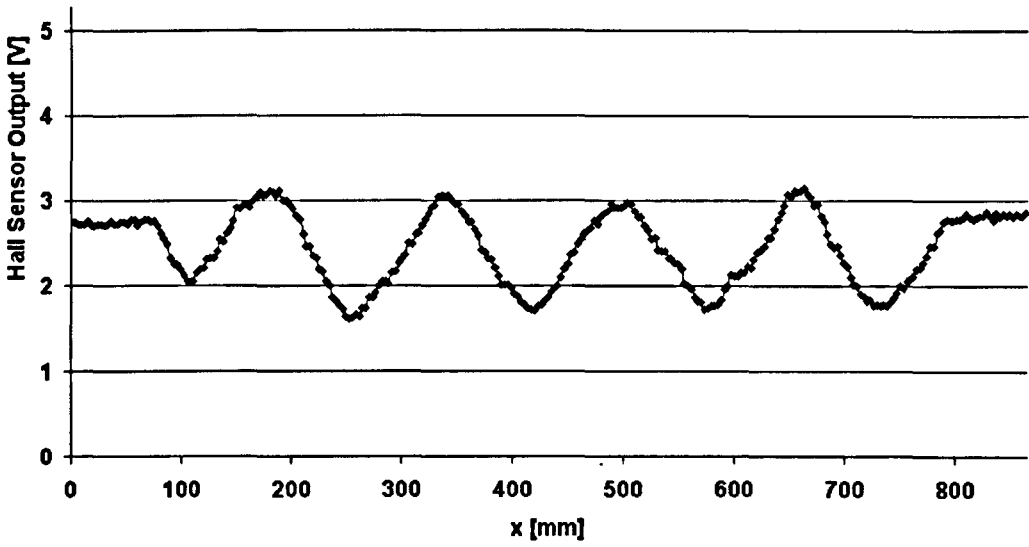
Figure 5.16: Periodic change of magnetic field caused by wheels.
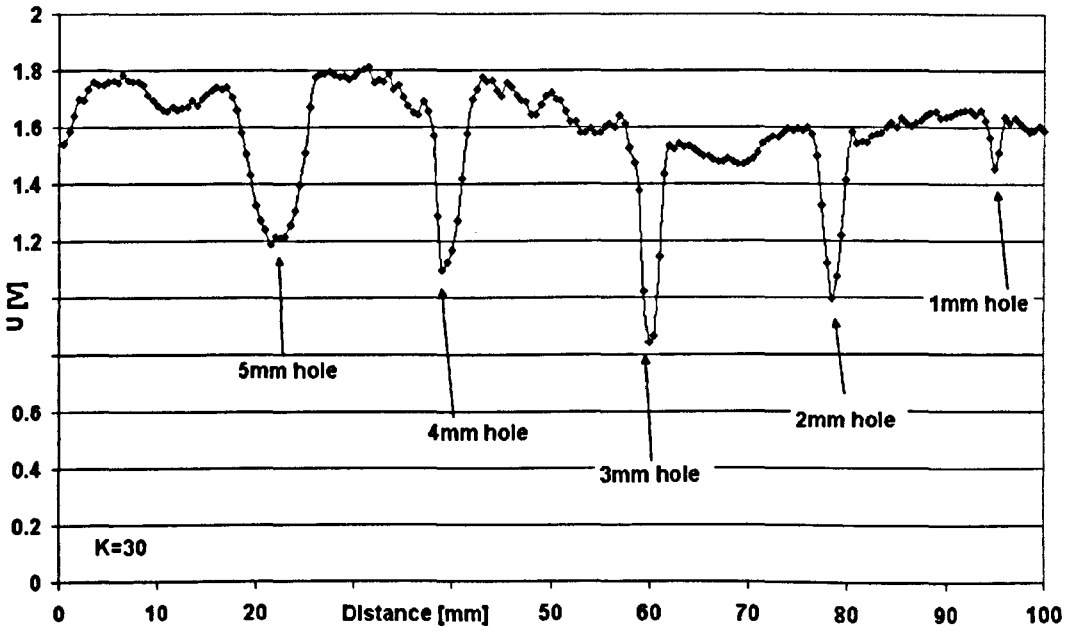
Figure 5.17: Detection of artificial flaws.
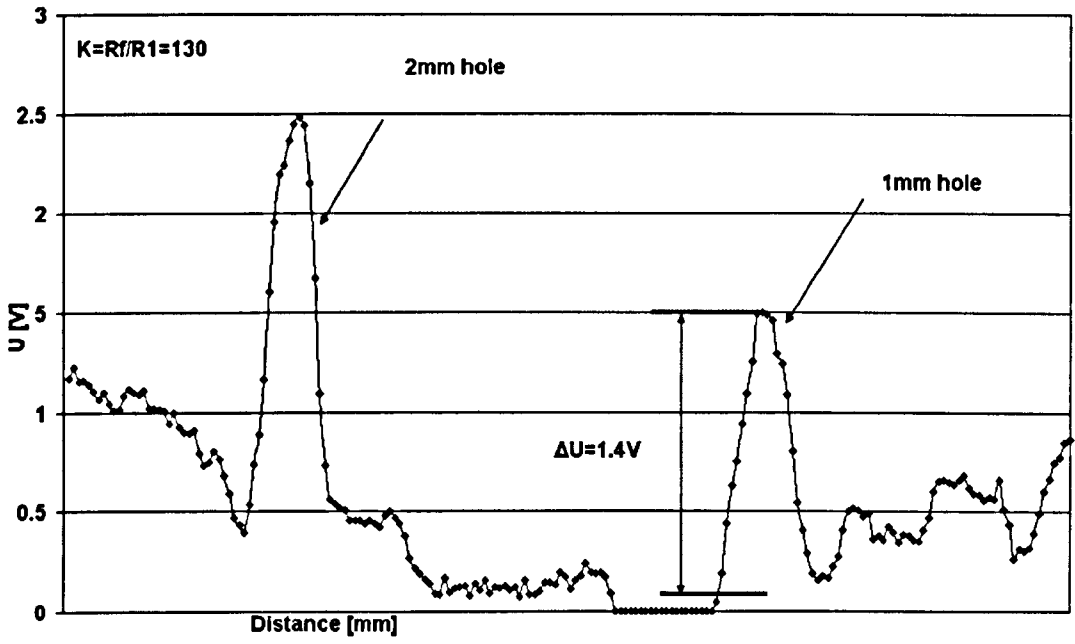
Figure 5.18: Quantitative validation of simulation.

A typical signal resulting from the set of artificial flaws described above without this low frequency component is presented in Fig. 5.17: Clearly visible are the voltage drops which indicate the positions of the drilled holes. Moreover, as shown in Fig. 5.18, the change in voltage supports the theoretical calculations of Section 5.3.1 quantitatively ($\Delta B = 0.3$ mT): The sensitivity of the Hall Sensor is $S = 50 \frac{mV}{mT}$ and the amplification factor of the signal conditioning circuitry $K = \frac{R_t}{R_1}$ is 30. Thus,

$$\Delta B = \Delta U \frac{1}{KS} = 0.215 \text{ mT} \tag{5.11}$$

The shape and size of the signal depend on the speed of the vehicle and the sampling rate. Hence, interpreting the raw signal on the micro controller without filtering allows for fast calibration without hardware changes. For different materials and types of defects, the corresponding parameters are adapted in the software, as described in the following section.
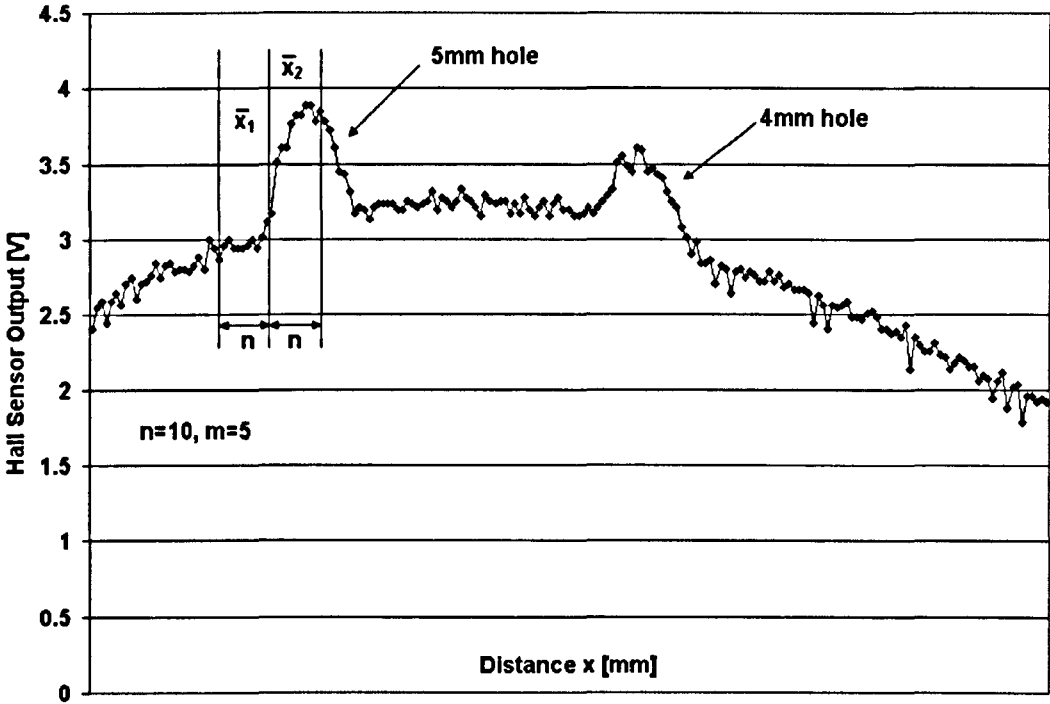
Figure 5.19: C-routine monitoring the average gradient of Hall sensor output voltage.

5.4.1 Interpreting the Data of a Single Hall Sensor

Fig. 5.19 shows the signal that results from a single Hall element passing over 5 mm and 4 mm boreholes from Fig. 5.13. To filter out the low frequency component caused by the rotating wheels and detect a defect, a C-routine running on the on board controller monitors the average gradient of the conditioned Hall voltage. The main part of this algorithm is a vector x containing the $2n$ last recent measurements. The difference between the average gradient of the first n elements $\bar{x}_1$ of this vector and the average gradient $\bar{x}_2$ of the last n readings build the detection criteria: A defect is present, if

$$\bar{x}_2 > \bar{x}_1 + b \tag{5.12}$$

is true for m consecutive samples, where b is a buffer value for controlling the sensitivity of the routine. This buffer effects the Probability of Detection as follows: Increasing b reduces the number of false positive hits, whereas a decrease of b leads to less false negatives — flaws are more likely to be detected.
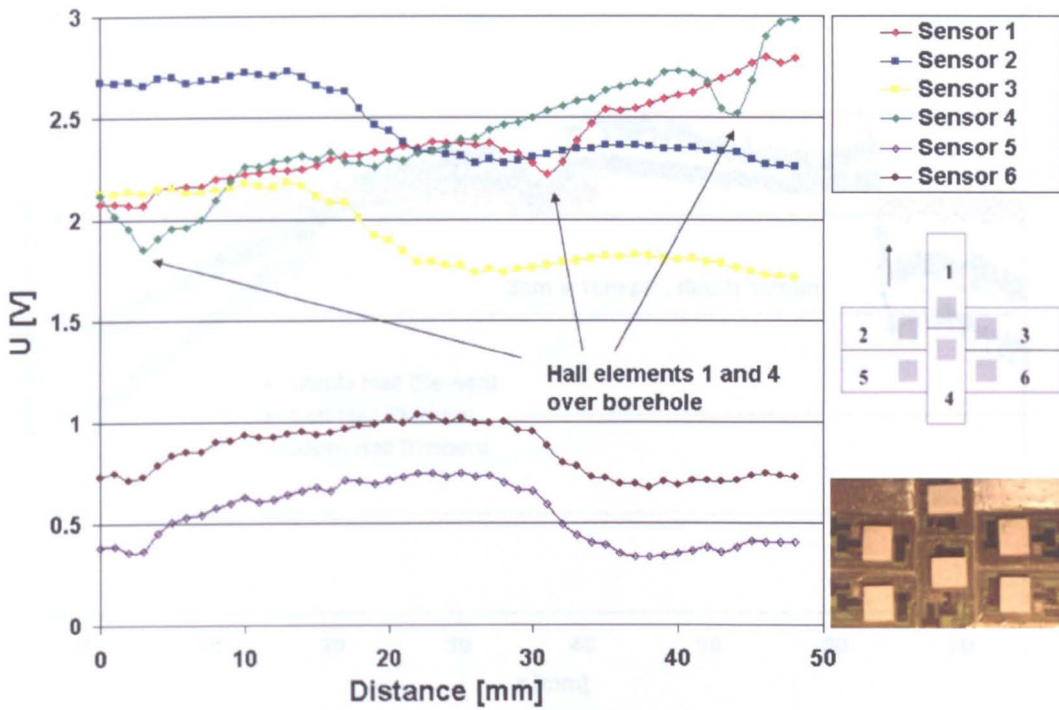
Figure 5.20: Six element Hall array - experimental results.

5.4.2 Interpreting the Data of Hall Sensor Arrays

To increase the surface coverage per travelled distance and to improve reliability, the performance of arrays of Hall sensors, illustrated in Fig. 3.13 and Fig. 5.20, is investigated. The output of each Hall element in Fig. 5.20 corresponds to its position and orientation within the array — Hall elements 1 and 4 are passing over the flaws of Fig. 5.13 and therefore yield a more distinct indication of defects compared to the data derived from a single element. The delay and the shape of signals caused by flaws varies between different materials and defect types and depends on the vehicle's travelling speed and the sampling rate. Hence, it takes considerable computational power to obtain unambiguous flaw indication. Arranging three Hall sensors in a linear configuration between the contact points of the magnetic wheels, as depicted in Fig. 3.13, reduces these software overhead and offers higher reliability. Due to the identical position of each sensor with regard to the vehicles longitudinal axis, all Hall elements pass over a flaw simultaneously, which leads to a typical signal shown in Fig. 5.21. When investigating large scale defects, the concurrent change of the three average gradients allows for a more distinct defect detection and improves the performance significantly. For smaller defects, the combined signal contains further information about size and position: With only the right element passing over a

118
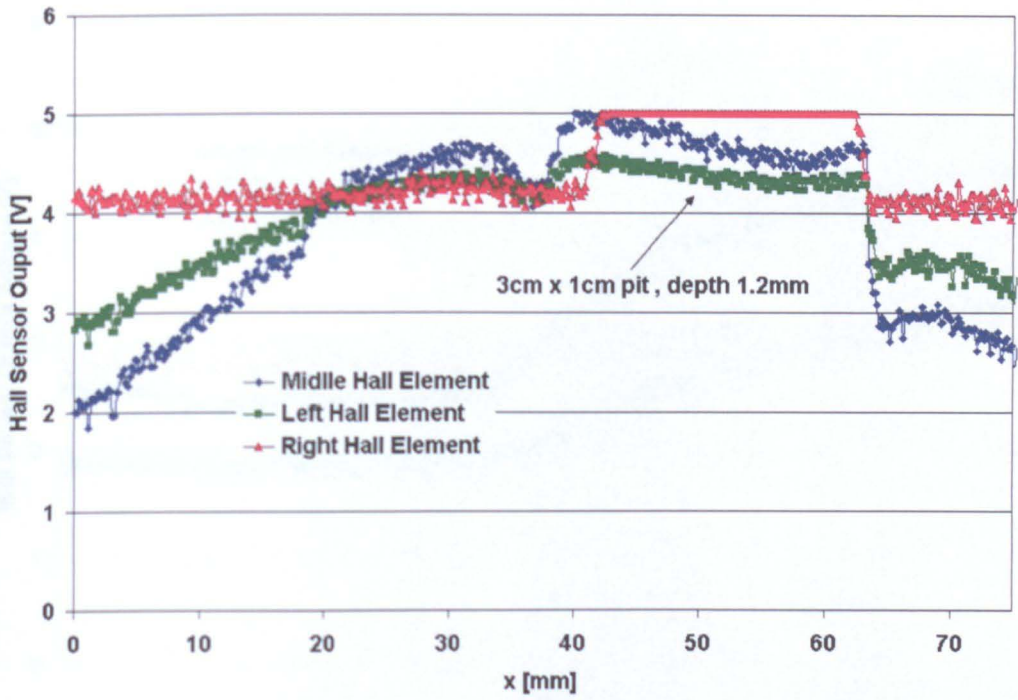
Figure 5.21: Output of three element Hall array passing over large scale defect on mild steel.

5 mm hole of Fig. 5.13, the output voltage of this element changes as expected while the remaining two elements do not indicate a defect, as shown in Fig. 5.22. Hence, the flaw is restricted to the area directly below the right element. However, if the middle Hall element passes over the same defect, both the left and right element respond, as shown in Fig. 5.23.
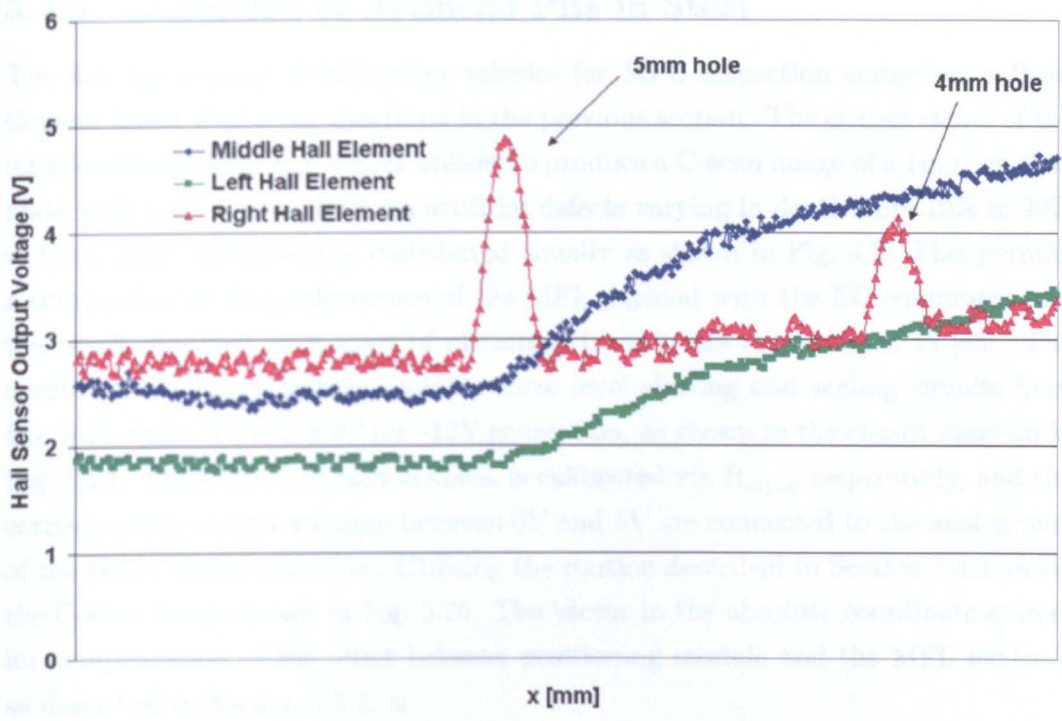
Figure 5.22: Obtaining information about defect position and size of small defects.
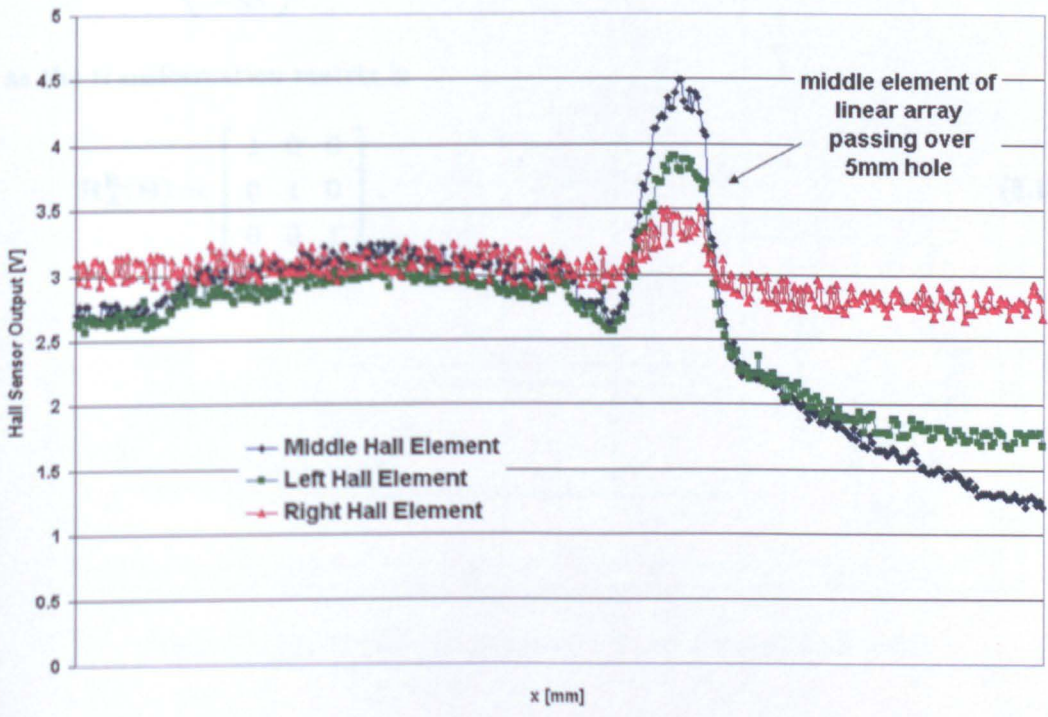
Figure 5.23: Middle Hall element passing over 5 mm defect.

5.4.3 Detection of Artificial Pits in Steel

The first generation of inspection vehicles for MFL inspection comprises a three element linear Hall array described in the previous section. The output signal of the middle element from Fig. 5.21 is utilised to produce a C-scan image of a 1m x 1m steel plate with a set of nine 3 x 1 cm artificial defects varying in depth from 10% to 90% of total plate thickness and distributed equally as shown in Fig. 4.8. This permits a comparison of the performance of the MFL payload with the EC equipment and the result obtained with a set of ultrasonic transducers as presented in [85]. The module for MFL inspection contains three level shifting and scaling circuits from Fig. 5.15 and a TC1044S IC for $-12V$ generation, as shown in the circuit diagram in Fig. 5.24. The output of each element is calibrated via $R_{in_{1-6}}$ respectively, and the corresponding output voltages between 0V and 5V are connected to the analog port of the HC11 micro controller. Utilising the routine described in Section 5.4.1 yields the C-scan image shown in Fig. 5.25. The vector in the absolute coordinate system for compensation of the offset between positioning module and the MFL payload, as described in Section 4.5.1, is

$$
\mathbf{x}_{mfl}^{A} = \begin{pmatrix} 0 \\ 0 \\ -85 \end{pmatrix} \text{mm}, \tag{5.13}
$$

as the transformation matrix is

$$
\mathbf{R}_{A}^{R}(\Theta) = \begin{bmatrix} 1 & 0 & 0 \\ 0 & 1 & 0 \\ 0 & 0 & 1 \end{bmatrix}. \tag{5.14}
$$
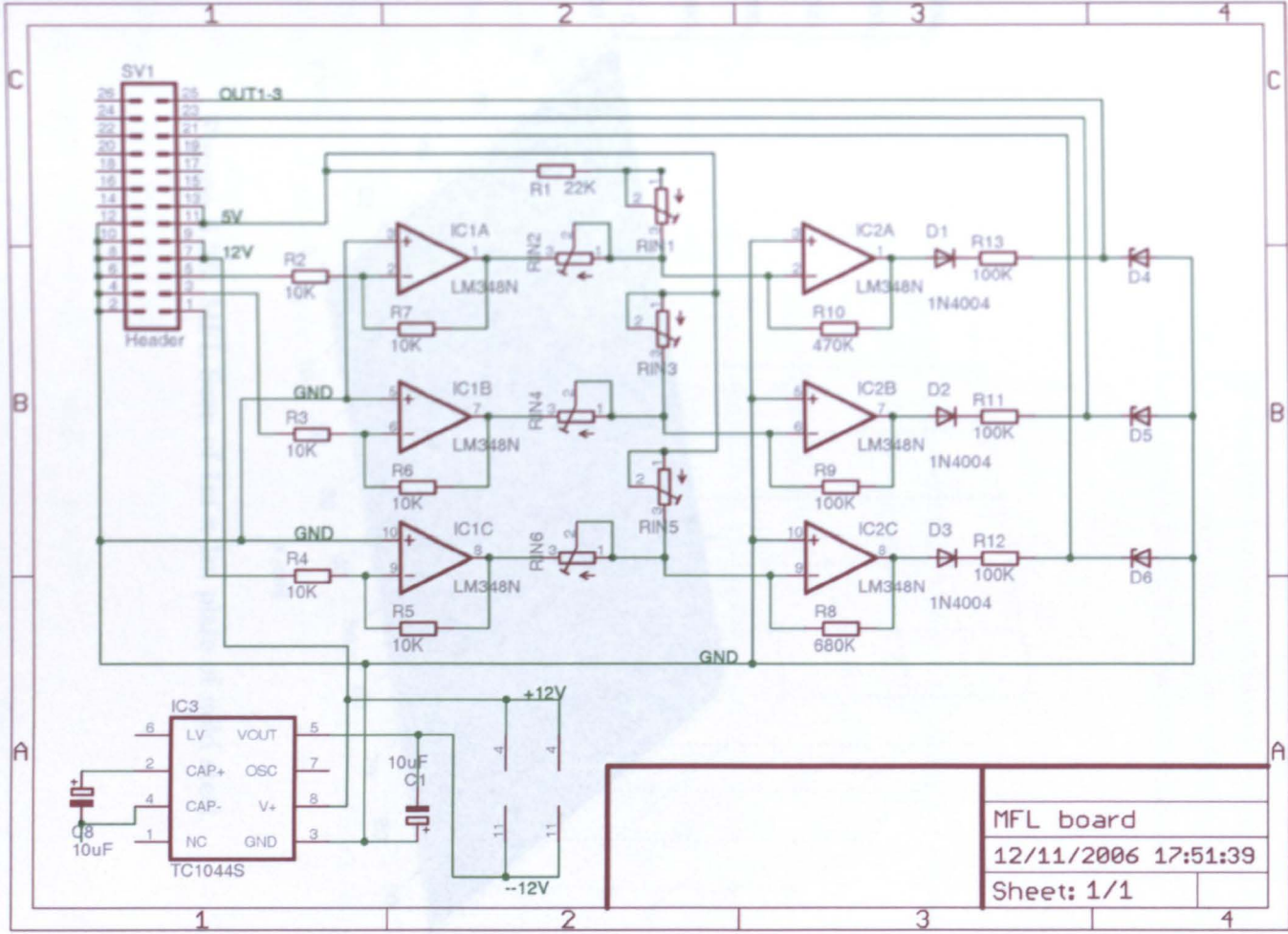
Figure 5.24: Signal conditioning - three element Hall array.
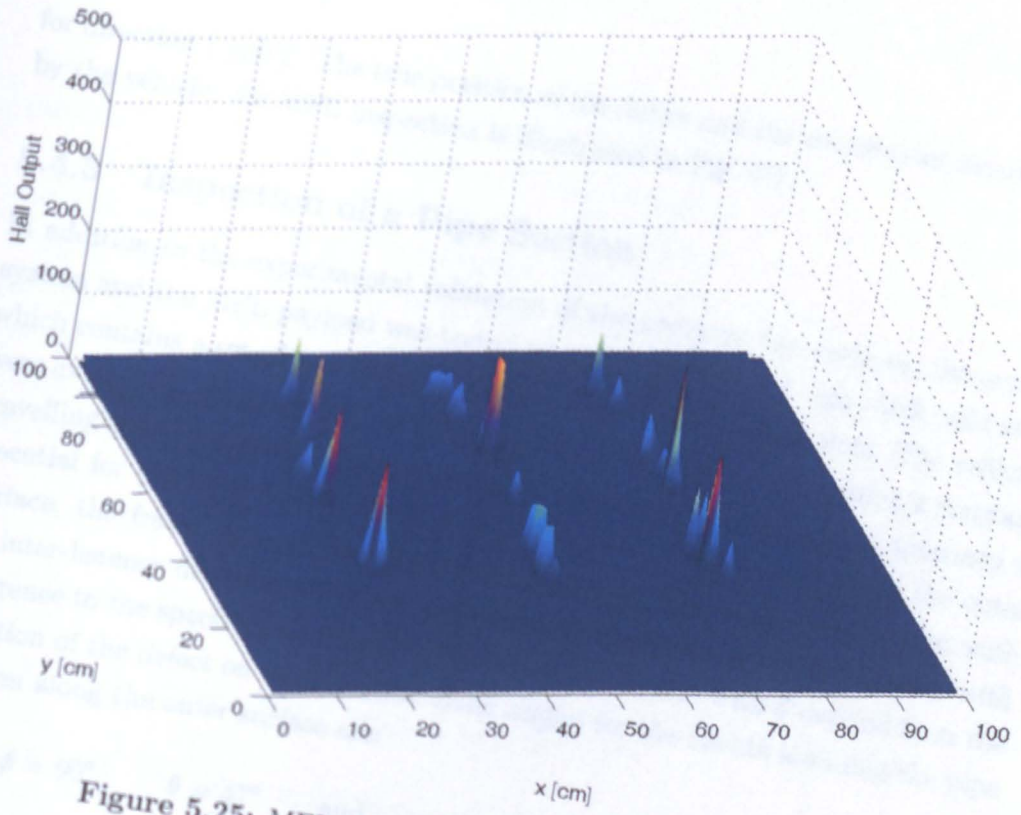
Figure 5.25: MFL Scan of 1m x 1m plate of mild steel.

123

5.4.4 Upside Down Inspection of an Inclined Steel Plate

The MFL payload described in the previous sections was tested via an upside down inspection of a 42° inclined plate of mild steel with identical experimental conditions as for the experiment with EC sensors described in Section 4.5.2. The rotary matrices according to Equations 4.9, 4.15 and 4.16 yield the vector for taking the offset between positioning module and actual NDE payload into account:

$$\mathbf{x}_{mfl}^{A} = \begin{pmatrix} 0 \\ -63 \\ 57 \end{pmatrix} \text{mm} \tag{5.15}$$

for direction 1 and 2. The true position of the defect and the coordinates ascertained by the vehicles for MFL inspection is illustrated in Fig. 4.7.

5.4.5 Inspection of a Pipe Section

In addition to the experimental validation of the previous two sections, the overall system and the MFL payload was tested on a pipe section of 1 mm thick mild steel which contains a set of two 20 mm long and 2 mm wide through slots. The vehicles were examining the specimen both from outside and inside. Maintaining a constant travelling speed via pulse width modulation while circling around the specimen is essential for the MFL inspection at this point. For the inspection along the outer surface, the frame with the listeners was positioned above the pipe section with an inter-listener distance of 197 cm, yielding the absolute coordinate system with reference to the specimen as illustrated in Fig. 5.26. Hence, with θ derived from the position of the defect on the pipe, the Euler angles for the robots scanning the pipe section along the outer surface are:

$$\phi = 90°, \qquad \theta = 47° \qquad \text{and} \qquad \psi = 0° \tag{5.16}$$

for scanning in direction 1 and

$$\phi = -90°, \qquad \theta = -47° \qquad \text{and} \qquad \psi = 0° \tag{5.17}$$

for direction 2. The rotary matrices according to Equation 4.9 are hence:

$$\mathbf{R}_{A}^{R}(\Theta)_{1} = \begin{bmatrix} 0 & -\cos\theta & \sin\theta \\ 1 & 0 & 0 \\ 0 & \sin\theta & \cos\theta \end{bmatrix} \tag{5.18}$$

and

$$R_A^R(\Theta)_2 = \begin{bmatrix} 0 & \cos\theta & -\sin\theta \\ 1 & 0 & 0 \\ 0 & \sin\theta & \cos\theta \end{bmatrix},$$

(5.19)

which yield the vectors for taking the offset between positioning module the MFL payload for directions 1 and 2 into account:

$$x_{m\text{fl}}^A = \begin{pmatrix} -63 \\ 0 \\ -58 \end{pmatrix} \text{mm}$$

(5.20)

The true coordinates of the artificial defects $[620; 990; -1070]^T$ mm and $[620; 1315; -1070]^T$ mm and their position ascertained by the inspection vehicles is visualised in Fig. 5.26. For the inspection along the inner surface of the specimen the inter-listener distance r is decreased to 54 mm and the frame is positioned directly in front of the open end of the pipe section in order to allow for line of sight contact between the robots and the listeners. The origin of this auxiliary coordinate system H is at $0_H = [0; 1970; -1360]^T$ and it is orientated with reference to the absolute system A as illustrated in Fig. 5.26. The Euler angles with respect to the reference frame H for the robots scanning the inner surface of the pipe section are

$$\phi = 227°, \qquad \theta = 90° \qquad \text{and} \qquad \psi = -90°$$

(5.21)

for scanning in direction 1 and

$$\phi = 227°, \qquad \theta = 90° \qquad \text{and} \qquad \psi = 90°$$

(5.22)

for direction 2. The rotary matrices according to Equation 4.9 are thus:

$$R_H^R(\Theta)_1 = \begin{bmatrix} 0 & \cos\phi & \sin\phi \\ 0 & \sin\phi & -\cos\phi \\ 1 & 0 & 0 \end{bmatrix}$$

(5.23)

and

$$R_H^R(\Theta)_2 = \begin{bmatrix} 0 & -\cos\phi & \sin\phi \\ 0 & -\sin\phi & -\cos\phi \\ 1 & 0 & 0 \end{bmatrix},$$

(5.24)

125

which yield the vectors for taking the offset between positioning module and actual NDE payload into account:

$$x_{mfl}^{H} = \begin{pmatrix} 63 \\ -58 \\ 0 \end{pmatrix} \text{ mm} \tag{5.25}$$

for direction 1 and 2. The defects are detected at $x_1^H = [560; -250; -940]^T$ mm, $x_2^H = [530; -260; -920]^T$ mm, $x_3^H = [540; -260; -630]^T$ mm and $x_4^H = [560; -250; -640]^T$ mm. Applying Equations 4.12 and 5.25 yield the corrected positions. The Euler angles for transforming these coordinates of the frame H into the absolute coordinate system A are

$$\phi = 0°, \qquad \theta = -90° \qquad \text{and} \qquad \psi = 0°, \tag{5.26}$$

which yield the rotary matrix

$$R_A^H(\Theta) = \begin{bmatrix} 1 & 0 & 0 \\ 0 & \cos\theta & -\sin\theta \\ 0 & \sin\theta & \cos\theta \end{bmatrix} = \begin{bmatrix} 1 & 0 & 0 \\ 0 & 0 & 1 \\ 0 & -1 & 0 \end{bmatrix}. \tag{5.27}$$

With

$$x_A = R_A^H(\Theta)x_H + 0_H \tag{5.28}$$

the corrected position of the defects in the absolute coordinate system A are $x_1^A = [622; 1030; -1052]^T$ mm, $x_2^A = [592; 1050; -1042]^T$ mm, $x_3^A = [592; 1340-1042]^T$ mm and $x_4^A = [622; 1330; -1052]^T$ mm, as illustrated in Fig. 5.26.
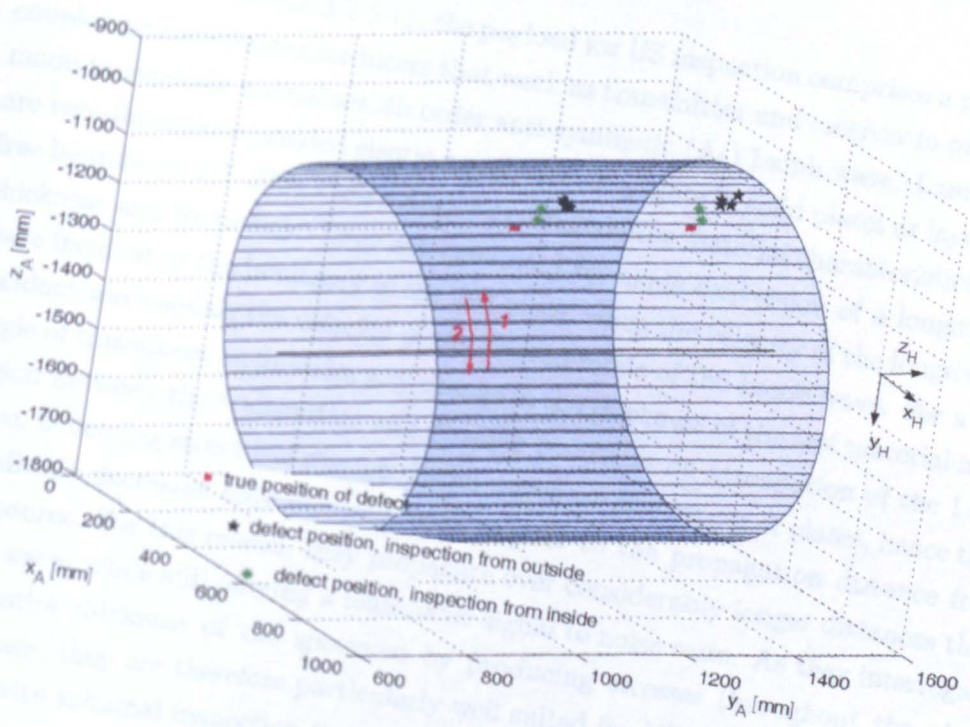
Figure 5.26: Position of detected defects on pipe section.

5.5 Ultrasonic and Visual Inspection - Theory

In terms of structural and material strength, the most serious defects are surface breaking and these are detectable by careful Visual Inspection [105]. In particular, weld defects such as severe undercutting or incompletely filled grooves can be discovered automatically with an on board camera system which can also provide valuable contextual and quality-control information such as surface shape and roughness. Complementary to Visual, EC and MFL Inspection, Ultrasonic (US) Inspection gives indication about non surface-breaking and internal defects within the test material.

As described in Section 3.2.5.11, the payload for US inspection comprises a pair of air coupled piezoelectric transducers that work as transmitter and receiver in pulse echo mode to generate a local zeroth order anti-symmetic (A_0) Lamb wave. Lamb waves are two-dimensional guided elastic waves that propagate in solid plates or layers with free boundaries [77, 233], their velocity depends on the material characteristics, plate thickness and frequency. They are generated by mode conversion of a longitudinal wave incident at the boundary of the test piece, when the velocity of the longitudinal incident wave equals the velocity of the desired mode of the Lamb wave. For a fixed angle of transducer inclination, any change in the thickness of the test material in the region between the transmitter and receiver results in an attenuation of the Lamb wave, indicating structural change. Lamb waves are free modes of plates, hence their amplitude decreases only inversely with respect to the propagation distance from the source. For this reason, they propagate over considerably longer distances than bulk waves while still offering a reasonable signal to noise ratio. As they interrogate the entire thickness of the specimen by producing stresses throughout the plate thickness, they are therefore particularly well suited for NDE of thin plates or pipe walls with minimal inspection time.

Fig. 5.27 shows the inspection vehicle with the transducers on the main hold as described in Section 3.2.5.9 and illustrated with more detail in the technical drawings A.28 — A.31.

5.6 Ultrasonic and Visual Inspection - Experimental Results

For evaluating the US inspection technique experimentally, a the set of artificial defects, described in Section 4.5.3 and shown in Fig. 4.8, has been produced within
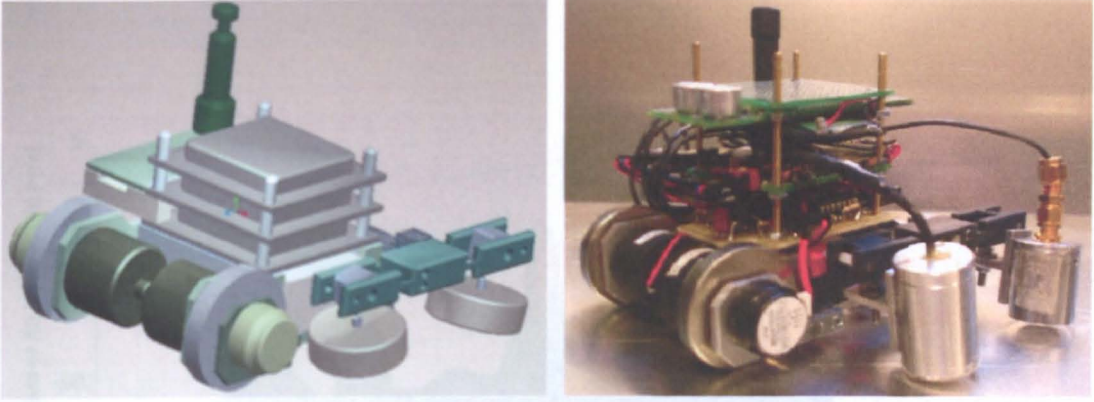
Figure 5.27: Vehicle with air coupled transducers.

a 1m x 1m aluminium plate of 1.5 mm thickness. The position of the centre of the two transducers in the robot fixed coordinate system corresponding to Equation 4.10 is

$$\mathbf{x}_{us}^{R} = \begin{pmatrix} -82 \\ -77 \\ -85 \end{pmatrix} \text{ mm.} \tag{5.29}$$

The two transducers work at 600 kHz and are inclined at 6.5° to create the corresponding incident angle for generating the A_0 Lamb wave in the aluminium test specimen. The amplitude of the received Lamb wave is measured and combined with data from the absolute positioning system to produce the C-Scan image shown in Fig. 5.28. The attenuation of the Lamb wave when the nine different defects are between transmitting and receiving transducer are clearly visible. Fig. 5.28 also indicates a defect at the left hand edge of the plate and on close visual inspection an indentation was discovered at this position, caused during the machining process of the plate.

For visual inspection, the wireless camera described in section 3.2.5.12 is mounted on the hold illustrated in Figures A.32 and A.33. It continuously transmits a live picture to the receiver which is connected to the host computer. The image can be captured and saved for later analysis together with the vehicles' position at any time. However, lighting remains an unresolved issue, as shown in Fig. 5.29.
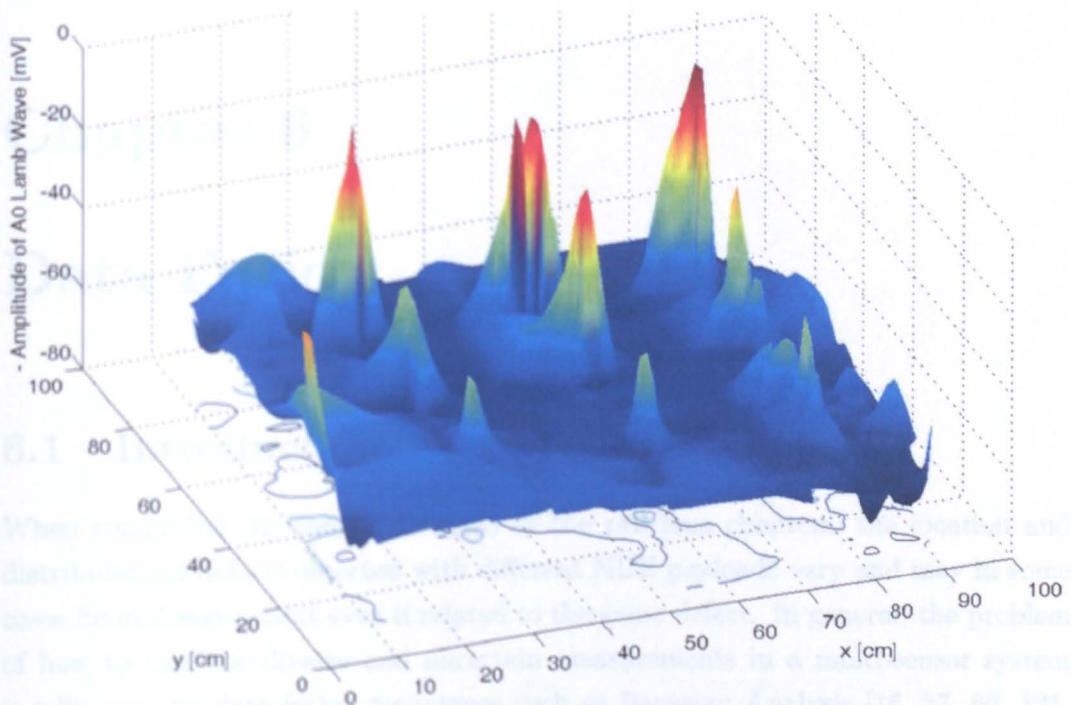
Figure 5.28: C-Scan image of aluminium plate.
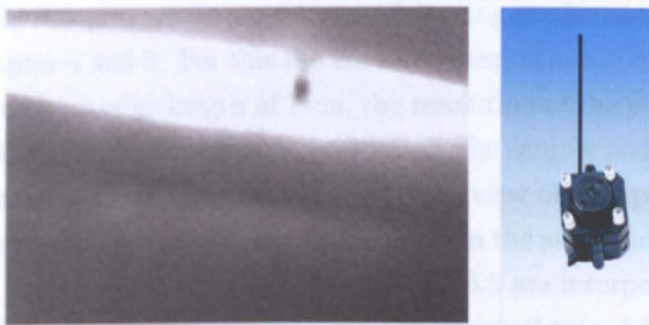
Figure 5.29: Wireless camera for visual inspection and image of 1 mm hole with reflexions of infra-red LEDs.

Chapter 6

Data Fusion

6.1 Introduction

When comparing the results obtained in the previous chapters, the location and distribution of defects detected with different NDE payloads vary and may in some cases be in disagreement even if related to the same defect. In general, the problem of how to combine diverse and uncertain measurements in a multi-sensor system is addressed by data fusion techniques such as Bayesian Analysis [16, 57, 66, 131, 135, 251], Dempster-Shafer Evidence Theory [50, 139, 176, 196], Fuzzy Logic [29, 118], Graph Pyramids [56, 201], Neural Networks [71, 116] and Wavelet Transforms [93, 230]. The objective of these techniques is to reduce uncertainty and increase the confidence level of a measurand by synergistic use of information from multiple sources, thus creating a consistent, accurate and intelligible data set. The most commonly used theories that have appeared in literature in the field of NDE data fusion are Bayesian probabilistic reasoning and Dempster-Shafer theory of evidence [99]. These methodologies are employed in the following sections to fuse the data sets obtained in Chapter 4 and 5. For this the 1m x 1m specimens are divided into square shaped 'pixels' with an edge length of 1 cm, the resolution of the positioning system. Each of these pixels relates to the same position on the sample and represents either a flawless surface or a defect. Fig. 6.1 shows the top view of the specimen indicating the true positions and depth of the artificial defects in the steel and aluminium plate as described in Section 4.5.3. Fig. 6.2, 6.3, 6.4 and 6.5 are interpolated plots of the original MFL, EC and US scan results. For the image obtained by US inspection, positions where the amplitude of the received lamb wave was below 40 mV are considered as defective.
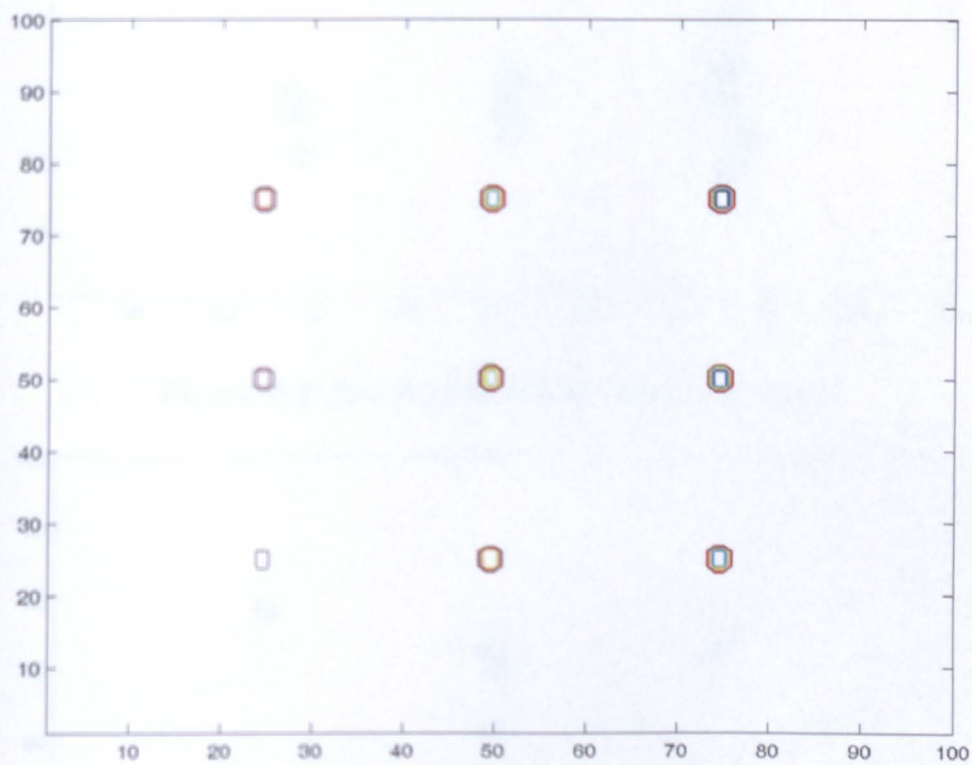
Figure 6.1: 1m x 1m plate with true position of defects.
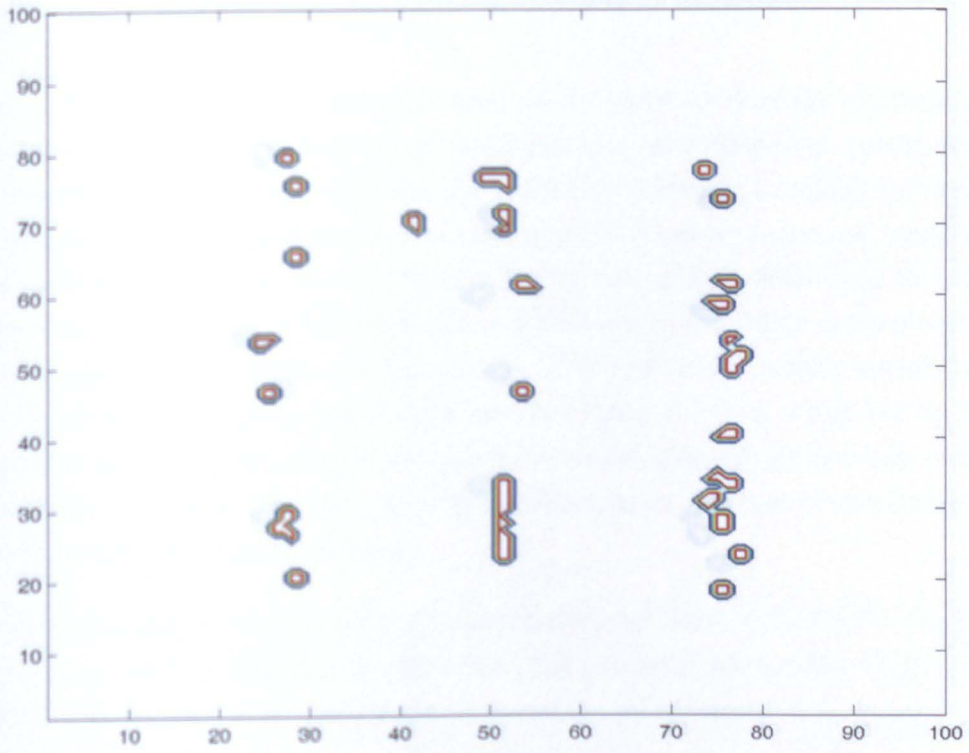
Figure 6.2: Result of MFL scan (steel), top view.
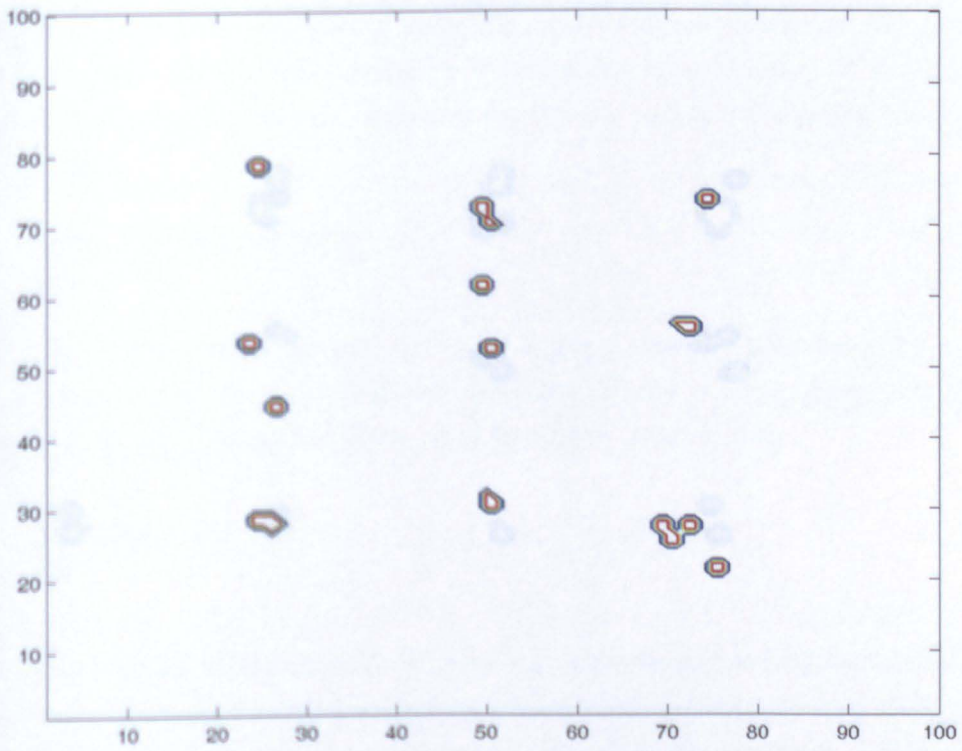
Figure 6.3: Result of EC scan (steel), top view.

133
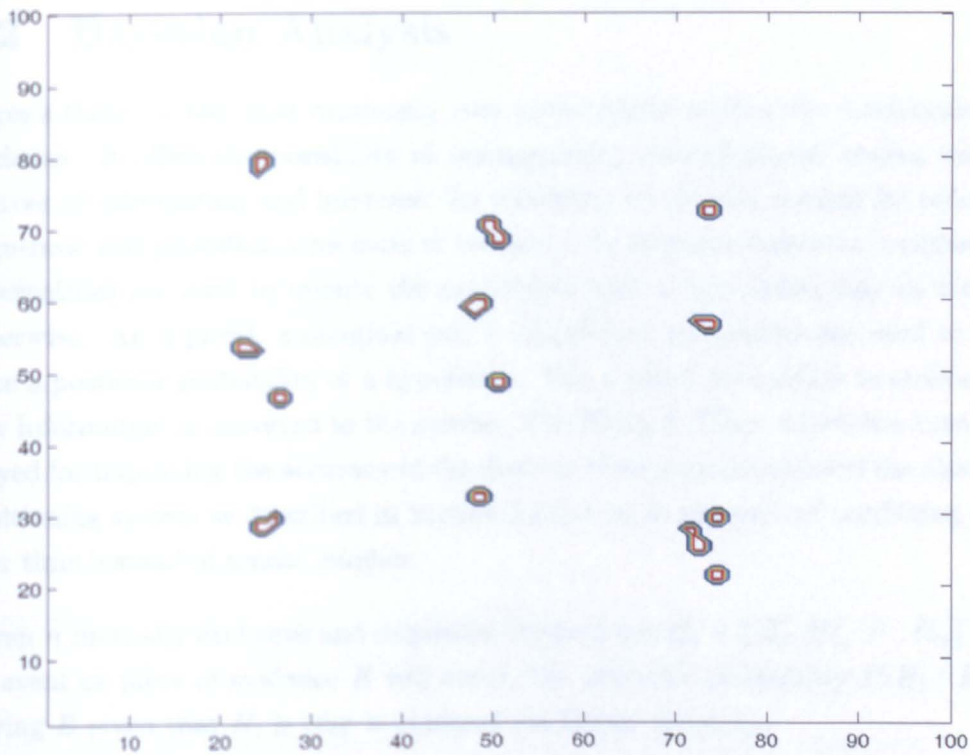
Figure 6.4: Result of EC scan (aluminium), top view.
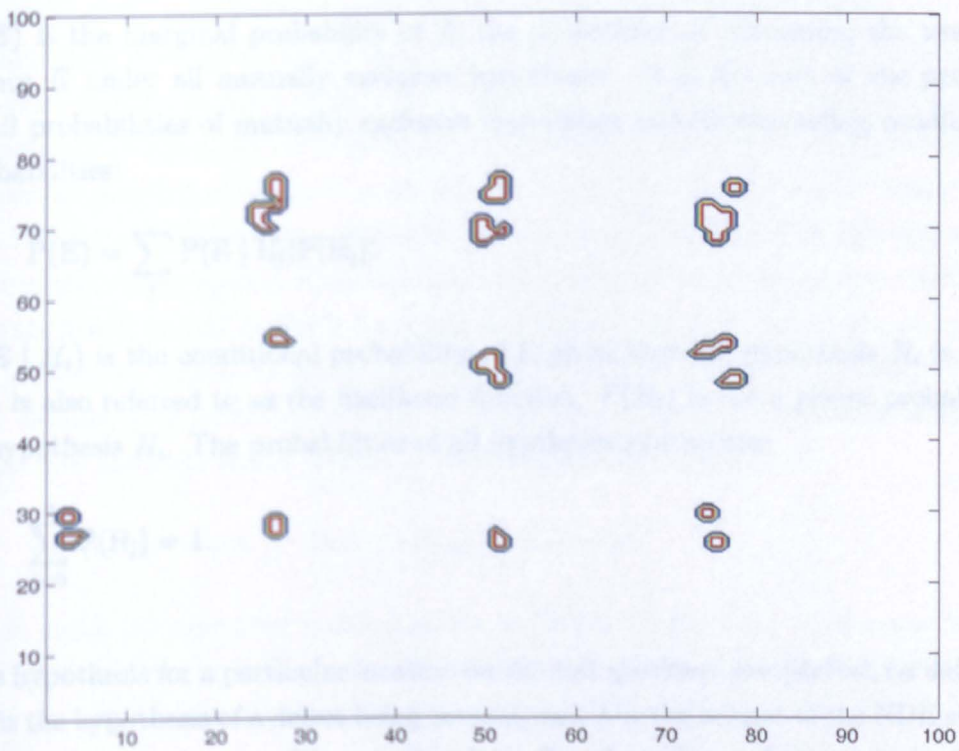
Figure 6.5: Result of Lamb Wave scan (aluminium), top view.

6.2 Bayesian Analysis

Bayes's theory is the most commonly used probabilistic method for combination of evidence. It offers the possibility of distinguishing inconsistencies among various sources of information and improves the reliability of decision making by reducing vagueness and providing a measure of certainty. In Bayesian inference, evidence or observations are used to update the probability that a hypothesis may be true or otherwise. An a priori, a marginal and a conditional probability are used to produce a posterior probability of a hypothesis. The a priori probability is updated as new information is conveyed to the system. The Kalman Filter, which has been employed for improving the accuracy of the discrete time measurements of the absolute positioning system as described in Section 3.3.3.4, is an example of combining data over time instead of sensor number.

Given n mutually exclusive and exhaustive hypotheses $H_i = \{H_0, H_1, \cdots, H_n\}$ that an event or piece of evidence E will occur, the posterior probability $P(H_i \mid E)$ of having E given that H_i is true is obtained via Bayes' theorem:

$$P(H_i \mid E) = \frac{P(E \mid H_i)\, P(H_i)}{P(E)}. \tag{6.1}$$

$P(E)$ is the marginal probability of E, the probability of witnessing the new evidence E under all mutually exclusive hypotheses. It is the sum of the product of all probabilities of mutually exclusive hypotheses and corresponding conditional probabilities:

$$P(E) = \sum_j P(E \mid H_j)P(H_j). \tag{6.2}$$

$P(E \mid H_i)$ is the conditional probability of E given that the hypothesis H_i is true, and is also referred to as the likelihood function. $P(H_i)$ is the a priory probability of hypothesis H_i. The probabilities of all hyptheses sum to one:

$$\sum_{j=0}^{n} P(H_j) = 1. \tag{6.3}$$

The hypothesis for a particular location on the test specimen are $\{$defect, no defect$\}$. H_0 is the hypothesis of a defect being present, and E is the output of the NDE sensor at the trilaterated x-y position on the plate. Based on the confusion matrix shown in Table 4.2 in Section 4.5.3, the conditional probabilities correspond to the True

TP = 0.8	FP = 0.2
FN = 0.2	TN = 0.8

Table 6.1: Confusion matrix for data fusion of the EC sensor taking the uncertainty of the positioning system into account.

TP = 0.7	FP = 0.3
FN = 0.3	TN = 0.7

Table 6.2: Confusion matrix for data fusion of the MFL sensor taking the uncertainty of the positioning system into account.

Positive and False Positive rate and are thus 0.8 for detecting a defect and 0.2. By calibrating of the buffer value as described in Section 5.4.1, a similar performance can be achieved with the MFL payload. In addition to these probabilities, the accuracy of the positioning system has to be taken into account: Even if the NDE sensors have detected a defect correctly, there may be an error in the trilaterated position. Hence, considering both the performance of the actual NDE sensor and the uncertainty of the positioning system, the probability of a defect being present at a particular position is assumed to be 80% for a positive result of the EC inspection and 70% for a defect detected with the MFL payload. Alternatively, the inaccuracy of the positioning system could be taken into account by a separte iterative step. The confusion matrix in Table 4.2 suggests 100% reliability for negative results (TN = 1). However, again taking the uncertainty of the positioning system into account and according to common practice, identical probabilities are assumed when the inspection methods report defects or flawless positions. Thus,

$$P_{ec}(E \mid H_0) = 0.8 \quad \text{and} \quad P_{mfl}(E \mid H_0) = 0.7,$$

which yields the confusion matrices shown in Tables 6.1 and 6.2: As the edge length of a pixel is 1 cm, and the defects in the test specimens described in section 4.5.3 are 3 cm x 1 cm, the a priori probability of containing a defect is:

$$P(H_0) = \frac{27}{10000}.$$
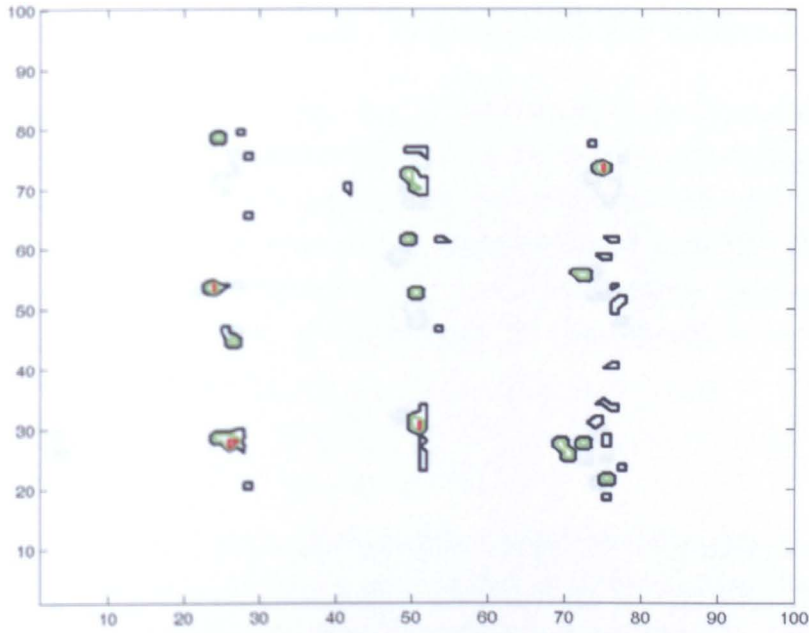
Figure 6.6: Result of Bayesian data fusion of MFL and EC scan.

That is, before inspecting the 1 x 1m plate each square centimetre contains a defect with the probability of 0.27%. If a defect is detected via EC inspection, this probability increases to 1.07%, while it decreases to 0.067% if the inspection yields a negative result. These two values are the new a priori probabilities for the MFL scan. Depending on whether a defect has been detected with this second method or not, the probability of a defect being present changes as illustrated in Fig. 6.6. The red lines indicate areas with a probability of 9.1 $P(H_0)$, so these positions are 9.1 times more likely to contain a defect than positions which have not been subject to inspection. The areas marked by green boundary lines have a posterior probability of containing a defect of

$$P(H_{i,j} \mid E) = 1.7\ P(H_0),$$

and for the areas within the blue lines

$$P(H_{i,j} \mid E) = 0.6\ P(H_0).$$

In the remaining white areas, where both inspection techniques do not report a defect, the probability of a defect being present is 9.3 times lower than without inspection.

Fig. 6.7 shows the fused image of the Lamb Wave and the Eddy Current scan of
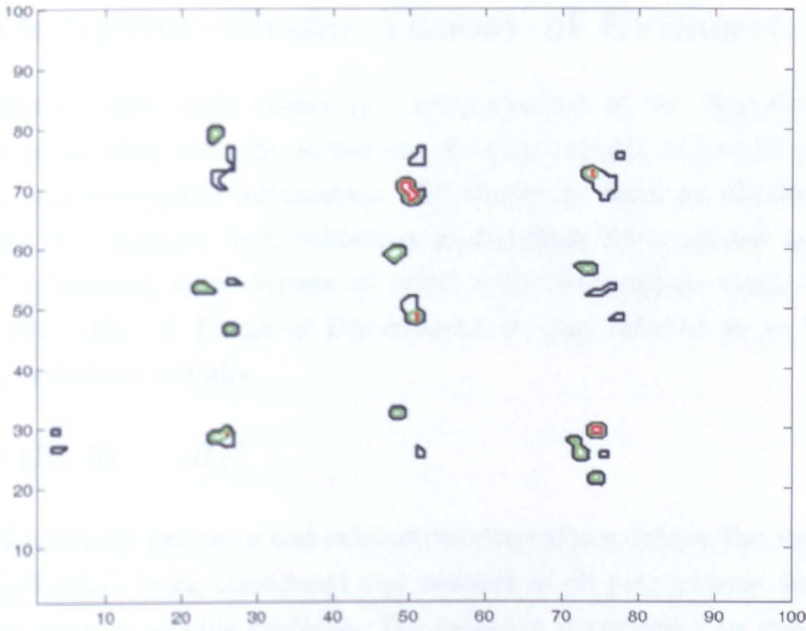
Figure 6.7: Result of Bayesian data fusion of Lamb Wave and EC scan.

TP = 0.9	FP = 0.1
FN = 0.1	TN = 0.9

Table 6.3: Confusion matrix for data fusion of the Lamb Wave sensor taking the uncertainty of the positioning system into account.

the aluminium plate. The confusion matrix for the US inspection is shown in Table 6.3. As in Fig. 6.6, the red lines indicate areas with a probability of 33 $P(H_0)$, and the areas marked by green lines have a posterior probability of containing a defect of

$$P(H_0 \mid E) = 2.24 \ P(H_0).$$

For the areas within the blue lines

$$P(H_0 \mid E) = 0.45 \ P(H_0),$$

and in the remaining white areas the probability of a defect being present is 36 times lower than before the inspection.

138

6.3 Dempster–Shafer Theory of Evidence

The Dempster-Shafer (DS) theory is a generalisation of the Bayesian theory of subjective probability with the advantage of being capable of handling uncertain, imprecise, and incomplete information. DS theory is based on obtaining degrees of belief for one question from subjective probabilities for a related question and a rule for combining such degrees of belief with independent items of evidence [99, 100, 101, 118]. A Frame of Discernment Θ, also referred to as Universe of Discourse, is defined initially:

$$\Theta = \{H_1, H_2, \cdots, H_N\} \tag{6.4}$$

This set of mutually exclusive and exhaustive alternatives defines the working space for the application being considered and consists of all propositions for which the information sources provide evidence. The evidence is expressed by mass-values m, which can also be distributed on subsets of the frame of discernment $A_i \in 2^\Theta$. These mass-values of subsets of Θ have to satisfy the conditions

$$0 \leq m(A_i) \leq 1, \qquad m(\phi) = 0 \tag{6.5}$$

and

$$\sum_{A_i \in 2^\Theta} m(A_i) = 1. \tag{6.6}$$

$m(A_i)$ represents the strength of evidence of a single hypothesis H_i or a union of hypothesises H_i. The exact belief in the proposition is represented by A. With these mass distributions, the belief and plausibility functions can be defined to assign a measure of the total belief and disbelief to each proposition represented by the subset of Θ:

$$Bel(A_i) = \sum_{A_j \subseteq A_i} m(A_j) \tag{6.7}$$

$$Pls(A_i) = \sum_{A_j \cap A_i \neq \phi} m(A_j) \tag{6.8}$$

with

$$Pls(A_i) = 1 - Bel(\bar{A}_i). \tag{6.9}$$

While the belief function *Bel* represents the minimum uncertainty value about A_i, the plausibility *Pls* is a measure of the maximum uncertainty value about this hypothesis and expresses how much belief is in A if all currently unknown facts were to support A. These two measures are also referred to as upper and lower probability functions and span the evidential interval $[Bel(A_i); Pls(A_i)]$. $Bel(\bar{A}_i)$ is the disbelief or doubt. For example, if tomorrow's weather forecast predicted a sunny day and one could believe this particular forecast to 80%, the evidential interval (EI) for a sunny day tomorrow was [0.8; 1]. If one cannot belief in the forecast there is no information — it could be sunny or not. This is the basic difference to the standard probability approaches, where the remaining 20% are assigned to the complementary hypothesis rather than to the frame of discernment.

In order to derive the mass distribution $m = m_1 \oplus m_2$ that contains the joint information provided by two different sources, the mass distributions m_1 and m_2 are combined with Dempster's orthogonal rule:

$$m(A_i) = (1 - K)^{-1} \times \sum_{A_p \cap A_q = A_i} m_1(A_p)\, m_2(A_q) \tag{6.10}$$

where

$$K = \sum_{A_p \cap A_q = \phi} m_1(A_p)\, m_2(A_q). \tag{6.11}$$

This changes to

$$m(A_i) = (1 - K)^{-1} \times \sum_{A_p \cap A_q = A_i} \prod_{1 \le i \le n} m_i(A_i) \tag{6.12}$$

with

$$K = \sum_{A_p \cap A_q = \phi} \prod_{1 \le i \le n} m_i(A_i) \tag{6.13}$$

for more than two sources. K can be interpreted as the measure of conflict between the two sources. The larger K, the more conflicting they are and the less sense their combination. If $K^{-1} = 0$, $m_1 \oplus m_2$ does not exist and m_1 and m_2 are called totally or flatly contradictory. $(1 - K)^{-1}$ in Equations 6.10 and 6.12 then serves as a normalisation term.

For the inspection of the steel and aluminium plates, the frame of discernment for

each pixel on the plates is:

$$\Theta = \{\text{defect}, \text{no defect}\}. \tag{6.14}$$

A basic probability assignment of 60% is designated to the results of EC, US and MFL inspection for easier interpretation of the resulting evidential interval and to avoid combining two high and inconsistent mass values. The mass distribution for fusing the EC and the MFL scan thus is:

	$m_{ec}(A_i) = 0.6$	$m_{ec}(\Theta) = 0.4$
$m_{mfl}(A_i) = 0.6$	0.36	0.24
$m_{mfl}(\Theta) = 0.4$	0.24	0.16

This yields, for positions where both MFL and the EC scan report identical results, an evidential interval of [0.84; 1] for this particular coordinate. So for the white regions in Fig. 6.8 there is 84% evidence that there is no defect at these positions with a plausibility of 100% supporting this conclusion. Similarly, the red areas mark defective regions with 84% evidence and 100% plausibility. The blue lines indicate regions where a defect has been detected with only one method but not with the other. Hence, according to Equation 6.10, after normalisation this yields an evidential interval of [0.375; 0.625]. With an evidence of 37.5% and a plausibility of 62.5% there is a defect present. The ignorance is 25% and the disbelief 37.5%, as there is no information about which one of the two results is erroneous.

Fig. 6.9 shows the fused image of the Lamb Wave and the EC scan of the aluminium plate. The mass distribution is identical to the fusion of the EC and MFL scan above. As in Fig. 6.8, for the white regions there is 84% evidence that there is no defect at these positions with a plausibility of 100% supporting this conclusion, and the red areas mark defective regions with 84% evidence and 100% plausibility. The blue lines indicate regions where with an evidence of 37.5% and a plausibility of 62.5% there is a defect present.
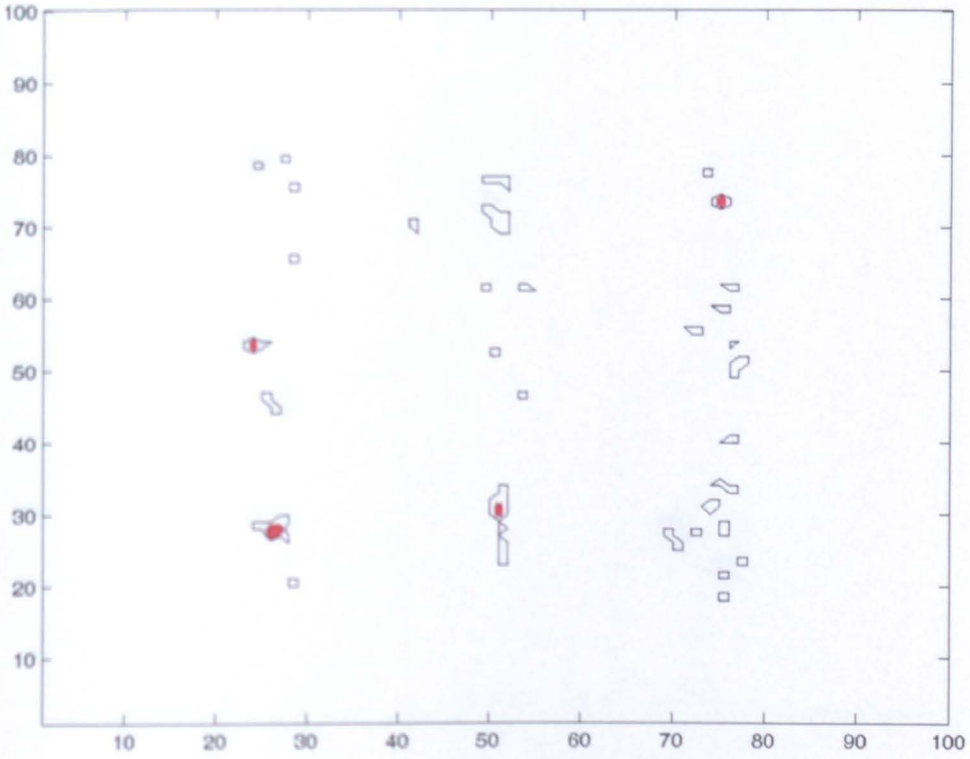
Figure 6.8: Result of Dempster-Shafer data fusion of MFL and EC scan.
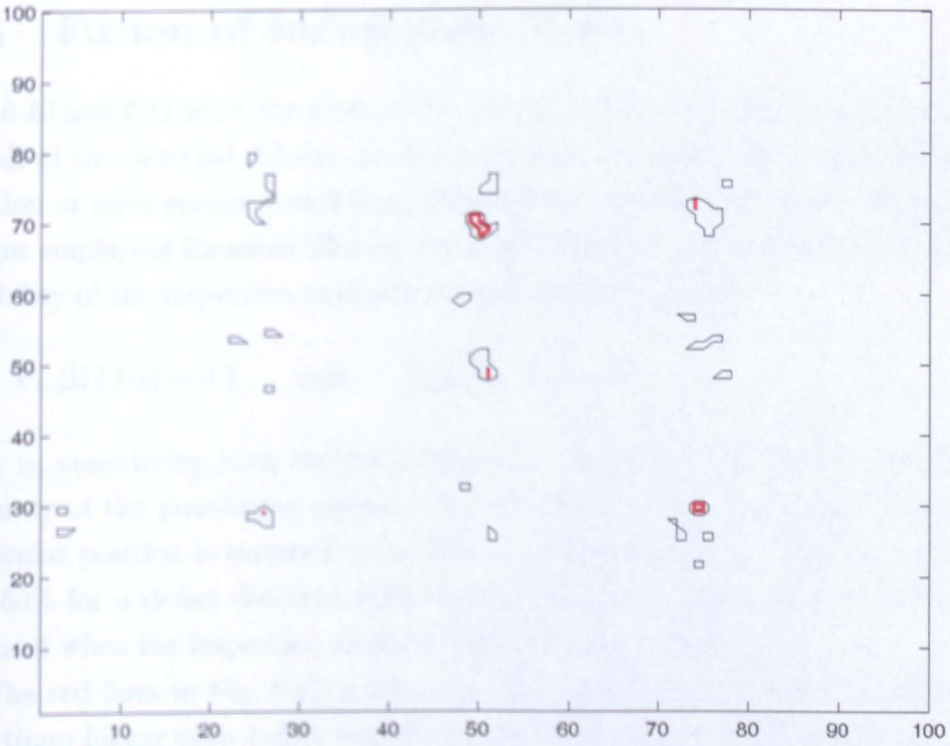
Figure 6.9: Result of Dempster-Shafer data fusion of Lamb Wave and EC scan.

142
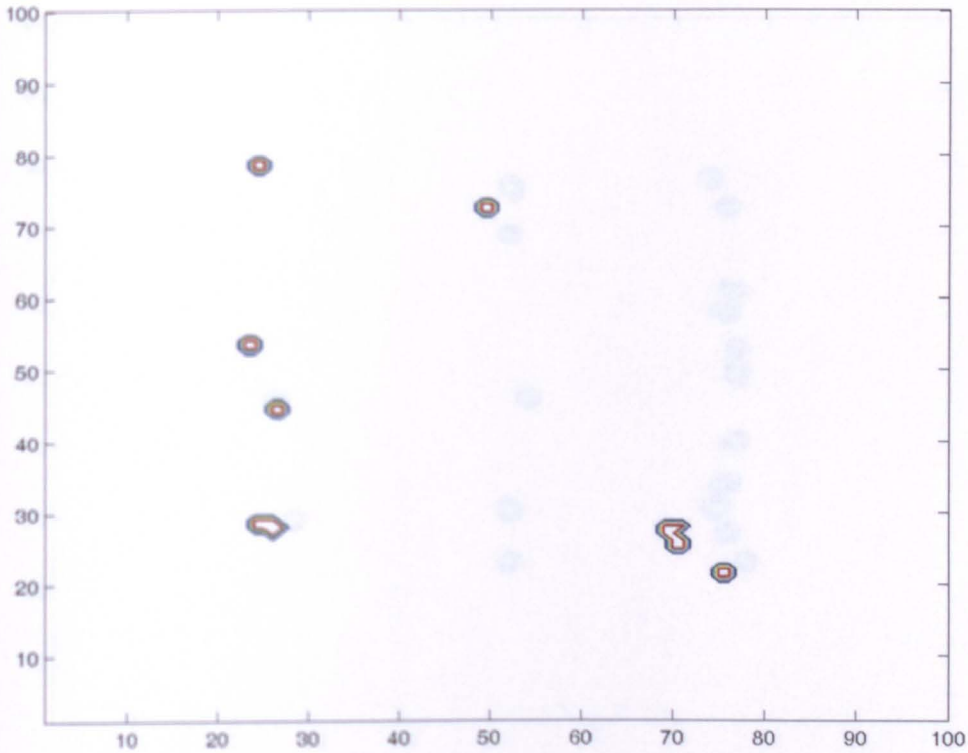
Figure 6.10: Result of incomplete EC scan, top view.

6.4   Fusion of Incomplete Data

Fig. 6.10 and 6.11 show the plots of the EC and MFL scan with a random selection
of half of the detected defects, simulating a scenario where due to insufficient cal-
ibration or poor surface conditions, some defects remain undetected. Fusing these
images employing Bayesian Theory yields the results shown in Fig. 6.12. The lower
reliability of the inspection methods is taken into account by:

$$P_{ec}(E \mid H_0) = 0.7 \quad \text{and} \quad P_{mfl}(E \mid H_0) = 0.6.$$

That is, considering both the performance of the actual NDE sensor and the un-
certainty of the positioning system, the probability of a defect being present at a
particular position is assumed to be 70% for a positive result of the EC inspection
and 60% for a defect detected with the MFL payload. Identical probabilities are
assumed when the inspection methods report flawless positions.

The red lines in Fig. 6.12 mark areas that contain a defect with a probability
1.55 times higher than before inspection, while the blue lines indicate regions with

143
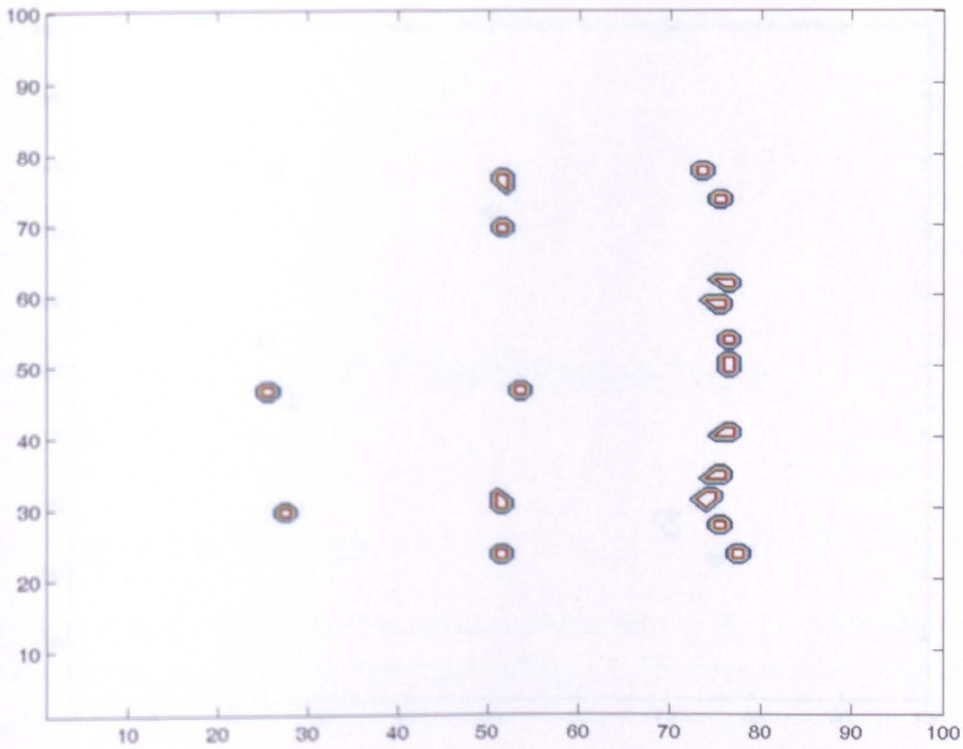
Figure 6.11: Result of incomplete MFL scan, top view.

a posterior probability of

$$P(H_0 \mid E) = 0.64 \ P(H_0).$$

In the remaining white areas in Fig. 6.12, where both inspection techniques do not report a defect, the probability of a defect being present is 3.5 times lower than before inspection.

Employing DS Theory for data fusion of the incomplete scans yields the result shown in Fig. 6.13. The green lines mark areas where with an evidence of 37.5% and a plausibility of 62.5% there is a defect present. The remaining white areas contain no defect, with an evidential interval of [0.84; 1].
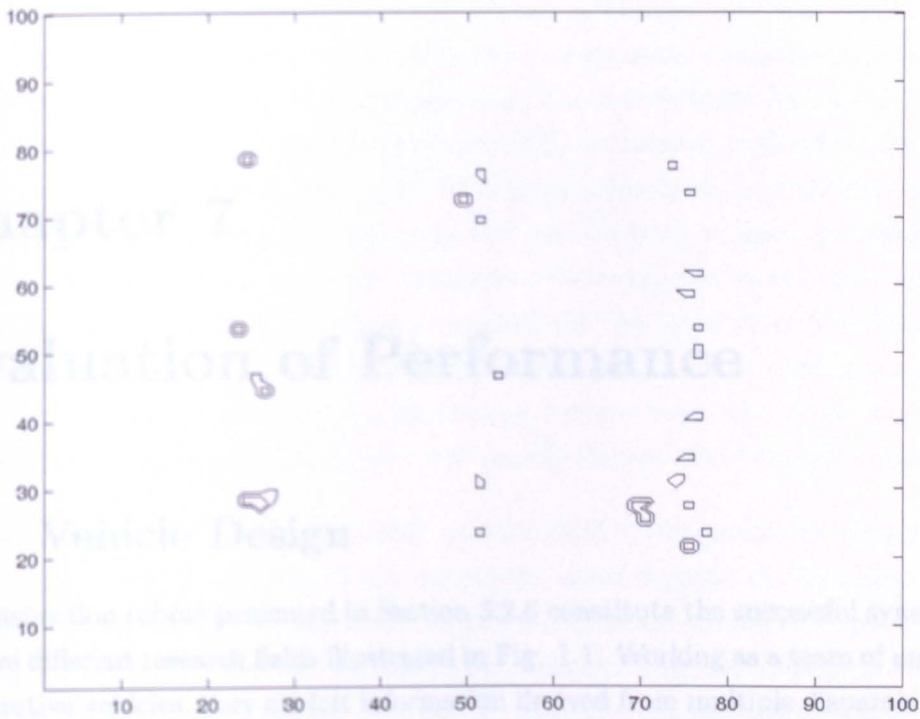
Figure 6.12: Result of Bayesian data fusion of incomplete MFL and EC scans.
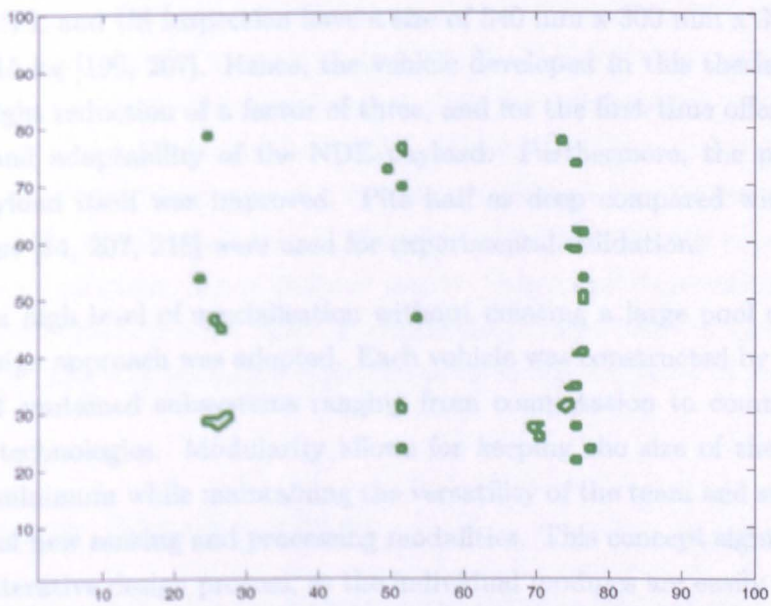
Figure 6.13: Result of Dempster-Shafer data fusion of incomplete MFL and EC scans.

145

Chapter 7

Evaluation of Performance

7.1 Vehicle Design

The inspection robots presented in Section 3.2.6 constitute the successful synergy of the five different research fields illustrated in Fig. 1.1. Working as a team of multiple cooperative vehicles, they exploit information derived from multiple disparate viewpoints simultaneously, thus perform tasks faster and more efficiently than a single unit while also being able to compensate for individual failures. The hardware cost per vehicle is approximately £300 excluding the positioning system, while standard commercial NDE equipment cost is in the order of £20K [266]. Typically, NDE robots for MFL and US inspection have a size of 540 mm x 300 mm x 300 mm and a weigh of 15 kg [190, 207]. Hence, the vehicle developed in this thesis achieves a size and weight reduction of a factor of three, and for the first time offers complete autonomy and adaptability of the NDE payload. Furthermore, the performance of NDE payload itself was improved. Pits half as deep compared with previous investigations [54, 207, 215] were used for experimental validation.

To achieve a high level of specialisation without creating a large pool of robots, a modular design approach was adopted. Each vehicle was constructed by assembling a set of self contained subsystems ranging from computation to communications and sensor technologies. Modularity allows for keeping the size of the individual robots to a minimum while maintaining the versatility of the team and supports the integration of new sensing and processing modalities. This concept significantly enhances the iterative design process, as the individual modules are easily replaceable for repair and test purposes.

A major requirement was small overall size to allow for application in areas which are difficult to access. For this reason, the wheels are mounted directly on the

output shaft of the motor-gearbox unit without additional and fault prone bevel gears, thus minimising the number of power transmission components. In order to reduce vehicle width in this arrangement, the motor units had to be as flat as possible to fit both the encoder and the MFL inspection payload on the same vertical axis. Ultrasonic motors were considered initially as a propulsion source, as they offer high power to weight ratio and can be used without gearboxes due to their high torque at low angular velocities. However, due to low efficiency and the large amount of drive electronics required for this type of motor, small DC motors were preferred. Similarly, stepper motors, which have a compact design and operate without encoders and gearboxes, require twice the power and drive electronics compared with DC motors and usually do not offer continuous rotation.

A brass extension on the output shaft was designed to magnetically decouple the motor units from the wheels. This component takes account of the difference in diameter of the code wheels and disc magnets and provides an effective shoulder for the wheels. A firm connection between this extension and the shaft is established by grub screws to avoid backlash between the output shaft and the encoders, which would affect precise motor control.

The propulsion system of mobile robots is by far the greatest consumer of energy, hence the main disadvantage of using gear heads is the reduction in motor efficiency. The units presented in Section 3.2.5.5 decrease the efficiency to 53%, but are necessary to provide sufficient torque and generate the desired travelling speed of the robot. The overall locomotion mechanism, with the arrangement and number of wheels as described in Sections 3.2.1 – 3.2.4, was successfully tested on a variety of three dimensional test specimens and surface conditions. Due to the high chassis clearance and the short overall length, the vehicles are theoretically capable of coping with steps and stairs, fins in hulls of vessels, bulges and depressions. However, as highlighted in Section 3.2.6, there is insufficient friction between the wheels and the surface, so that the minimum required radius of these corners in practice is 40 mm.

7.2 Power Management

Li-Po batteries currently offer the highest energy densities [41] and are commercially available as cells with a nominal voltage of 3.7V. As described in Section 3.2.5.3, three of these cells are serially connected as the main power source providing 11.1V for more than three hours. The voltage of a fully charged Li-Po cell is 4.2V and
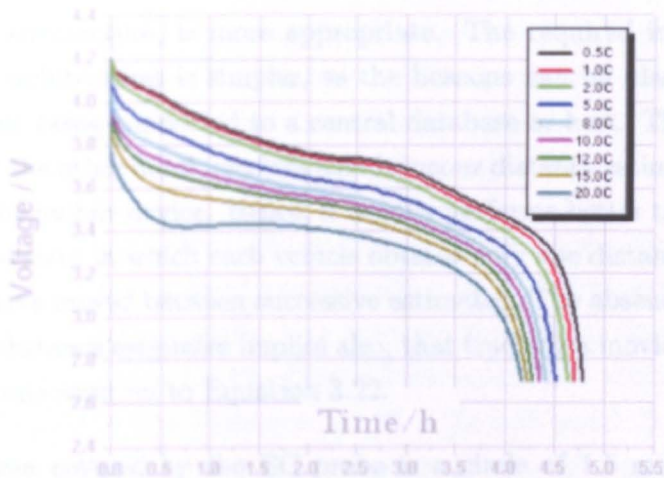
Figure 7.1: Discharge curve for single Kokam Li-Po cell [283].

it displays the discharge rate characteristics as shown in Fig. 7.1. While the drop below 12V after 25 minutes of operation does not affect the motors or the telemetry module, it has serious implications for the NDE sensors, in particular the MFL drive circuitry. For measuring the magnetic field strength, the output of the Hall Elements is directly proportional to the supply voltage. Hence, for reliable operation over the entire battery discharge cycle, a regulated 12V supply is required. According to Fig. 3.9, this component must supply up to 300mA in total.

The overall concept of utilising a three cell Li-Po battery as the main source and generating further regulated positive and negative supply voltages by DC-DC converters, such as the MAX660, MAX 638 or the TC1044S IC, proved to be the optimal solution with regard to miniaturisation, efficiency and weight reduction. However, implementing a low battery detection circuit is essential to prevent damage of the Li-Po cells, as explained in Section 3.2.5.3.

7.3 Vehicle Positioning

The implementation of two separate positioning systems as detailed in Section 3.3 allows for reliable control of the robotic team, as the on-board PI-loop for straight line and velocity control reduces the communication requirements significantly to higher level commands. However, for a high number of inspection vehicles with active beacons, a contention of the ultrasound channel of the absolute positioning system may occur [289]. In this case, a mobile architecture with the listeners on the vehicles and the active beacons on the fixed reference frame, referred to as

passive mobile architecture, is more appropriate. The required infrastructure for passive mobile architectures is simpler, as the beacons can be placed at arbitrary positions without being connected to a central database or host. The active mobile architecture, on the other hand, receives simultaneous distance estimates at multiple receivers from the mobile device. Hence, it usually performs better tracking than the passive mobile system in which each vehicle obtains only one distance estimate at a time and may have moved between successive estimates. The absence of guaranteed simultaneity of distance estimates implies also, that tracking a moving object entails more than just one solution to Equation 3.22.

The effective area covered by the EC probe is a circle of 1.5 mm diameter, the width of the ferrite core. For EC scans with a preprogrammed search pattern, the accuracy of the positioning system is hence insufficient, as the scan regions would have to be exactly 1 mm apart. Furthermore, the lack of orientation information of the absolute positioning system poses severe limitations on the 'target mode', as described in Section 3.4.3. Alternatively, the orientation of the robot could be obtained by determining its position at the two different points in time t_1 and t_2. If these positions are 100 mm apart within the circular area of 50 cm around the point of highest accuracy, the resolution would theoretically be 1.5°, with the frame positioned 80 cm above the surface. With the variance of the position measurement in this area being reduced to less than 3 cm by using the average value of five distance samples for static measurements or by implementing a Kalman Filter, as described in Section 3.3.3.4, the vehicle's orientation could be determined even more exactly.

Independent from the beacon and listener system, the performance of the odometric position measurement has been improved by calibration based on the UMBmark experiment, as shown in Section 3.3.2. The individual contribution of the two dominant systematic errors, as described in Section 3.3.2.3, was measured and their effect was compensated by varying the parameters in the on-board software. However, the code wheel is located on the output shaft of the gear head, which limits the resolution of the encoder to 300 pulses per wheel revolution. This limits the response time of the internal control loop, and deviations up to 3 mm from the ideal straight path may occur. Furthermore, the performance of the gyroscope, the second component of the relative positioning system, can be improved. The A/D port of the micro controller only supports 8-bit conversion, which together with the integration error yields an accuracy for turning manoeuvres that is of the same order than the accuracy, which can be achieved by deriving the changes in orientation

from the number of encoder pulses and the wheel diameter. A more powerful micro controller supporting 10-bit A/D conversion would significantly improve the quality of the gyroscope data, and could also be utilised to implement a Kalman filter for fusion of gyroscope and encoder readings.

Despite these limitations however, the solution proposed in Section 3.3 was proven to be sufficient for the current developmental state, in particular under consideration of the cost of commercially available high accuracy positioning systems, which may be as high as £10K – £20K for the fixed infrastructure and additional £2.5K for each robot [285]. As shown in Figures 4.7, 4.10, 5.25, 5.26 and 5.28, it is well suited for obtaining the position information necessary to produce plots of the defects with reference to the investigated specimen.

7.4 NDE Payload and Inspection Results

Both MFL- and EC inspection offer different advantages depending on the particular application and the material of the specimen. As shown in Chapters 4 and 5, shallow pits and thickness loss are easily detectable with the MFL method, while the EC sensor shows superior performance at small deep defects and cracks. If the critical flaw size is less than 2.6 mm, it is possible that its position may be precisely in the gap between two sensing elements of the linear Hall array, it may therefore remain undetected. In this case, with a sensitive area of 5 mm x 5 mm, the MFL inspection method is three times faster than an EC scan. However, if the defect is greater than this, MFL inspection can be as much as thirteen times faster than the EC method, where the effective area covered by a single scan is just 1.5 mm wide. The EC probe is also less suitable for curved surfaces and pipes of small diameters, as the sensor head consists of a 5 mm x 10 mm sensor flat area. Additionally, the sensitivity of the EC sensor can be improved, as the current coils have been manufactured manually and hence are not precisely matched.

For MFL and EC inspection a constant minimum sensor lift-off is essential. Keeping the probe in contact with the surface utilising the spring loaded lever design has proven to be an effective solution for both methods. However, as the inspection of the steel plate described in Section 5.4.3 shows, false positives in the proximity of defects may occur when the castor wheel passes through one of the artificial pits, causing a change in lift-off distance of the Hall plates.

The two reported false positives which have occurred during the upside down MFL

inspection described in Section 5.4.4 indicate that this technique is less robust compared with the EC method, even though the electronic drive circuitry is significantly simpler. For both inspection methods, an initial calibration of the payload on a mock-up defect is required prior to optimum autonomous operation, to set the value for the criterion in Fig. 2.3. True Positives can be detected with a probability close to 100% with the number of False Negatives being zero, when the vehicles are calibrated on explicitly smaller defects than the critical ones. For this purpose, the raw NDE signal needs to be sent to the host computer. The telemetry module adds a fixed package overhead of 13.2 ms to all packets sent from the inspection vehicle to the host, which restricts the transmission rate significantly, and only permits a maximum sample frequency of 20 ms. To accomodate a higher sampling rate, a standard RS-232 wire is required for this initial calibration and the converted analogue input voltage of the NDE sensors is sent to the host as an 8-bit value, where it is stored for analysis and interpretation. Transferring the value to the host via the continuously open COM1 port takes approximately 3 ms, which has to be compensated for by a 3 ms sleep command when the vehicle is performing the inspection without transmitting the raw NDE data to the host.

A major advantage of the US sensor is the suitability for a wider range of materials, and the capability of detecting defects within the test structure. Utilising Lamb Waves, thin plates and pipes can be inspected with minimum inspection time, as shown in Section 5.6. Contrary to Visual Inspection, US inspection is sensitive to different kinds of defects within the material, and is therefore the ideal technique to complement the EC and MFL payload. However, the main challenge is the development of the extensive drive electronics for autonomous battery powered operation.

As shown in Fig. 4.5, the EC sensor is sensitive to 0.3 mm wide cracks, and 0.15 mm deep simulated corrosion pits are detected with a probability of 90%, as presented in Section 4.5.3. Large scale NDE devices, like trolleys that contain heavy-duty magnets for inspecting steel floors, as presented in [20], are usually tested with defects with a minimum depth of 0.5 - 2 mm and diameters ranging from 0.34 mm to several millimeters [55, 158]. The main objective of the robotic team, the reliable detection of real world defects on engineering structures, has hence been successfully achieved.
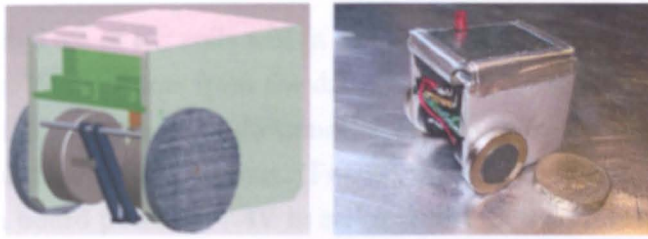
Figure 7.2: 31 x 33 x 35 mm prototype.

7.5 Graphical User Interface

The Graphical User Interface presented in Section 3.4.1 provides convenient testing and robot path plotting facilities while leaving the user to decide about the degree of robot autonomy offering Manual Control, Target- and Autonomous Scan Modes. The current 3D coordinates of each robot, displayed at the top left corner of the interface, is updated every second with the trilaterated position estimate. In particular the fluctuations of the vehicles' z-position, which is calculated utilising the fourth power of the erroneous distance samples d_1, d_2 and d_3 of Equation 3.25 in Section 3.3.3, could be reduced by implementing an outlier rejection routine. The latest cricket distance measurement in such a routine is compared with the previous four to detect obvious incorrect measurements. Smoothing the trajectory even further can be achieved by utilising the average value of these five recent distance measurements for trilateration. Furthermore, by accessing the three serial ports actively rather than waiting for the latest distance sample to be sent to the host, as described in Section 3.4.2, the routine is not affected by the possible absence of a signal of a particular beacon, which may be temporary out of the direct line of sight.

7.6 Alternative Design Concepts

In addition to the inspection vehicle presented in Section 3.2.6, two alternative design concepts with absolute priority on miniaturisation and on weight reduction were investigated for evaluation purposes. Figures 7.2 and A.34 show a size reduced vehicle for EC inspection. It is based on a Microstamp-11 micro controller, a 35 mm x 25 mm board with the HC11 processor described in Section 3.2.5.1. Hence, no additional compiler software is required and the C-code presented in Section 3.5 can be used. The main wheels are two 3 mm thick disc magnets with an outer diameter of 19 mm and an inner diameter of 12 mm, while the third support point is a rounded brass stud in the back of the robot, shown in Fig. A.36. Surface inspection

is performed with a set of EC coils with a ferrite core of 0.75 mm on a pivoted lever, illustrated in Fig. A.39. Apart from the drive circuitry for this NDE payload, which could be easily integrated as an additional layer on top of the motor driver board, the vehicle is completely autonomous. Two 60 mAh Li-Po cells, 13 x 22 x 4.5 mm each, provide on board power at 7.4V in series, which is transformed to +5V by the regulator of the controller board. As visible in Fig. 7.2, the two main boards form an integral part of the robot chassis together with the vertical aluminium plates on the sides.

Due to the severe size constraints, this prototype does not contain a positioning module, wheel encoders or a gyroscope. Considering its low cost, it is in fact suitable for the swarm coordination approach suggested in [60], where the spatial distribution of multiple vehicles in an environment is modelled by density functions. Instead of knowing the exact position of each individual inspection vehicle, a large number of robots is deployed on the structure under inspection, scanning in a random pattern and indicating detected defects by a full stop and flashing the LED on the top. However, this requires a miniature proximity switch for collision avoidance in the front of the vehicles.

Two 6V DC micromotors serve as propulsion source for the size reduced prototypes. Though offering compact dimensions of 6 mm thickness and 15 mm diameter, their maximum torque of 0.3 mNm is not sufficient for inclined surfaces or vertical walls, and the rotational speed does not allow for slow vehicle movements. Therefore these motors have to be used with integrated gear heads, the 1512 series from Faulhaber [277], for future developments. As there is no space for a ball caster or a castor wheel in the back of the vehicle, adhesion at the third point of contact poses a problem. A sliding magnet increases the friction unacceptably, and with only two magnetic wheels the vehicle is restricted to upwards movements on vertical walls. A further drawback of the miniature design are the less sensitive EC coils. As shown in Fig. 7.3, the change in phase angle above a defect is smaller compared with the larger coils in Fig. 4.5, which necessitates greater complexity in the drive electronics. In general, the miniature prototype of Fig. 7.2 is characterised by severely reduced functionality and reflects the limit of the current departmental manufacturing capabilities.

Hence, a weight optimised prototype was designed for investigating the potential for applying one of the alternative adhesion techniques presented in Section 2.3, which require the vehicle to be as light as possible. Experiments with double sided tape glued onto the wheels of the vehicle in Fig. 3.15 have shown, that the robot may
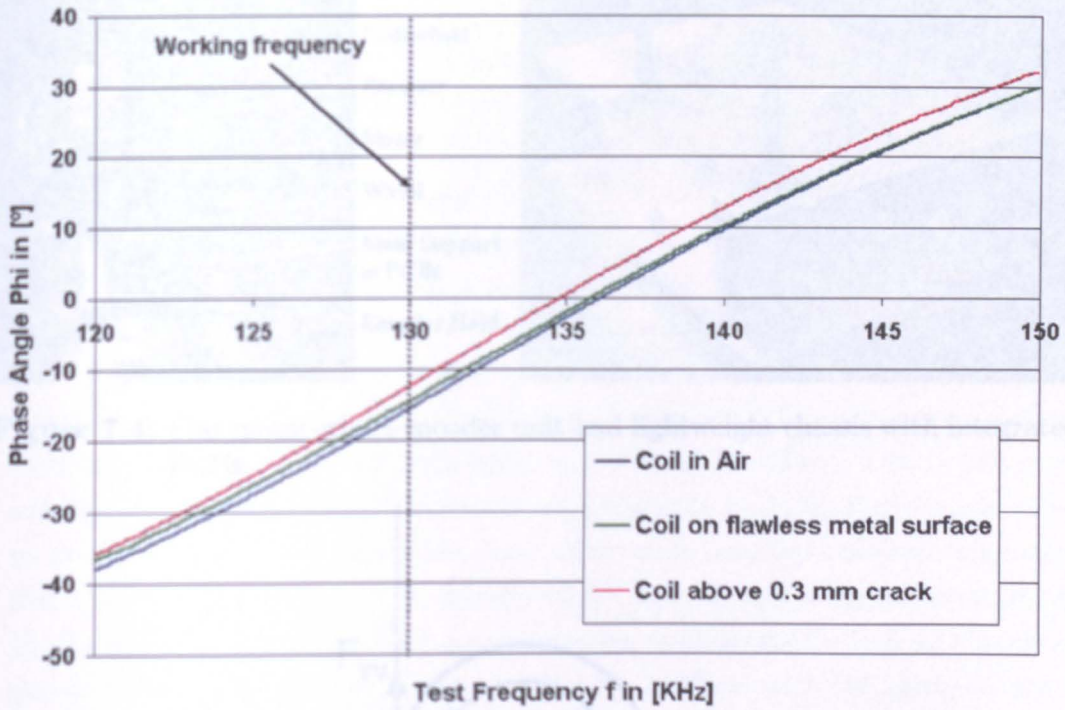
Figure 7.3: Effect of lift-off and crack on phase angle Phi of EC coils with 0.75 mm ferrite core.

operate on inclined non-ferromagnetic surfaces of up to 45° and adhere statically to vertical walls. However, after approximately five minutes of operation the tape loses its adhesion due to dirt and dust on the test surface. The lighter the robot, the better the performance. According to Fig. 3.10, the magnetic wheels and the aluminium frame with the shaft extensions contribute 37% to the overall robot weight. For this reason, the PCBs are used as supporting structures and lightweight motor-wheel-encoder units were developed, as shown in Fig. 7.4. Without gearheads however, the motors suffer from similar drawbacks to the ones of the size optimised prototype previously discussed. In these configurations the robots neither support autonomous floor to wall transfers nor continous inspection of three-dimensional test structures. In contrast, the design proposed in Section 3.2.6 has proven to be suitable for a large variety of inspection tasks, and therefore further work was focused on the gradual improvement of the vehicle shown in Fig. 3.15.

Due to insufficient friction, a minimum radius of 40 mm is required for autonomous transition of a magnetic floor to a magnetic wall, as described in Section 3.2.6. Fig. 7.5 shows the decomposition of forces which act on the magnetic wheels at the moment of transition at a 90° concave corner. F_{rv} is the vertical frictional force, F_{rh}

154
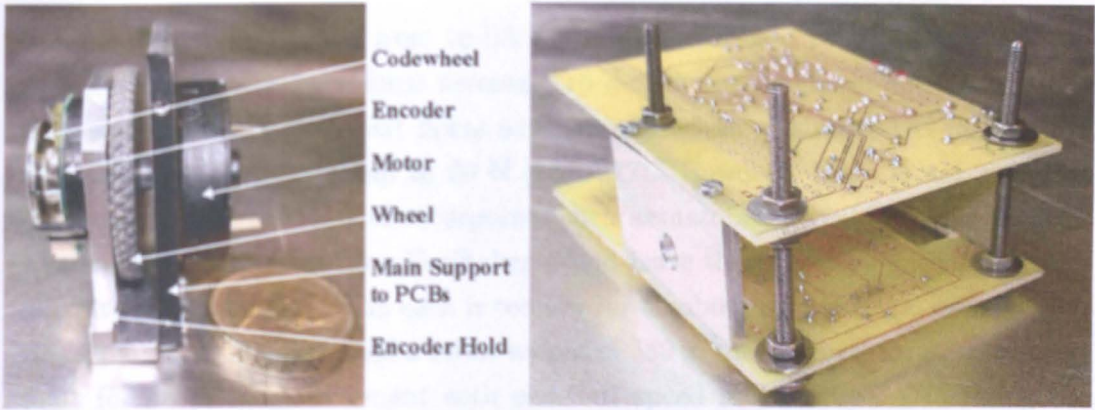
Figure 7.4: Flat motor-wheel-encoder unit and lightweight chassis with integrated PCBs.
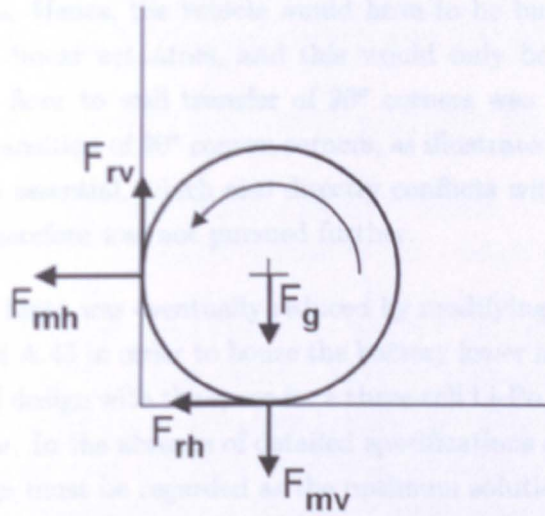
Figure 7.5: Decomposition of forces on magnetic wheel at transition from floor to wall.

the horizontal frictional force and F_{mh} and F_{mv} the horizontal and vertical magnetic forces. For an autonomous transition the following condition must apply:

$$F_{rv} > F_{mv} + F_g \qquad (7.1)$$

The vertical frictional force results from the normal force to the surface, the horizontal magnetic force, and the friction coefficient:

$$F_{rv} = \mu F_{mh}, \qquad (7.2)$$

with the coefficient of friction μ according to Table 3.1. An additional force pointing in the same direction as F_{rv} could be imposed by linear actuators which are mounted

between the motors in the front to lift the vehicle. These actuators would have to provide 50N in total, the force necessary to detach the magnetic wheels from the floor-surface. State of the art linear actuators based on miniature DC motors and a spindle nut offer forces up to 60 N [264, 277]. However, there is not sufficient space between the motors to incorporate such actuators, as visible from Fig. 3.15. The smaller 1512 series from Faulhaber would leave the necessary space, but their maximum torque of 30 mNm each is too low for climbing up a vertical wall. With a wheel diameter of 38 mm and a robot weight of 580 g, the required torque per wheel shaft for an upward movement with constant speed is 55 mNm. Decreasing the wheel diameter would theoretically reduce this number, but as the wheels have to be clearly larger than the outer diameter of the wheel encoders (22 mm), this is no solution in practice. Hence, the vehicle would have to be build significantly wider to incorporate the linear actuators, and this would only be a feasible approach, if the autonomous floor to wall transfer of 90° corners was a major requirement. Similarly, for the transition of 90° convex corners, as illustrated in Fig. 3.17, a higher chassis clearance is essential, which also directly conflicts with the miniaturisation requirement and therefore was not pursued further.

The overall vehicle hight was eventually reduced by modifying the chassis according to Figures A.42 and A.43 in order to house the battery lower in the chassis. Fig. 7.6 shows the improved design with the space for a three-cell Li-Po battery at the bottom centre of the vehicle. In the absence of detailed specifications of the particular NDE problem, this design must be regarded as the optimum solution.

7.7 Data Fusion

Both the MFL scan in Fig. 5.25 and the EC scan in Fig. 4.10 show a representative map of the defects in the test specimen. However, in particular when one of the underlying inspection techniques is characterised by poor reliability and thus defects may remain undetected, a significantly more complete image can be obtained by fusing the data, as presented in Chapter 6. Variations, with regard to the location of defects, may result both from the different sensitivities of the inspection methods and from inaccuracies of the positioning system.

Estimating the a priori probabilities of defect occurrence for Bayesian Analysis, as described in Section 6.2, usually presents a problem for real world situations. In these cases, where no prior knowledge of the specimen and the type of defect is available, it is common practice to assume 50% for $P(H_0)$ [100]. The resulting
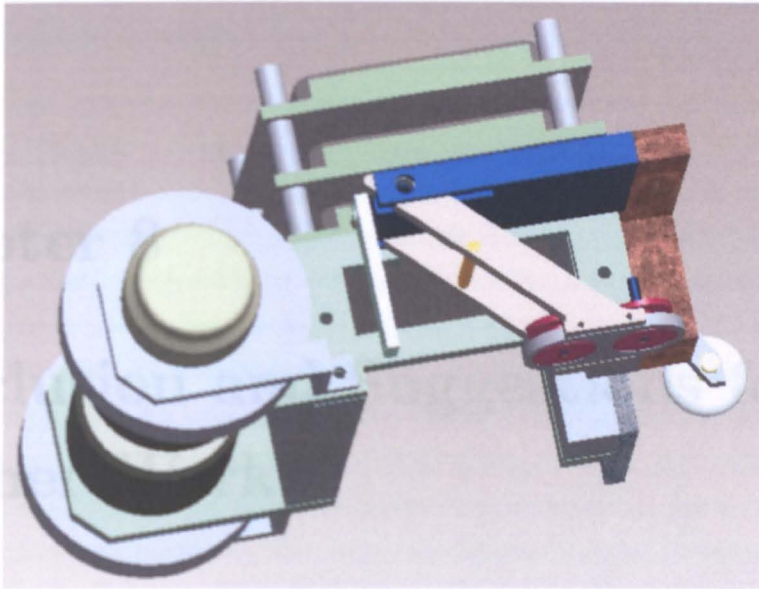
Figure 7.6: Improved vehicle design with lower battery position.

image with this a priori probability shows identical results to Figures 6.6 and 6.7 as the posterior probability is expressed relative to the a priori probability.

Chapter 6 shows that NDE data fusion, in general, improves the confidence in the produced image and assists in decision making when conflicting or uncertain information occurs between the inspection techniques. Displaying the results in a statistical format along with a colour-coded image facilitates signal interpretation and reduces the time investment for a human operator even further.

157

Chapter 8

Conclusion and Suggestions for Further Work

8.1 Conclusions

8.1.1 General Overview

An novel automated inspection system, comprising a team of heterogeneous robots, has been developed and successfully tested under laboratory conditions. The inspection vehicles achieve a size and weight reduction of a factor of three compared with designs that have previously been reported in literature, while for the first time offering complete autonomy and adaptability of the NDE payload. Experiments show that the vehicles are capable of reliably performing a range of inspection tasks and defects of 1 mm size and pits of 0.3 mm depth can be reliably detected. True Positives can be detected with a probability close to 100% with the number of False Negatives being zero, when the NDE payload was calibrated on a defect that is significantly smaller in comparison to critical defects anticipated in the test structure. In addition to plane, two dimensional test specimens, the system is also suitable for three dimensional ferromagnetic structures. The inspection robots exploit magnetic adhesion and offer capabilities for automated transition from horizontal to vertical surfaces. For overall system control, the Graphical User Interface 'RobCon' has been developed, which is running on a host computer and inter-vehicle communication is achieved using wireless links.

8.1.2 System Design

As climbing skills are required in order to cope with a variety of inclined or curved surfaces and ceilings, a compact generic vehicle design has been developed which offers minimum overall size. The prevalence of hard and flat surfaces normally found in the field of NDE has determined the most suitable locomotion mechanism and the optimum type and configuration of wheels. This design involves permanent magnets that provide both the holding force and the source of the magnetic field for inspection with Hall Elements. To employ additional techniques for Ultrasonic-, Visual- and Eddy Current Inspection without creating a large pool of robots, a vehicle base has been developed, which can be equipped with different NDE payloads. Consisting of a number of changeable modules for propulsion, navigation, power management, processing and communication, this approach allows for easy future modifications and simplifies the iterative design process greatly.

Each vehicle is equipped with a miniature gyroscope and a set of optical wheel encoders, which yield the input data for a local PI-control loop. This control loop is running on board to maintain a constant travelling velocity and allow for sufficient straight line accuracy. The performance of this odometry system has been improved significantly by applying the UMBmark calibration routine. After calibration, the centre of gravity of the cluster of clockwise turns of this experiment has been improved from [-65 mm; -49 mm] to [-3 mm; 9 mm]. The main drawback of relative position measurement is the long term inaccuracy, thus an absolute positioning system based on trilateration has been implemented, which utilises the distance measurements between the beacon on top of each robot and three listeners at known locations. The listeners are mounted on a hinged frame and connected to a portable computer to maintain mobility of the system. By utilising these two complementary positioning systems, the communication requirements between the vehicles and the host PC are reduced significantly. Depending on the arrangement of the listeners, an accuracy of up to 0.64 cm can be achieved for the absolute position measurement. The Graphical User Interface, which has been developed and runs on the Host PC, shows the coordinates of each team member and the detected flaws. Automated scans are supported as well as semi-automatic and manual scan modes. Each vehicle can be addressed individually and its 3D path plotted with reference to the origin of the portable frame.

8.1.3 NDE Payload and Results

NDE test equipment for autonomous on board operation has been developed with focus on MFL and Eddy Current Inspection. The differential Eddy Current probe has been developed, which consists of two differential coils operating at resonance at a resonant frequency of 145 KHz, with the main components of the drive- electronics being an on board signal generator and a phase comparator. A significant reduction of overall weight and power consumption of the robots for MFL inspection has been achieved by utilising the magnetic field created by the wheels both for adhesion and as the source field for the NDE signal. A spring loaded lever is essential to maintain constant lift-off of the sensors and highest reliability for MFL and EC inspection has been achieved by initially calibrating the payload on a mock-up defect. The full potential of employing a variety of different NDE methodologies has been exploited by the implementation of data fusion techniques. By simultaneously applying Bayesian Analysis and Dempster-Shafer Evidence Theory to the NDE data, any uncertainties often associated with multiple inspection results have been greatly reduced. This has resulted in the provision of a consistent, more accurate and intelligible data set.

8.2 Suggestions for Further Work

The main purpose of the inspection vehicles is to facilitate reliable NDE. Hence, further work should start with a refinement of the NDE payloads and an improvement of defect sensitivity. In particular, the ultrasonic test system for on board operation requires further development, which should include both small size air coupled transducers and the transmit and receive electronics for lamb wave inspection. To complement this inspection technique and to detect cracks smaller than $300\mu m$, which are found in pressure vessels in nuclear power plants, further work should also focus on the refinement of the circuitry and coils for eddy current inspection. A more compact coil arrangement and a flexible sensor arm supported by a spherical joint could improve the flexibility of deploying the probe, and the use of surface mount components and better matching coils would reduce the space requirement while significantly enhancing the signal to noise ratio of the output signal. Thus, deriving quantitative information and classification of defects is possible. Furthermore, dosing the magnetic saturation from the wheels for MFL inspection and incorporating better visual inspection is essential, as well as performing a systematic set of tests to estimate the confusion matrices in Section 6.2. Eventually, the NDE signal could be identified automatically, as suggested in [158] and [172]. Implementing incremental learning algorithms with confidence estimation, signals generated by potentially critical defects could be automatically distinguished from those generated by benign discontinuities.

The robots and sensors need to be evaluated under real world conditions and the communication and positioning systems tested in industrial environments like storage tanks or pipelines. Utilising more than three listeners for obtaining the absolute position would reduce the limitations that arise from the line of sight confinement of the listener-beacon system. As described in Section 4.5.1, on three dimensional structures the angles of the rotation matrix $R_A^R(\Theta)$ for compensation of the offset between positioning module and actual NDE payload are essential. For this, on board inclinometers could be used as proprioceptive sensors to measure the current inclination when the vehicles are moving along these structures, while a detector in the front of the robot could ensure that the material of the specimen is ferromagnetic to avoid sudden loss of adhesion during climbing. As the navigation problem is not restricted to 2-D space, host and vehicle should also be able to determine how to avoid obstacles, whether to climb over or drive around them. In this regard, cooperative behaviour could be implemented to overcome the friction problem described in Section 3.2.6, by utilising a second team member which pushes temporarily against

161

the back of the vehicle that is about to perform the floor to wall transfer illustrated in Fig. 3.16. In this manner, the normal force against the vertical wall is increased, and with it the vertical friction force F_{rv} in Fig. 7.5. To prevent damage to the main battery, an automated 'return to host' routine could be activated as soon as the voltage drops below 3.4V per cell. Ideally the robots would then automatically connect to a charging station and continue inspection when they are recharged.

In general, further work may cover two areas: Firstly, miniaturisation of the current vehicle design inspired by natural swarms such as termites, wasps and ants. Starting with the size optimised prototype presented in Section 7.6, low cost vehicles could be developed that fit into a $1cm^3$ cube with reduced functionality and limited on board intelligence. Employing recent advances in Swarm Robotics and multi agent systems research, a team of these robots is suitable for inspection of engineering structures with severely restricted accessibility. Due to the size constraints of the vehicle and the physical shape of the test structure, the implementation of a sophisticated positioning systems or navigation algorithms is currently impossible. Instead, a Swarm-Intelligence (SI) based technique could be employed. This statistical approach is characterised by intrinsically probabilistic swarm coordination — robust inspection and coverage of a regular structures is achieved by imitating biological examples provided by swarming, herding and shoaling phenomena of social insects [59]. Programmed with simple behaviours and equipped with a miniature infra red proximity switch in the front for obstacle detection and collision avoidance, a large number of miniature vehicles could be deployed on the structure which return to a marked starting position within a previously defined time frame. The vehicles would stop at defects, indicating the need for closer examination. In addition to the miniature EC coils described in Section 7.6, potential NDE sensors for such miniature robots constitute integrated micro machined silicon Hall-type sensor arrays. These devices for MFL inspection offer an absolute sensitivity of 300 $\frac{mV}{T}$ with a resolution of 32 μT. A 32 x 8 element Hall sensor array covers an area as small as 1 mm^2, with an active area per probe of 6 μm^2 [12, 86, 119].

The second area for further work is the development of a group of remote sensing agents with increased on board computing power that do not require a Host PC for overall system control. While still being of small scale, these robots would offer full sensing, positioning and communication capabilities. Using Wifi or Bluetooth links, team members could exchange information, send support calls to a robot with a more suitable NDE payload where an imperfection is encountered and concentrate their efforts in a particular area. Carrying a novel 50mm x 30mm x 26 mm 'Inerti-

aCam' produced by Intersense [281] as part of the inertial-optical motion tracking system, the six degrees of freedom of each robot could be determined with an orientation accuracy of up to 0.1° and a position accuracy of 2 – 5 mm. This would not only significantly simplify the distributed control of the vehicles, but also allow for collaborative localisation. The fiducials of the position reference system could be carried by the team members themselves. Thus, with individual robots serving as beacons and the remaining vehicles positioned with reference to them, a previously installed infrastructure in shielded or narrow inspection environments would not be required. Furthermore, a collaboration with the miniature vehicles is imaginable. The more intelligent sensing agents could serve as team leaders and organise the positioning of the smaller robots, which are capable of accessing the crucial inspection areas.

Appendix A

Technical Drawings and Structograms

Section A.1 of this appendix contains the general technical drawings for the parts that are identical in all inspection vehicles. Section A.2 contains the specific parts for the Eddy Current Sensor, Section A.3 covers the hold for the Hall Sensor Array, Section A.4 the sensor hold for the US transducers and Section A.5 the hold for the wireless camera. Section A.6 contains the drawings for the miniature prototype, Section A.7 three drawings for an improved vehicle design with a lower battery position and Section A.8 the structograms of the subroutines of the on board program.

A.1   General Vehicle Configuration

Figure A.1: Main Assembly

165

The text content in the title block reads:
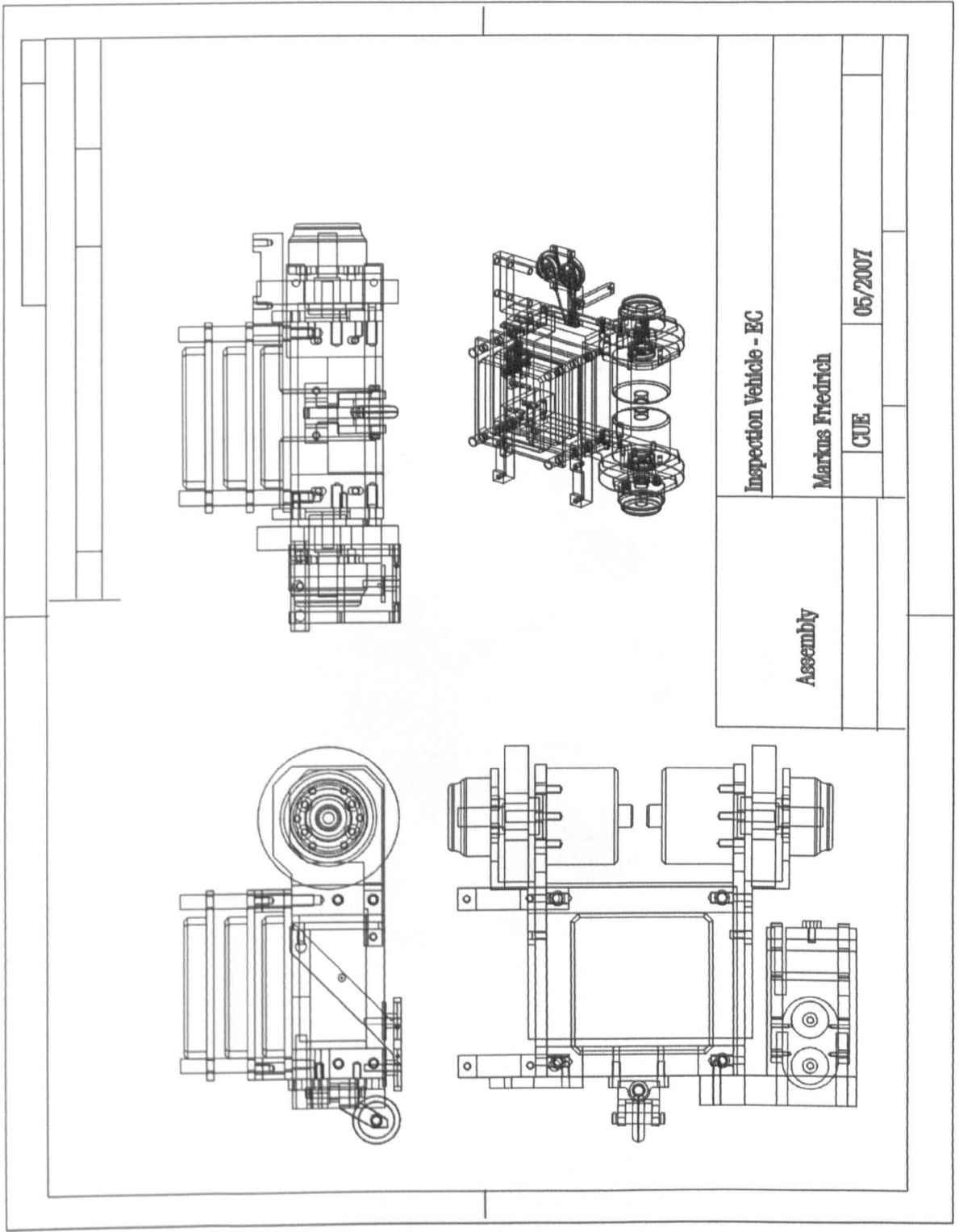
Inspection Vehicle - EC

Markus Friedrich

05/2007

CUE
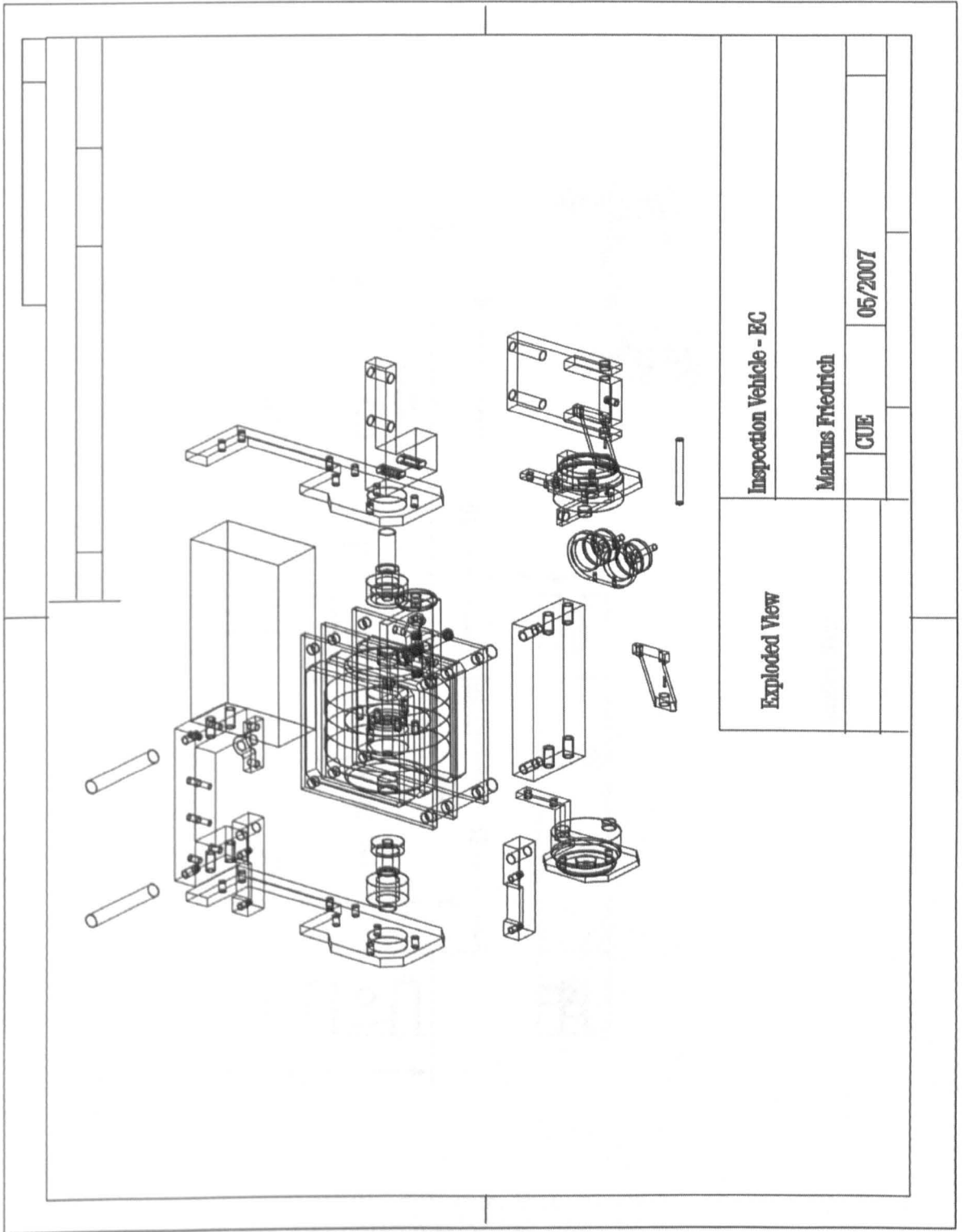
Exploded View

Figure A.2: Main Assembly - Exploded View
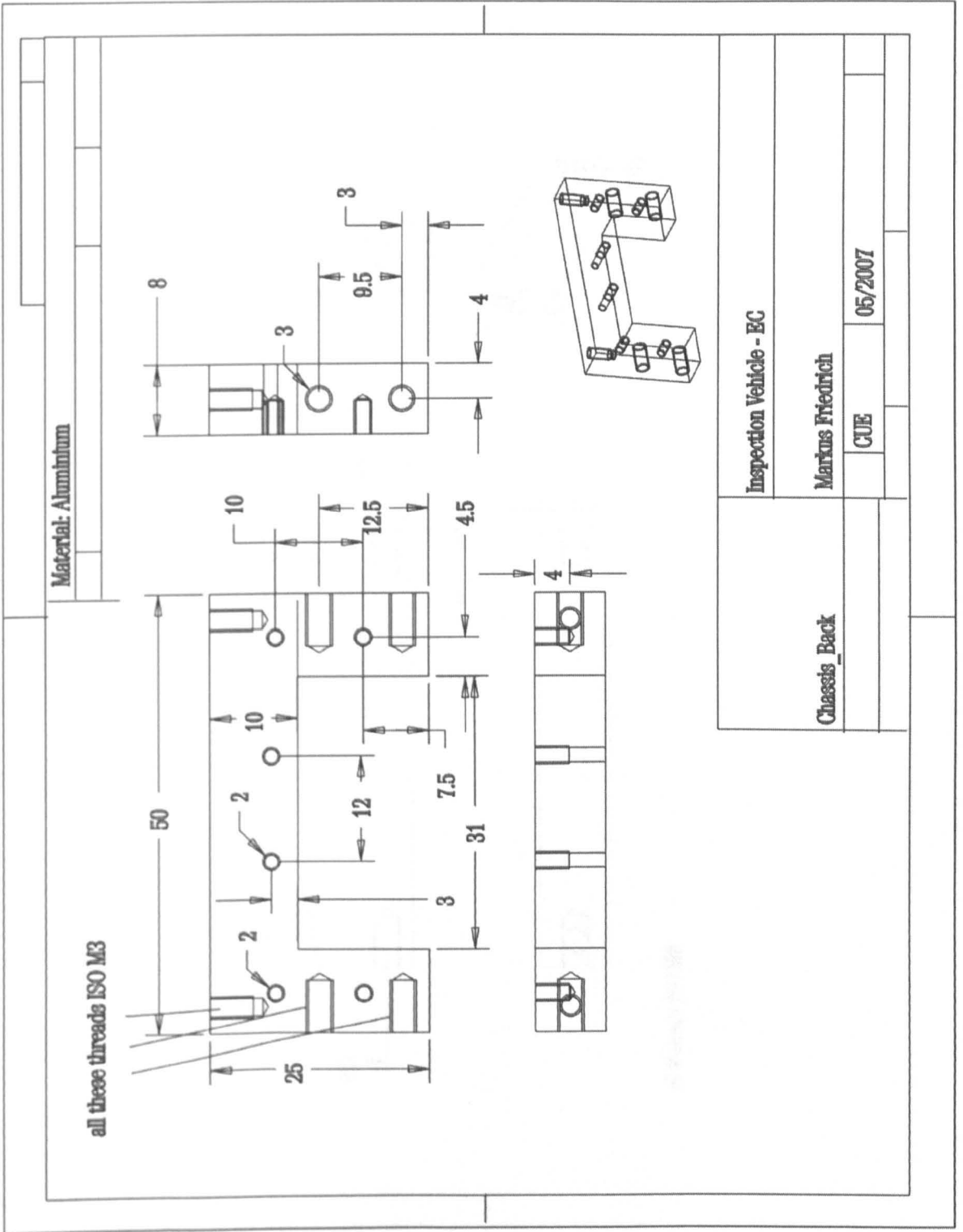
Figure A.3: Chassis - Back Plate
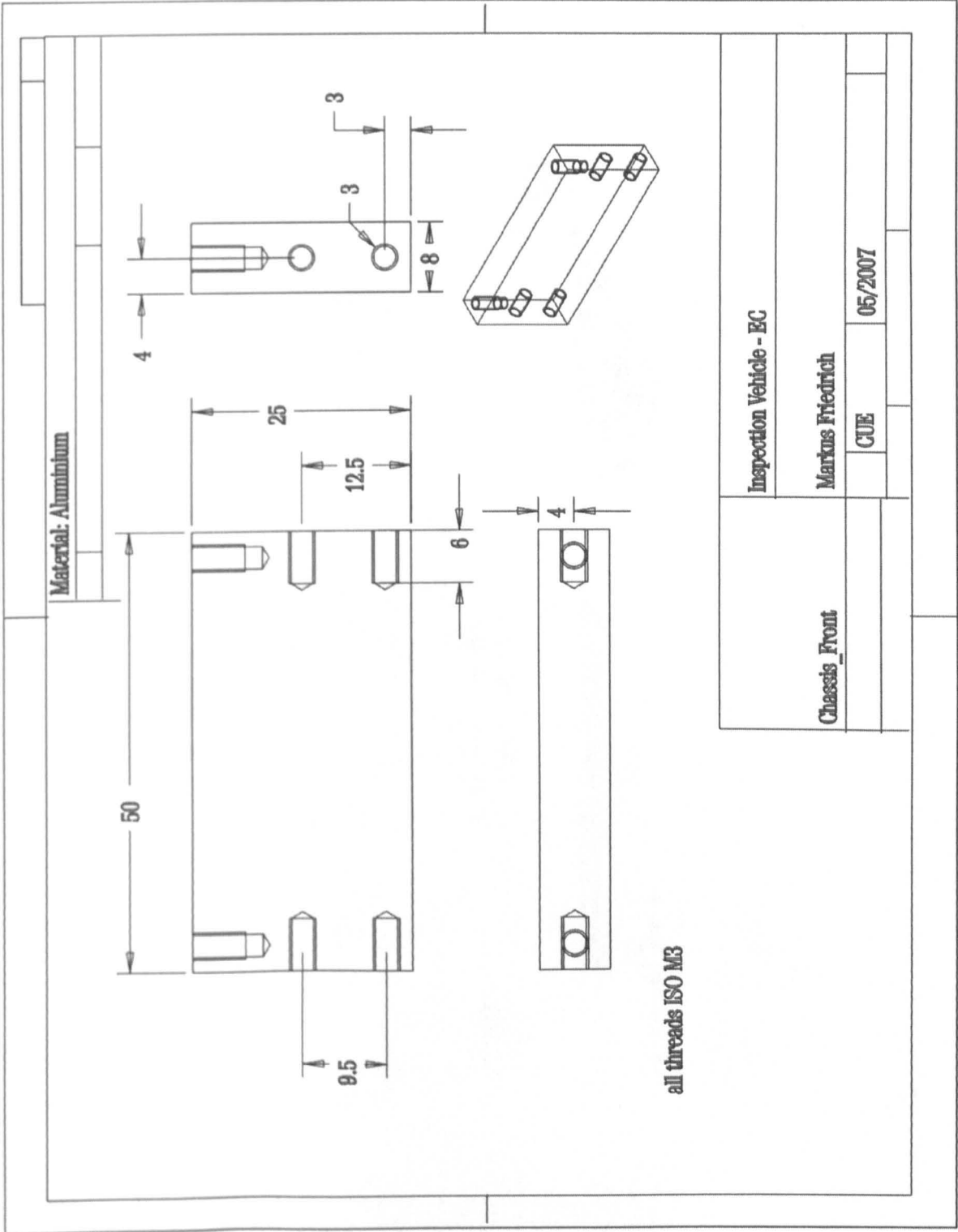
Figure A.4: Chassis - Front Plate
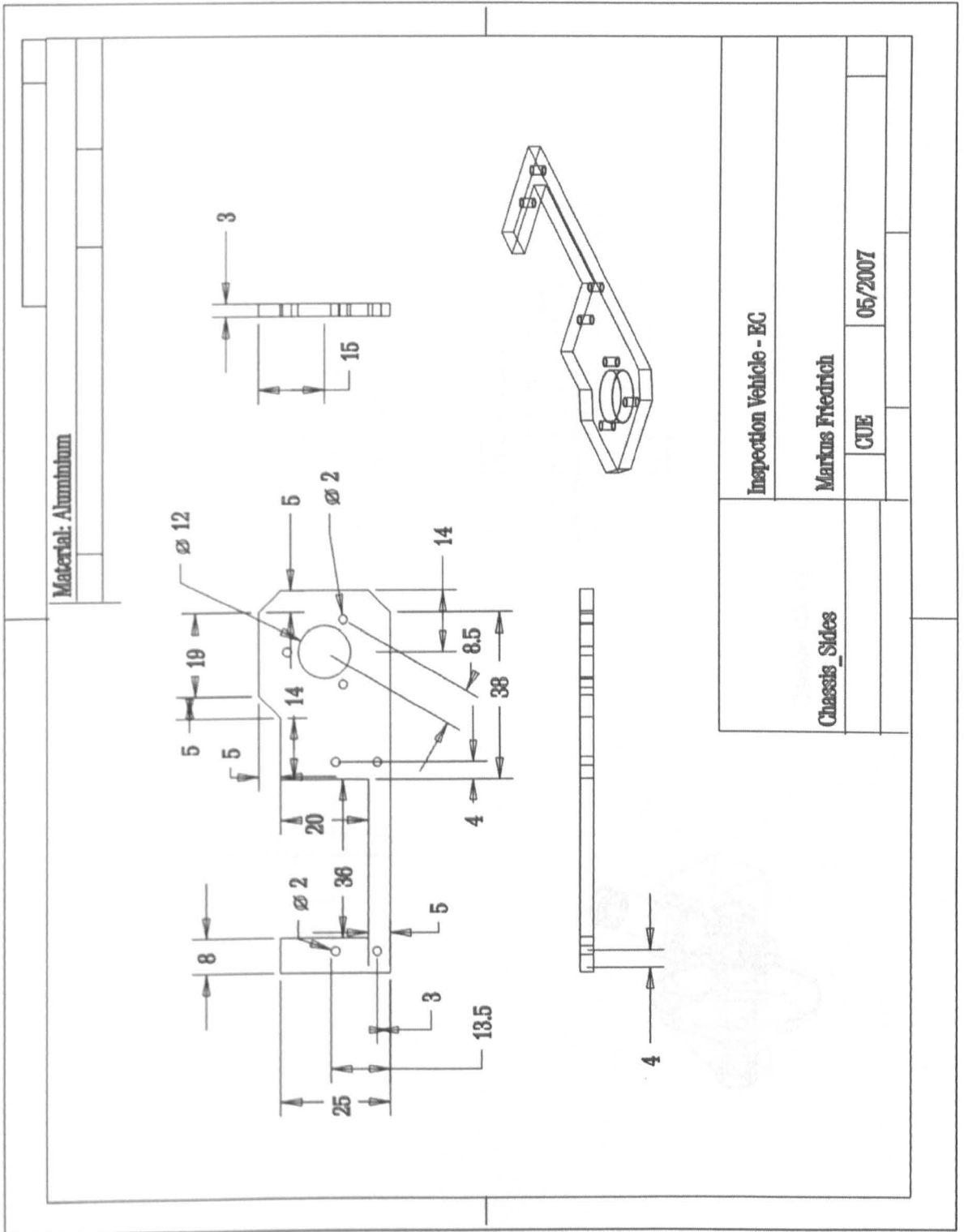
Figure A.5: Chassis - Side Plates
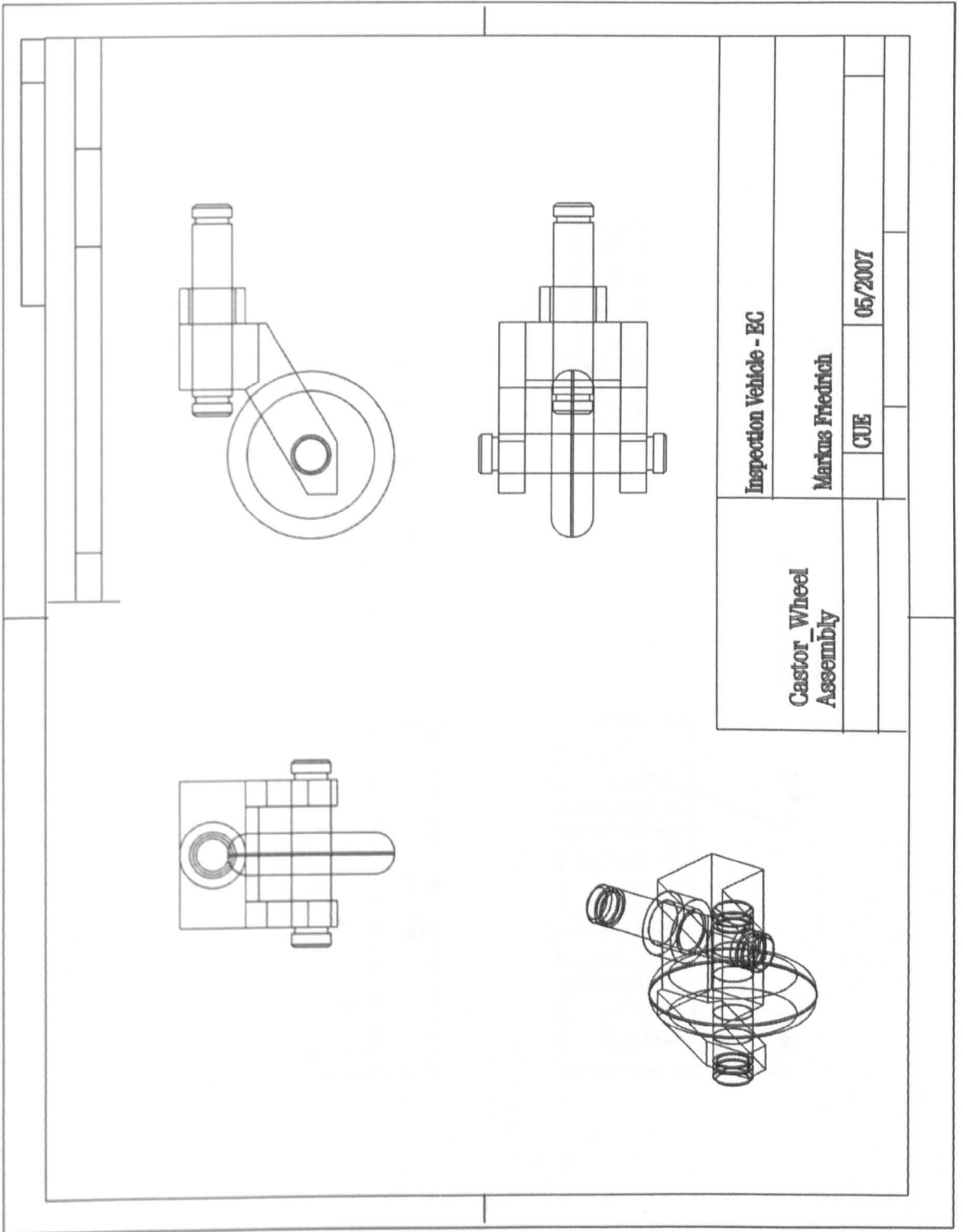
Figure A.6: Castor Wheel Assembly
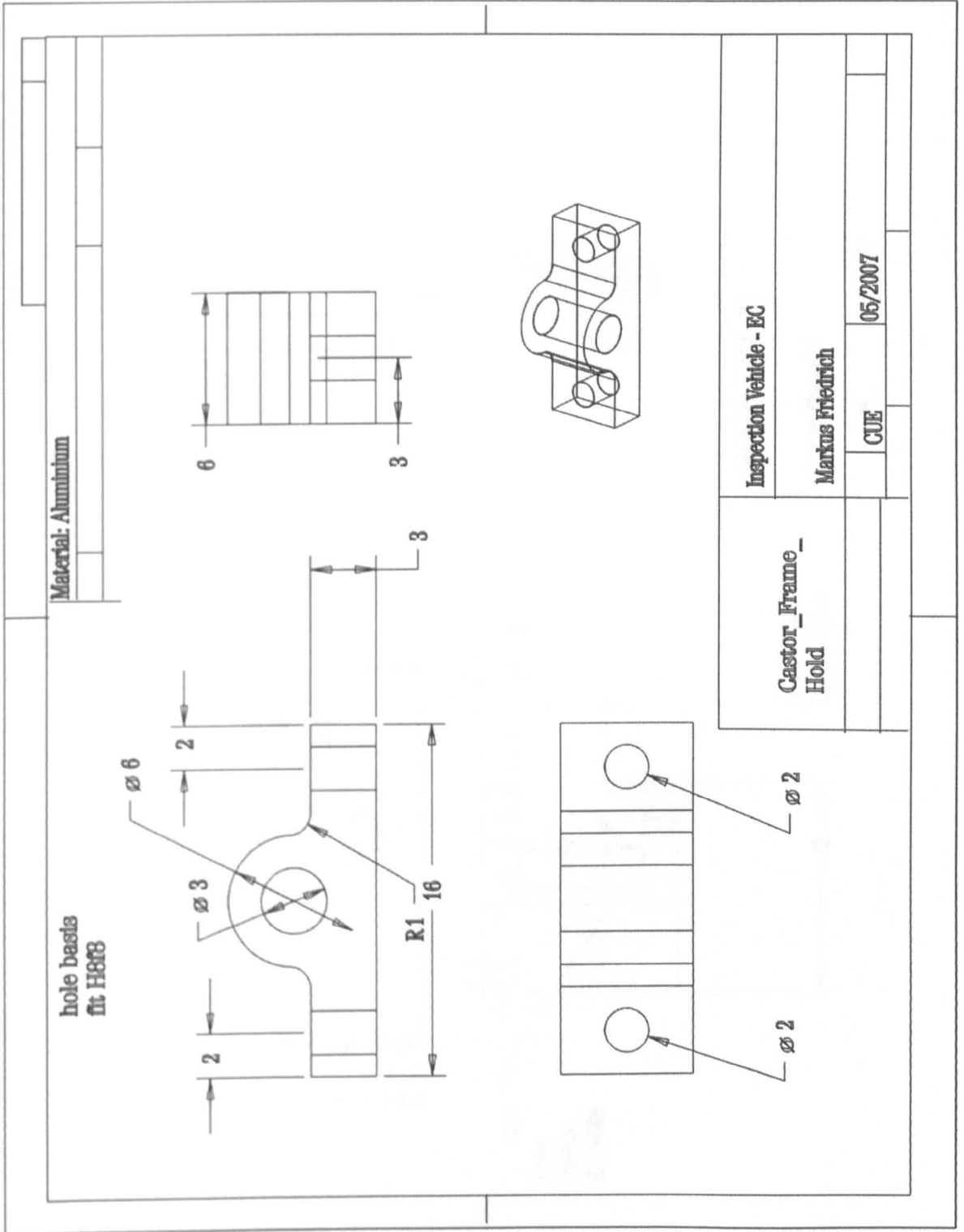
Figure A.7: Main Hold for Castor Assembly
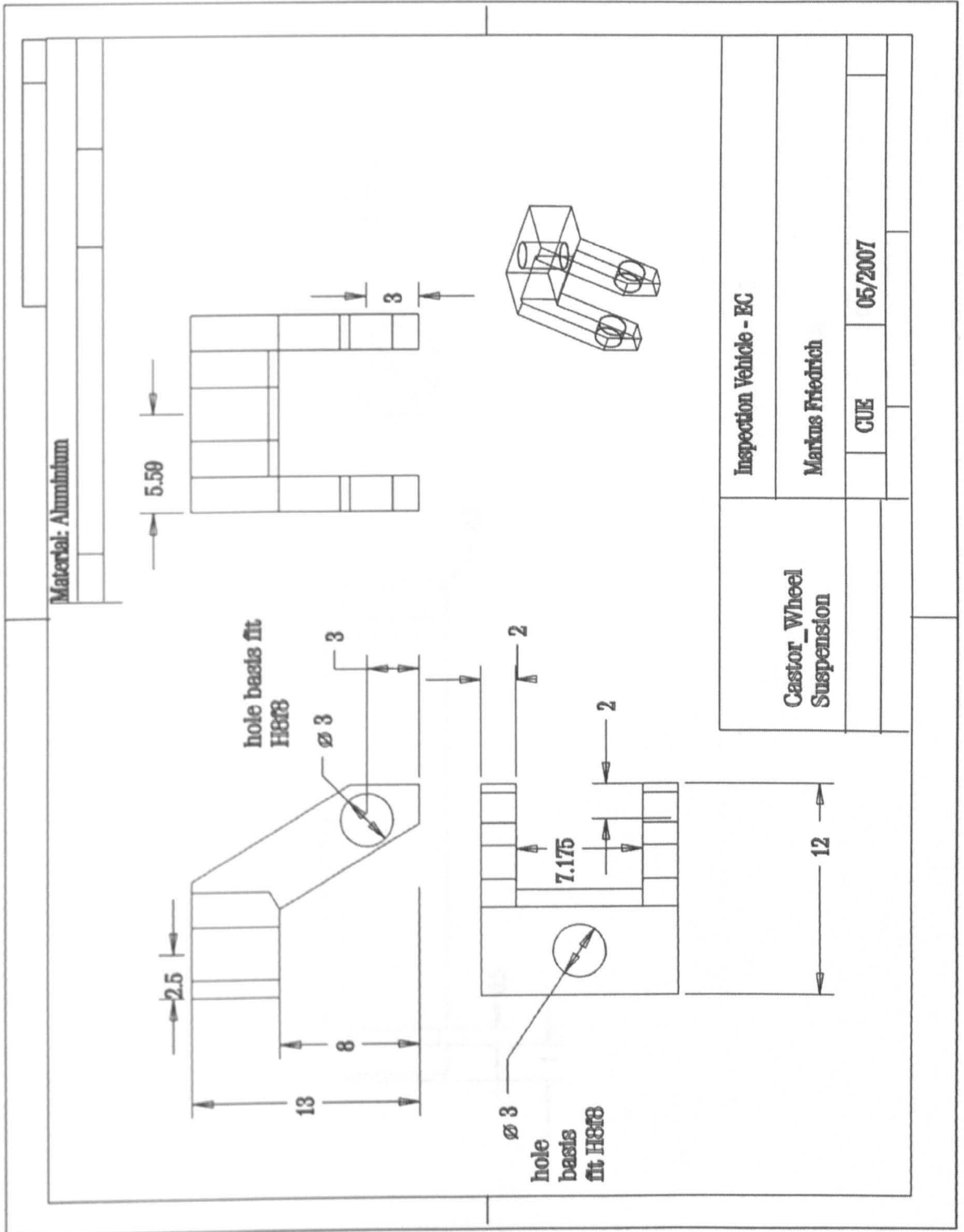
Figure A.8: Castor Wheel Suspension
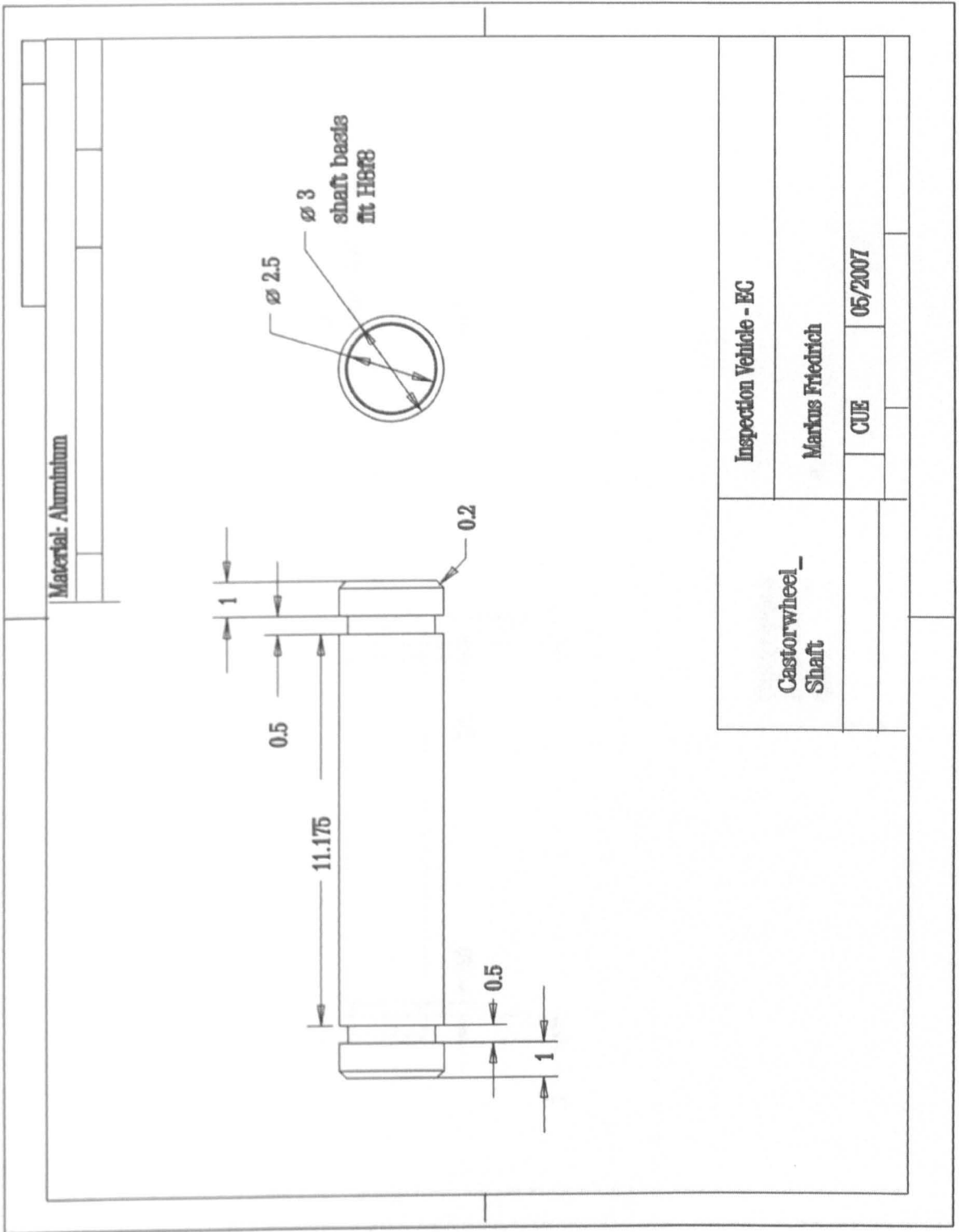
Figure A.9: Castorwheel - Shaft

173
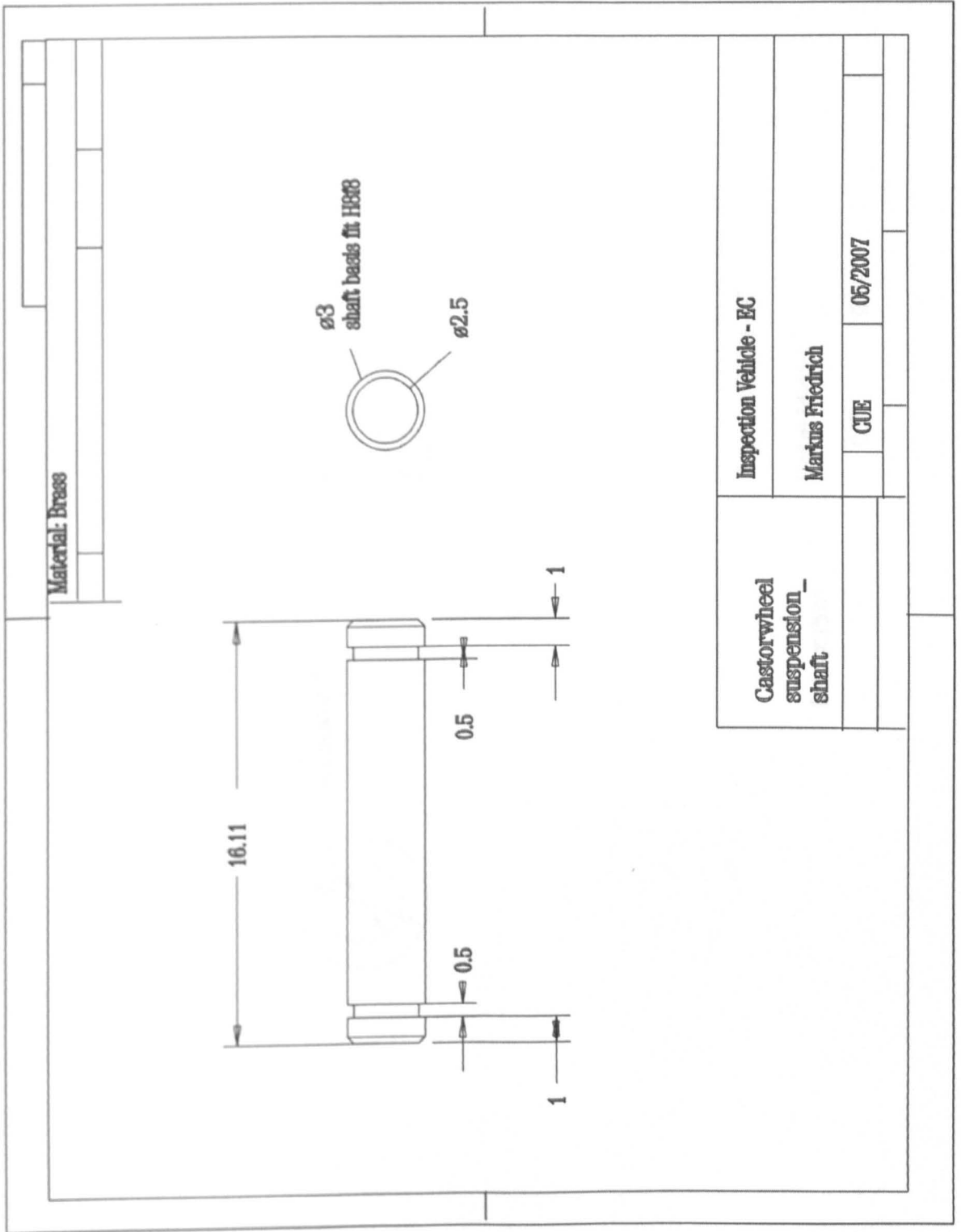
Figure A.10: Castorwheel Suspension - Shaft
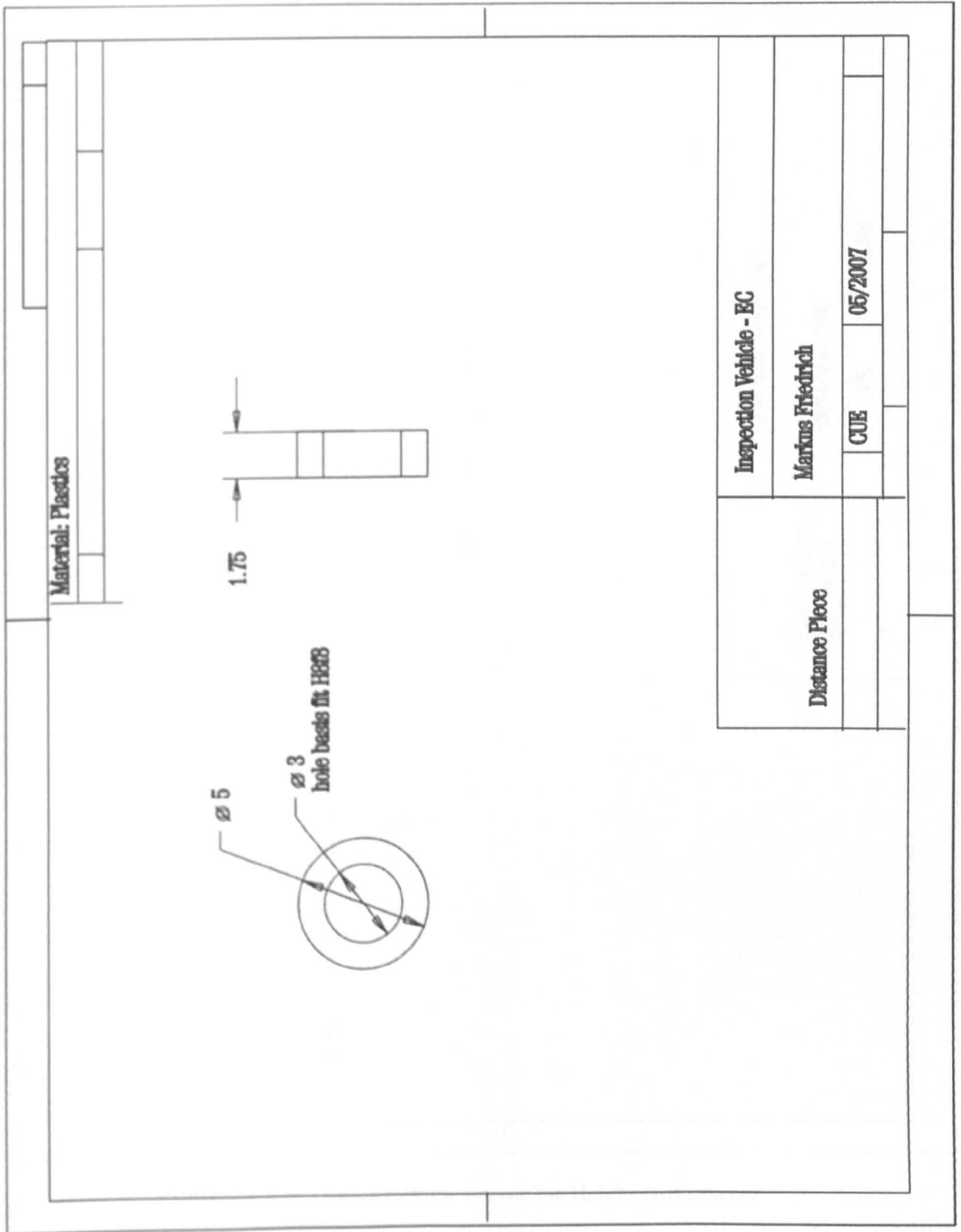
Figure A.11: Distance Piece Castor - Wheel/Fork

Material: Plastics

Ø 5

Ø 3.5

2.7

distancepiece_
hight_castor

Inspection Vehicle - EC

Markus Friedrich

CUE   05/2007
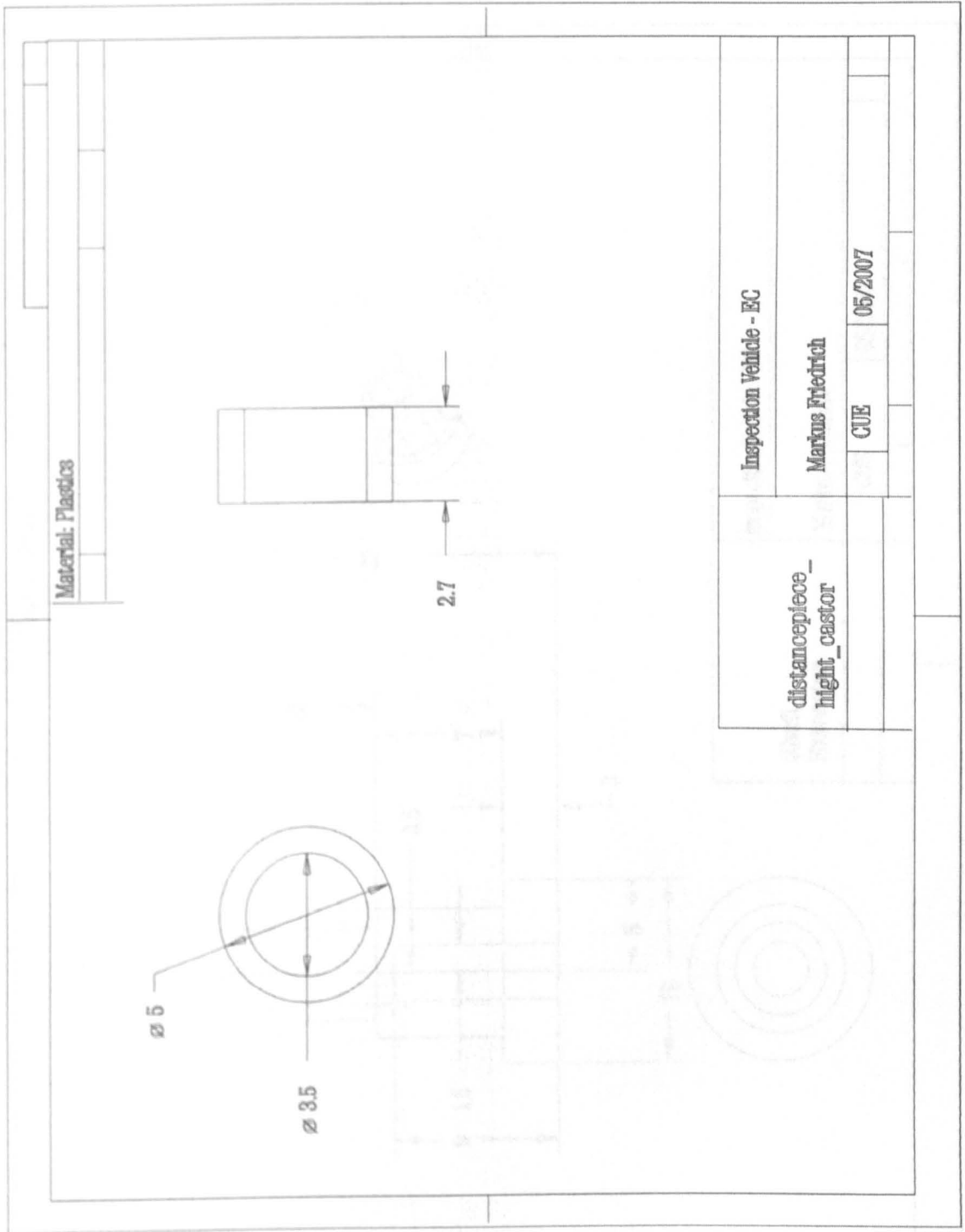
Figure A.12: Distance Piece Castor for Height Adjustment
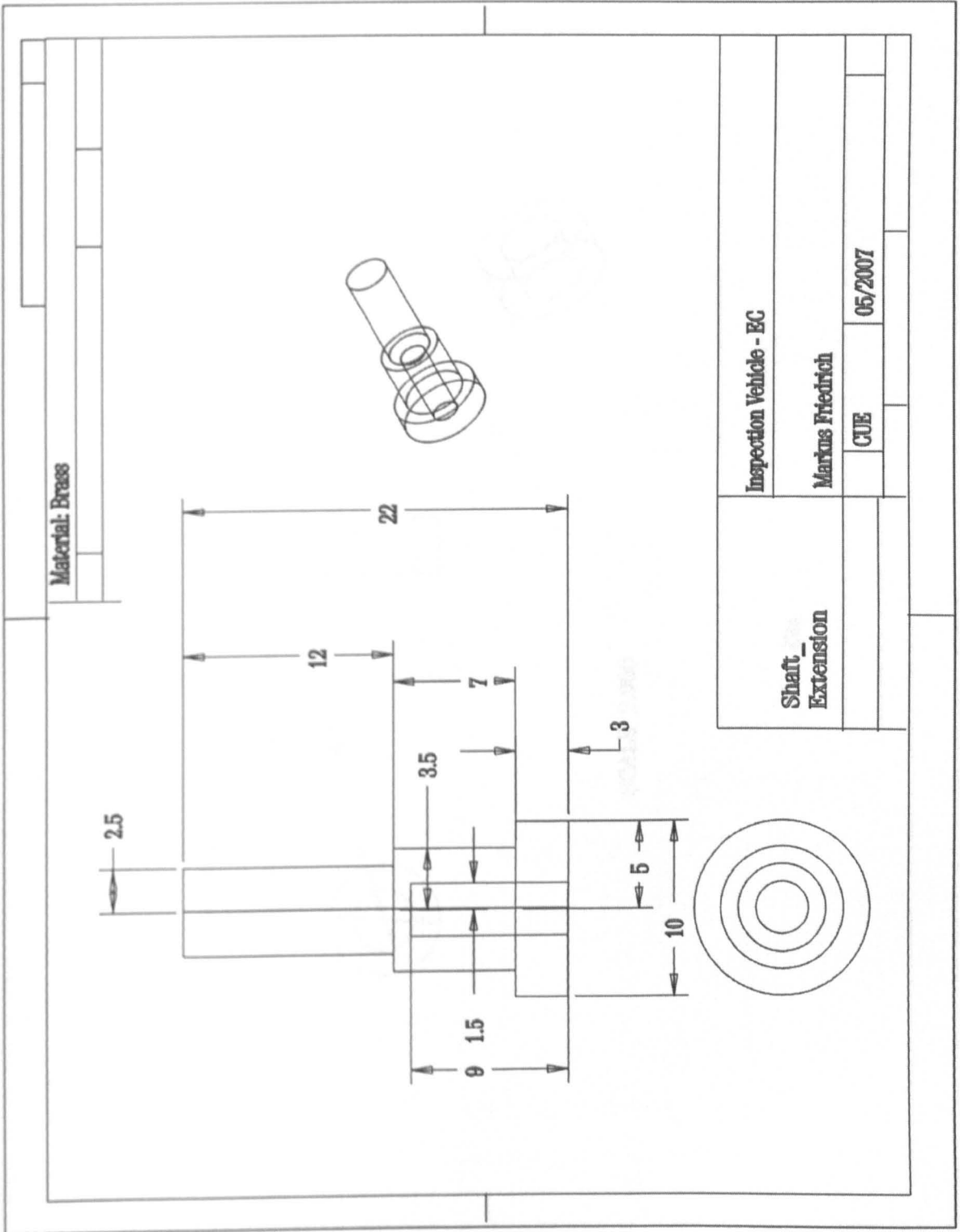
Figure A.13: Shaft Extension for DC Motors

Material: Brass

⌀ 12.7

6.35

⌀ 7

SCALE 2.000

Wheel_Rim

Inspection Vehicle - EC

Markus Friedrich

CUE   05/2007
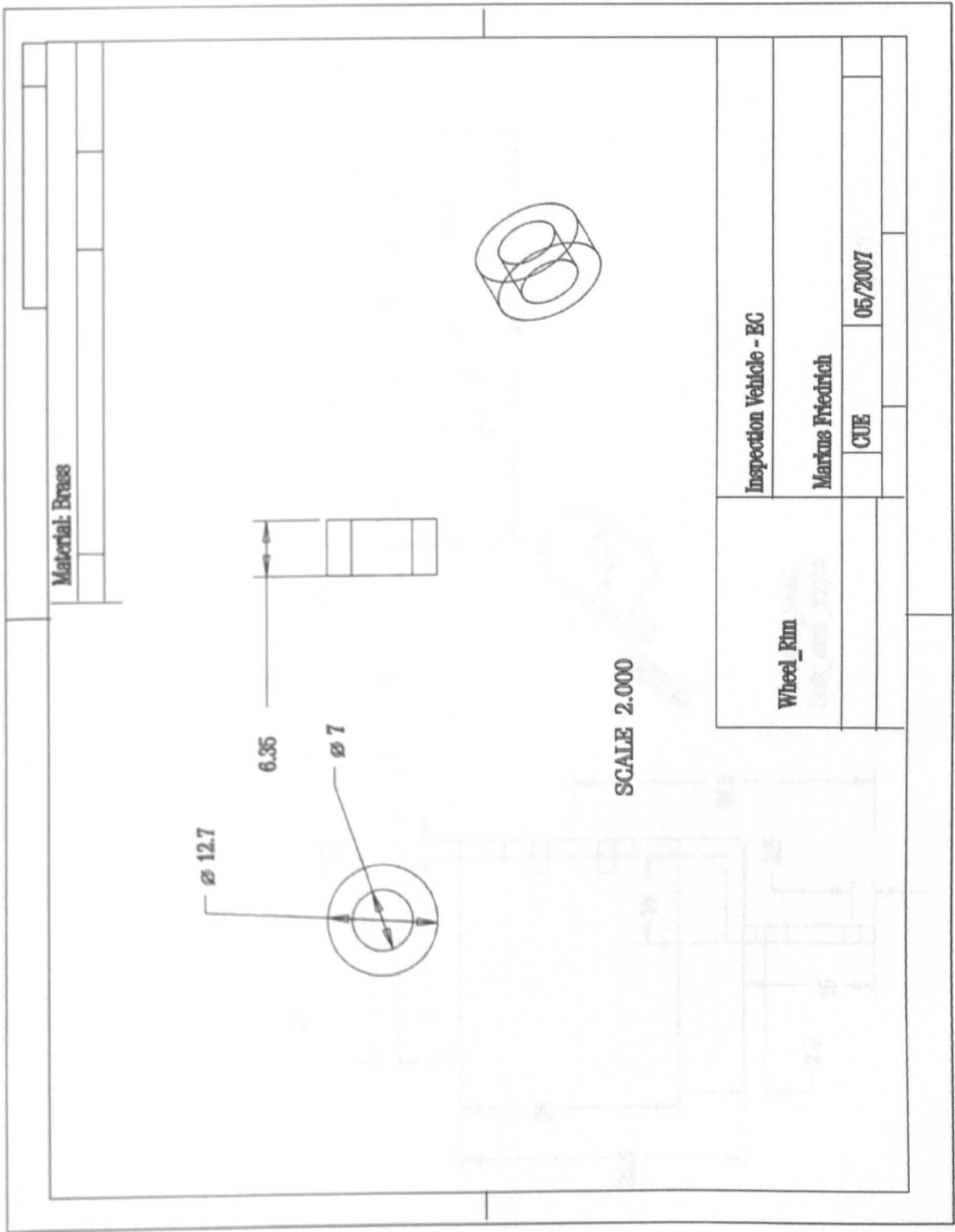
Figure A.14: Wheel Rim

178
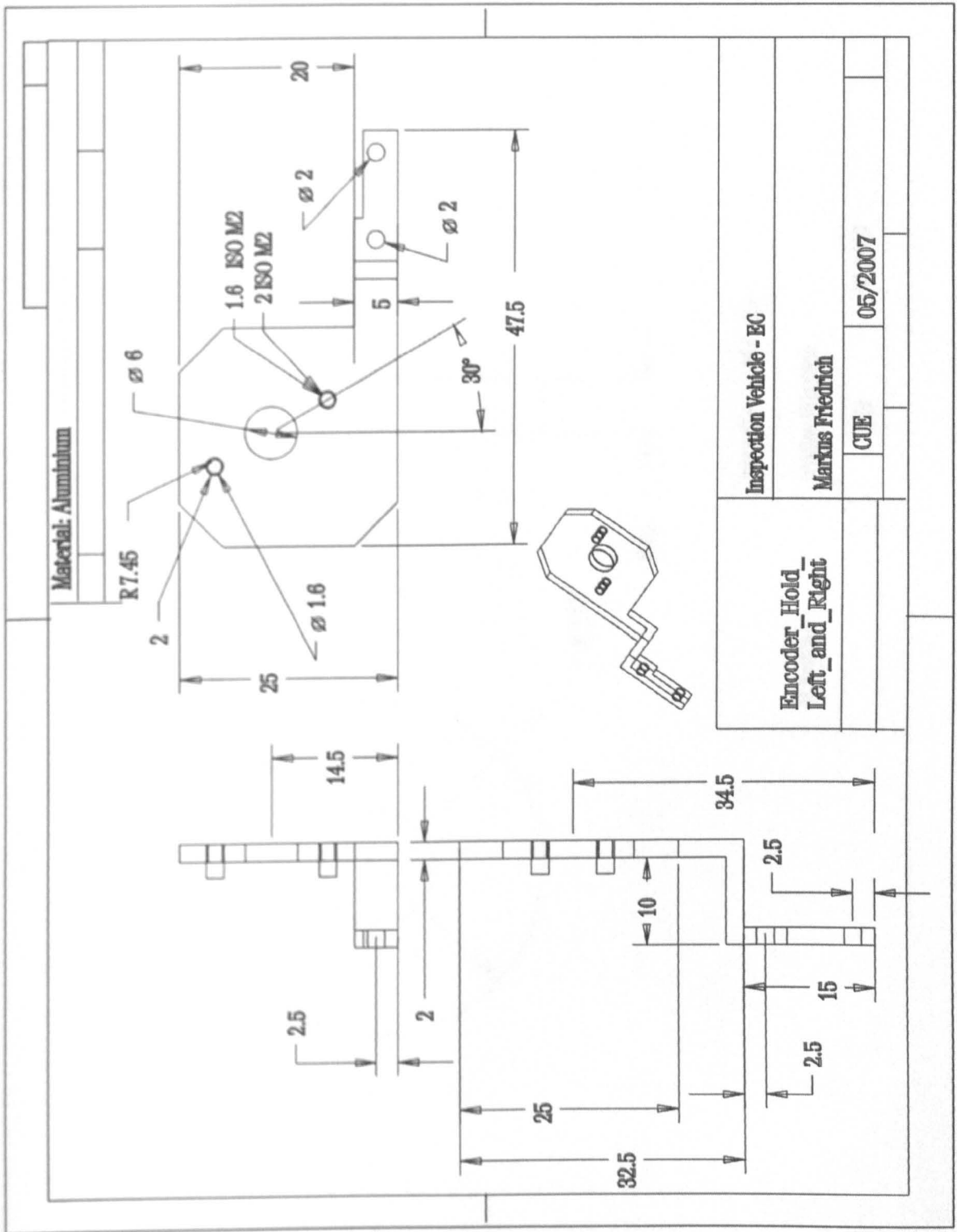
Figure A.15: Hold for Optical Encoders
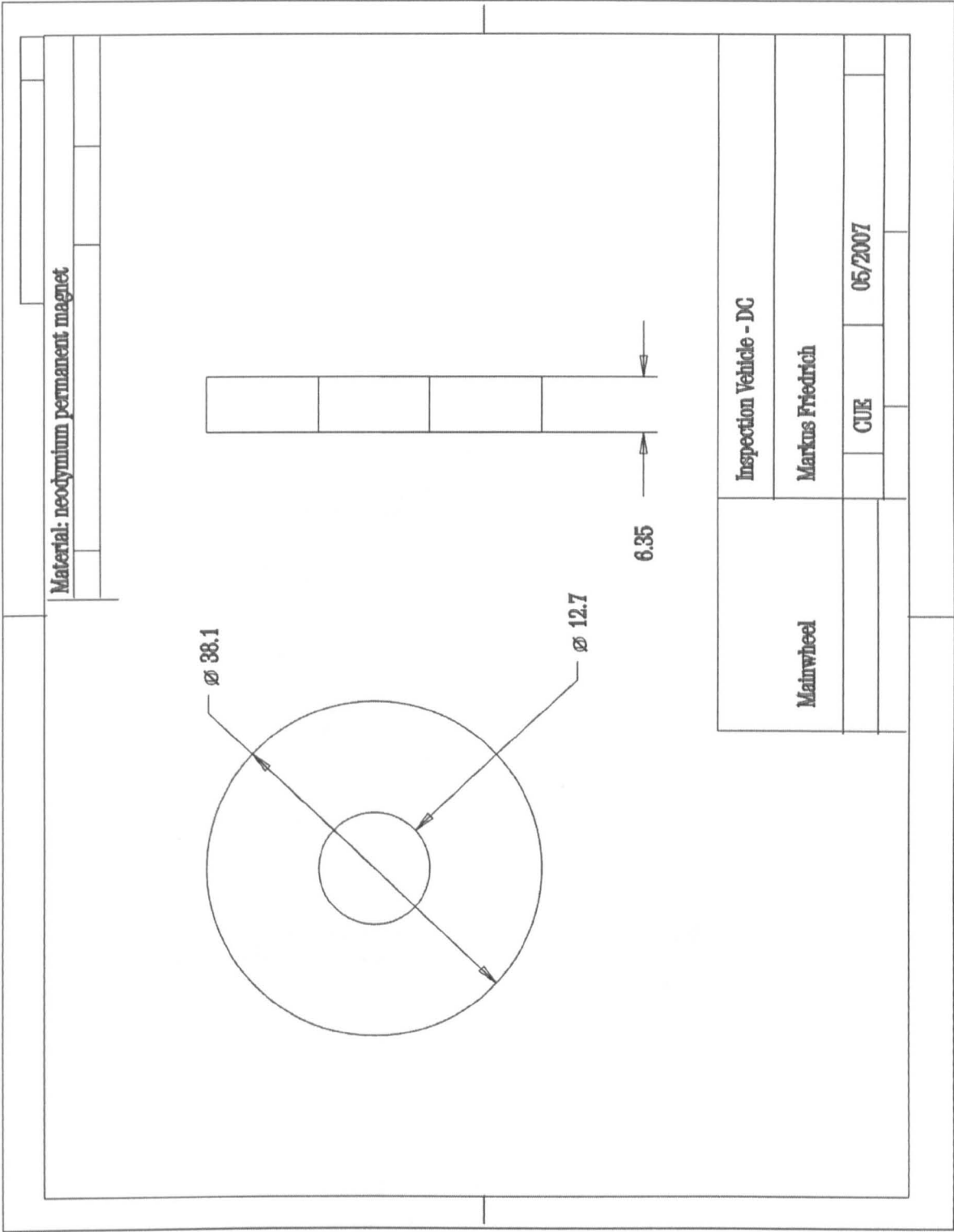
Figure A.16: Main Wheels

180
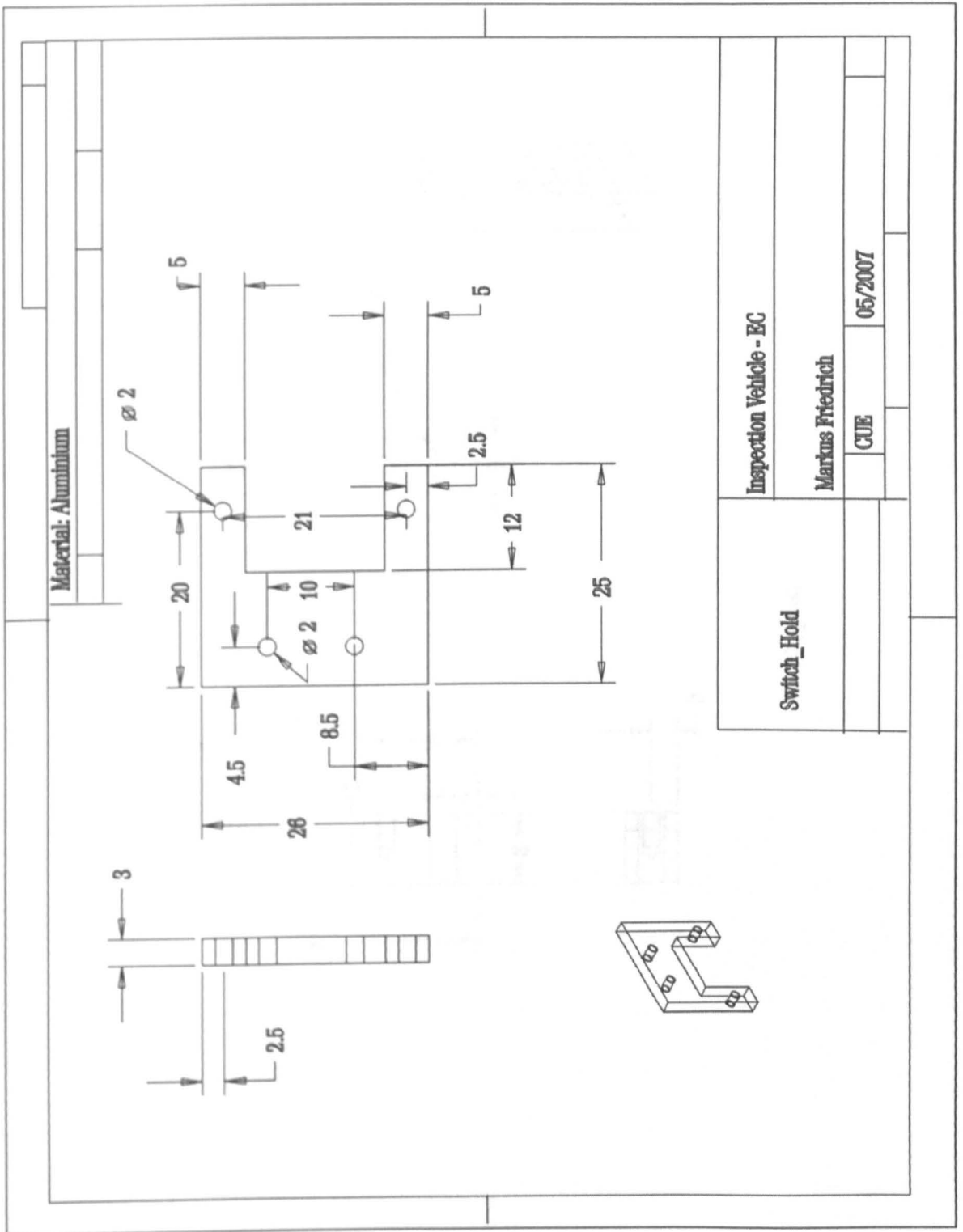
Figure A.17: Hold for Power Switch
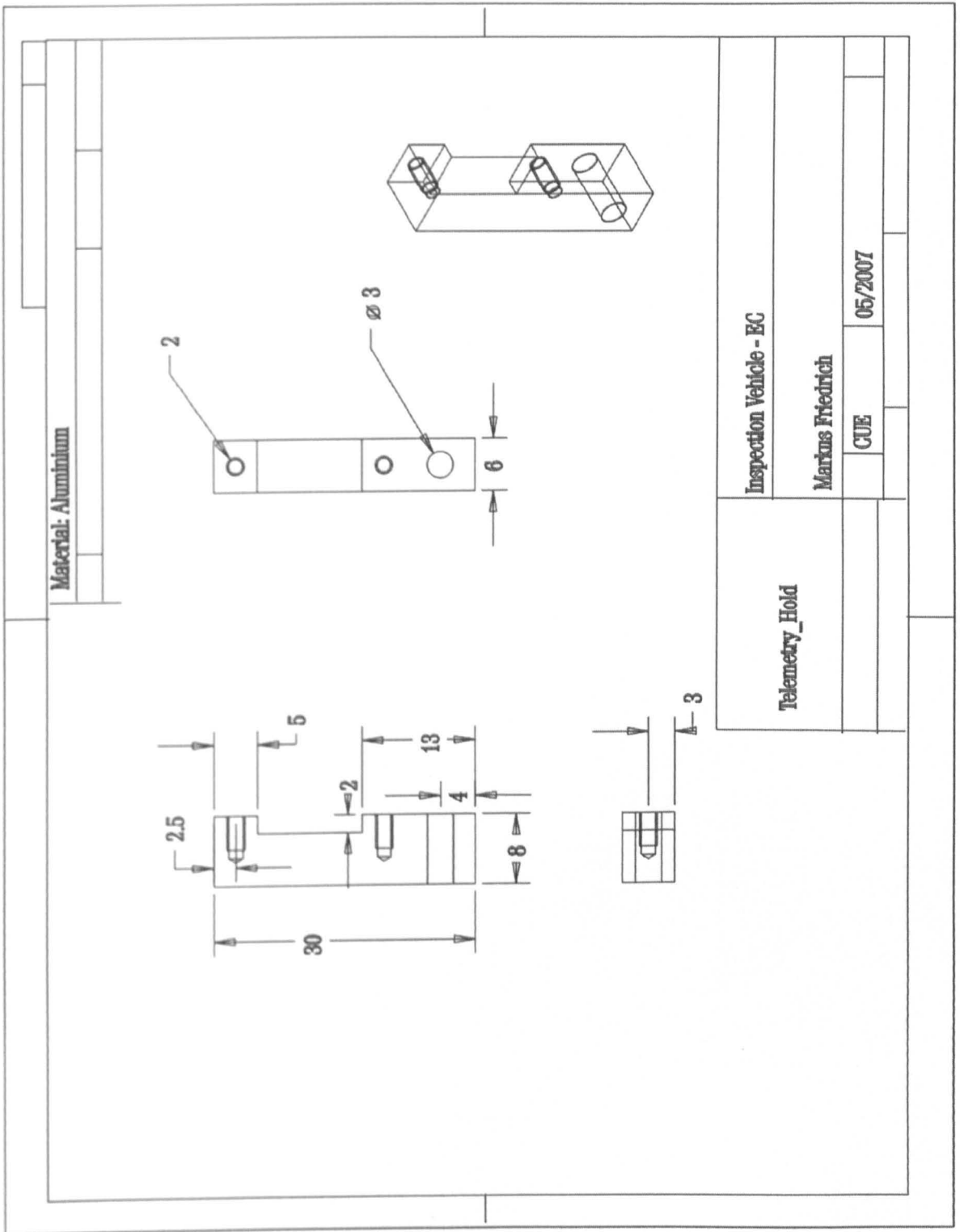
Figure A.18: Hold for Telemetry Module

A.2 Eddy Current Sensor
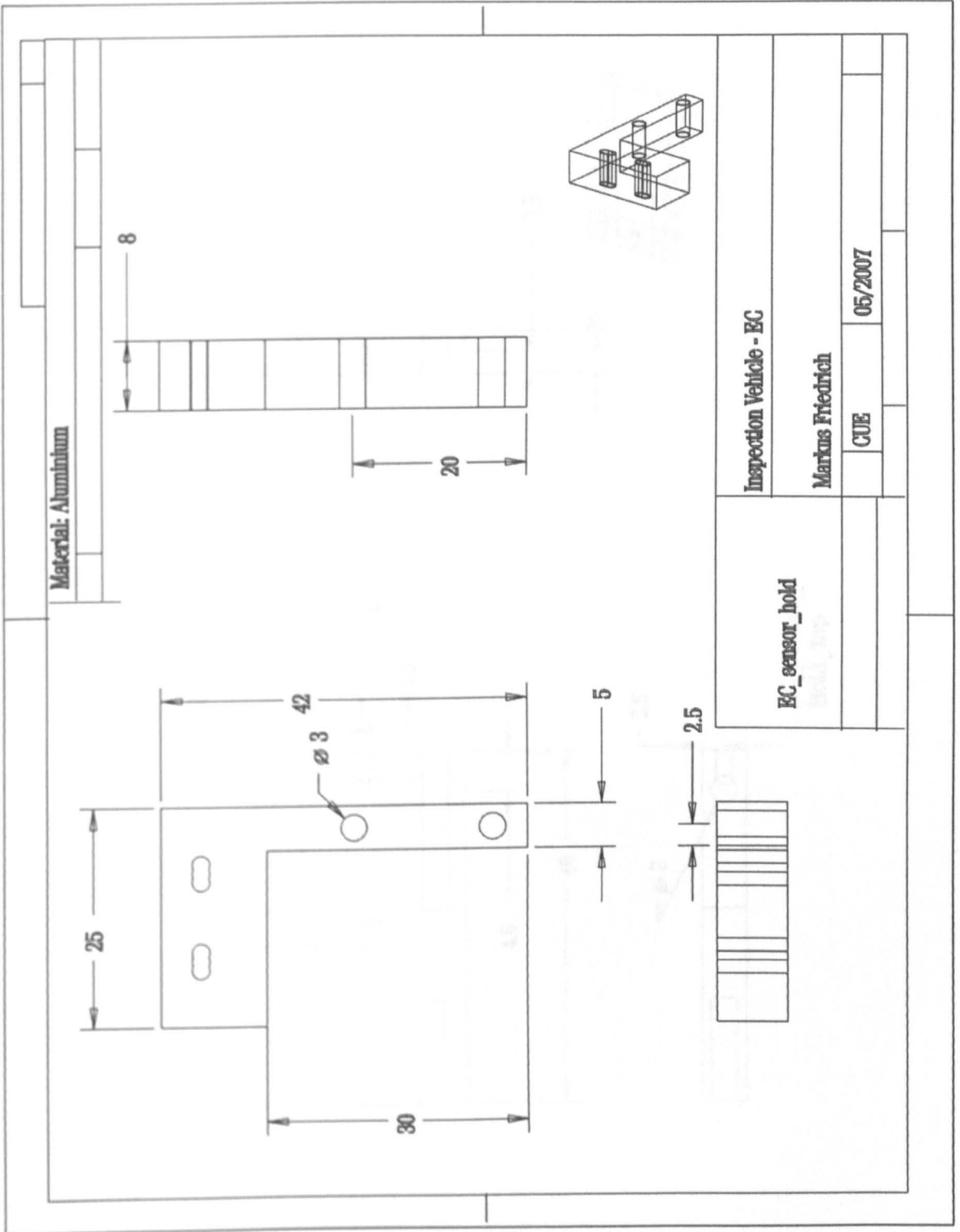
Figure A.19: Main Hold for EC Sensor
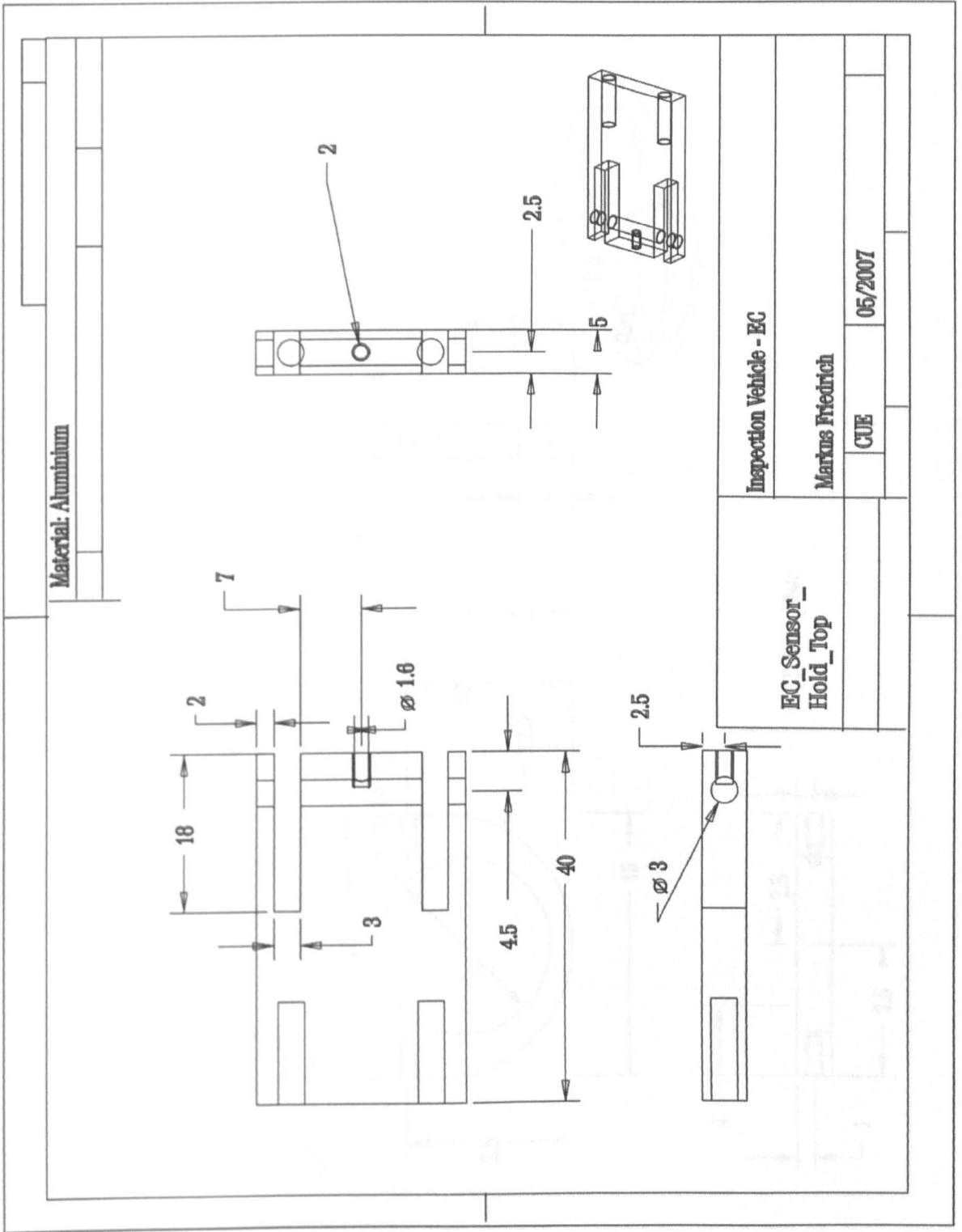
Figure A.20: EC Sensor Hold - Top Section

185
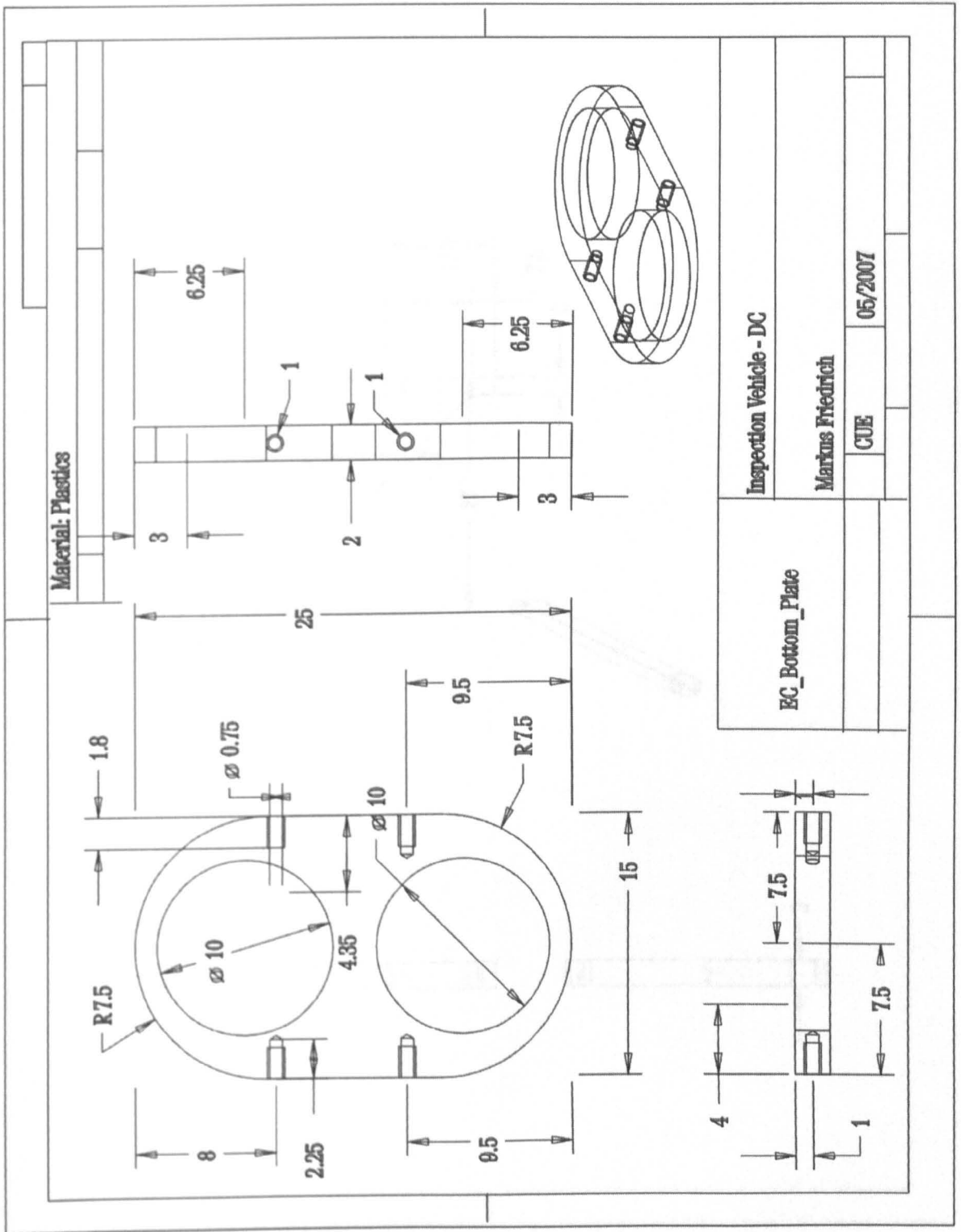
Figure A.21: Bottom Plate EC Sensor
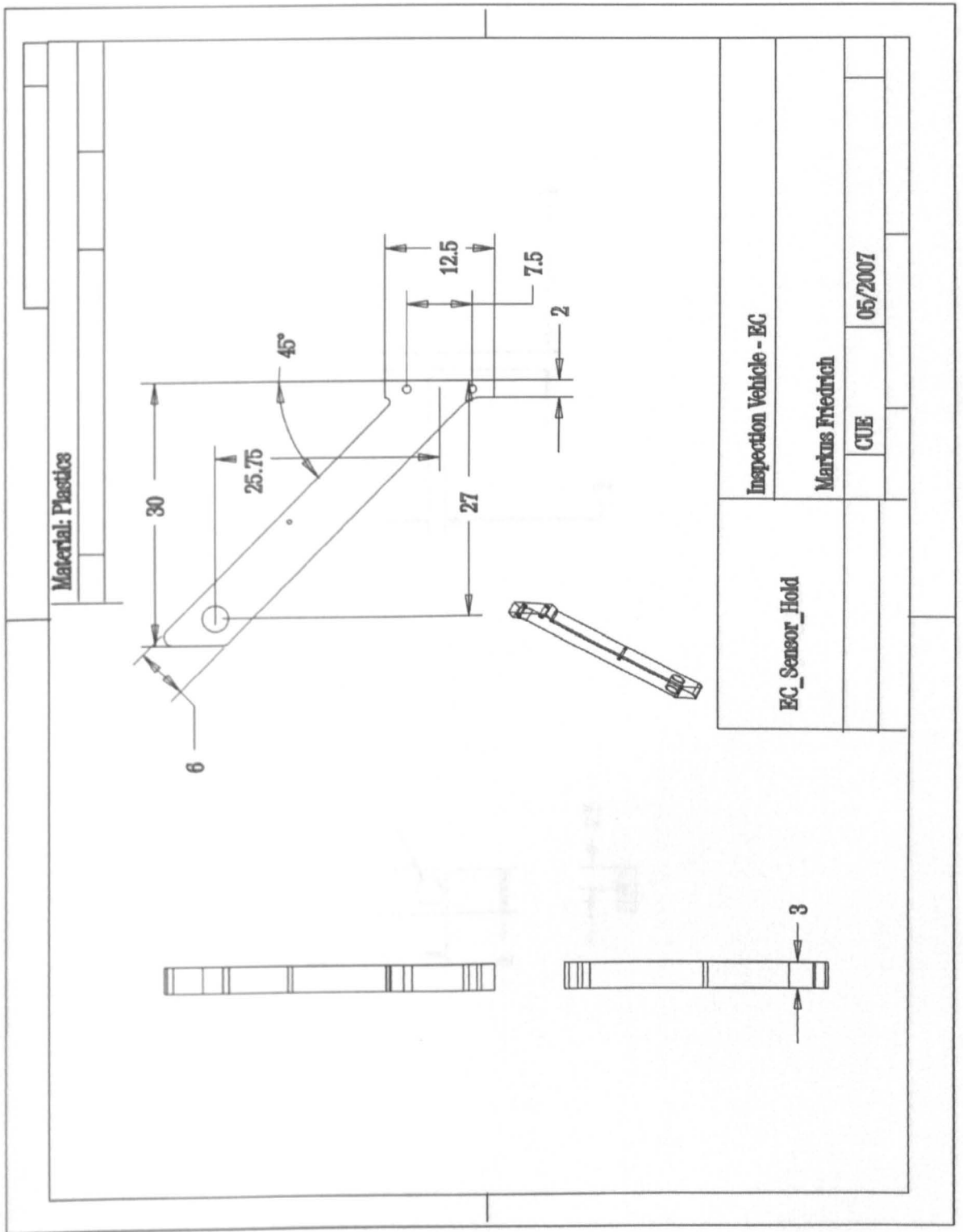
Figure A.22: EC Sensor - Left and Right Lever
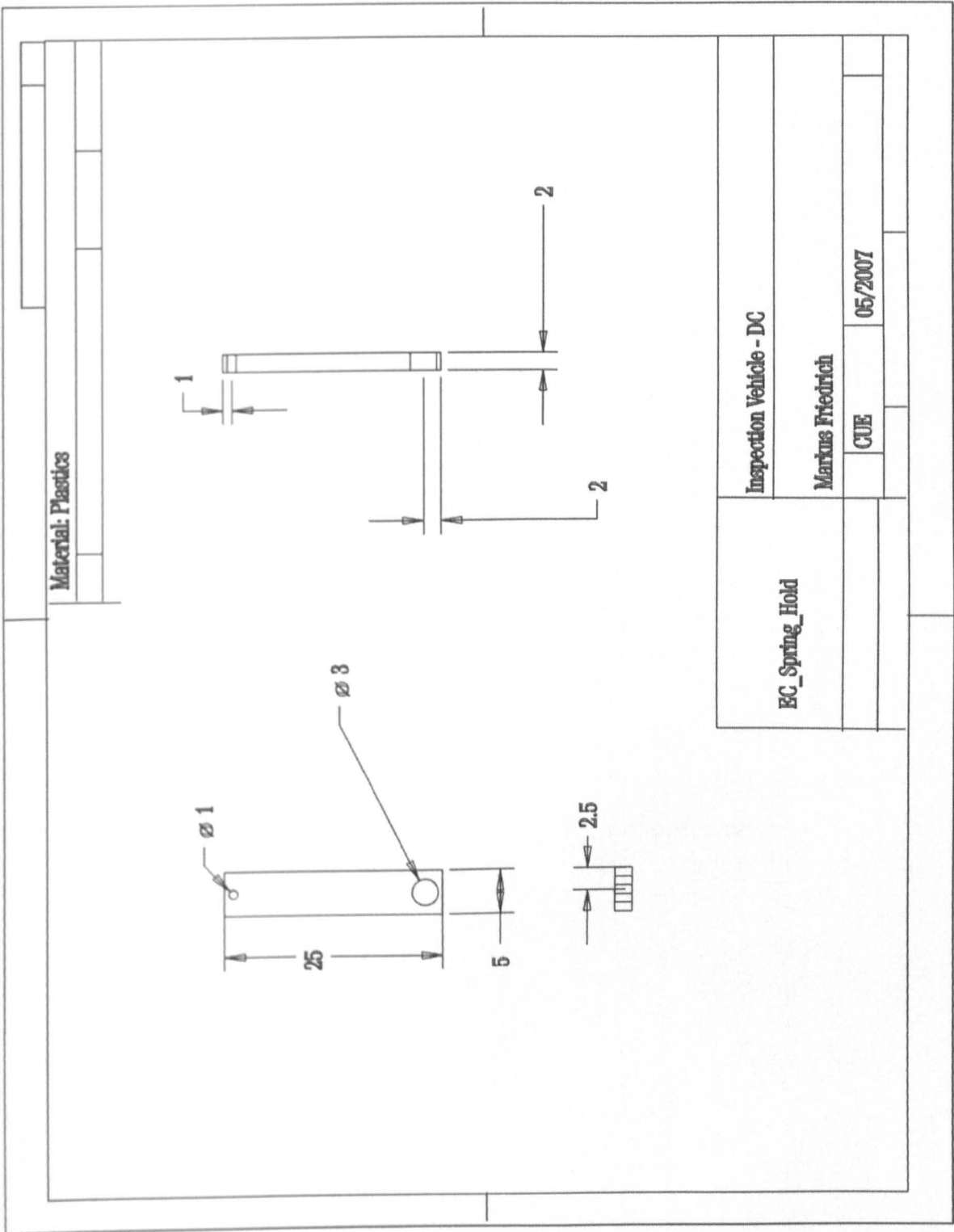
Figure A.23: EC Sensor - Spring Hold

A.3 Hold for Hall Sensor Array
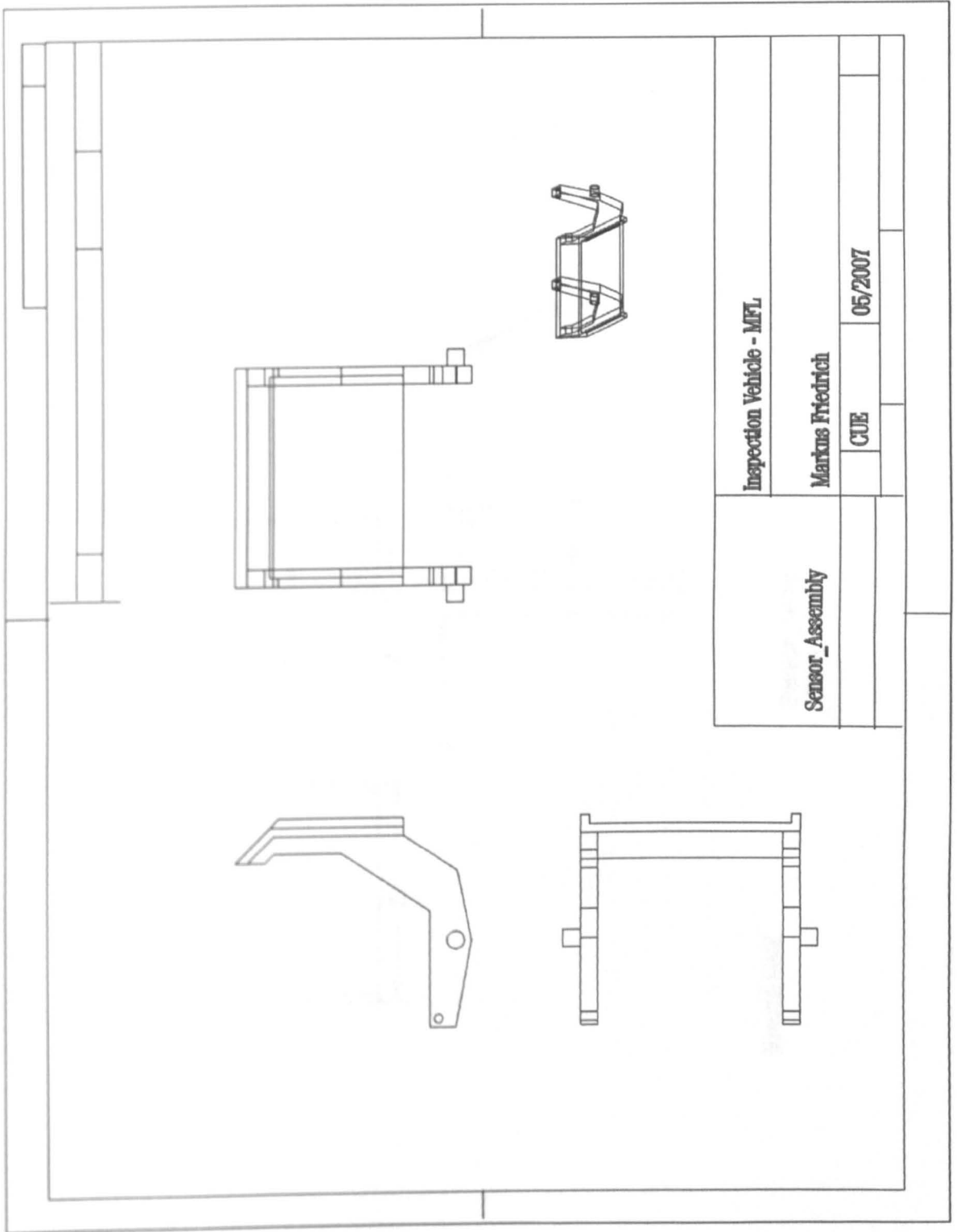
Figure A.24: Hold for Hall Array - Assembly
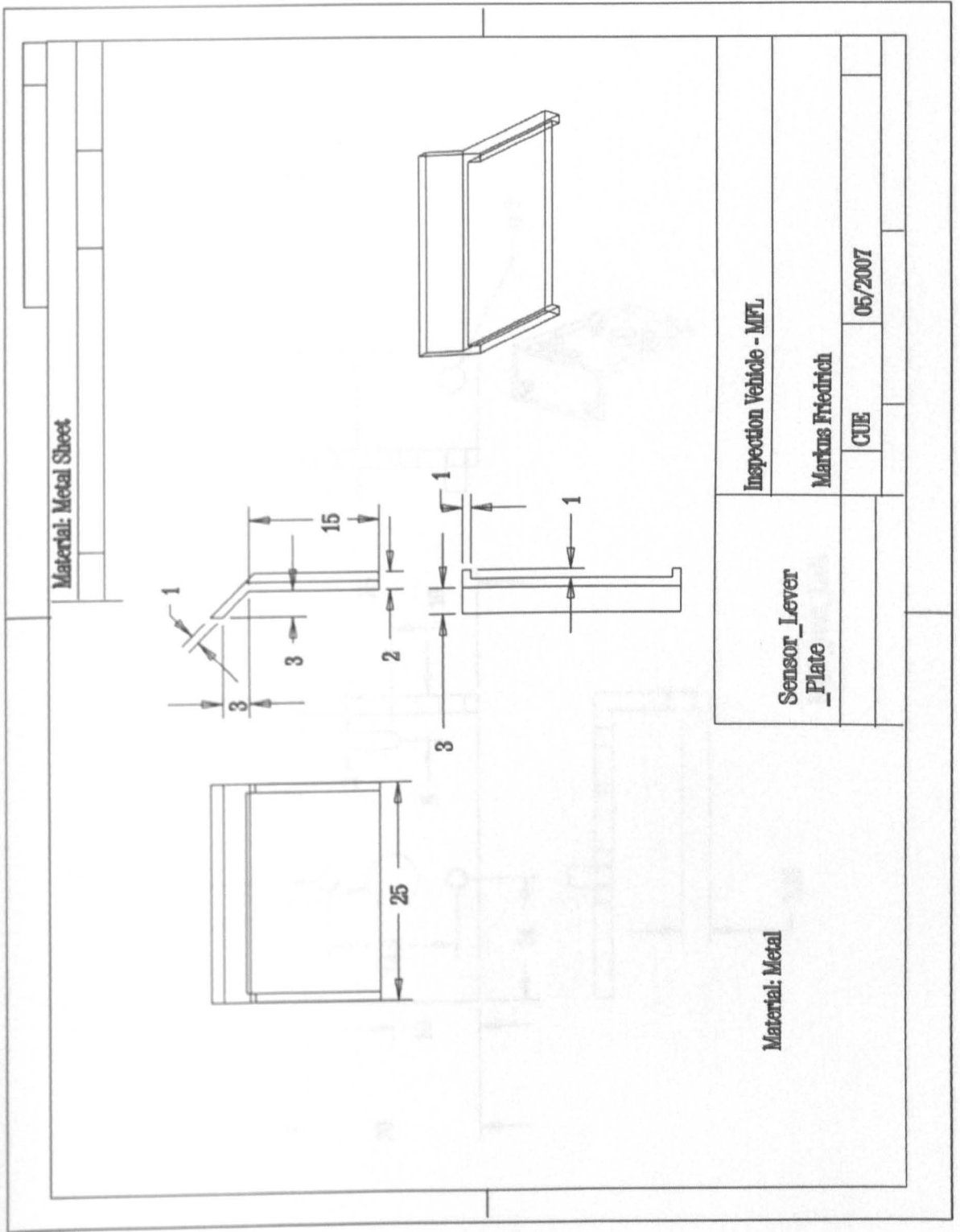
Figure A.25: Bottom Plate for Hall Array
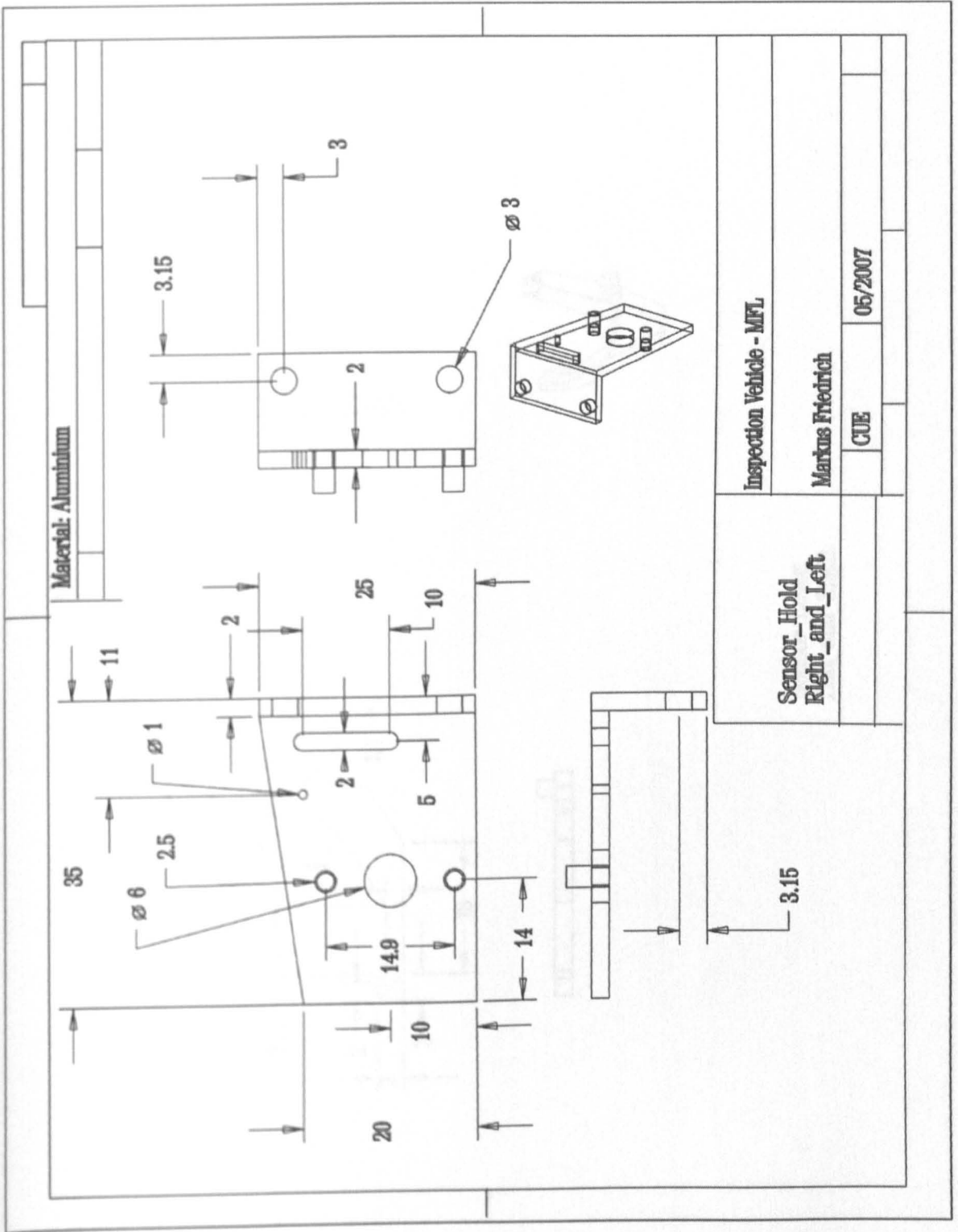
Figure A.26: Sensor Hold for Hall Array
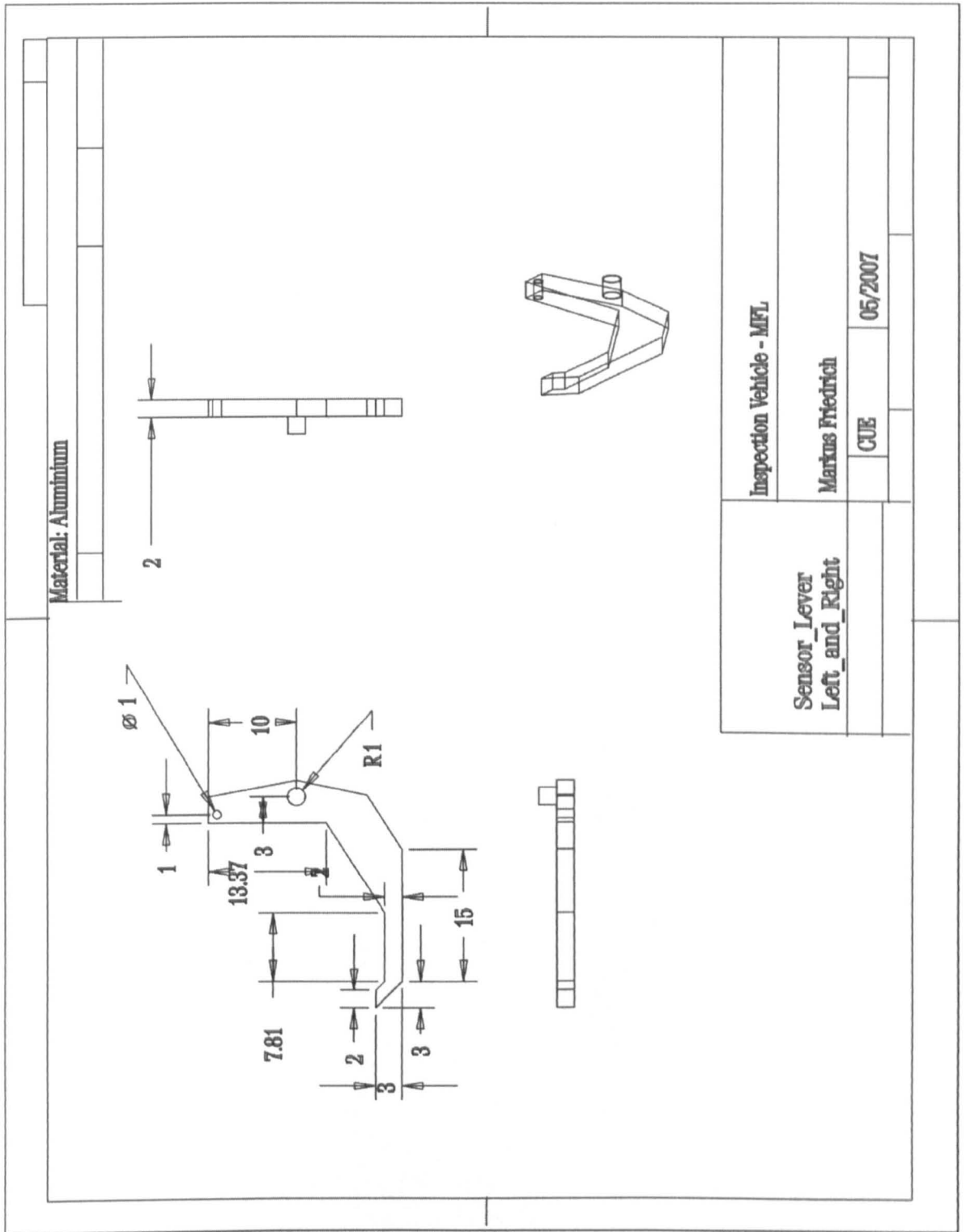
Figure A.27: Sensor Levers Hall Array - Sides

A.4 Sensor Hold for US Transducers
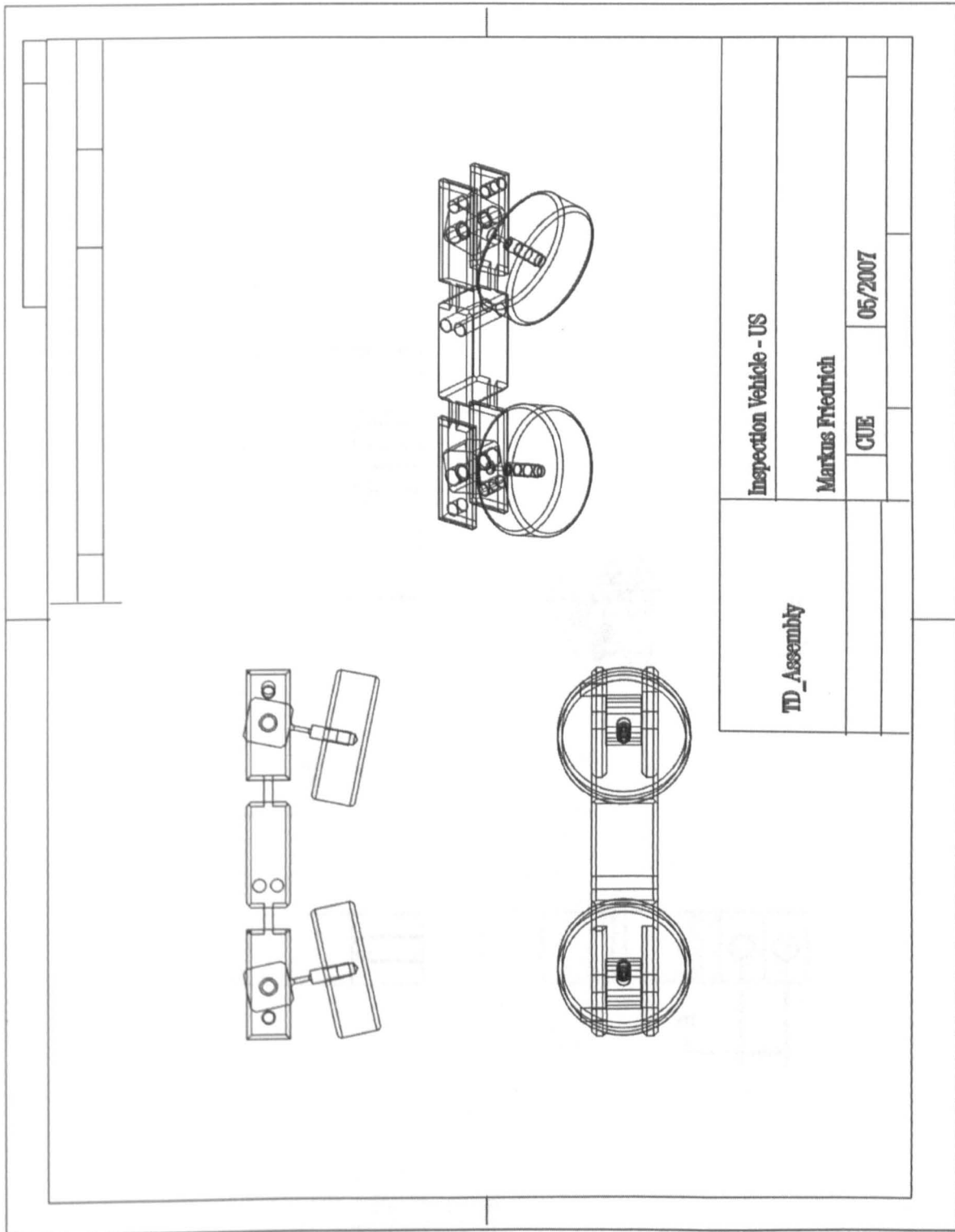
Figure A.28: Sensor Hold for US Transducers - Assembly
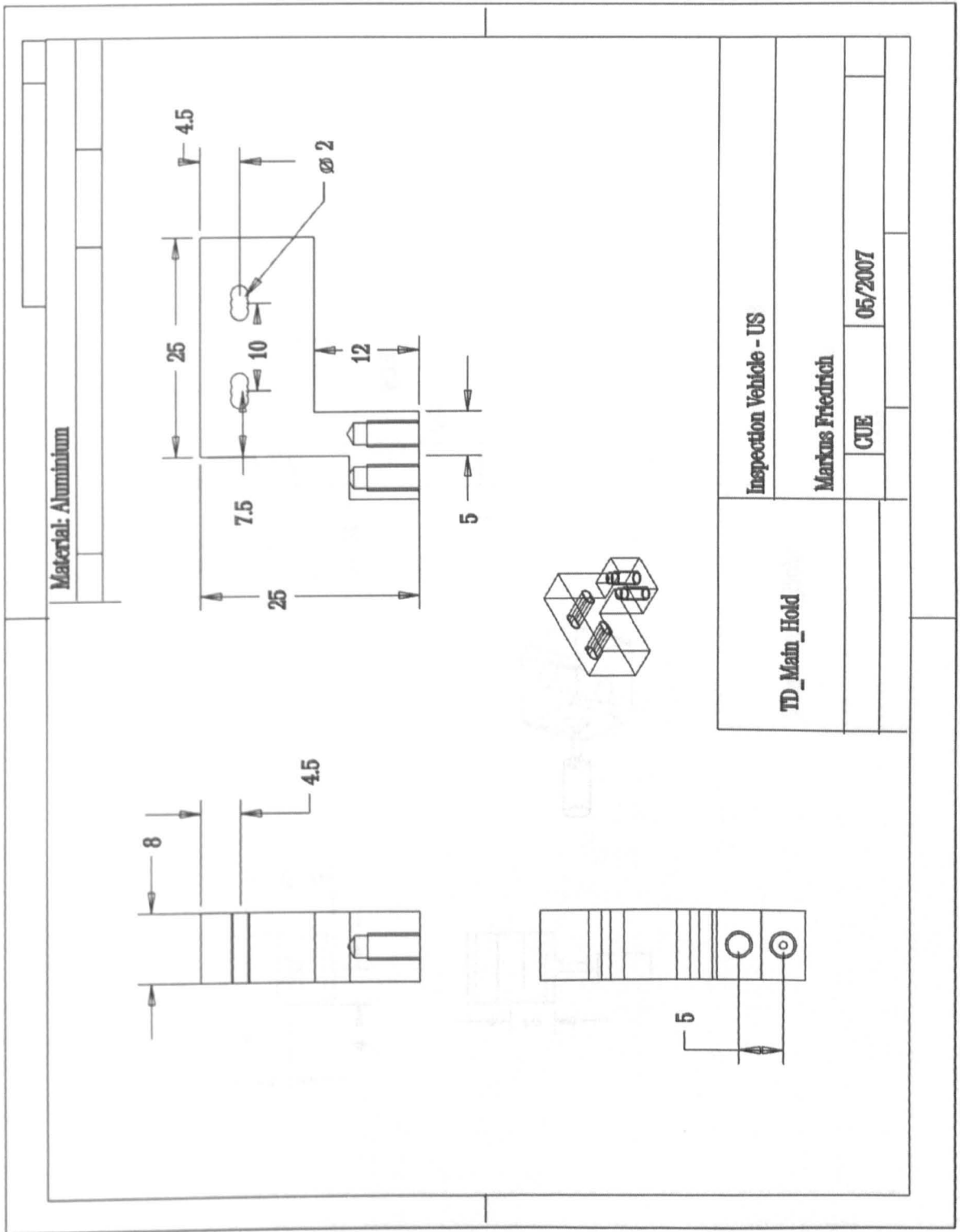
Figure A.29: Main Hold for US Transducers
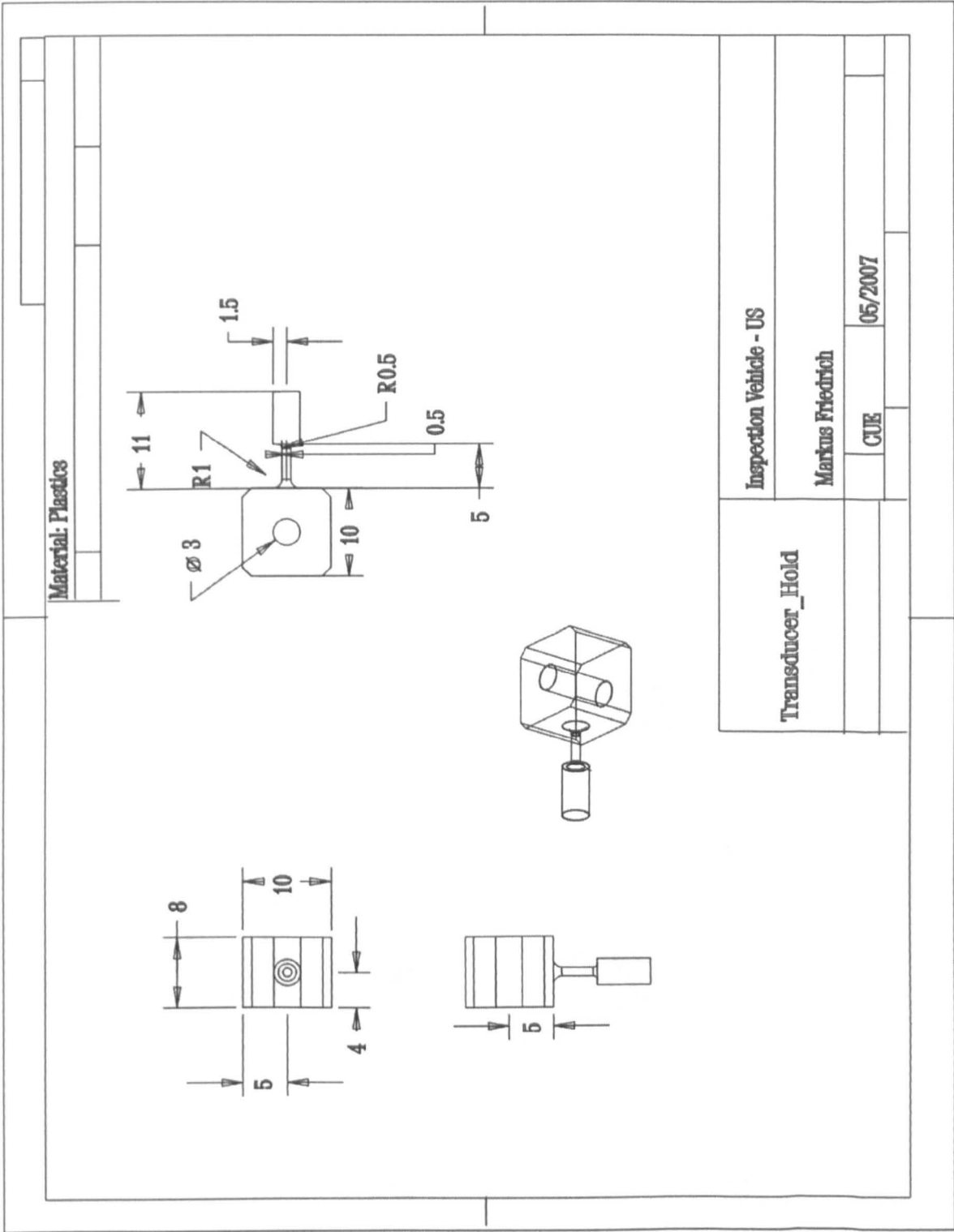
Figure A.30: Pivotal Cube for US Transducers
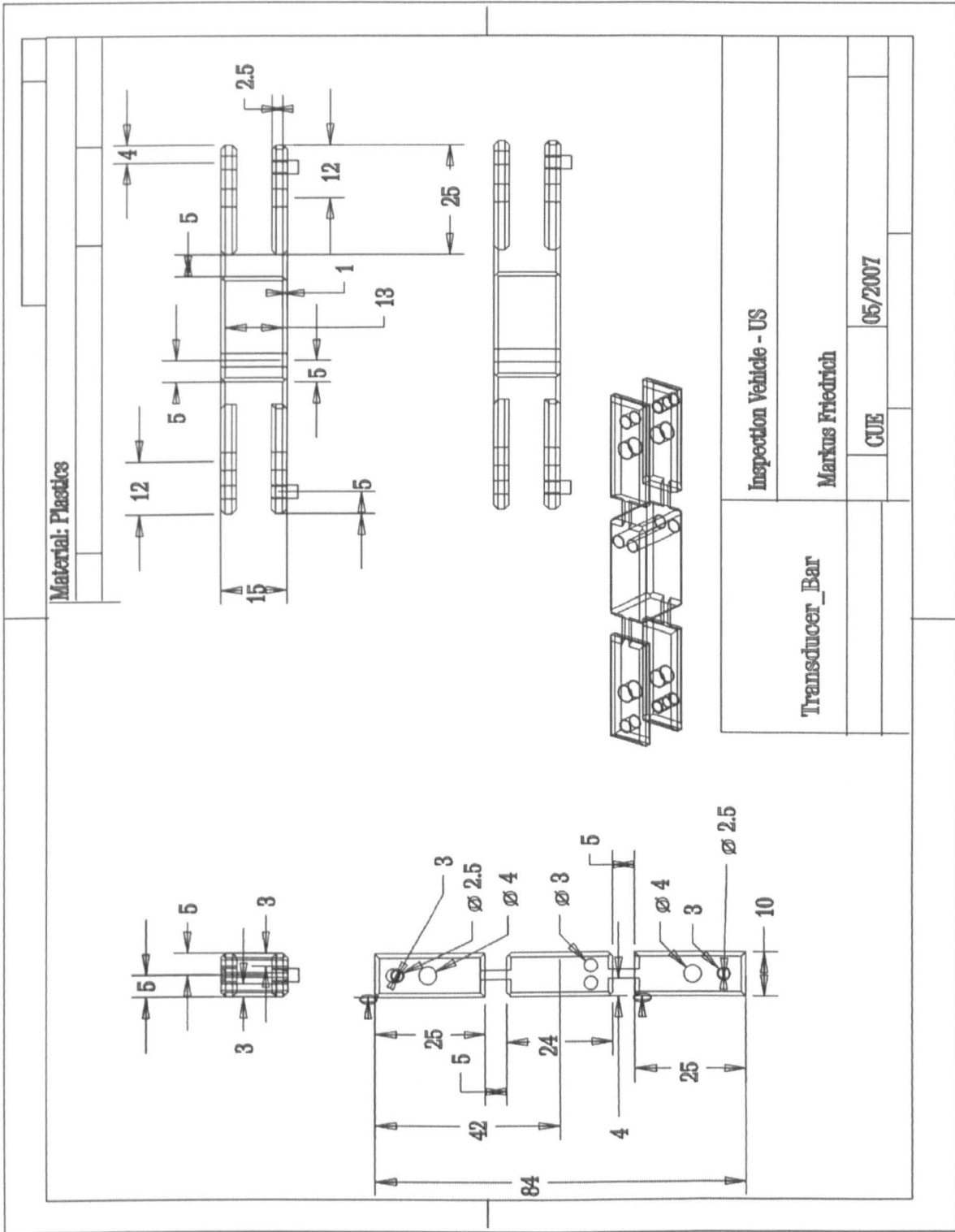
Figure A.31: Main Sensor Bar for US Transducers

A.5 Hold for Wireless Camera
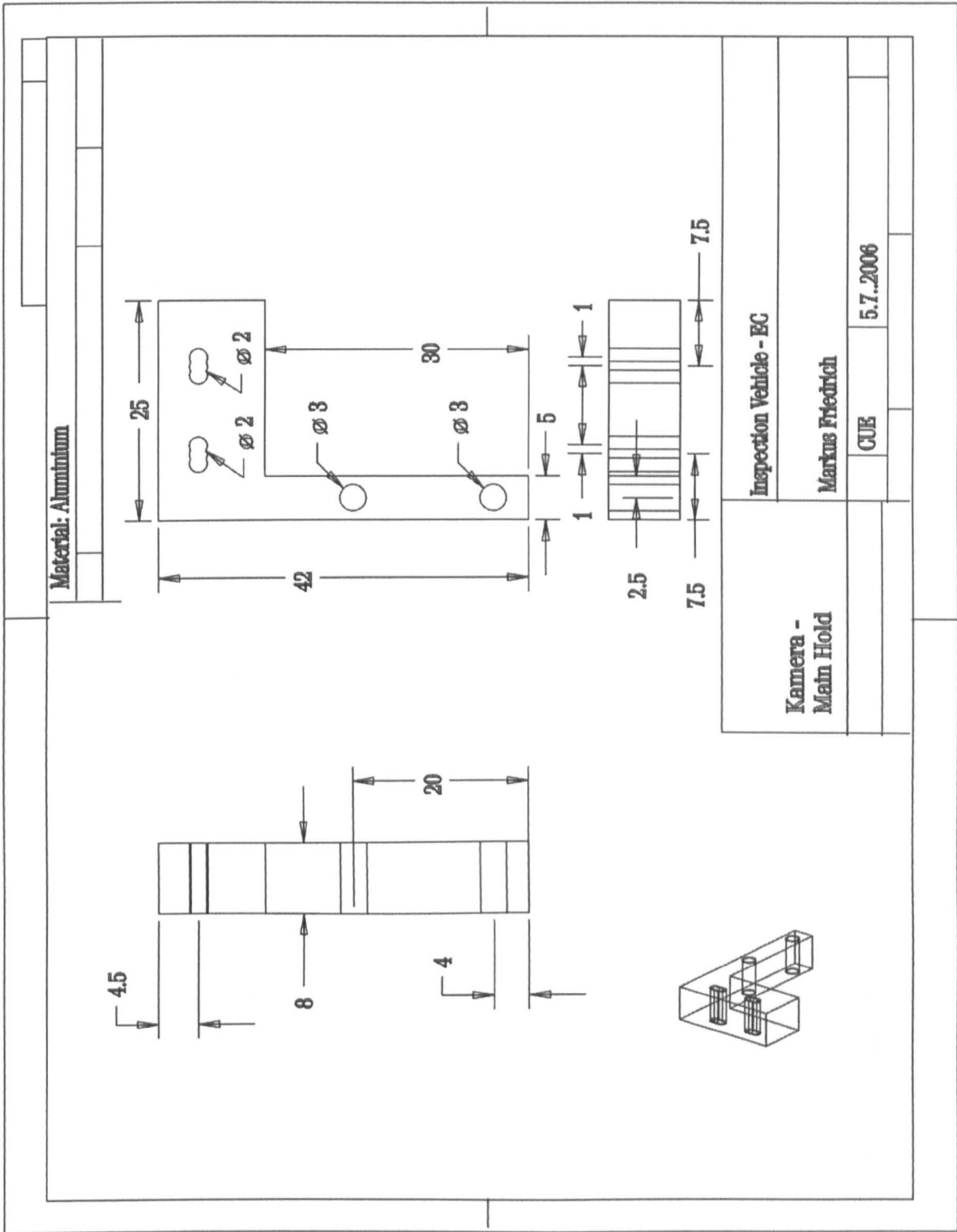
Figure A.32: Main Hold for Wireless Camera
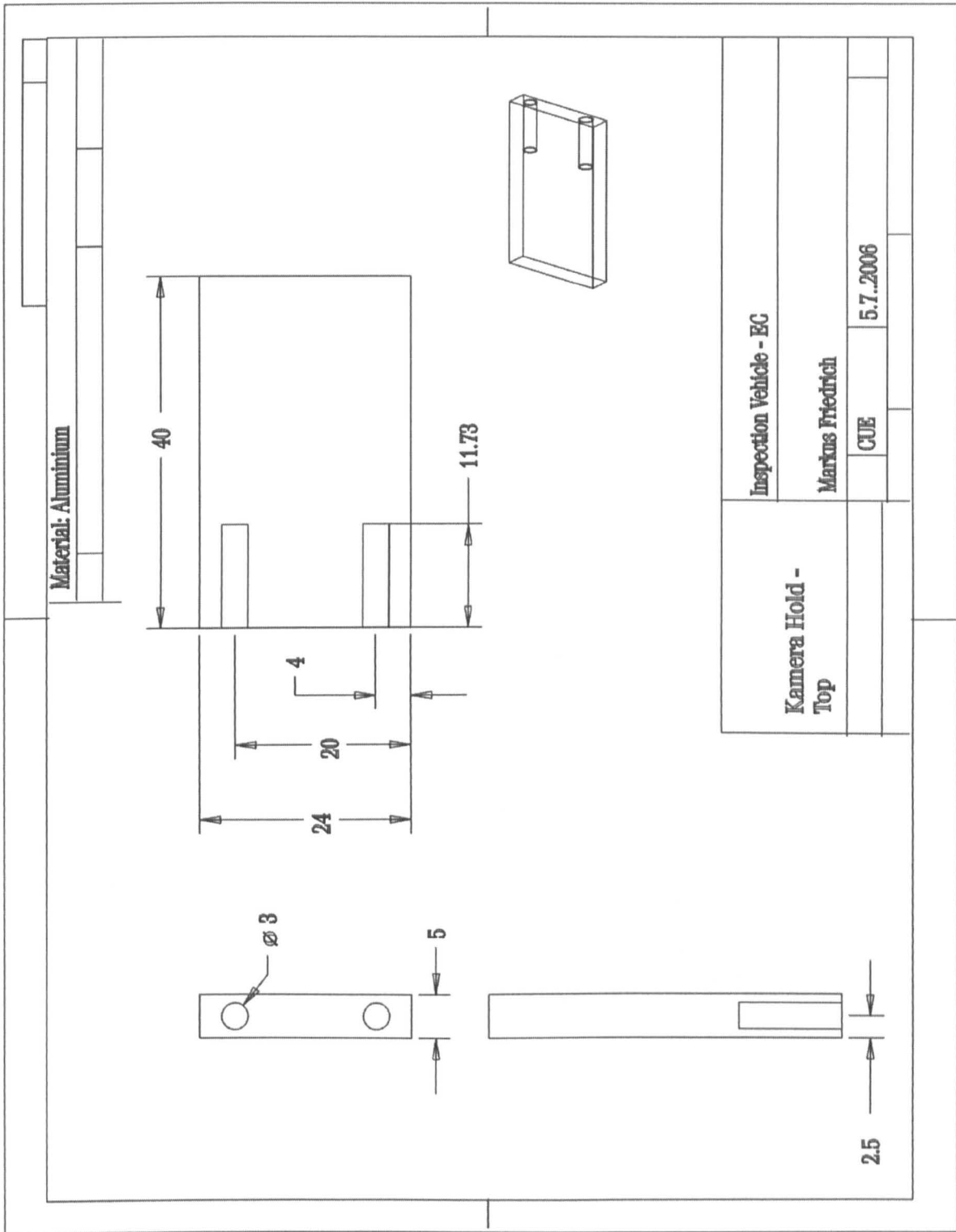
Figure A.33: Hold for Wireless Camera - Top Section

A.6   Miniature Design Prototype
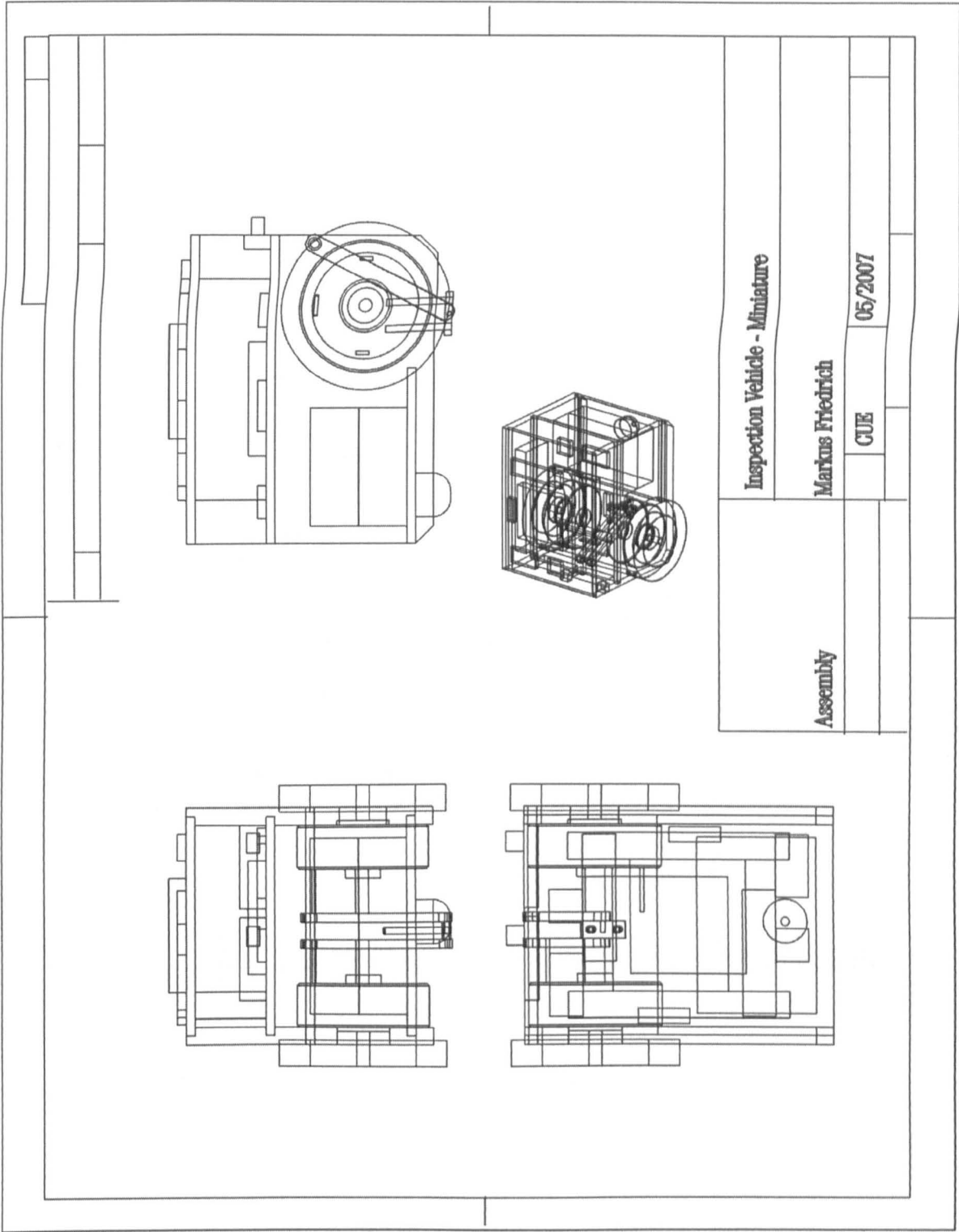
Figure A.34: Miniature Prototype - Assembly
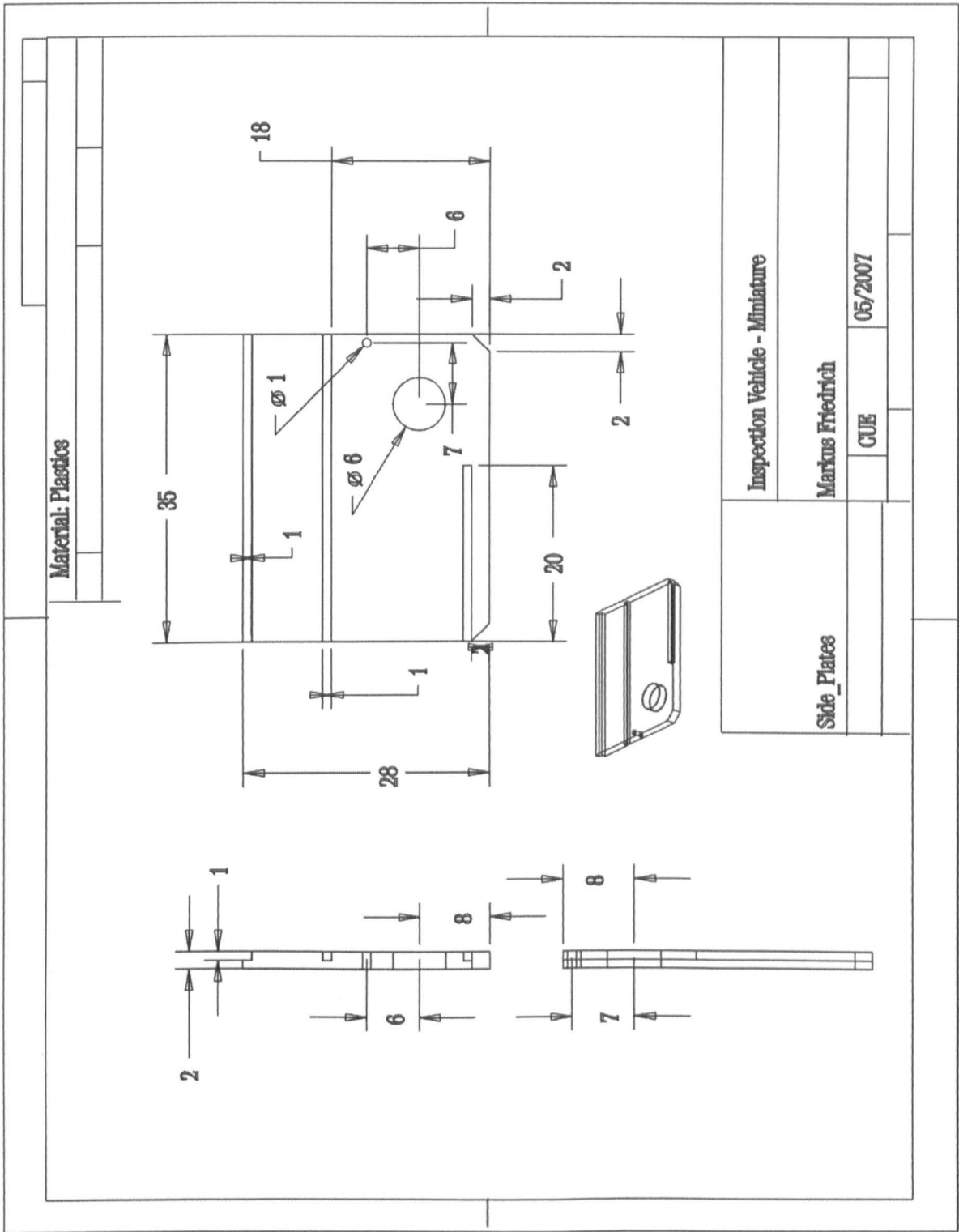
Figure A.35: Miniature Prototype - Side Plates
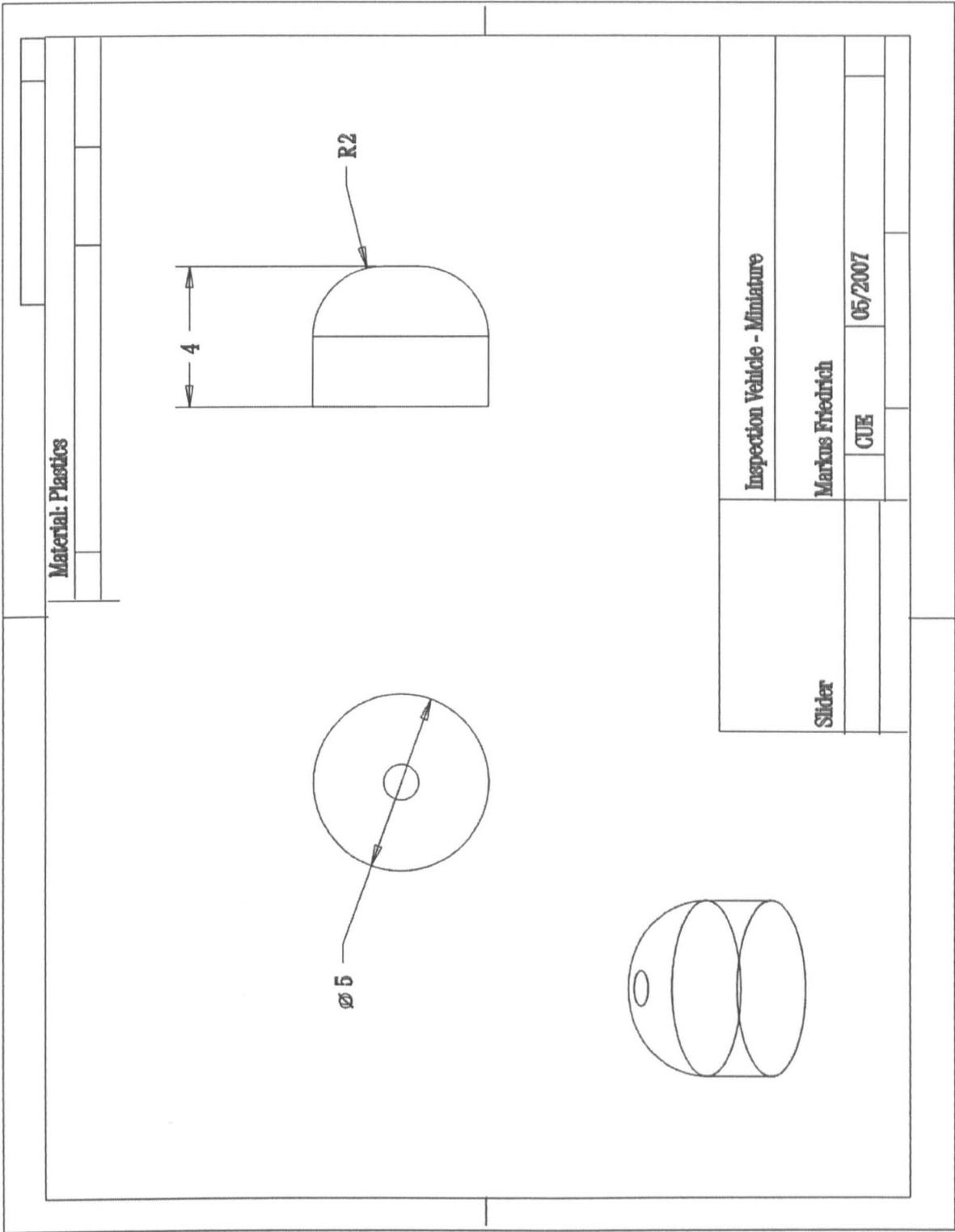
Figure A.36: Miniature Prototype - Back Support
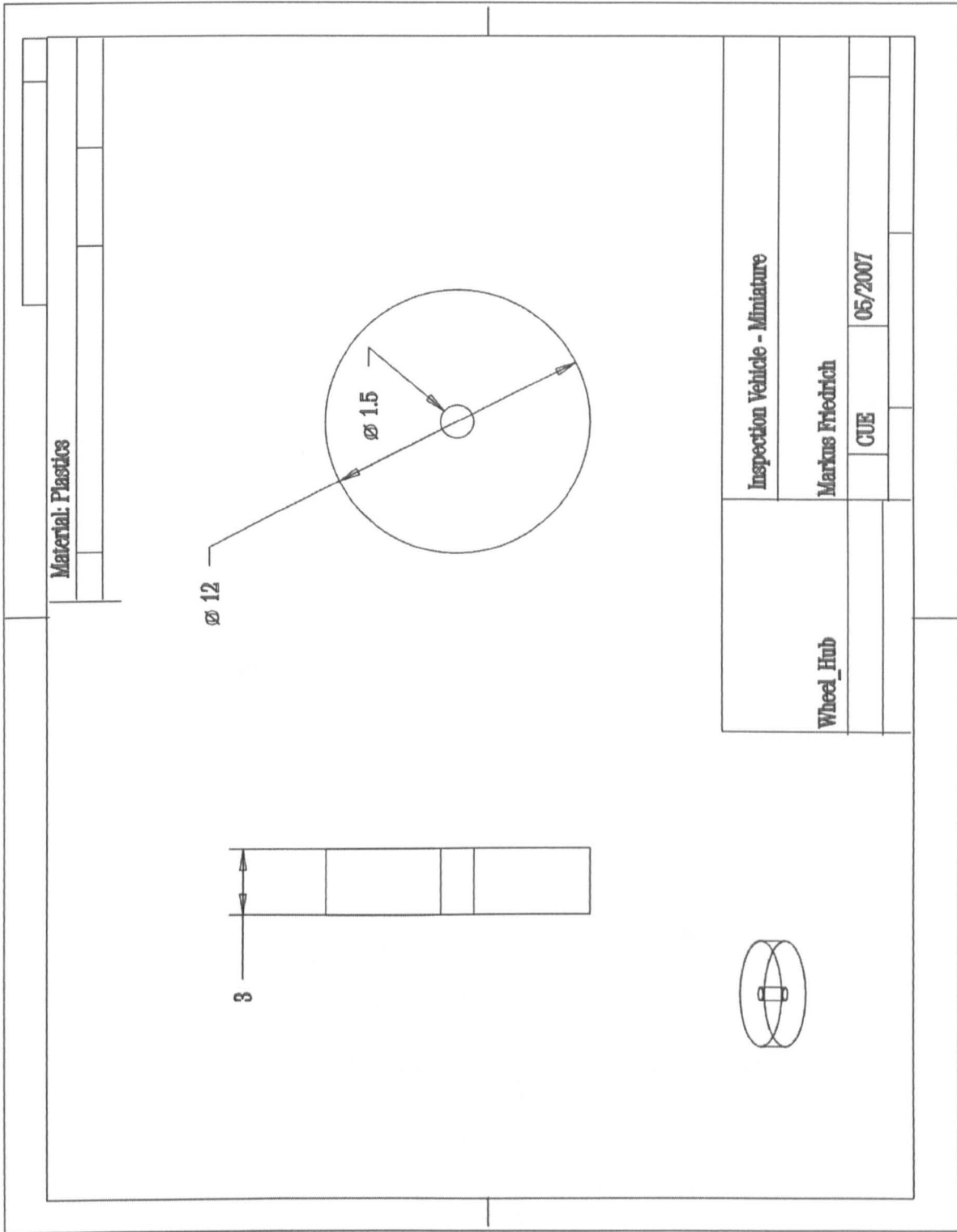
Figure A.37: Miniature Prototype - Wheel Hub
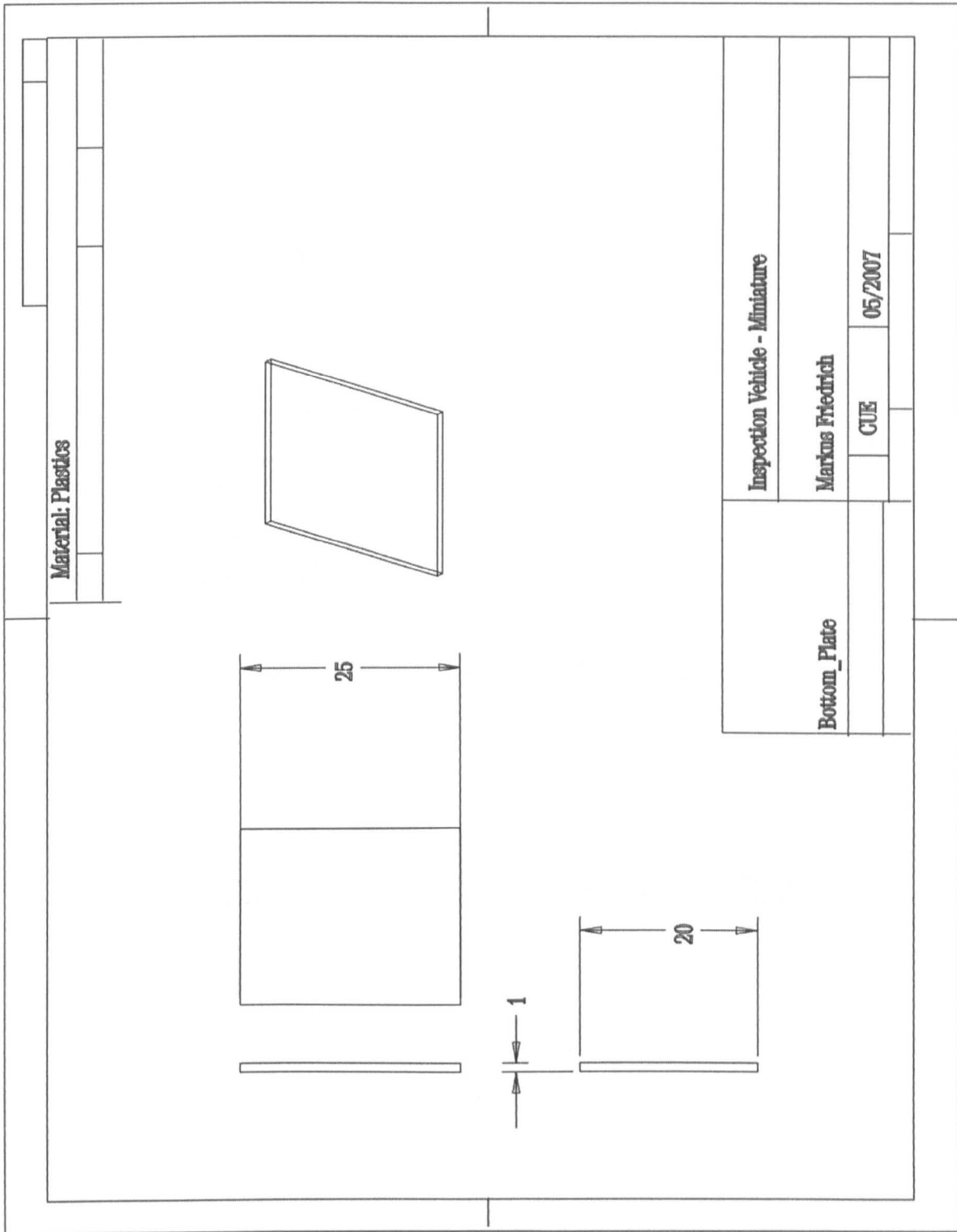
Figure A.38: Miniature Prototype - Bottom Plate for EC Sensor
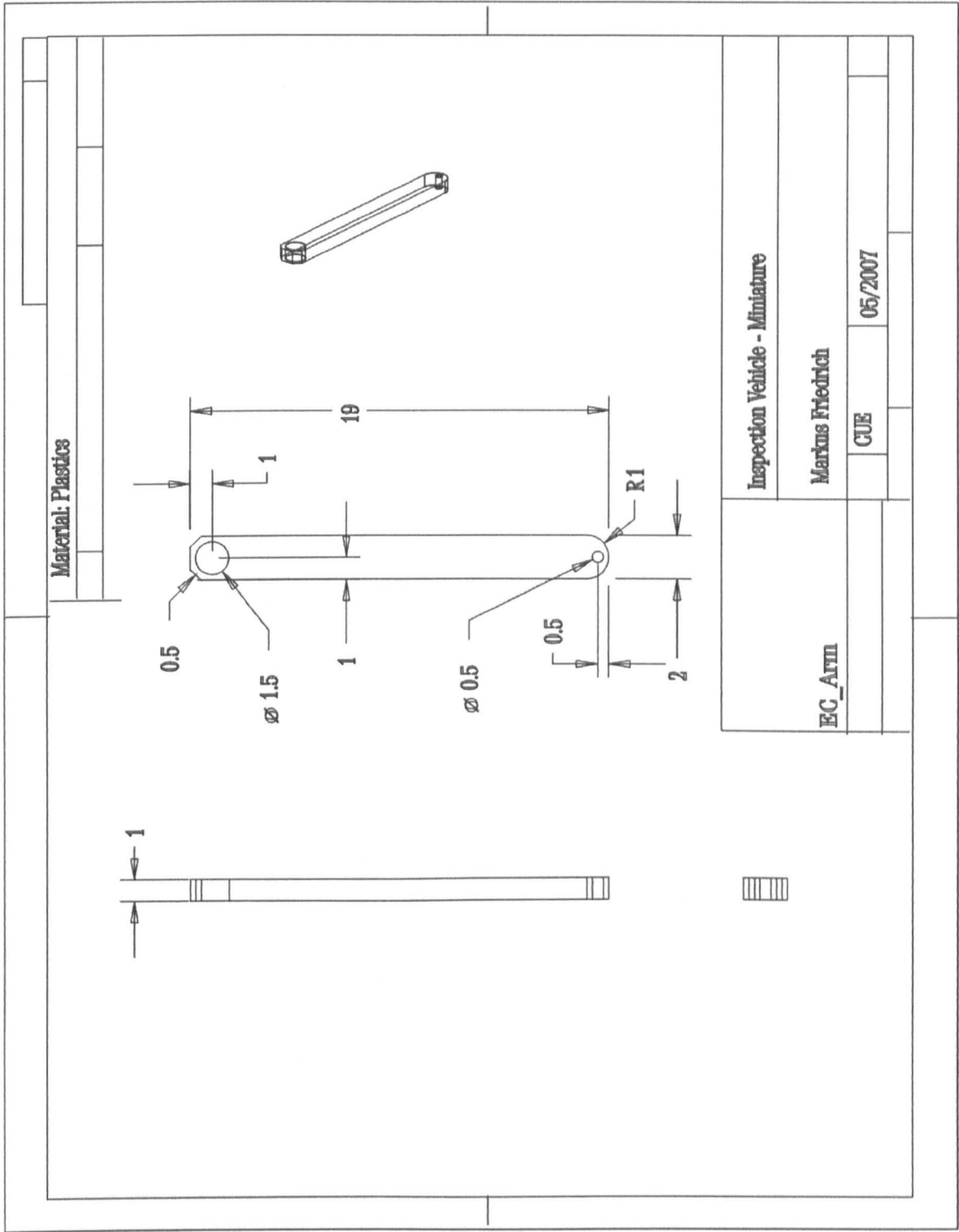
Figure A.39: Miniature Prototype - Levers for EC Sensor
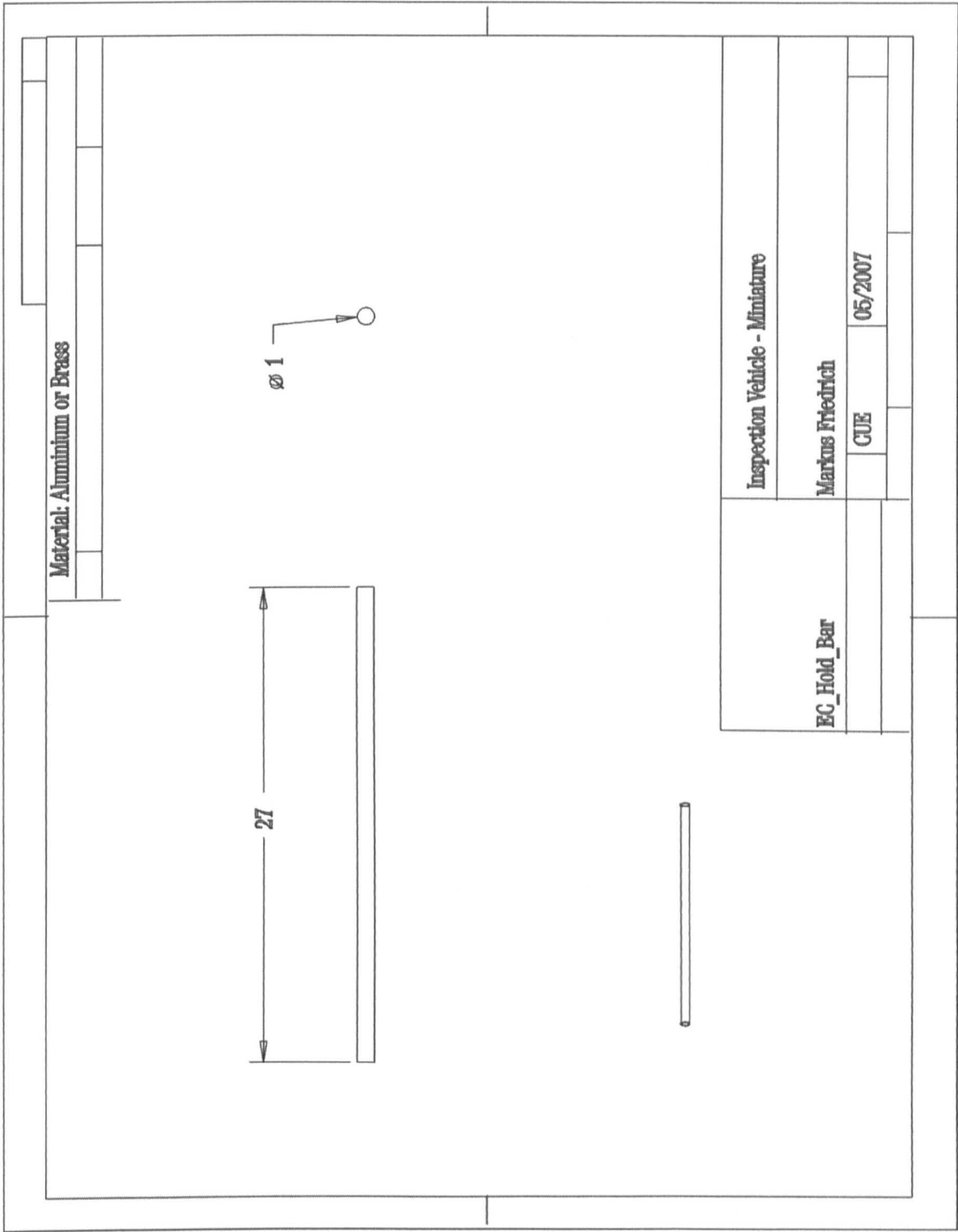
Figure A.40: Miniature Prototype - Bar for EC Lever

A.7 Improved Design with Lower Battery Position

Figure A.41: Battery Plate for improved design with lower battery position

Figure A.42: Chassis side plates for improved design with lower battery position

Figure A.43: Encoderholds for improved design with lower battery position

213

A.8   Structograms of On board programs

initialise motors and set driving direction
iniatialise variables and counters
reset encoder readings and integral counter for straight line control

```
for(c1=0; c1<40; c1++)
    average =0;
    for (c2=0; c2<20; c2++)
        enable A/D conversion
        last_twenty_readings[c2] = ADR1;
        average = average + last_twenty_readings[c2];
    average = average/20;
    evaluation[c1] = average;  // new reading into test array

while [(straight == 1) && (detected == 0)]
    c2=0; c1=0;
    while [(NDE_active == 1) && (c1 < 100)]
        for (i=0; i<20; i++)
            last_twenty_readings[c2] = ADR1;
            if (c2>18) // averaging over 20 samples to reduce noise
              Y                                                          N
                average = 0;
                for (i=0; i<20; i++)
                    average = average + last_twenty_readings[i];
                average = average/20;
                c2=0;
                evaluation[39] = average;  // reading new averaged  signal into vector
                for(i=0; i<20; i++)
                    overallaverage1 = overallaverage1 + evaluation[i];
                    evaluation[i] = evaluation[i+1]; // move one position left
                overallaverage1 = overallaverage1/20;
                for(i=20; i<40;i++)
                    overallaverage2 = overallaverage2 + evaluation[i];
                    evaluation[i] = evaluation[i+1]; //  move one position left
                overallaverage2 = overallaverage2/20;
                if (overallaverage2 > (overallaverage1 + 30))
                  Y                                             N
                    measure = overallaverage2-overallaverage1;
                    detected = 1;
                msleep(3) // sampling time between signals
                overallaverage1=0;    overallaverage2=0;
            c1++; c2++
    if (correction_counter>8)
      Y                                                          N
        correct for physical difference between left and right wheel
    read encoder pulses left and right wheel
    evaluate PI-loop
    set new power left and right motor
    process_command(); //  check serial port for new command
stop motors; detected = 0;
while(straight == 1)
send variable "measure" to host as indication for defect size
```

Figure A.44: Structogram of the subroutine for EC scanning.

215

initialise motors and set driving direction
iniatialise variables and counters
reset encoder readings and integral counter for straight line control

for(c1=0; c1<30; c1++)
enable A/D conversion
evaluation[c1] = ADR1;

while [(straight == 1) && (detected == 0)]
c1=0;

while [(NDE_active == 1) && (c1 < 100)]
enable A/D conversion
evaluation[29] = ADR1; // new reading into test array

for (i=0; i<15; i++)
evaldiff1 = evaldiff1 + (evaluation[i+1] - evaluation[i]);
evaluation[i] = evaluation[i+1]; // move one position left
// obtaining average gradient of left 15 elements in vector evaluation[]

for(i=15; i<30; i++)
evaldiff2 = evaldiff2 + (evaluation[i+1] - evaluation[i]);
evaluation[i] = evaluation[i+1]; // move one position left
// obtaining average gradient of left 15 elements in vector evaluation[]

if (evaldiff2 > (evaldiff1 + 14))

Y ——————————————————————————— N

indicator = indicator + 1;	indicator=0;
measure = measure + (evaldiff2 - evaldiff1);	measure=0;

if (indicator >5)

Y ——————————————————————————— N

detected=1;
msleep(3); // sampling time between measurements
evaldiff1=0; evaldiff2=0; c1++;

if (correction_counter>8)

Y ——————————————————————————— N

correct for physical difference between left and right wheel
read encoder pulses left and right wheel
evaluate PI-loop
set new power left and right motor
process_command(); // check serial port for new command

stop motors; detected = 0;

while(straight == 1)
send variable "measure" to host as indication for defect size

Figure A.45: Structogram of the subroutine for MFL scanning.

initialise motors
initialise variables
set direction
start motors
while ({[(left_clicks_sum + right_clicks_sum)/2] < L} && (nde_active = 1))
msleep(control_interval);
if (correction_counter > threshold)
Y   N
correct for physical difference between left and right wheel
read encoders
evaluate PI-loop
set new power left and right motor
process_command(); // check serial port for new command
stop motors

Figure A.46: Structogram of the subroutine for a 1 m straight path.

initialise motors
set turning speed
set direction
start motors
while [(right_clicks_sum < threshold) && (left_clicks_sum < threshold)]
read encoders
update right_clicks_sum and left_clicks_sum
msleep(control_interval_turning)
stop motors

Figure A.47: Structograms of the subroutines for 90° left and right turns.

stop motors

Figure A.48: Structogram of the subroutines for stopping NDE scans.

initialise motors
set direction
start motors

Figure A.49: Structograms of the subroutines for basic left and right turns and driving backwards.

217

```
while(NDE_active ==1)
    while( overall_encoder_pulses_left_and_right < side_length1)
        forward
    right90
    while( overall_encoder_pulses_left_and_right <side_length2)
        forward
    right90
    while( overall_encoder_pulses_left_and_right <side_lenght1-sensor_width)
        forward
    right90
    while( overall_encoder_pulses_left_and_right <side_length2)
        forward
    right90
```
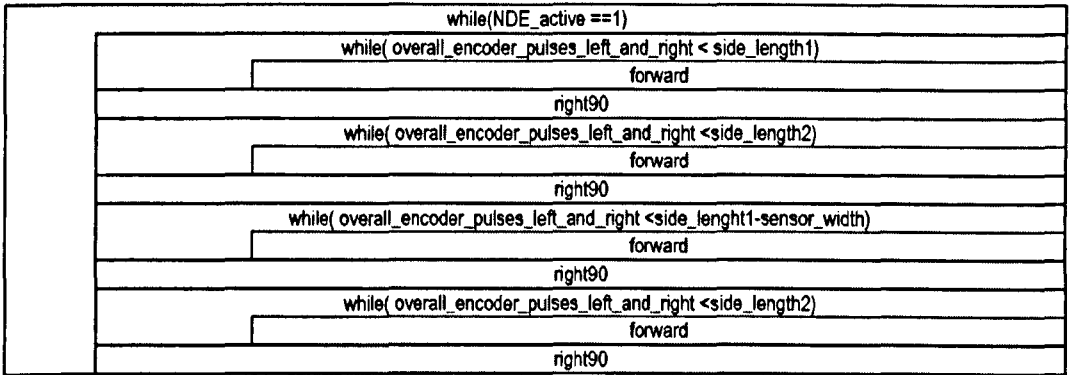
Figure A.50: Structograms of the subroutines for clockwise scans.

```
while(NDE_active ==1)
    while( overall_encoder_pulses_left_and_right < side_length1)
        forward
    left90
    while( overall_encoder_pulses_left_and_right <side_length2)
        forward
    left90
    while( overall_encoder_pulses_left_and_right <side_lenght1-sensor_width)
        forward
    left90
    while( overall_encoder_pulses_left_and_right <side_length2)
        forward
    left90
```
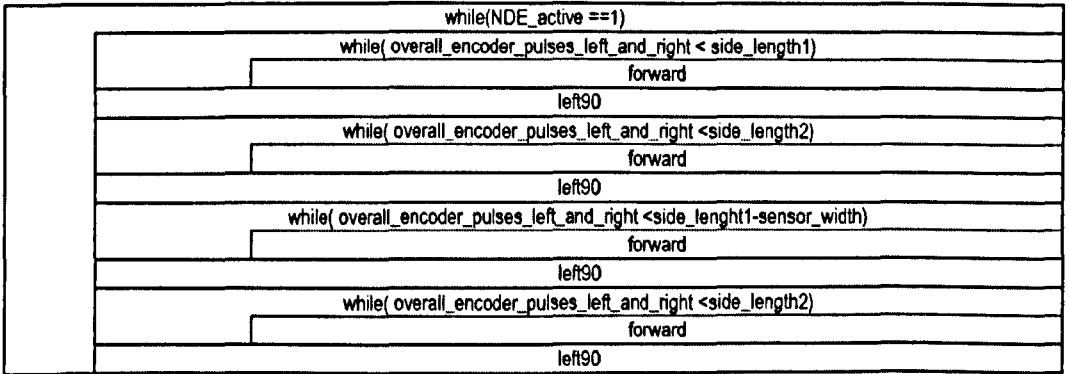
Figure A.51: Structograms of the subroutines for counter clockwise scans

```
NDE_active =1;
```
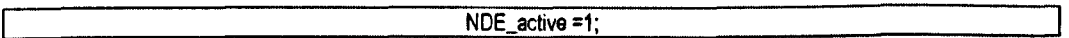
Figure A.52: Structogram of the subroutines for starting NDE scans.

218

Bibliography

[1] E. Acar, H. Choset, Y. Zhang and M. Schervish, "Path Planning for robotic demining: robust sensor based coverage of unstructured environments and probabilistic methods," *Int. Journal of Robotics Research*, vol. 78, pp. 441—466, 2003.

[2] M. Afzal and S. Udpa, " Advanced signal processing of magnetic flux leakage data obtained from seamless gas pipeline," *NDT&E International*, vol. 35, pp. 449—457, 2002. 1

[3] R. Akkiraju, P. Keskinocak, S. Murthy, and F. Wu, "An agent-based approach for scheduling multiple machines," *Appl. Intell.*, vol. 14, pp. 135–144, 2001. 10

[4] D.N. Alleyne, "The non-destructive testing of plates using ultrasonic lamb waves," PhD Thesis, Imperial College of Science, Technology and Medicine, University of London, 1991.

[5] M. Almonacid, R. J. Saltarn, R. Aracil, and O. Reinoso, "Motion planning of a climbing parallel robot," *IEEE Transactions on Robotics and Automation*, vol. 19, pp. 485—489, June 2003. 13

[6] B.P. Amavasai, F. Caparrelli, A. Selvan, M. Boissenin, J.R. Travis and S. Meikle, "Machine vision methods for autonomous micro-robotic systems," *Kybernetics*, vol. 34, pp. 1421—1439, 2005. 8

[7] B.W. Andrews, K.M. Passino and T.A. Waite, "Social foraging theory for robust multiagent system design," *IEEE Transactions on Automation Science and Engineering*, vo. 4, pp. 79—86, Jan. 2007. 9

[8] G. Antonelli, S. Chiaverini and G. Fusco, "Exciting trajectories for mobile robot odometry calibration," in *Preprints 7th IFAC Symp. Robot Control*, Wroclaw, Poland, Sep. 2003, pp. 429–434. 51

[9] G. Antonelli, S. Chiaverini, and G. Fusco, "A calibration method for odometry of mobile robots based on the least-squares technique: theory and experimental validation", *IEEE Transactions on Robotics and Automation*, vol. 21, pp. 994—1004, Oct. 2005. 51

[10] D. M. Aslam and G.D. Dangi, "Design, fabrication and testing of a smart robotic foot," *Robotics and Autonomous Systems*, vol. 51, pp. 207—214, 2005. 7, 12

[11] K. Autumn, M. Sitti, Y.A. Liang, A.M. Peattie, W.R. Hansen, S. Sponberg, T. Kenny, R. Fearing, J.N. Israelachvili and R.J. Full, "Evidence for van der Waals Adhesion in Gecko State," *National Academy of Sciences*, vol. 99, pp. 12252—12256, 2002. 13

219

[12] T. Aytur, P.R. Beatty and B. Boser, "An Immunoassay Platform Based on CMOS Hall Sensors," in *Proc. of IEEE international Conference on Sensors*, 2002, pp. 126—129. 162

[13] C. Balaguer , A. Gimnez , J.M. Pastor, V.M. Padrn and M. Abderrahim, "A Climbing Autonomous Robot for Inspection Applications in 3D Complex Environments," *Robotica*, vol. 18, pp. 287—297, May 2000. 11

[14] T. Balch and R.C. Arkin, "Behavior-Based Formation Control for Multirobot Teams," *IEEE Transactions on Robotics and Automation*, vol. 14, pp. 926—939, Dec. 1998. 9

[15] Stuart R. Ball, "Embedded Microprocessor Systems," 2nd ed., Amsterdam, Boston, Elsevier/Newnes, 2004. 34

[16] R. Bellazzi, P. Magni and G. De Nicolao, "Bayesian analysis of blood glucose time series from diabetes home monitoring," *IEEE Transactions on Biomedical Engineering*, vol. 47, pp. 971—975, July 2000. 131

[17] C. Bererton and P. K. Khosla, "Towards a team of robots with repair capabilities: A visual docking system," in *Proc. 7th Int. Symp. Exp. Robot*, 2001, pp. 333-342. 9

[18] C. Bererton and P. K. Khosla, "Towards a team of robots with reconfiguration and repair capabilities, in *Proc. IEEE Int. Conf. Robot. Autom.*, 2001, pp. 2923-2928. 9

[19] J. Bisson, F. Michaud, and D. Letourneau, "Relative positioning of mobile robots using ultrasounds, in *Proc. of IEEE Int. Conf. on Robotics and Automation* , 2003, pp. 1783—1788. 15

[20] B. Blakeley, C. Emmanouilidis and K. Hrissagis, "Above-ground storage tank inspection using the 'robot inspector'," *Insight*, vol. 47, pp. 705—708, 2005. 19, 102, 151

[21] A. Boenisch and F.H. Dijkstra, "Magnetic Flux and SLOFEC Inspection of Thick Walled Components," in *Proc. of 15th World Congress of Non Destructive Testing*, 2000. 17, 85, 102, 109

[22] P. Bonnifait, P. Bouron, P. Croubill, and D. Meizel, "Data fusion of four ABS sensors and GPS for an enhanced localization of car-like vehicles," in *Proc. IEEE Int. Conf. Robot. Autom.*, Seoul, Korea, May 2001, pp. 1597-1602. 16

[23] A. Bonvilain and N. Chaillet, "Microfabricated thermally actuated microrobot," in *IEEE International Conference on Robotics and Automation*, vol. 3, pp. 2960—2965, 2003. 7

[24] J. Borenstein and L. Feng, "Correction of systematic odometry errors in mobile robots," in *Proc. of IEEE/RSJ International Conference on Intelligent Robots and Systems*, 1995, pp. 569—574. 51

[25] J. Borenstein, H.R. Everett and L Feng, "Where am I? Systems and Methods for Mobile Robot Positioning," University of Michigan, 1996. 51

[26] J. Borenstein and L. Feng, "Measurement and correction of systematic odometry errors in mobile robots," *IEEE Trans. Robot. Autom.*, vol. 12, no. 6, pp. 869-880, Dec. 1996. viii, 51, 53

[27] J. Borenstein, H. R. Everett, L. Feng and D. Wehe, " Mobile robot positioning: Sensors and techniques," *Journal of Robotic Systems*, vol. 14, pp. 231—249, 1998. 14, 15, 51, 75

[28] B. Bos, S. Sahln and J. Andersson, "Automatic Scanning with Multi-Frequency Eddy Current on Multi-Layered Structures," *Aircraft Engineering and Aerospace Technology*, vol. 75, pp. 491—496, 2003. 85

[29] Tony Boutros and Ming Liang, "Mechanical fault detection using fuzzy index fusion," *International Journal of Machine Tools and Manufacture*, vol. 47, pp. 1702—1714, September 2007. 131

[30] F. Brandt, W. Brauer, and G. Wei, "Task assignment in multiagent systems based on vickrey-type auctioning and levelled commitment contracting," in *Proc. Cooperative Information Agents Workshop*, Boston, MA, 2000, pp. 95–106. 10

[31] T. Bräunl, "Embedded Robotics — Mobile Robot Design and Applications with Embedded Systems," Springer-Verlag Berlin, Heidelberg, 2003. 82

[32] D.E. Bray and D. McBride, "Nondestructive Testing Techniques," Wiley, New York, 1992. 18

[33] T. Bretl, T. Miller, S. Rock and J.C. Latombe, "Climbing Robots in Natural Terrain," in *Proc. of 9th International Symposium on Artificial Intelligence, Robotics and Automation in Space*, 2003. 11

[34] T. Bretl, "Problem Motion Planning of Multi-Limbed Robots Subject to Equilibrium Constraints: The Free-Climbing Robot," *The International Journal of Robotics Research*, vol. 25, pp. 317—342, April 2006. 11

[35] W. Brockmann, "Concept for Energy-Autarkic, Autonomous Climbing Robots," in *Proc. of 8th International Conference on Climbing and Walking Robots*, London, 2005. 11

[36] H.B. Brown, M.V. Weghe, C.A. Bererton, P.K. Khosla, "Millibot Trains for Enhanced Mobility," *IEEE/ASME Transactions on Mechatronics*, vol 7., pp. 252—461, 2002. 10

[37] W. Burgard, M. Moors, D. Fox, R. Simmons and S. Thrun, "Collaborative multi-robot exploration," in *Proc. of IEEE International Conference on Robotics and Automation*, 2000, pp. 476—481. 11

[38] G. Campion, G. Bastin and B. D'Andre'a-Novel,"Structural Properties and Classification of Kinematic and Dynamic Models of Wheeled Mobile Robots," *IEEE Transactions on Robotics and Automation*, vol. 1, pp. 47—62, 1996. 27

[39] Cao, Y., U., Fukunaga, A., S., Kahn, A., Cooperative Mobile Robotics: Antecedents and Directions, Journal Autonomous Robots, vol. 4, No. 1, pp. 7—27, 1997.

[40] G. Caprari, K.O Arras and R. Siegwart, "The autonomous miniature robot Alice: from prototypes to applications," in *Proceedings of IEEE/RSJ International Conference on Intelligent Robots and Systems*, 2000, pp. 793—798. viii, 8

221

[41] G. Caprari, A. Colot, R. Siegwart, J.Halloy and J.L. Deneubourg, "Animal and robot mixed societies: building cooperation between microrobots and cockroaches, " IEEE Robotics and Automation Magazine, vol. 12, pp. 58—65, June 2005. 8, 37, 147

[42] G. Caprari, and R. Siegwart, "Mobile micro-robots ready to use: Alice," in *Proc. of IEEE/RSJ International Conference on Intelligent Robots and Systems*, 2005, pp. 3295—3300. 8

[43] A. A. Carvalho, I.C. Silva, J.M.A. Rebello, R.O. Carneval, and J.A.B. Farias, "Inspection of ship hulls using automated ultrasonic inspection," *BINDT Insight*, vol. 47., No. 12, 2005. 18, 19

[44] A.A. Carvalho, I.C. Silva, L.V.S. Sagrilo, M.H.S. Siqueira, R.R. Silva and R.O. Carneval, "Automated multi-channel system for ultrasound inspection on a FPSO type ship hull," in *Proc. of 8th European Conference on Non-Destructive Testing*, 2002. 19

[45] J.A. Castellanos, J. Neira, J.D. Tardos, "Multisensor fusion for simultaneous localization and map building," IEEE Transactions on Robotics and Automation, vol. 17, pp. 905—908, Dec. 2001. 16

[46] M. D. Cecco, "Sensor fusion of inertial-odometric navigation as a function of the actual manoeuvres of autonomous guided vehicles", *Measurement Science and Technology*, pp. 643—653, 2003. 16

[47] T. Chadzelek, J. Eckstein, and E. Schr, "Multirobot path planning by predicting structure in a dynamic environment," in *Proc. 8th Canadian Conf. Computational Geometry*, Ottawa, Canada, Aug. 1996, pp. 131–136. 10

[48] L. Chaimowicz, M.F.M. Campos and V. Kumar, "Dynamic Role Assignment for Cooperative Robots," in *Proc. of IEEE International Conference on Robotics and Automation*, 2002, pp. 293—298. 7

[49] P. Chatzakos, Y. P., Markopoulos, K. Hrissagis and A. Khalid, "On the Development of a Modular External-pipe Crawling Omni-directional Mobile Robot," in *Proc. of 8th International Conference on Climbing and Walking Robots*, London, 2005. 1, 2, 13, 33

[50] T.M. Chen and V. Venkataramanan, "Dempster-Shafer theory for intrusion detection in ad hoc networks, " *IEEE Internet Computing*, volume 9, pp. 35—41, Dec. 2005. 131

[51] B.-H. Cho, S.H. Byun, C.H. Shin, J.B. Yang, S.I. Song and J.M. Oh,"KeproVt : underwater robotic system for visual inspection of nuclear reactor internals," *Nuclear Engineering and Design*, vol. 231, pp. 327—335, July 2004. 19

[52] H.R. Choi and S.M. Ryew, "Robotic system with active steering capability for internal inspection of urban gas pipelines", Mechatronics, pp. 713—736, 2002. 12

[53] P. C. Chu and J. E. Beasley, "A genetic algorithm for the generalised assignment problem," *Comput. Oper. Res.*, vol. 24, no. 1, pp. 17–23, 1997. 10

[54] L. Clapham and D.L. Ahterton, "Magnetic Flux Leakage Inspection of Oil and Gas Pipelines," in *Proc. of Annual Conference of Metallurgists of the Canadian Institute of Mining and Metallurgy*, 1998, pp. 313—326. 44, 146

[55] S.O. Connor, L. Clapham and P. Wild, "Magnetic Flux Leakage Inspection of Tailor-Welded Blanks," *Measurement Science and Technology*, vol. 13, pp. 157—162, 2002. 103, 151

[56] D. Conte, P. Foggia, J.-M. Jolion and M. Vento, "A graph-based, multi-resolution algorithm for tracking objects in presence of occlusions," *Pattern Recognition*, vol. 39, pp. 562—572, April 2006. 131

[57] K. Copsey, N. Gordon and A. Marrs, "Bayesian analysis of generalized frequency-modulated signals," *IEEE Transactions on Signal Processing*, vol. 50, pp. 725—735, March 2002. 131

[58] A. Coreeia da Cruz and M. Ribeiro, "RobTank Inspec – in service robotized inspection tool for hazardous products storage tanks," *Industrial Robot*, vol. 32, pp. 157—162, 2005. 12, 18, 19

[59] N. Correll and A. Martinoli, "Collective inspection of regular structures using a swarm of miniature robots"in *Proc. of 9th Int. Symp. on Experimental Robotics*, Singapore, June 2004. 10, 162

[60] N. Correll and A. Martinoli, "A challenging application in Swarm robotics: the autonomous inspection of complex engineered structures." in *Bulletin of the Swiss Society for Automatic Control*, vol. 46, pp. 15—19, 2007. 10, 153

[61] N. Correl and A. Martinoli, "Towards optimal control of self-organized robotic inspection systems," in*Proc. of the Eight IFAC Int. Symp. on Robot Control*, Sept. 2006, Italy, paper No. R-035. 10

[62] K. Daltorio, S. Gorb, D.S. Horchler, R.S. Ritzmann and R.D. Quinn, "A robot that climbs walls using micro-structure polymer feed," in *Proc. of 8th International Conference on Climbing and Walking Robots*, 2005. 13

[63] P. Dario, R. Valleggit, M.C. Carrozzat, M.C. Montesit and M. Coccot "Review microactuators for microrobots: a critical survey," *Journal Micromech, Microeng.*, vol. 2, pp. 141—157, 1992. 7

[64] J.P. Desai, J.P. Ostrowski, V. Kumar, "Modeling and control of formations of nonholonomic mobile robots," IEEE Trans. on Robotics and Automation, vol. 17, pp. 905—908, 2001. 16

[65] R.J. Ditchburn and S.K. Burke, "Planar rectangular spiral coils in eddy-current non-destructive inspection," *NDT&E International*, vol. 38, pp. 690 – 700, 2005. 85

[66] A. Dogandzic and B. Zhang, "Bayesian NDE Defect Signal Analysis," *IEEE Transactions on Signal Processing*, vol. 55, pp. 372—378, Jan. 2007. 131

[67] B.R. Donald, C.G. Levey, C.D. McGray, I. Paprotny and D. Russ, "An untethered, electrostatic, globally controllable MEMS micro-robot," Journal of Microelectromechanical Systems, vol. 15, pp. 1—15, Feb. 2006. 7

[68] M. Dorigo, M. Birattari, C. Blum, L.M. Gambardella, F. Mondada and T. Sttzle, "Ant colony optimization and swarm intelligence," *4th International Workshop ANTS 2004*, vol. 3, pp. 107—118, 2004. 10

[69] A. Drenner, M.A. LaPoint, I. Burt, K. Cannon, C. Hays, A.D. Kottas and N.P. Papanikolopoulos, "Increasing the Scout's effectiveness through local sensing and ruggedization," in *Proc. of IEEE International Conference on Robotics and Automation*, 2004, pp. 1406—1411. 9

[70] D.D. Duncan, J.L. Champion, K.C. Baldwin and D.W. Blodgett, "Optical Methods in Nondestructive Evaluation — theory, techniques and applications," Marcel Decker, New York, 2002. 18

[71] O. Duran, K. Althoefer and L. D. Seneviratne, "Automated Pipe Defect Detection and Categorization Using Camera/Laser-Based Profiler and Artificial Neural Network," *IEEE Transactions on Automation Science and Engineering*, vol. 4, pp. 118—126, January 2007. 131

[72] M. Egerstedt and H. Xiaoming, "Formation constrained multi-agent control," in *IEEE Int. Conf. Robotics and Automation*, vol. 4, 2001, pp. 3961–3966. 16

[73] N. Elkmann, T. Felsch, M. Sack, J. Saenz and J. Hortig, "Innovative service robot systems for facade cleaning of difficult-to-access areas," in *Proc. of IEEE/RSJ International Conference on Intelligent Robots and System*, 2002, pp. 756—762. 12

[74] Y. Endo, D. C. Mackenzie, and R. C. Arkin, "Usability evaluation of high-level user assistance for robot mission specification," *IEEE Trans. Syst., Man, Cybern. C, Appl. Rev.*, vol. 34, no. 2, pp. 168–180, May 2004. 10

[75] R. Estana, J. Seyfried, F. Schmoeckel, M. Thiel, A. Buerkle and H. Woern, "Exploring the Micro- and Nanoworld with Cubic Centimetre-Sized Autonomous Microrobots," *Industrial Robot*, vol. 31, pp. 159—178, 2004. 8

[76] Z. Fan, G. S. Pereira, V. Kumar, "Cooperative Localization and Tracking in Distributed Robot-Sensor Networks", in *Tsingua Science and Technology*, vol. 10, pp. 91—101, February 2005. 16

[77] R. Farlow and G. Hayward, "Real-time ultrasonic techniques suitable for implementing non-contact NDT systems employing piezoceramic composite transducers", *Insight*, vol. 36, No. 12, pp. 926—935, 1994. 128

[78] S. Farritor and S. Dubowsky, "On Modular Design of Field Robotic Systems ", *Autonomous Robots*, vol. 10, pp. 57—65, Jan. 2001. 33

[79] J.T. Feddema, C. Lewis and D.A. Schoenwald, "Decentralized Control of Cooperative Robotic Vehicles: Theory and Application," *IEEE Transactions on Robotics and Automation*, vol. 18, No. 5, pp. 852—864, 2002. 16

[80] Y. Fei, X. Zhao and J. Wan, "Motion Analysis of a Modular Inspection Robot with Magnetic Wheels," in *Proc. of Sixth World Congress on Intelligent Control and Automation*, vol. 2, pp. 8187—8190, 2006. 33

[81] D. Floreano, N. Schoeni, G. Caprari and J. Blynel, "Evolutionary Bits'n'Spikes," *Artifcial Life*, vol. 8, pp. 335—344, 2002. 8

224

[82] A.M. Flynn, R.A. Brooks, W.M. Wells and D.S. Barrett, "Intelligence for miniature robots," *Sensors & Actuators*, vol. 20, pp. 187—196, 1989. 7

[83] D. Fox, J. Hightower, H. Kauz, L. Liao and D. Patterson, "Bayesian Techniques for Location Estimation," in *Proc. of Workshop on Location-aware Computing, UBI-COMP Conference*, Seattle, WA, October 2003.

[84] M. Friedrich, L. Gatzoulis, W. Galbraith and G. Hayward, "Small inspection vehicles for non-destructive testing applications", in *Proc. of 8th International Conference on Climbing and Walking Robots*, 2005, pp. 927—934.

[85] M. Friedrich, W. Galbraith, G. Hayward, "Autonomous Mobile Robots for Ultrasonic NDE," in *Proc. of IEEE International Ultrasonics Symposium*, Vancouver, Canada, October 2006, pp. 902—905. 121

[86] J. Frounchi, M. Demierre, Z. Randjelovic and R.S. Popovic, "Integrated Hall Sensor Array Microsystem, in *Proc. of IEEE Solid-State Circuits Conference*, 2001, pp. 248—249. 162

[87] Y. Fukaya, A. Torii, K. Doki and A. Ueda, "Motion of a miniature robot driven by rapid deformation of piezoelectric element," in *Proceedings of International Symposium on Micromechatronics and Human Science*, 2003, pp. 323—328. 7

[88] Y. Gabriely and E. Rimon, "Spiral-stc: An Online Coverage Algorithm of Grid Environments by a Mobile Robot," in *Proc. of IEEE Conference on Robotics & Automation*, vol. 1, pp. 954—960, 2002.

[89] D. Geer, "News: Small Robots Team Up to Tackle Large Tasks," *IEEE Distributed Systems Online*, vol. 6, Nr. 12, 2005. 9

[90] G.A. Georgiou, "Derivation, Probability of Detection (PoD) curves — Derivation, applications and limitations," *Health and Safety Executive*, Research Report 454, Jacobi Consulting Limited, London, 2006. 20

[91] B.P. Gerkey and M.J. Mataric, "Sold!: Auction Methods for Multirobot Coordination" IEEE Transactions on Robotics and Automation, vol. 18, pp. 758—768, Oct. 2002. 9

[92] E. Ginzel, "Introduction to the Statistics of NDT," *NDT.net — e-Journal of Nondestructive Testing*, vol. 11, No. 5, 2006. 20

[93] A. Gonzaga and A. Kawanaka, "Wavelet-based Bayesian analysis of generalized long-memory process Acoustics," in *Proc. of IEEE International Conference on Speech, and Signal Processing*, 2005, pp. 309—312. 131

[94] Y. Gotoh and N. Takahashi, "3-D Nonlinear Eddy-Current Analysis of Alternating Magnetic Flux Leakage Testing – Analysis of One Crack on Two Cracks," *IEEE Transactions on Magnetics*, vol. 38, vol. 38, pp. 1209—1212, 2002. 85

[95] A. F. Grandt, "Fundamentals of structural Integrity: Damage Tolerant Design and Nondestructive Evaluation," John Wiley, Hoboken, New Jersey, 2004. 18

[96] R. Grabowski and P. Khosla, "Localization techniques for a team of small robots," in *Proc. of International Conference on Intelligent Robots and Systems*, 2001, pp. 1067—1072. 9, 11, 75

225

[97] R. Grabowski, P. Khosla and H. Choset, "Autonomous exploration via regions of interest," in *Proc. of IEEE/RSJ International Conference on Intelligent Robots and Systems*, 2003, pp. 1691—1696. 9

[98] J.C. Grieco, M. Prieto, M. Armada and P. Gonzalez de Santos, "A Six-legged Climbing Robot for High Payloads," in *Proc. of the IEEE, Int. Conference on Control Applications*, 1998, pp. 446—450. 18

[99] X. Gros, "NDT Data Fusion," John Wiley & Sons, New York, 1997. 131, 139

[100] X. Gros, J. Sousigue and K. Takahashi, "NDT data fusion at pixel level," *NDT&E International*, vol. 32, pp. 283—292, 1998. 139, 156

[101] X. Gros, Z. Liu, K. Tsukada and K. Hanasaki, "Experimenting with Pixel-Level NDT Data Fusion Techniques, " *IEEE Transactions on Instrumentation and Measurement*, vol. 49, pp. 1083—1090, Oct. 2000. 139

[102] R. Gross, M. Dorigo and Y. Masaki, "Self-assembly of Mobile Robots: From Swarmbot to Super-Mechano Colony," in *Proc. of the 9th Int. Conf. on Intelligent Autonomous Systems*, 2006, pp. 487—496. 10

[103] R. Gro, M.Bonani, F. Mondada and M. Dorigo, "Autonomous Self-Assembly in Swarm-Bots," *IEEE Transactions on Robotics*, vol. 22, pp. 1115—1130, Dec. 2006. 10

[104] R. Gro, E. Tuci, M. Dorigo, M. Bonani, and F. Mondada, "Object transport by modular robots that self-assemble, in *Proc. of IEEE Int. Conf. Robot. Autom.*, 2006, pp. 2558-2564. 10

[105] R. Halmshaw, "Non-Destructive Testing," 2nd edition, Edward Arnold, London, 1991. 18, 86, 87, 103, 128

[106] E. Haemmerle, P. Winton, and S. Fett, " Multipath-mitigating Indoor Carrier-phase Position Tracking System," *Proc. of Position Location and Navigation Symposium*, 2004, pp. 671—673. 16

[107] J. Hansen, "The eddy current inspection method," *Insight*, vol. 46, pp. 279-281, 2004. 85

[108] R. Harle, A. Hopper, "Deploying and Evaluating a Location-Aware System," in *Proc. of the 3rd international Conference on Mobile Systems, Applications, and Services*, 2005, pp. 219—232.

[109] A. Harter, A. Hopper, P. Steggles, A. Ward, P. Webster, "The anatomy of a context-aware application," *Wireless Networks*, vol. 8, March 2002. 15

[110] M. Hazas and A. Ward, "A bovel broadband Ultrasonic Location System. in *Proceedings of Fourth International Conference on Ubiquitous Computing*, 2002, pp. 264—280. 15

[111] A. J. Higgins, "A dynamic tabu search for large-scale generalised assignment problems," *Comput. Oper. Res.*, vol. 28, pp. 1039-1048, 2001. 10

[112] C. Hillenbrand and K. Berns, "A climbing obot based on under pressure adhesion for the inspection of concrete walls," in *35th International Symposium on Robotics*, March 2004, pp. 119—123. 11

[113] A. Howard, "Multi-robot Simultaneous Localization and Mapping using Particle Filters," *The International Journal of Robotics Research*, vol. 25, pp. 1243—1256, Dec. 2006. 11

[114] A. Iborra, B. Alvarez, F. Ortiz, F. Marin, C. Fernandez and J.M. Fernandez-Merono, "Service robot for hull-blasting", *in Proc. of 27th Annual Conference of the IEEE Industrial Electronics Society*, 2001, pp. 2178—2183, 2001. 12, 18

[115] K. lkuta," Micromachine-its current state and future," *Micro-Machine System*, vol. 3, pp. 60—64, 1991. 7

[116] S. F. Jiang, C. M. Zhang and C. G. Koh, "Structural Damage Detection by Integrating Data Fusion and Probabilistic Neural Network," *Advances in Structural Engineering*, vol. 9, pp. 445—458, August 2006. 131

[117] L. Jetto, S. Longhi and D. Vitali, "Localization of a wheeled mobile robot by sensor data fusion based on a fuzzy logic adapted Kalman filter," *Control Eng. Pract.*, vol. 7, pp. 763—771, 1999. 16, 54

[118] V. Kaftandjian, Y.M. Zhu, O. Dupuis and D. Babot, "The Combined Use of the Evidence Theory and Fuzzy Logic for Improving Multimodal Nondestructive Testing Systems," *IEEE Transactions on Instrumentation and Measurement*, vol. 54, pp. 1968—1977, 2005. 131, 139

[119] J. B. Kammerer, L. Hbrard, V. Frick, P. Philippe and F. Braun, "Horizontal Hall Effect Sensor With High Maximum Absolute Sensitivity," IEEE *Sensors*, vol. 3, pp. 700—707, 2003. 162

[120] I. Kelly and A. Martinoli, "A scalable, on-board localisation and communication system for indoor multi-robot experiments," *Sensor Review*, vol. 24, pp. 167—180, 2004. 16

[121] J. Kim and J. Lee, "RISYS: An advanced reactor vessel inspection system with underwater mobile robots," Korea Atomic Energy Research Institute, Taejon, Korea, 2000. 18

[122] D. Kim, L. Udpa and S. Udpa, "Remote field eddy current testing for detection of stress corrosion cracks in gas transmission pipelines," *Materials Letters*, vol. 58, pp. 2102 – 2104, 2004. 85

[123] K. Komoriya and E. Oyama, "Position estimation of a mobile robot using optical fiber gyroscope (OFG)," in *Proc. IEEE/RSJ Int. Conf. Intell. Robots Syst.*, Munich, Germany, Sep. 1994, pp. 143-149. 16

[124] M. Kowalski, P. Dutkiewicz, M. Lawniczak and M. Michalski, "SAFARI inspection robot motion strategy," in *Proceedings of the Third International Workshop on Robot Motion and Control*, 2002, pp. 93—100. 12

[125] M.J.B. Krieger, J.B. Billeter and L. Keller "Ant-like task allocation and recruitment in co-operative robots," in *Nature*, pp. 992—995, 2000. 9

227

[126] S. Krosuri and M. Minor, "A Multifunctional Hybrid Hip Joint for Improved Adaptability in Miniature Climbing Robots," in *IEEE International Conference on Robotics and Automation*, 2003, pp. 312—317. 12

[127] K. S. Kwok, B. J. Driessen, C. A. Phillips, and C. A. Tovey, "Analyzing the multiple-target-multiple-agent scenario using optimal assignment algorithms," *J. Intell. Robot. Syst.*, vol. 35, pp. 111–122, 2002. 10

[128] J.M. Lee, K. Son, M.C. Lee, J.W. Choi, S.H. Han and M.H. Lee, "Localization of a mobile robot using the image of a moving object, " *IEEE Transactions on Industrial Electronics*, vo. 50, pp. 612—619, June 2003. 16, 54

[129] K. Lerman, C. Jones, A. Galstyan and M.J. Matatic, "Analysis of Dynamic Task Allocation in Multi-Robot Systems," *The International Journal of Robotics Research*, vol. 25, pp.225—241, March 2006. 9

[130] Z. Li, J. Chen and J. Feng, "Design of an Omni-Directional Mobile Microrobot (OMMR-I) for a micro-factory with 2mm electromagnetic micromotors," *Robotica*, vol. 23, pp. 45—49, 2005. 8

[131] T. I. Lin and J. C. Lee, "Bayesian analysis of hierarchical linear mixed modeling using the multivariate t distribution," *Journal of Statistical Planning and Inference*, vol. 137, pp. 484—495, February 2007. 131

[132] D. Longo and G. Muscato, "The Alicia 3 Climbing Robot," *IEEE Robotics & Automation Magazine*, Special Issue on Climbing Robots, 2006. 12

[133] B.L. Luk, D.S. Cooke, S. Galt, A.A. Collie and S. Chen, "Intelligent legged climbing robot for remote maintenance applications in hazardeous environments," *Robotics and Autonomous Systems*, vol. 53, pp. 142—152, 2005. 12

[134] B.L. Luk, K.P. Liu, A.A. Collie, D.S. Cooke and S. Chen, "Tele-operated Climbing and Mobile Service Robots for Remote Inspection and Maintenance in Nuclear Industry," *Industrial Robot*, vol. 33, pp. 194—204, 2006. 12, 18, 19

[135] D. Mackay, "Information Theory, Inference, and Learning Algorithms," Cambridge University Press, 2003. 131

[136] J. Makar and R. Desnoyers, "Magnetic Field Techniques for the inspection of steel under concrete cover," *NDT&E International*, vol. 34, pp. 445—456, Oct. 2001. 103, 109

[137] R. Madhavan, K. Fregene and L.E. Parker, "Distributed heterogeneous outdoor multi-robot localization," Center for Eng. Syst. Adv. Res., Oak Ridge Nat. Lab., TN, USA, in IEEE International Conference on Robotics and Automation (ICRA), vol. 1, pp. 374—381, 2002 11

[138] X. Maldague, "Applications of Infrared Thermography in Nondestructive Evaluation," *Trends in Optical Nondestructive Testing*, Elsevier, pp. 591—609, 2000. 18

[139] J.A. Malpica, M.C. Alonso and M.A. Sanz, "DempsterShafer Theory in geographic information systems: A survey," *Expert Systems with Applications*, vol. 32, pp.47—55, January 2007. 131

[140] X. Maldague and P. Moore, "Infrared and Thermal Testing — Nondestructive Testing Handbook," 3rd edition, American Society for Nondestructive Testing, Columbus, Ohio, 2001. 18

[141] C. Mandache, L. Clapham, "A Model for Magnetic Flux Leakage signal predictions," *Journal of Physics D: Applied Physics*, vol. 36, pp. 2427—2431, 2003. 102, 103

[142] K. Mandal and D.L. Atherton, "A study of Magnetic Flux-Leakage signals," *Applied Physics*, vol 31, pp. 3211—3217, 1998. 1, 102, 103, 106

[143] W. Mao, L. Clapham and D.L. Atherton, "Effects of alignment of nearby corrosion pits on MFL," *NDT&E International*, vol. 36, pp. 111-116, 2003. 102

[144] A. Martinelli, "The accuracy on the parameter estimation of an odometry system of a mobile robot," in *Proc. IEEE Int. Conf. Robot. Autom.*, Washington, DC, May 2002, pp. 1378-1383.

[145] P. Maybeck, "Stochastic Models, Estimation and Control," vol. 1, Academic Press, 1979. 67, 68

[146] G. McComb, "The Robot Builder's Bonanza", New York, McGraw-Hill, 2000.

[147] P. J. McKerrow, "Introduction to Robotics", Singagpore, Addison-Wesley, 1993. 24

[148] R.C. McMaster, P. McIntire and M.L. Mester, "Nondestructive Testing Handbook", vol. 4, Electromagnetic Testing, 2nd edition, American Society for Nondestructive Testing, 1986.

[149] C. Menon, M. Murphy and M. Sitti, "Gecko Inspired Surface Climbing Robots", in *Proc. of IEEE International Conference on Robotics and Biomimetics*, 2004, pp. 431—436. 13

[150] C. Menon and M. Sitti, "A Biomimetic Climbing Robot Based on the Gecko," *Journal of Bionic Engineering*, vol. 3, pp. 115—125, September 2006. 13

[151] D. Mirshekar-Syahkal and R.F. Mostafavi, "1-D probe array for ACFM inspection of Large Metal Plates," *IEEE Transactions on Instrumentation and Measurement*, vol. 51 , pp. 374—382, 2002. 18

[152] K. Miya, "Recent Advancement of Electromagnetic Nondestructive Inspection Technology in Japan," *IEEE Transactions on Magnetics*, vol. 38., pp. 321—326, 2002. 85

[153] T. Miyake, and H. Ishihara," Mechanisms and basic properties of window cleaning robot," in *Proceedings of Advanced Intelligent Mechatronics*, 2003, pp. 1372—1377. 12

[154] N. Miyata, J. Ota, T. Arai, and H. Asama, "Cooperative transport by multiple mobile robots in unknown static environments associated with realtime task assignment," *IEEE Trans. Robot. Automat.*, vol. 18, no. 5, pp. 769-780, Oct. 2002. 10

[155] E.P. Mix, "Introduction to Nondestructive Testing," John Wiley & Sons, New York, 1987. ix, 86

[156] F. Mondada, M. Bonani, A. Guignard, S. Magnenat, C. Studer, and D. Floreano, "Superlinear physical performances in a SWARM-BOT," in *Proc. 8th Eur. Conf. Artif. Life*, Berlin, 2005, pp. 282–291. 10

[157] F. Mondada, L. M. Gambardella, D. Floreano, S. Nolfi, J.-L. Deneubourg, and M. Dorigo, "SWARM-BOTS: Physical interactions in collective robotics," *IEEE Robot. Autom. Mag.*, vol. 12, , pp. 21–28, 2005. 10

[158] A. Montgomery, P. Wild and L. Clapham, "Defect characterisation using magnetic flux leakage inspection of tailor-welded blanks, *Insight* Vol. 46, pp. 260—264, 2004. 151, 161

[159] A.I. Mourikis, and S.I. Roumeliotis, "Performance Analysis of Multirobot Cooperative Localisation," *IEEE Transactions on Robotics*, vol. 22, No. 4, pp. 666—681, 2006. 16

[160] Y. Nagaya, T. Takagi, T. Uchimoto and H. Haoyu, "Identification of Multiple Cracks from Eddy-Current testing signals with noise sources by image processing and inverse analysis," *IEEE Transactions on Magnetics*, vol. 40, pp. 1112—1115, 2004. 87

[161] L.E. Navarro–Serment, R. Grabowski, C.J. Paredis and P.K. Khosla, "Millibots," *IEEE Robotics and Automation Magazine*, vol. 9, pp. 31—40, 2002. 9, 37

[162] H. Nishikawa, T. Sasaya, T. Shibata, T. Kaneko, N. Mitumoto, S. Kawakita, and N. Kawahara, "In-pipe wireless micro locomotive system," in *Proc. of International Symposium on Micromechatronics and Human Science*, 1999, pp. 141—147. 8

[163] R. OGrady, R. Gro, M. Bonani, F. Mondada, and M. Dorigo, "Selfassembly on demand in a group of physical autonomous mobile robots navigating rough terrain," in *Proc. of 8th Eur. Conf. Artif. Life*, 2005, pp. 272–281. 10

[164] T. Oldberg, "Erratic Measure," *NDT.net — e-Journal of Nondestructive Testing*, vol. 4, No. 5, 1999. 20

[165] J. Orlin, "A polynomial-time primal network simplex algorithm for minimum cost flows," *in Proc. 7th Annu. ACM/SIAM Symp. Discrete Algorithms*, 1996, pp. 474–481. 10

[166] R.T. Pack, J.L. Christopher and K. Kawamura, "A Rubbertuator-Based Structure-Climbing Inspection Robot," in *Proc. of the IEEE International Conference on Robotics and Automation*, 1997, pp. 1869—1874. 11

[167] Z. Pan and Z. Zhu, "Miniature Pipe Robots," *Industrial Robot*, vol. 30, pp. 575—583, 2003. 7, 8, 12, 18

[168] G.S. Park and E.S. Park, "Improvement of the Sensor System in Magnetic Flux Leakage-Type Nondestructive Testing (NDT)," *IEEE Transactions on Magnetics*, vol. 38, pp. 1277—1280, 2002. 102, 103, 109

[169] E.M. Petriu, T.E. Whalen, R. Abielmona and A. Stewart, "Robotic Sensor Agents: a New Generation of Intelligent Agents for Complex Environment Monitoring, *IEEE Instrumentation & Measurement Magazine*, vol. 7, pp. 46—51, 2004. 9, 33

[170] E.M. Petriu, T.E. Whalen and R. Abielmona, "Autonomous robotic sensor agents, in *Proc. of 1st IEEE Int. Workshop on Robotic Sensing*, 2003. 9, 33

[171] E.M. Petriu, G.G. Patry, T.E. Whalen, A.H. Al-Dhaher, and V.Z. Groza, "Intelligent robotic sensor agents for environment monitoring," in *Proc. of IEEE Int. Symp. on Virtual Intelligent Measurement Syst.*, Girdwood, AK, pp. 14–19, May 2002. 9

[172] R. Polikar, L. Udpa, S. Udpa and V. Honavar, "An Incremental Learning Algorithm with Confidence Estimation for Automated Identification of NDE Signals," *IEEE Transactions on Ultrasonics, Ferroelectrics, and Frequency Control*, vol. 51, pp. 990—1001, 2004. 161

[173] N.B. Priyantha, "The Cricket Indoor Location System," PhD Thesis, Massachusetts Institute of Technology, June 2005. 57

[174] J. Pugh and A. Martinoli, "Relative localization and communication module for small-scale multi-robot systems," in *Proc. of IEEE International Conference on Robotics and Automation*, 2006, pp. 188—193. 16

[175] S. Qin and W. Cui, "Effect of corrosion models on the time-dependent reliability of steel plated elements," *Marine Structures*, No. 16, pp. 15—34, 2003. 1

[176] B. Quost, T. Denoeux and M. H. Masson, "Pairwise classifier combination using belief functions," *Pattern Recognition Letters*, vol. 28, pp. 644—653, April 2007. 131

[177] P. Ramuhalli, L. Udpa and S. Udpa, "Electromagnetic NDE Signal Inversion by Function-Approximation Neural Networks," *IEEE Transactions on Magnetics*, vol.38, pp. 3633—3643, Nov. 2002. 102

[178] G.N. Ranky, "Mobile Robot Sensor and Networking Design to Enable Cooperative Behaviour", *Industrial Robot*, vol. 34, pp. 21—25, 2007. 10, 33

[179] I.M. Rekleitis, G. Dudek and E.E. Milios, "Multi-robot cooperative localization: a study of trade-offs between efficiency and accuracy," in *Proc. of IEEE/RSJ International Conference on Intelligent Robots and System*, 2002, pp. 2690—2695. 11

[180] S. Roh, "Differential-drive in-pipe robot for moving inside urban gas pipelines," *IEEE Transactions On Robotics*, vol. 21, pp. 1—17, 2005.

[181] B. Rooks, "Robotics outside the metals industries," *Industrial Robot*, pp. 205—208, 2005. 1, 2

[182] G.L. Rosa, M. Messina, G. Muscato, G. and R. Sinatra, "A low-cost lightweight climbing robot for the inspection of vertical surfaces," *Mechatronics*, vol. 12, pp. 71—96, 2002. 11

[183] B. Ross, J. Bares and C. Fromme, "A Semi-Autonomous robot for stripping paint from large vessels," *The International Journal of Robotics Research*, vol. 22, pp. 617—626, August 2003. 18

[184] S.I. Roumeliotis, G. S. Sukhatme and G. A. Bekey, "Circumventing dynamic modeling: evaluation of the error-state Kalman filter applied to mobile robot localization," in *Proc. IEEE Int. Conf. on Robotics and Automation*, 1999, pp. 1656—1663. 16, 54

[185] S.I. Roumeliotis and G.A. Bekey, "Collective localization: a distributed Kalman filter approach tolocalization of groups of mobile robots," in *Proc. of Int. Conf. on Intelligent Robots and Systems*, 2001, pp. 2958—2965. 16

[186] N. Roy and S. Thrun, "Online self-calibration for mobile robots," in *Proc. IEEE Int. Conf. Robot. Autom.*, Detroit, MI, May 1999, pp. 2292-2297. 16

[187] P.E. Rybski, S. Stoeter, M. Gini, D.F. Hougen and N.P. Papanikolopoulos, "Performance of a Distributed Robotic System Using Shared Communication Channels," in *Proc. of IEEE International Conference on Robotics and Automation*, 2002, pp. 713—727. 9

[188] P.E. Rybski, N.P. Papanikolopoulos, S.A. Stoeter, D.G. Krantz, K.B. Yesin, M. Gini, R. Voyles, D.F. Hougen, B. Nelson and M.D. Erickson, "Enlisting rangers and scouts for reconnaissance and surveillance," *IEEE Robotics & Automation Magazine*, vol. 7, pp. 14—24, Dec. 2000. 9

[189] J. Snchez, F. Vzquez and E. Paz, "Machine vision guidance system for a modular climbing robot used in shipbuilding," in *Proc. of International Conference on Climbing and Walking Robots*, 2005. 12, 18, 23

[190] T. P. Sattar, H.E. Leon Rodriguez, J. Shang and B. Bridge, "Automated NDT of Floating Production Storage Oil Tanks with a Swimming and Climbing Robot," in *Proc. of 8th International Conference on Climbing and Walking Robots*, London, 2005. 2, 18, 19, 102, 146

[191] T.P. Sattar, M. Alaoui, S. Chen and B. Bridge, "A magnetically adhering wall climbing robot to perform continuous welding of long seams and non-destructively test the welds on the hull of a container ship," in *Proceedings of the Eighth IEEE Conference on Mechatronics and Machine Vision*, 2001, pp. 408-414. 2, 18, 19

[192] U. Scarfogliero, C. Stefanini and P. Dario, "A Bioinspired Concept for High Efficiency Locomotion in Micro Robots: the Jumping Robot Grillo," in *Proc. of IEEE International Conference on Robotics and Automation*, 2006, pp. 4037—4042. 24

[193] R. D. Schraft, A. Wolf and G. Schmierer, "A modular lightweight construction system for climbing robots", *First International Symposium on Climbing and Walking Robots*, November 26th-28th, Brussels, Belgium, 1998. 11

[194] R. Se-gon and H. Choi, "Strategy for navigation inside pipelines with differential-drive inpipe robot," in *Proc. of IEEE International Conference on Robotics and Automation* , 2002, pp. 2575—2580. 12, 18

[195] P. Seidel, S. Wunderlich, F. Schmidl and L. Doerrer, "Improvement of Spatial and Field Resolution in NDE Systems using Superconducting Sensors," *IEEE Transactions on Applied Superconductivity*, vol. 11, pp. 1176—1179, 2001. 85, 103

[196] G. Shafer, "A Mathematical Theory of Evidence," Princeton, NJ: Princeton University Press, 1976. 131

[197] S. Shoval, I. Zeitoun and E. Lenz, "Implementation of a Kalman filter in positioning for autonomous vehicles, and its sensitivity to the process parameters," *Int. J. Adv. Manuf. Technol.*, vol. 13, pp. 738-46, 1997. 16, 54, 67

[198] M. Siegel, "Scaling issues in robot-based sensing missions," in *Proceedings of the 20th IEEE Instrumentation and Measurement Technology Conference*, 2002, pp. 1497—1500. 7

[199] R. Siegwart and I. Nourbakhsh, "Introduction to Autonomous Mobile Robots", Cambridge, MIT Press, 2004. viii, 24, 26, 30, 31

[200] R. Simmons, D. Apfelbaum, W. Burgard, D. Fox, M. Moors, S. Thrun and H. Younes, "Coordination for Multi-Robot exploration and mapping," in *Proc. of the International Conference on Artificicial Intelligence*, Austin Tx, August 2000. 11

[201] C. Grasset-Simon, G. Damiand and P. Lienhardt, "nD generalized map pyramids: Definition, representations and basic operations," *Pattern Recognition*, vol. 39, pp. 527—538, April 2006. 131

[202] M. Sitti and R. Fearing, "Synthetic gecko foot-hair micro/nano-structures for future wall-climbing robots," in *Proc. of IEEE International Conference on Robotics and Automation*, 2003, pp. 1164—1170. 13

[203] M. Sitti, "Microscale and Nanoscale Robotic Systems," *IEEE Robotics and Automation Magazine*, vol. 14, pp. 53—60, March 2007. 13

[204] L. Shuliang, Z. Yanzheng, G. Xueshan, X. Dianguo and W. Yan, "A wall climbing robot with magnetic crawlers for sand-blasting. Spray-Painting and Measurement", *High Technology Letters*, vol. 10, pp. 86—88, 2000. 12

[205] A. Smith, H. Balakrishnan, M. Goraczko and N. Priyantha, "Tracking moving devices with the cricket location system," in *Proc. of 2nd Int. Conf. on Mobile Systems, Applications, and Services, Boston*, 2004, pp. 190—202. 16, 54, 57

[206] T. Sogi, Y. Kawaguchi, H. Morisaki, K. Ohkawa, N. Kai and H. Hayakawa, "Inspection robot for spherical storage tanks," in *Proc. of Conference of the IEEE Industrial Electronics Society*, 2000, pp. 393—398. 12, 18

[207] X. Song, X. Wu, X. and Y. Kang, "An Inspection Robot for Boiler Tube using Magnetic Flux Leakage and Ultrasonic Methods," *Insight*, vol. 46, pp. 275—277, 2004. 18, 19, 146

[208] F.W. Spencer, "Visual Inspection Research Project Report on Benchmark Inspections", Technical Report U.S. Department of Transportation, Federal Aviation Administration, Washington D.C., 1996. 17

[209] J. Spletzer, A.K. Das, R. Fierro, C.J. Taylor, V. Kumar and J.P. Ostrowski, " Cooperative localization and control for multi-robot manipulation," *in Proc. IEEE/RSJ International Conference on Intelligent Robots and Systems*, 2001, pp. 631—636. 16

[210] J.R. Spletzer and C.J. Taylor, "A bounded uncertainty approach to multi-robot localization," in *Proc. of IEEE/RSJ International Conference on Intelligent Robots and Systems*, 2003, pp. 1258—1265. 7

[211] S. Stoeter, and N.P. Papanikolopoulos, "Autonomous Stair-Climbing With Miniature Jumping Robots," *IEEE Transactions on Systems, Man, and Cybernetics*, vol. 35, pp. 313—323, 2005. 9

[212] A. Stoytchev and R. C. Arkin, "Dynamic task assignment in a multiagent/multitask environment based on module conflict resolution," Proc. *IEEE Int. Conf. Robotics and Automation*, Seoul, Korea, May 2001, vol. 4, pp. 3987–3992. 10

[213] M. Studer and K. Peters, "Multi-scale sensing for damage identification," *Smart Materials and Structures*, vol. 13, pp. 283—294, April 2004.

[214] K. Suzumori, S. Wakimoto and M. Takata," A miniature inspection robot negotiating pipes of widely varying diameter, in *Proc. of IEEE International Conference on Robotics and Automation*, 2003, pp. 2735—2740. 12, 18

[215] J. Tao, Q. Peiwen and T. Zhengsu, "Development of Magnetic Flux Leakage pipe inspection robot using Hall sensors," in *Proc. of IEEE Int. Symp. on Micro-Nanomechatronics and Human Science*, 2004, pp. 325—329. 18, 20, 102, 146

[216] H. Takahashi, M. Morisawa, and K. Ohnishi, "Mobility of a mobile robot, Dept. of Syst. Design Eng.," in *Proc. of 8th IEEE International Workshop on Advanced Motion Control*," 2004, pp. 253—257. 24

[217] M. Takeda, K. Namura, K. Nakamura, N. Shibaike, T. Haga and H. Takada, "Development of Chain-Type Micromachine for Inspection of Outer Tube Surfaces", in *Proc. of 13th Annual International Conference on Micro Electro Mechanical Systems*, pp. 805—810, 2000. 18, 87

[218] N.A. Thacker and A.J. Lacey, "Tutorial: The Likelihood Interpretation of the Kalman Filter," Imaging Science and Biomedical Engineering Division, Medical School, University of Manchester, May 2006. 67

[219] Y.K. Tham, H. Wang and E. Teoh, "Multi-sensor fusion for steerable four-wheeled industrial vehicles," *Control Eng. Pract.*, vol. 7, pp. 1233—48, 1999. 16

[220] J.M. Thomson, "An Eddy Current Array Instrument for Offshore Application," PhD Thesis, University of Strathclyde, Centre for Ultrasonic Engineering, 1991. 87, 89, 93

[221] S. Thrun, W. Burgard and D. Fox, "Probabilistic Robotics," MIT Press, Cambridge, 2005. 67

[222] R. Tinos, L.E. Navarro-Serment and C.J.J. Paredis, "Fault tolerant localization for teams of distributed robots," in *Proc. of IEEE/RSJ International Conference on Intelligent Robots and Systems*, 2001, pp. 1061—1066. 9

[223] D.J. Todd, "Walking machines, and Introduction to Legged Robots", Kogan Page Ltd, 1985.

[224] C.C. Tsai, "A localization system of a mobile robot by fusing dead-reckoning and ultrasonic measurements," *IEEE Transactions on Instrumentation and Measurement*, vol. 47, pp. 1399—1404, Oct. 1998.

[225] S.K. Tso, Y.H. Fung, W.L. Chow, G.H. Zong and R. Liu, "Design and Implementation of a Glass-wall Cleaning Robot for Highrise Buildings," in *Proceedings of the World Automation Congress Eighth International Symposium on Robotics with Applications*, 2000, Paper ID: ISORA123. 12

234

[226] S.K. Tso, J. Zhu and B.L. Luk, "Prototype Design of a Light-Weight Climbing Robot Capable of Continuous Motion," in *Proceedings of the Eighth IEEE Conference on Mechatronics and Machine Vision in Practice*, 2001, pp. 235238. 12

[227] S.K. Tso, K.L. Fan, Y.H. Fung, L. Han, D.W. Tang, K.P. Liu and F. Tong, "Inspection of large tile walls for high-rise buildings based on a mechatronic mobile system," in *Proc. of IEEE International Conference on Advanced Intelligent Mechatronics*, 2003, pp. 669—672. 12

[228] E. Tuci, R. Gro, V. Trianni, M. Bonani, F. Mondada, and M. Dorigo, "Cooperation through self-assembling in multi-robot systems," *ACM Trans. Auton. Adapt. Syst.*, vol. 1, 2006. 10

[229] P. Ulam and R.C. Arkin, "When good communication go bad: communications recovery for multi-robot teams,"in *Proc. of IEEE International Conference on Robotics and Automation* , 2004, pp. 3727—3734. 7

[230] M. O. Ulfarrson, J. A. Benediktsson and J. R. Sveinsson, "Data fusion and feature extraction in the wavelet domain," *Int. Journal of Remote Sensing*, vol. 24, pp. 3933–3945, 2003. 131

[231] O. Unver, A. Uneri, A. Aydemir and M. Sitti, "Geckobot: a Gecko Inspired Climbing Robot Using Elastomer Adhesives," in*Proc. of IEEE International Conference on Robotics and Automation*, 2006, pp. 2329—2335. 13

[232] D. Vasic, V. Bilas and D. Ambrus, "Pulsed Eddy-Current Nondestructive Testing of Ferromagnetic Tubes," *IEEE Transactions on Instrumentation and Measurement*, vol. 53, pp. 1289—1294, 2004. 87

[233] I.A. Viktorov, "Rayleigh and Lamb waves - Physical theory and applications", Plenum Press, New York, 1967. 128

[234] G. S. Virk, "CLAWAR design tools to support modular robot design," in *Proc. of 8th International Conference on Climbing and Walking Robots*, London, 2005. 33

[235] R. Want, A. Hopper, V. Falco and J. Gibbons, "The active badge location system, Association for Computing Machinery (ACM)," *Transactions on Information Systems*, vol. 10, pp. 91—102, 1992.

[236] G. Wei and C. Jianxin, "A Transducer Made Up of Fluxgate Sensors for Testing Wire Rope Defects," *IEEE Transactions on Instrumentation and Measurement*, vol. 51, pp. 120—124, 2001. 102, 106

[237] J. Wein and S. A. Zenios, "Massively parallel auction algorithms for the assignment problem," in *Proc. 3rd Symp. Frontiers of Massively Parallel Computation*, Nov. 1990, pp. 90–99. 10

[238] G. Welch, and G. Bishop. "An Introduction to the Kalman Filter," Department of Computer Science, University of North Carolina, Chapel Hill, 2004. 69

[239] B. Wincheski, J. Simpson, E. Scales and R. Louie, "Development of giant magnetoresistive inspection system for detection of deep fatique cracks under airframe fasteners," *Review of Progress in Quantitative NDE*, vol. 21A, pp. 1007—1010, 2002. 85

[240] S.E. Wright, D. Sanders and S. Chen, "Predicting terrain Contours Using a Feed-Forward Neural Network,", *Engineering Applications of Artifcial Intelligence*, vol. 16, pp. 465–472, 2003. 12

[241] J.M. Sabater, R.J. Saltaren, R. Aracil, E. Yime and J. Azorin, "Teleoperated parallel climbing robots in nuclear installations," *Industrial Robot*, vol. 33, pp. 381—386, 2006.

[242] R. Saltaren, R. Aracil, O. Reinoso and M.A. Scarano, "Climbing parallel robot: a computational and experimental study of its performance around structural nodes." *IEEE Transactions on Robotics*, vol. 21, pp. 1056—1066, Dec. 2005. 13

[243] H. Schempf, B. Chemel and N. Everett, "Neptune: above-ground storage tank inspection robot System," in IEEE Robotics & Automation Magazine, vol. 2, pp. 9—15, 1995. 19

[244] W. Shen, J. Gu and Y. Shen, "Permanent magnetic system design for the wall-climbing robot," in *Proc. of IEEE International Conference on Mechatronics and Automation*, vol. 4, pp. 2078—2083, 2005. 12

[245] W. Shen; J. Gu and Y. Shen, "Proposed wall climbing robot with permanent magnetic tracks for inspecting oil tanks," in *Proc. of IEEE International Conference Mechatronics and Automation*, vol. 4, pp. 2072—2077, 2005. 12

[246] R.L. Tummala, R. Mukherjee, X. Ning, D. Aslam, H. Dulimarta, X. Jizhong, M. Minor and G. Dang, "Climbing the Walls," *IEEE Robotics and Automation Magazine*, vol. 9, pp.10—19, Dec. 2002. 12

[247] J. Xiao, M. Minor, H. Dulimarta, N. Xi, R. Mukherjee and R.L. Tummala, "Modeling and Control of an Under-actuated Miniature Crawler Robot," in *Proc. of IEEE International Conference on Intelligent Robots and Systems*, vol. 3, pp. 1546—1551, Nov. 2001. 12

[248] J. Xiao, N. Xi, J. Xiao, J. Tan, "Multi-sensor referenced gait control of a miniature climbing robot," in *Proc. of IEEE/RSJ International Conference on Intelligent Robots and Systems*, 2003, pp. 3656—3661. 12

[249] J. Xiao; A. Calle, A. Sadegh, A. and M. Elliott, "Modular wall Climbing Robots with Transition Capability", in *Proc. of IEEE International Conference on Robotics and Biomimetics*, 2005, pp. 246—250. 13

[250] T. Yano, T. Suwa, M. Murakami and T. Yamamoto, "Development of a Semi Self-Contained Wall Climbing Robot with Scanning Type Cups," in *Proc. of the Intelligent Robot Systems Conference*, 1997, pp. 900—905. 11

[251] K. Yu and J. Stander, "Bayesian analysis of a Tobit quantile regression model," *Journal of Econometrics*, vol. 137, pp. 260—276, March 2007. 131

[252] N. Yusa, Z. Chen, K. Miya, T. Uchimoto, and T. Takagi, "Large-scale Parallel Computation for the Reconstruction of Natural Stress Corrosion Cracks from Eddy Current Testing Signals," *NDT&E International*, vol. 36, pp. 449—459, 2004. 85

[253] A. Zagler, F. Pfeiffer, "MORITZ: a pipe crawler for tube junctions," in: *Proc. of IEEE International Conference on Robotics and Automation*, 2003, pp. 2954–2960. 12

[254] H. Zhang, S. Dong, Z. Shu-yi, T. Wang, Z. Zhang and L. Fan, "Ultrasonic Micro-Motor Using Miniature Piezoelectric Tube with Diameter of 1.0 mm," *Ultrasonics*, vol. 44, pp. 603–606, 2006. 40

[255] Q.X. Zhang, Z.G. Ren and Z.W. Zhao, "Development of a 3W window-cleaning robot for high-rise buildings," in *Proceedings of the Eighth IEEE Conference on Mechatronics and Machine Vision in Practice*, pp. 257–260, 2001. 12

[256] H. Zhang, J. Zhang, G. Zong, W.Wang and R. Liu, "Sky Cleaner 3: a Real Pneumatic Climbing Robot for Glass-Wall Cleaning, *IEEE Robotics & Automation Magazine*, vol. 13, pp. 32—41, March 2006. 12

[257] Y. Zhang and G. Yan, "In-pipe Inspection Robot with Active Pipe-Diameter Adaptability and Automatic Tractive Force Adjusting," *Mechanism and Machine Theory*, doi:10.1016/j.mechmachtheory.2006.12.004, 2007. 12

[258] Yanzheng Zhao, Zhuang Fu, Qixin Cao and Yan Wang, "Development and Applications of Wall-Climbing Robots with a Single Suction Cup," *Robotica*, vol. 22, pp. 643—648, Nov 2004. 11

[259] H. Zhou and S. Sakane, "Sensor planning for mobile robot localization based on probabilistic inference using Bayesian network," in *Proc. 4th IEEE Int. Symp. Assembly and Task Planning*, May 2001, pp. 7–12. 16

[260] A. Zhu and S. X. Yang, "A Neural Network Approach to Dynamic Task Assignment of Multirobots," *IEEE Trans. on Neural Networks*, vol. 17, pp. 1278—1287, Sept. 2006. 10

[261] C. Zhu, "In-pipe Robot for Inspection and Sampling Tasks," *Industrial Robot*, vol. 37, pp. 39—45, 2007. 12

[262] R. Zlot, A. Stentz, M.B. Dias and S. Thayer, "Multi-robot exploration controlled by a market economy," in Proc. of IEEE International Conference on Robotics and Automation, 2002, pp. 3016-3023. 11

[263] Cricket v2 User Manual, Cricket Project, MIT Computer Science and Artificial Intelligence Lab Cambridge, MA 02139, January 2005 58, 75

[264] www.a-drive.de, 28.5.2007 156

[265] www.accurexmeasure.com/indoor_laser_gps.htm, 23.2.2007 15

[266] www.advanced-ndt.co.uk, 23.2.2007 146

[267] www.ais4ndt.com, 23.2.2007 12

[268] www.allegromicro.com, 23.2.2007 103

[269] www.ansoft.com, 23.2.2007 104, 105

[270] www.ansys.com, 23.2.2007 104

[271] www.clarifyingtech.com/public/robots/robots_public.html, 22.2.2007 13

[272] www.comsol.com, 23.2.2007 104

[273] www.cosmosm.com, 23.2.2007 104

[274] www.diracdelta.co.uk/science/source/f/r/friction/source.html, 23.2.2007 47

[275] www.engineershandbook.com/Tables/frictioncoefficients.htm, 23.2.2007 47

[276] www.engr.uvic.ca/~pmauro/, 22.2.2007 11

[277] www.faulhaber.de, 23.2.2007 40, 153, 156

[278] www.hilgraeve.com/index.html, 23.2.2007 58

[279] www.imagecraft.com, 23.2.2007 34

[280] www.infolytica.com, 23.2.2007 104

[281] www.intersense.com, 23.2.2007 15, 163

[282] www.inuktun.com/nanomag.htm, 23.2.2007 12

[283] www.kokam.com/english/product/kokam_Lipo_02.html, 23.2.2007 xi, 148

[284] www.megatron.de, 23.2.2007 41

[285] www.metris.com, 6.6. 2007 150

[286] www.ndtint.com/crawl.htm, 23.2.2007 12

[287] www.info.newscientist.com/article.php?c_id=6831&jlnk=csl1030, 23.2.2007 1

[288] http://investing.reuters.co.uk, 13.3.2007 1

[289] www.nms.lcs.mit.edu/cricket/, 23.2.2007 15, 57, 59, 148

[290] www.omniinstruments.co.uk/gyro/gyro.html, 23.2.2007

[291] www.paric.co.nz/index.html, 23.2.2007 16

[292] www.ptc.com, 23.2.2007 46

[293] www.quickfield.com, 23.2.2007 104

[294] www.robotic.diees.unict.it/robots/venom/venom.htm, 23.2.2007 12

[295] www.romanlab.com, 23.2.2007

[296] www.sonitor.com, 23.2.2007 15

[297] www.technologicalarts.com/myfiles/microload.html 25.2.2007 34

[298] www.ubisense.net, 23.2.2007

[299] www.usdigital.com/products/e4/index.shtml, 23.2.2007 41

[300] www.vectorfields.com, 23.2.2007 104

[301] EU project IST-2001-33567 8